

PAPER

Solar energy utilization in the direct photocarboxylation of 2,3-dihydrofuran using CO₂

Michele Aresta,^{ab} Angela Dibenedetto,^{bc} Tomasz Baran,^{bd}
Szymon Wojtyła^d and Wojciech Macyk^d

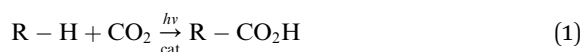
Received 23rd April 2015, Accepted 1st July 2015

DOI: 10.1039/c5fd00040h

The conversion of CO₂ into high energy products (fuels) and the direct carboxylation of C–H bonds require a high energy input. Energy cannot be derived from fossil carbon, in this case. Solar energy can be used instead, with a low environmental impact and good profit. We have studied the use of white light or solar energy in the photoreduction of CO₂ and in photocarboxylation reactions, using different semiconductors modified at their surface. Two examples of reduction of CO₂ to methanol and CO will be summarized, and two cases of carboxylation of organic substrates. The case of carboxylation of 2,3-dihydrofuran will be discussed in detail.

Introduction

Today, the introduction of a carboxylic group into an organic molecule occurs *via* synthetic methodologies characterized by low Carbon Fraction Utilization (CFU) and high Carbon Footprint (CF). Some years ago, we undertook a critical analysis of such issues and suggested that the direct carboxylation of C–H bonds (eqn (1)) represents one of the most effective ways to reduce CO₂ emissions and save fossil carbon.^{1,2} Such new syntheses may require a quite different approach than thermal reactions. In fact, a critical barrier that can occur for the reaction, represented by C–H activation, must be overcome. The use of the photochemical technology may be of great help, if photocatalysts able to activate the C–H bond using visible light are developed (eqn (1)).



^aChBE, NUS, 4 Engineering Drive 4, Singapore 117585, Singapore

^bIC²R, Tecnopolis, via Casamassima km3, Valenzano 70018, Bari, Italy

^cCIRCC, Via Celso Ulpiani 27, Bari 70126, Italy

^dFaculty of Chemistry, Jagiellonian University in Kraków, Ingardena 3, 30-060 Kraków, Poland

On the other hand, CO₂ can be used as a source of carbon for the production of C₁ and C_n energy rich molecules, a process that would also be of great interest if fossil carbon was not used to provide the energy required for the reduction to occur, and if the hydrogen was sourced from water or waste organics. Furthermore, the use of solar energy as a primary energy source would be of fundamental importance.³

We have started a programme on the photochemical conversion of CO₂ using newly synthesized semiconductor-based photocatalysts that are able to operate under visible and/or solar light and have applied such systems to a number of reactions implying CO₂ conversion: either fixation into organic substrates of the entire molecule, or reduction to C₁ and C_n molecules using water or abundant and cheap polyols as a source of hydrogen.

Fig. 1 shows the matching of some semiconductor band gaps and CO₂ reduction potentials in 2ne⁻ transfer processes in water compared to the higher energy 1e⁻ transfer.⁴

In this paper we recall the concept on which the catalysts are based on and present some very recent applications in both carboxylation reactions and CO₂ reductions. We discuss new results relevant to the carboxylation of a quite intriguing substrate, 2,3-dihydrofuran (2,3-DHF).

The new-concept photocatalysts and their application

The photocatalysts have been engineered by carrying out a surface modification of semiconductors such as TiO₂, ZnS and several others. As Fig. 1 shows, TiO₂ has a band gap energy of 3.2 eV that makes it not particularly suited for visible light utilization in CO₂ conversion. In fact, TiO₂ alone is better used under UV irradiation in oxidation processes that convert recalcitrant pollutant organics either in water or in air, thus producing CO₂. Moreover, due to a high oxidation potential of holes photoinduced in the valence band of titanium dioxide, reoxidation of the reduction product is plausible. The use of UV-light in CO₂ conversion would not be an efficient use of solar light, making the process both economically not viable

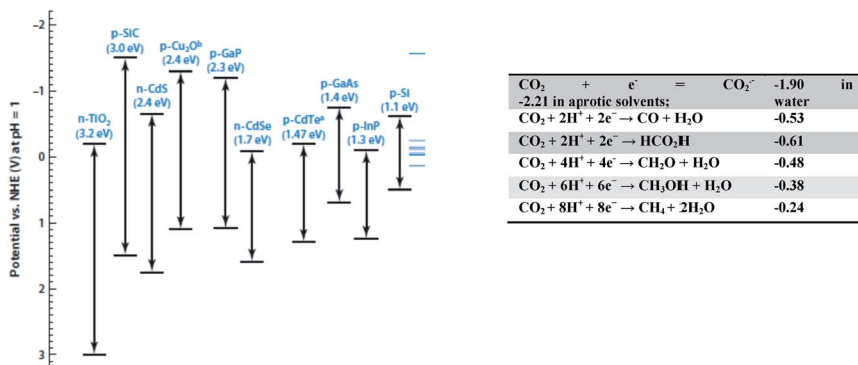


Fig. 1 Comparison of the band gap energies of some semiconductors with the reduction potentials of CO₂ in aqueous solutions (pH = 1) for selected one- and multi-electron transfer processes.⁴

1 and environmentally not acceptable. Nevertheless, it is possible to modify the
spectral properties of titanium dioxide in several modes, as shown in Fig. 2.

5 Modifications of semiconductors with species that are either “hole” (to the VB)
or “electron” (to the CB) injectors may sensibly extend the spectral response of the
photocatalysts and enhance their use with exploitation of solar light. This concept
may be applied to a number of semiconductors which do not absorb in the visible
region, but more in the UV. So, TiO₂ modified with fluorochromates has been
10 advantageously used in the reduction of NAD⁺ into NADH used as an “e⁻ and H⁺”
vector to enzymes which reduce CO₂ to methanol.⁵⁻⁷

15 Another approach to enhance solar light utilization is to increase the quantum
efficiency of processes driven by near-UV light (*e.g.* within the range of 320–400
nm) instead of questing for broadening the spectral response of the wide band
gap semiconductors. This goal can be achieved for instance by surface functional-
ization of semiconductors with co-catalysts improving efficiency of charge
separation and interfacial electron transfer processes. For example, nano-
particles of elemental platinum deposited on the surface of TiO₂ act as electron
sinks and enhance photoreduction of the adsorbed electron acceptor (*e.g.* O₂).⁸⁻¹¹
20 A similar methodology was successfully applied by us to zinc sulfide photo-
catalysts. As mentioned above, ZnS is an interesting photomaterial having a band
gap energy larger than TiO₂ (3.6 *vs.* 3.2 eV). Due to its redox properties, it may have
a good potential for C–H activation. Unfortunately, ZnS alone does not show good
photoactivity. However, we have synthesized ZnS decorated with Ru nanoparticles¹²
and used it for the carboxylation of C–H bonds with a different activation
25 energy: either activated CH₂ moieties as in CH₃COCH₂COCH₃ (acac) or
terminal CH₃, as shown in eqn (2).

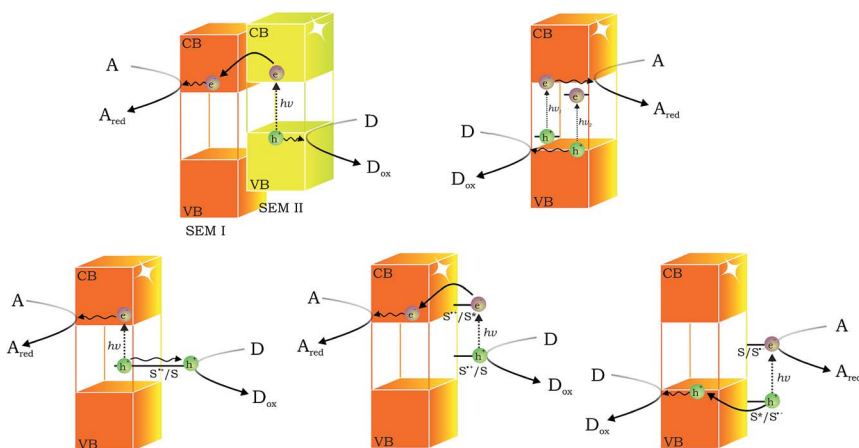
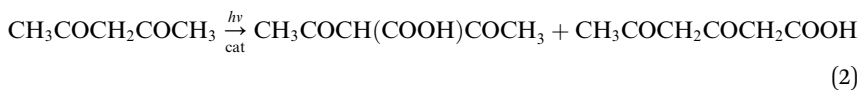


Fig. 2 Mechanisms of wide band gap semiconductor photosensitization. (A) Formation of composite semiconductors, (B) bulk doping resulting in the formation of acceptor or donor levels, (C) direct photosensitization (optical charge transfer), (D) dye-photosensitization involving an electron injection to the conduction band from the excited photosensitizer, (E) dye-photosensitization involving a hole injection to the valence band from the excited photosensitizer.



In this photochemical process the formation of the radical anion $\text{CO}_2^{\cdot-}$ has been demonstrated to be the key issue. The photomaterial used (ZnS) has the correct band gap energy for its generation, while Ru enhances the light harvesting capacity and drives the carboxylation reaction under sunlight irradiation. It is worth noting that acetylacetone can be carboxylated using chemical catalysts (typically a base such as the phenate anion) and affords only $\text{CH}_3\text{COCH}(\text{COOH})\text{COCH}_3$. The use of the photocatalyst enables the activation of the C–H bond of the terminal methyl group, affording the terminal carboxylic acid $\text{CH}_3\text{COCH}_2\text{COCH}_2\text{COOH}$. It is noteworthy that the C–H bonding energy is quite different in the CH_2 and CH_3 moieties. The former is activated due to tautomerism that brings the hydrogen onto the oxygen atom (eqn (3)). In the presence of bases, the OH moiety is deprotonized and prompted to interact with CO_2 . The terminal- CH_3 moiety is not activated and does not react in thermal reactions, but it does in photochemical processes.



ZnS decorated with ruthenium and p-type photocatalysts built on the same concept have been found to be active in the photoreduction of carbon dioxide to formic acid and carbon monoxide¹³ in protic solvents. p-Type semiconductors, in contrast to n-type materials, have rarely been studied for carbon dioxide conversion. We have found that wide-band gap semiconductors (like CuI and NiO) characterized by a band gap energy of 3.6–4.0 eV and a very low potential of the conduction band edge (in the range of –3.0 to –3.4 V vs. SHE) or also materials having a band gap energy equal to 3.1 eV and the potential of conduction band edge of –2.1 V vs. SHE can be usefully applied in the photoreduction of CO_2 .¹⁴ For example, under full solar light irradiation using isopropanol as the hole scavenger, CO_2 was reduced to CO, CH_4 and/or HCOOH. The preparation method (annealing temperature) plays a key role in determining the activity of the catalyst and its selectivity towards one of the products.

Results and discussion

Characterization of the catalysts

The properties of Ru@ZnS-A and Ru@ZnS-B used in this work have already been published.^{12,13} Here, we report some new additional properties that have recently been determined, namely the diffuse reflectance spectra and the photocurrent measurement, which are useful for determining the spectral region within which the catalysts are active, and the EDX analysis. The band gap energies were estimated from diffuse reflectance spectroscopy. Obtained spectra (reflectance, R , vs. wavelength, λ) have been transformed to Kubelka–Munk function (KM) according to the equation: $\text{KM} = (1 - R)^2/2R$ (Fig. 3). Spectra of bare ZnS and materials decorated with ruthenium are similar, *i.e.* ruthenium does not influence the absorption onset. The band gap energy was calculated according to Tauc theory as published elsewhere.^{12,13} ZnS-A shows a smaller bandgap energy (3.47 eV) than

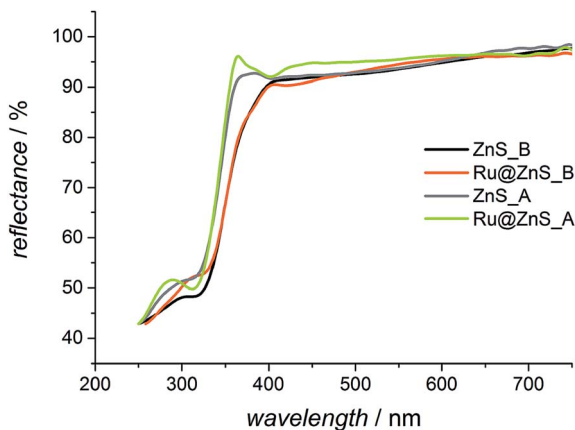


Fig. 3 Diffuse reflectance spectra of the synthesized photocatalysts transferred to Kubelka–Munk function.

ZnS-B (3.64 eV). Materials decorated with ruthenium (0.5% of Ru) have band gap energies of 3.57 and 3.65 eV for Ru@ZnS-A and Ru@ZnS-B, respectively. The prepared materials offer strong reduction properties (for example, the conduction band edge of ZnS-B is *ca.* -2.5 V vs. SHE) as learnt from spectroelectrochemical measurements published elsewhere.¹³

UV-Vis analysis nicely corresponds to the results of photocurrent measurements. Irradiation of the ZnS-A-covered electrode with near-UV-Vis light (solar light) results in anodic photocurrent generation (375 nm track), as shown in Fig. 4. The use of only visible light decreases the intensity of the photocurrent (see wavelength 405 and 465 nm in Fig. 4). Application of light of longer wavelengths, 520, 595 and 630 nm, did not result in photocurrent generation.

The characterization of materials has been done by EDX analysis. Energy-dispersive X-ray spectra of ZnS-A and 1%Ru@ZnS-A are shown in Fig. 5. Both materials show typical signals of zinc and sulphur. Moreover, the spectrum of 1%

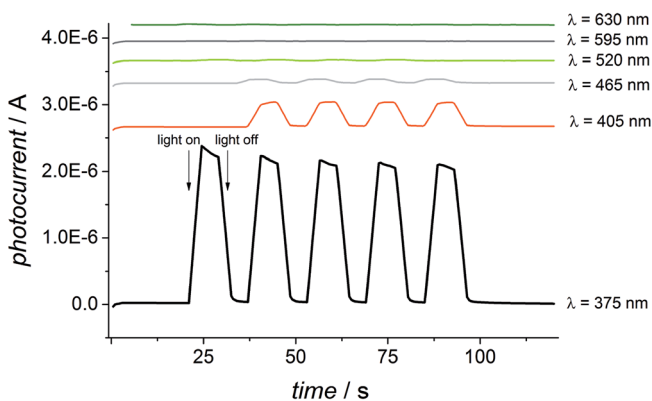


Fig. 4 Photocurrent measurements: ZnS-A electrode irradiated with chopped light of 375, 405, 465, 520, 595, 630 nm wavelength.

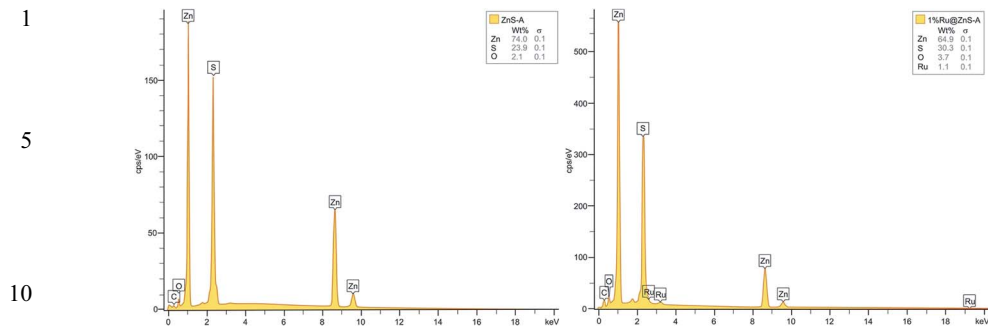


Fig. 5 Energy-dispersive X-ray spectra of ZnS-A and 1%Ru@ZnS-A.

Ru@ZnS-A also shows signals assigned to ruthenium (2.69 and 19.27 keV). Raman spectroscopy excluded the formation of ruthenium(IV) oxide, since bands at 515 and 626 cm^{-1} , characteristic for this compound (RuO stretching modes) were not found. This is in accordance with the XRD features of the materials,¹² previously published, which confirm the presence of Ru(0).

The SEM image of Ru@ZnS-A (Fig. 6) shows that the material is composed of irregular aggregates of various sizes ranging from several nanometers up to 4 micrometers. DLS measurements prove that the average particle sizes are in the range of hundreds of nanometers. SEM-EDX analysis proves the chemical composition of the material. All materials have relatively high specific surface areas (BET measurements) in the range of 55–105 $\text{m}^2 \text{g}^{-1}$, as published elsewhere.¹² The specific surface area of the ZnS samples decorated with ruthenium is reduced when compared to bare materials.

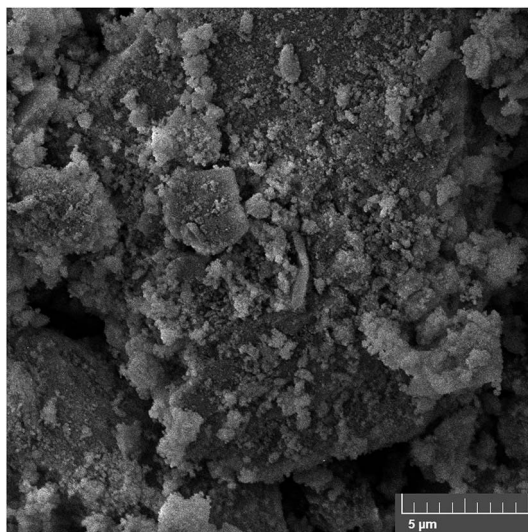


Fig. 6 SEM of Ru@ZnS-A.

The target molecule and the observed reactions

In this paper, we focus on the discussion of the photoconversion of intriguing molecules, such as 2,3-dihydrofuran (2,3-DHF) (Fig. 7), at room temperature under inert gas or in the presence of CO₂ dissolved in aprotic or protic solvents.

DHF is an interesting molecule as it contains a multiplicity of bonds having quite different energies. Table 1 shows the nature of the bonds and their average energies.

Thus, this molecule has several reactive sites. Despite such complexity, it is foreseeable that the most reactive position will be the allylic –CH₂– moiety, corresponding to the lower energy of the C–H bond, while C–C and C–O bond splitting may occur as secondary events (Table 1). However, in principle, H-extraction should occur, and occurs, at C-4, affording an allylic radical (Fig. 8). In order to check whether the photocatalyst would be able to promote C–H bond cleavage, we carried out a cyclic-voltammetry (CV) analysis. The CV measurements on a solution of 2,3-DHF are shown in Fig. 9. The voltammogram shows an irreversible peak at 1.35 V *versus* the non-aqueous silver electrode (Ag/Ag⁺), corresponding to the oxidation of 2,3-DHF. The oxidation potential of 2,3-DHF (1.55 V *vs.* SHE) is lower than the potential of the ZnS valence band edge (1.8 V *vs.* SHE²⁰), thus the photoinduced oxidation of 2,3-DHF by VB holes is thermodynamically possible.

Such species can evolve in two different ways (Fig. 10), affording either 2,5-dihydrofuran (2,5-DHF) or, *via* a C–O splitting and structural rearrangement, the formyl-cyclopropane molecule (F-Cyp), or even the linear crotonaldehyde (C-ald). Such photoinduced-isomerization products have been observed when 2,3-DHF was directly irradiated using UV-light.¹⁸

We now show that white (solar) light in the presence of a photocatalyst can induce the isomerization. This adds a complexity to the system as one can ask if the interaction of the substrate with CO₂ will occur prior to or after isomerization of the substrate and, thus, whether carboxylated forms of the rearrangement products can also be expected. Therefore, we have investigated the reactivity of the pure substrate and the reactivity of it in the presence of CO₂ under the same experimental conditions (solvent, radiations, irradiation time, temperature, concentration). The study was carried out at a double scale: at a micro-scale in a pressurized NMR tube and in a larger photoreactor having a volume of 10 mL, allowing sample withdrawal for GC analysis. Moreover, in order to establish if proton donors may influence the reaction, two different solvents were used, chloroform and methanol. We shall discuss the behaviour of 2,3-DHF in the two solvents separately, comparing the role of Ru@ZnS-A and Ru@ZnS-B.

Photocarboxylation in chloroform

Fig. 11a shows the modification of the ¹³C NMR spectrum of 2,3-DHF during irradiation under an Ar atmosphere, in chloroform, in presence of Ru@ZnS-A.



Fig. 7 The 2,3-dihydrofuran molecule.

Table 1 Bonds in 2,3-dihydrofuran and their average energy in kJ mol^{-1}

Bond	Number of bonds	Average energy kJ mol^{-1}	Ref.
$\text{sp}^3\text{C}-\text{sp}^3\text{C}$	1	346	15
$\text{sp}^3\text{C}-\text{sp}^2\text{C}$	1	386–390	16
$\text{sp}^2\text{C}-\text{sp}^2\text{C}$	1	610	15
$\text{sp}^3\text{C}-\text{H}$	4	411	17
$\text{sp}^2\text{C}-\text{H}$	2	422	18
$\text{sp}^3\text{C}-\text{O}$	1	358	15
$\text{sp}^2\text{C}-\text{O}$	1	418	19

Fig. 11b shows the same system when Ru@ZnS-B is used. It is noteworthy that within 2 h of irradiation, in the presence of Ru@ZnS-A , all of the starting substrate is converted (disappearance of resonances at 146, 99.5, 69.5 and 29.3 ppm typical of 2,3-DHF). Two major products are formed, namely, 2,5-DHF (signals at 104 and 63 ppm) and formylcyclopropane, which are identified through the signals at 205, 31 and 14 ppm. Crotonaldehyde, the alternative isomerization product derived from ring-opening, is absent as its resonances at 194.4, 154.3, 134.6 and 18 ppm are not found in the spectrum.²¹ Other very minor products are also formed (*ca.* 1% yield), while signals of ethanol are present from the beginning, most probably an impurity derived from the work-up of the photocatalysts. Interestingly, the use of Ru@ZnS-B increases the amount of formylcyclopropane, while producing the same isomerization products. It is worth noting, that the NMR spectra do not show any change with respect to starting 2,3-DHF in the absence of irradiation and in the presence of the photocatalyst.

Fig. 11 presents the products formed in CHCl_3 when the photoconversion is carried out under 0.7 MPa of CO_2 in a high pressure NMR-sapphire tube using Ru@ZnS-B as the photocatalyst. Ru@ZnS-A gives the same products, but at lower concentrations. As well as the signals due to the isomerization products, it is quite evident that the insurgence of some new signals, some of which can be ascribed to species formed upon incorporation of CO_2 . In particular, the signals at 178, 144, 100, 62 and 50 ppm are due to the new species. A careful comparison of the ^{13}C -spectra of the reaction solution with those of the photoisomerization products found under Ar, and then of the expected carboxylation products, brings us to the conclusion that the major photocarboxylation product is 2,5-dihydrofuran-2-

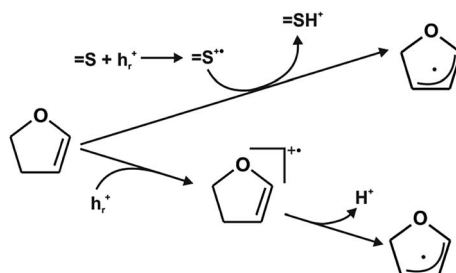


Fig. 8 Radical formation in 2,3-DHF upon irradiation.

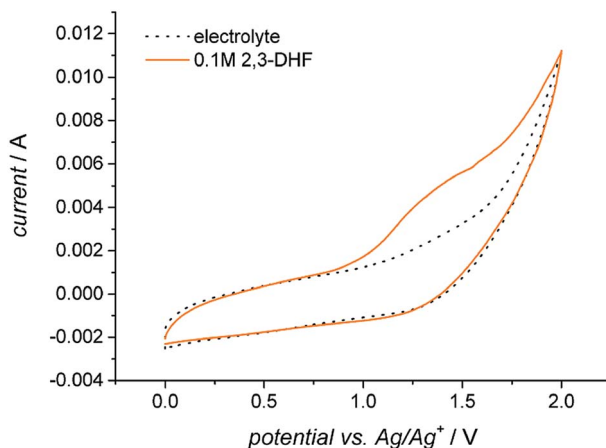


Fig. 9 Cyclic voltammogram of 0.1 mol L⁻¹ 2,3-dihydrofuran in acetonitrile with lithium perchlorate (0.1 mol L⁻¹) as the electrolyte. Scan rate: 50 mV s⁻¹.

carboxylic acid (2-COOH-2,5-DHF). Such species have ¹³C-NMR signals at 184 (COOH), 104 (C=C), 63 (CH₂) and 60 (CH-COOH) ppm. The absence of a signal at 140 ppm (characteristic of the O-bonded C in the O-CH=CH- moiety) confirms the isomerization of the starting material. A simulation of the ¹³C-NMR spectrum made using CS Chem Draw Ultra 6 (Cambridge Software Corporation) shows that 2-COOH-2,5-DHF (Fig. 12A) has signals at 176, 129, 89 and 68 ppm, while 4-COOH-2,3-DHF (Fig. 12B) has computed signals at 177, 144, 100, 80 and 32 ppm. Finally, 2-COOH-1-formyl-cyclopropane has computed peaks at 204, 184, 36 and 6–15 ppm. The signals found in the ¹³C-spectrum of the mixture irradiated with visible light in the presence of Ru@ZnS-B shows, in addition to the signals of 2,5-DHF and 1-formyl-cyclopropane, two series of new signals at: 184, 126, 81 and 68 ppm due to 2-COOH-2,5-DHF and lower signals attributable to 2-COOH-2,3-DHF at 184, 145, 102, 80 and 29 ppm. The absence of signals in the high part of the spectrum excludes the formation of the carboxylated form of 1-formyl-cyclopropane. The formation of the two carboxylated isomers can be explained by the coupling of the radical shown in Fig. 6 with the CO₂^{•-} radical anion. The new C-C bond is formed at C-2, and the double bond migrates to the 3–4 carbons or to the 4–5 carbons, the latter with less favourable energetics as it implies H-migration. As reported above, 2-COOH-2,3-DHF is present at a lower concentration. Besides the signals of the products reported above, weak resonances due to THF and furan are also found, which also occur in solutions irradiated in the absence of CO₂. A new signal due to methanol also appears (50 ppm), which is not

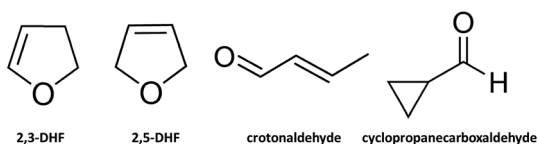


Fig. 10 2,3-DHF and the products of its photocatalytic isomerization (inert atmosphere).

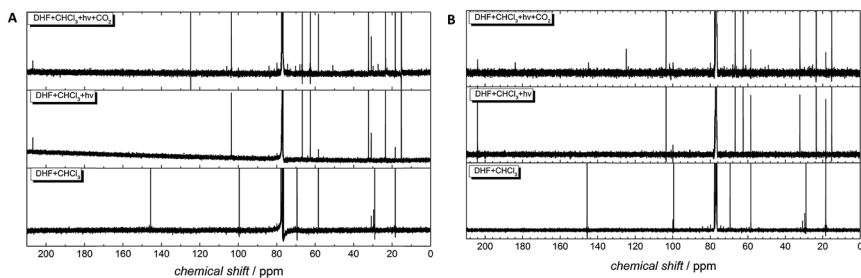


Fig. 11 ^{13}C -NMR spectra of 2,3-DHF and after 2 h of using Ru@ZnS-A (A) and Ru@ZnS-B (B) as photocatalysts: the starting product is quantitatively converted into isomerization products. In absence of CO_2 , carboxylated products are not formed.

found in the absence of CO_2 , and this is quite interesting but not surprising as we have shown that CO_2 can be reduced to methane, formic acid or methanol under irradiation in the presence of the ZnS photocatalysts or others (such as CuI).¹³

In order to obtain further information on the compounds formed, we have produced a ^1H -NMR spectrum of the mixture. The resulting spectrum is quite complex due to the many signals of the various isomers. The only significant signals are those of the aldehydic (9.75 ppm in CDCl_3) and carboxylic groups (11.3 ppm in CDCl_3 , not seen in CD_3OD most probably due to the hydrogen bonding and H-D exchange that causes broadening).

In order to confirm the structural features of the carboxylated forms obtained through the multinuclear NMR, a GC-MS analysis of the reaction solution in methanol produced on a large scale was carried out, allowing the identification of various products. Several peaks were found in the GC of the solution irradiated in the absence and presence of CO_2 , corresponding to the isomers described above. Under CO_2 , the 2-COOH-2,3-DHF peak appeared, attributed on the basis of its fragmentation showing m/z values at: 114 (molecular peak), 85, 69, 45 (carboxylic group) and 41.

Carboxylation in methanol

The carboxylation in methanol has features different from those of the same reaction in CHCl_3 . A single carboxylated isomer is formed in this solvent, namely 2-COOH-2,3-DHF. This product is also formed in a higher concentration than in chloroform, reaching over 25% of the total of the starting product, after 10 h with 1%Ru@ZnS-A as the photocatalyst (Fig. 13B compares the various photocatalysts: ZnS-A, 1%Ru@ZnS-A, ZnS-B and 1%Ru@ZnS-B). The accumulation of the carboxylated products over 10 h can be explained assuming that:

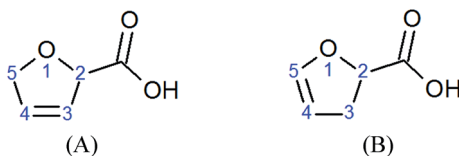


Fig. 12 (A) 2-COOH-2,5-DHF and (B) 2-COOH-2,3-DHF.

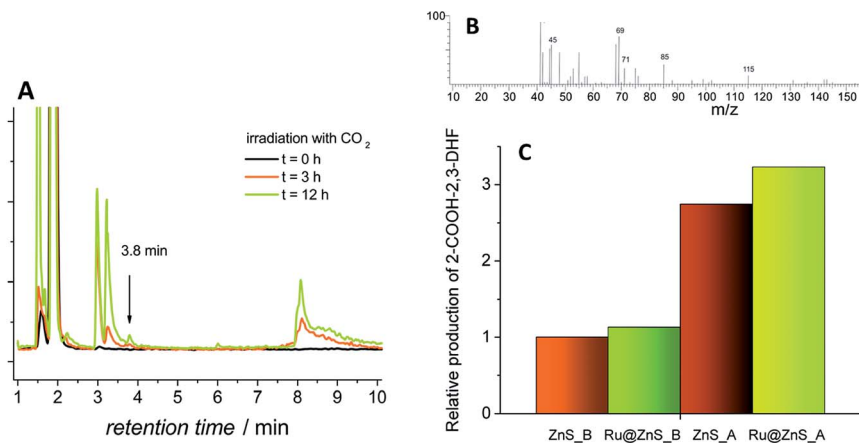


Fig. 13 GC-MS analysis of the reaction solution during photocatalytic carboxylation of 2,3-DHF in methanol. (A) Gas-chromatograms of samples withdrawn at different times during the photocatalytic tests in methanol using 1%Ru@ZnS-A as a photocatalyst with irradiation times of 0, 3 and 12 h, (B) the MS spectrum on the peak at 3.8 min, and (C) the relative formation of 2-COOH-2,3-DHF in the presence of ZnS-A (set equal to 1), 1% Ru@ZnS-A, ZnS-B and 1%Ru@ZnS-B after 10 hours of irradiation of a 2,3-DHF solution in methanol.

1. The isomerisation is fast and the isomerized product can then be carboxylated. This is not the case as discussed in the next sub-chapter.

2. The isomerisation rate in methanol is slower than in chloroform or the lifetime of the radical shown in Fig. 8 is longer in methanol, so that a more extended carboxylation is observed with time, with higher selectivity.

In order to collect data on the formation rate of the carboxylated product and on the activity of the catalysts, we have carried out extended irradiations of the solution up to 12 h and compared the catalysts. Fig. 13 reports an example of the evolution of the chromatograms with time, the MS spectrum of the peak at 3.8 min due to 2-COOH-2,3-DHF, and the relative activity of the different photocatalysts. Fig. 13C clearly shows that the Ru-decorated ZnS materials are more active than bare sulphides. Using Ru@ZnS-A as the photocatalyst and collecting data at fixed time intervals (30 min) over 12 h, it was possible to obtain preliminary information about the kinetics of the conversion of the starting material. Fig. 14 shows the percentage of conversion of 2,3-DHF into 2-COOH-2,3-DHF with time. It is interesting to note that at the time of 12 h all the starting materials was converted either into the isomerisation product or its carboxylated form, as demonstrated by ^{13}C NMR.

Does the carboxylation occur concurrently with the photoisomerisation or after it?

As reported above, the only carboxylation products observed in CHCl_3 are 2-COOH-2,3(or 2,5)-DHF, while no carboxylated forms of F-Cyp were found. The question came to our mind of whether the carboxylation is concurrent with the isomerisation or whether it follows this step. We have carried out a simple experiment to answer such a question. We first irradiated the 2,3-DHF solution

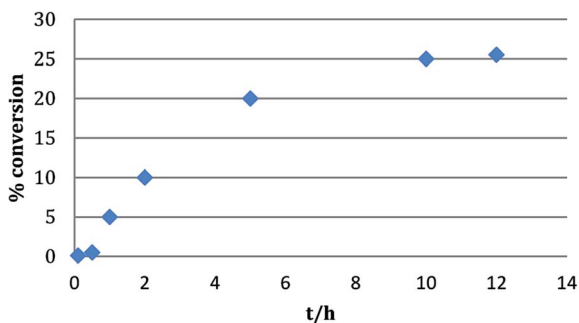


Fig. 14 Photoconversion of 2,3-DHF into 2-COOH-2,3-DHF using Ru@ZnS-A as the photocatalyst.

under argon in CHCl_3 and in the presence of the photocatalyst Ru@ZnS-B or Ru@ZnS-A and, when the photoconversion of 2,3-DHF into 2,5-DHF and 1-formyl-cyclopropane was complete, CO_2 was admitted and the irradiation continued. The analysis of the reaction mixture after irradiation (2 h) showed that there was no further conversion of 2,5-DHF nor 1-formyl-cyclopropane, thus inferring that the carboxylation occurs on the radical species (shown in Fig. 8) more than on the products of photoisomerization. The carboxylation of the substrates formed upon isomerisation of 2,3-DHF takes place under quite different conditions than those described in this paper.

Conclusions

The irradiation of a solution of 2,3-DHF in CHCl_3 in the presence of Ru@ZnS-B under inert atmosphere causes isomerization of the starting product into 2,5-DHF and 1-formyl-cyclopropane. This reaction proceeds *via* the formation of allylic radicals (hydrogen abstraction from 2,3-DHF), identical to those formed in the reaction of 2,5-DHF oxidation by valence band holes generated upon the irradiation of ZnS and CdS.^{22–25} Since the radical is stabilized by its two resonance structures, its lifetime is sufficient to enable bimolecular reactions. When methanol is used, the photoisomerization reaction requires a longer time.

When the irradiation is carried out under CO_2 atmosphere in CHCl_3 , the carboxylation of the substrate occurs affording two isomeric products, namely 2-COOH-2,3-DHF and 2-COOH-2,5-DHF. The carboxylation occurs by coupling of a $\text{CO}_2^{\cdot-}$ radical anion with the allylic radical. The formation of the $\text{CO}_2^{\cdot-}$ radical under the operative conditions has been confirmed by our recent studies involving spin-trapping and EPR measurements.²⁶ The generation of this very reactive radical is thermodynamically feasible due to the high reduction abilities of electrons excited to the conduction band of zinc sulphide. Moreover, the presence of ruthenium nanoparticles enhances adsorption of carbon dioxide and improves the charge separation, which is reflected in the diminished recombination efficiency and the pronounced $\text{CO}_2^{\cdot-}$ formation.²⁶ When the photo-carboxylation is carried out in methanol, 2-COOH-2,3-DHF is formed as the only product. This allowed us to carry out preliminary kinetic studies and calculate the photocarboxylation yield to be 25% after 10 h.

1 The photocarboxylation process discussed here is another example of a
possible application of photocatalytic systems in the synthesis of chemicals.
Although the overall efficiency of the process can be improved, the actual pho-
toconversion is quite interesting (25% of 2,3-DHF converted after 10 h, or 0.025
5 M) and mimics a reductive path of photosynthesis (reduction of carbon dioxide)
utilizing the UV part of the solar radiation.

10 Experimental part

Synthesis of photocatalyst

Zinc sulphide (ZnS-A) was prepared according to methods published elsewhere.¹²
Under an argon atmosphere, using Schlenk's system, a solution of Na₂S (0.1 mol)
15 in 25 mL of distilled water was added dropwise to the aqueous solution of ZnSO₄
(0.1 mol, 25 mL). The mixture was stirred for twenty four hours, filtrated, washed
with water to neutrality and dried at room temperature under vacuum. Another
sample of zinc sulphide (ZnS-B) was also prepared under a nitrogen atmosphere.
A solution of sodium hydroxide (10 g) in distilled water (20 mL) was added
20 dropwise to a solution of ZnSO₄ (0.01 mol, 20 mL), as already described.¹² The
primarily formed solid Zn(OH)₂ was dissolved as [Zn(OH)₄]²⁻. Afterwards, 40 mL
of a thiourea solution (1.52 g) was added. The mixture was heated to 353 K for 48
h. After separation *via* centrifugation, the powder was washed with H₂O and dried
25 at 333 K. Ruthenium nanoparticles were deposited as follows: 1 g of ZnS was
suspended in an aqueous solution of RuCl₃ · xH₂O (10 mL, 10 mM) under an argon
atmosphere. A concentrated ethanol solution of NaBH₄ was added dropwise (in a
big excess) under ultrasonic agitation. Then the powder was filtered off and
washed with water under argon, dried and stored under a nitrogen atmosphere.

30 Characterization of materials

Diffuse reflectance spectra of photocatalysts were measured using a UV-Vis
spectrophotometer (UV-3600 type, Shimadzu), equipped with an integrating
sphere (15 cm diameter). 25 mg of analysed samples were ground with 0.5 g of
BaSO₄. Barium sulphate was also used as the reference material. Hydrodynamic
particle diameters were measured using Zetasizer NanoZS (Malvern). The scan-
ning electron microscope (Vega 3 LMU, Tescan) was equipped with a LaB₆
cathode. EDX spectra were recorded using the EDX detector (Oxford Instruments,
40 X-act, SDD 10 mm²). The photoelectron spectra were measured using a mono-
chromatized aluminium AlK α source ($E = 1486.6$ eV) and a low energy electron
flood gun (FS40A-PS) to compensate the charge on the surface of the non-
conductive samples. A typical three-electrode set-up was employed for photo-
current analysis. The electrolyte solution was 0.1 M KNO₃. Platinum and Ag/AgCl
were used as auxiliary and reference electrodes, respectively. The working elec-
trodes were prepared by casting the samples onto ITO conductive foil. Light
emitting diodes of various wavelengths (*Instytut Fotonowy*) were used as light
50 sources. The measurements were collected using the potentiostat (PGSTAT 302N,
Autolab).

Cyclic voltammetry

CV experiments were carried out using a BioLogic SP-150 potentiostat. The measurements were collected at a scan rate of 100 mV s^{-1} . The electrochemical cell consisted of three electrodes: the glassy-carbon electrode (working electrode), the nonaqueous Ag/Ag^+ (reference electrode) and platinum wire (counter electrode). The reference electrode was prepared by placing a clean silver wire into an electrolyte (0.01 M tetrabutylammonium perchlorate in acetonitrile) containing silver ions (0.01 M AgNO_3). The electrodes were placed in a Teflon cuvette filled with 0.1 mol dm^{-3} LiClO_4 solution in anhydrous acetonitrile. Oxygen was thoroughly removed from the electrolyte by purging with argon before (15 min) and during the experiment.

Photocatalytic tests

2,3-Dihydrofuran, a Sigma-Aldrich product, was carefully distilled under reduced pressure prior to photocatalytic tests. It was stored at 4°C and used for up to 30 days after distillation. Chloroform was dried with alumina, distilled and stored under a nitrogen atmosphere. Methanol was distilled under a nitrogen atmosphere, dried using molecular sieves and distilled again. The photocatalyst (1 g dm^{-3}) was suspended (by sonication) in the solvent (5 or 10 mL) and the organic substrate (0.1 mol dm^{-3} unless otherwise stated) was added. CO_2 was bubbled through the suspension for 3 minutes to remove oxygen and afterwards the mixture was closed under an elevated pressure of carbon dioxide (7–8 bar) in a sapphire tube reactor, unless otherwise stated. Photocatalytic tests were carried out in a closed reactor using a XBO-150 lamp as the light source equipped with a cut-off filter (360 nm). Samples of the reaction mixture were collected periodically, filtered through syringe filters and analysed. The progress of the reaction was monitored by GC-MS (Shimadzu QP5050) equipped with a DB 5 MS 30 m capillary column. Nuclear Magnetic Resonance (NMR) experiments were carried out using a 400 MHz Varian INOVA apparatus and 600 MHz Bruker Advance.

Acknowledgements

IC^2R srl is acknowledged for having made available the photocatalytic equipment. The authors wish to thank Anna Regiel-Futyra for SEM measurements. The support from the Foundation for Polish Science within the VENTURES Project (2011-8/1) and TEAM Project (2012-9/4), co-financed by the European Union, Regional Development Fund, is highly acknowledged by TB and SW, respectively. Some equipment was purchased with the financial support of the European Regional Development Fund in the framework of the Polish Innovation Economy Operational Program (contract no. POIG.02.01.00-12-023/08).

References

- 1 *Carbon Dioxide as a Source of Carbon*, ed. M. Aresta and G. Forti, Springer Netherlands, Dordrecht, 1987.
- 2 *Developments and Innovation in Carbon Dioxide (CO₂) Capture and Storage Technology*, ed. M. M. Maroto-Valer, Woodhead Publishing, 2010, vol. 1, pp. i–iii.

- 1 3 E. Barton Cole and A. B. Bocarsly, in *Carbon Dioxide as Chemical Feedstock*, ed.
M. Aresta, Wiley-VCH Verlag GmbH & Co. KGaA, 2010, pp. 291–316.
- 4 M. Aresta, A. Dibenedetto and E. Quaranta, *Reaction Mechanisms in Carbon
Dioxide Conversion*, Springer-Verlag, Berlin Heidelberg, 2015.
- 5 2013.
- 6 A. Dibenedetto, P. Stufano, W. Macyk, T. Baran, C. Fragale, M. Costa and
M. Aresta, *ChemSusChem*, 2012, **5**, 373–378.
- 7 M. Aresta, A. Dibenedetto, T. Baran, A. Angelini, P. Łabuz and W. Macyk,
Beilstein J. Org. Chem., 2014, **10**, 2556–2565.
- 10 8 D. W. Bahnemann, J. Moenig and R. Chapman, *J. Phys. Chem.*, 1987, **91**, 3782–
3788.
- 9 J. Lee and W. Choi, *J. Phys. Chem. B*, 2005, **109**, 7399–7406.
- 10 A. A. Ismail and D. W. Bahnemann, *Green Chem.*, 2011, **13**, 428–435.
- 15 11 A. A. Ismail and D. W. Bahnemann, *J. Phys. Chem. C*, 2011, **115**, 5784–5791.
- 12 T. Baran, A. Dibenedetto, M. Aresta, K. Kruczała and W. Macyk,
ChemPlusChem, 2014, **79**, 708–715.
- 13 T. Baran, S. Wojtyła, A. Dibenedetto, M. Aresta and W. Macyk, *Appl. Catal., B*,
DOI: 10.1016/j.apcatb.2014.09.052.
- 20 14 T. Baran, S. Wojtyła, A. Dibenedetto, M. Aresta and W. Macyk, 2015, data not
published.
- 15 L. G. Warde, *Organic Chemistry, Hardcover*, 2009.
- 16 R. Morrison and R. Boyd, *Organic chemistry, Hardcover*, 1992.
- 17 S. J. Blanksby and G. B. Ellison, *Acc. Chem. Res.*, 2003, **36**, 255–263.
- 25 18 K. M. Ervin, S. Gronert, S. E. Barlow, M. K. Gilles, A. G. Harrison,
V. M. Bierbaum, C. H. DePuy, W. C. Lineberger and G. B. Ellison, *J. Am.
Chem. Soc.*, 1990, **112**, 5750–5759.
- 19 G. da Silva, C.-H. Kim and J. W. Bozzelli, *J. Phys. Chem. A*, 2006, **110**, 7925–7934.
- 30 20 H. Kisch, *Semiconductor Photocatalysis: Principles and Applications*, Wiley-VCH,
2015.
- 21 F. Osada, H. Furukawa, M. Matsubara, T. Imai and K. Tsukiyama, Fukuoka,
2012.
- 22 R. Künneth, C. Feldmer, F. Knoch and H. Kisch, *Chem.–Eur. J.*, 1995, **1**, 441–
448.
- 35 23 H. Keck, W. Schindler, F. Knoch and H. Kisch, *Chem.–Eur. J.*, 1997, **3**, 1638–
1645.
- 24 A. Reinheimer, A. Fernández and H. Kisch, *Z. Phys. Chem.*, 1999, **213**, 129–133.
- 25 G. Hörner, P. Johne, R. Künneth, G. Twardzik, H. Roth, T. Clark and H. Kisch,
Chem.–Eur. J., 1999, **5**, 208–217.
- 40 26 T. Baran, A. Dibenedetto, M. Aresta, K. Kruczała and W. Macyk,
ChemPlusChem, 2014, **79**, 708–715.

45

50

PAPER

Electrocatalytic conversion of CO₂ to produce solar fuels in electrolyte or electrolyte-less configurations of PEC cells

C. Ampelli, C. Genovese, B. C. Marepally, G. Papanikolaou, S. Perathoner and G. Centi

Received 10th May 2015, Accepted 10th June 2015

DOI: 10.1039/c5fd00069f

The electrocatalytic reduction of CO₂ is studied on a series of electrodes (based on Cu, Co, Fe and Pt metal nanoparticles deposited on carbon nanotubes or carbon black and then placed at the interface between a Nafion membrane and a gas-diffusion-layer electrode) on two types of cells: one operating in the presence of a liquid bulk electrolyte and the other in the absence of the electrolyte (electrolyte-less conditions). The results evidence how the latter conditions allow productivity of about one order of magnitude higher and how to change the type of products formed. Under electrolyte-less conditions, the formation of >C₂ products such as acetone and isopropanol is observed, but not in liquid-phase cell operations on the same electrodes. The relative order of productivity in CO₂ electrocatalytic reduction in the series of electrodes investigated is also different between the two types of cells. The implications of these results in terms of possible differences in the reaction mechanism are commented on, as well as in terms of the design of photoelectrocatalytic (PEC) solar cells.

Introduction

There is an increasing interest in the literature on solar fuels,^{1–10} although different concepts are often associated to this definition. Solar fuels are indicated here as those having a carbon-negative footprint, because they utilize emitted CO₂ to produce energy carriers or chemicals through the use of renewable energy (RE) sources. The net effect is thus of introducing RE into the energy or chemical production cycle. The type of products obtained in this process is relevant, because they should preferably be *drop-in* liquid-fuels according to both economic and sustainability perspectives. In fact, it is often forgotten that there are many problems (economic, normative, authorization *etc.*) associated with the introduction of new products requiring a novel infrastructure. Being on such a large scale as the problem of energy is, a “sustainable” transition to a low-carbon

Dept. DIECH, Section Industrial Chemistry, University of Messina, CASPE/INSTM and ERIC aisbl, V.le F. Stagno D'Alcontres 31, 98166 Messina, Italy. E-mail: centi@unime.it

1 economy is only possible by the development of energy vectors and raw materials
for chemistry, which smoothly integrate in the actual system and infrastructure,
minimizing the above issues. Liquid products are necessary to allow energy-
5 efficient and low cost transport over long distances and storage for a long time,
one of the actual main advantages of oil and derivate energy carriers.

We previously discussed the above aspects in more detail, in relation to the
need to develop a sustainable low-carbon energy and chemical production
method.^{11–14} In this vision, CO₂, biomass and solar energy are the three key
10 elements around which future sustainable scenarios for energy and chemical
production should be developed.^{12,15} Critical factors to enable this scenario are
the development of new approaches for the electrochemical conversion of CO₂, a
key step towards artificial leaf-type devices.^{7,16} Many reviews have recently dis-
cussed the electrocatalytic conversion of CO₂,^{17–23} as well as artificial leaf-type or
15 photosynthetic devices,^{7,10,24–29} although only a few of them are cited.

A common aspect is the presence of a bulk electrolyte used to close the electric
circuit in the electrocatalytic cell or photoelectrocatalytic (PEC) devices. We have
shown, however, that a different approach is possible, indicated as electrolyte-less
(EL), because a bulk liquid electrolyte is absent.³⁰ The ionic conduction is realized
20 through a membrane having the photo- and electro-catalysts on the two opposite
faces of the membrane, while the electronic conduction is realized through an
external wire.³¹ This EL approach allows the conversion of CO₂ electrocatalytically
to >C1 products,^{32–34} while essentially C1 products, with traces of C2 products are
detected in the presence of an electrolyte.^{35–40}

EL design for PEC solar cells shows some advantages: (i) it is possible to
operate at higher temperatures, allowing process intensification and the use of
solar concentrators; (ii) the problems related to CO₂ adsorption/diffusion in the
liquid phase are eliminated; (iii) the sealing and design of the cell is greatly
simplified; (iv) gas-cap formation on the electrode (which may largely decrease the
30 performance) is avoided; (v) operations under pressure are simplified; (vi) light
scattering and absorption by the liquid are avoided; (vii) corrosion of the electrode
(a main issue in conventional PEC cells) is virtually absent. However, the greatest
advantage is the more effective (from cost and energy perspectives) recovery of the
liquid products of CO₂ reduction, because they can be collected from the gas
35 stream leaving the EL-PEC cell and not from the liquid electrolyte, requiring
distillation or other costly separation procedures. However, the electrodes in a EL-
PEC cell, or the hemi-cell for the electrocatalytic reduction of CO₂, should be
different from the conventional ones utilized in PEC or electrochemical cells. In
fact, together with good electron conductivity, the electrode for the electro-
40 reduction of CO₂ should guarantee a good transport of the protons coming from
the membrane to the active centers for CO₂ reduction.

There is thus an intriguing question as to whether this difference in electrode
characteristics is responsible for the different type of products observed experi-
45 mentally during the electrocatalytic reduction of CO₂ or instead there are intrinsic
differences in terms of reactivity and reaction mechanism deriving from the
presence or not of a bulk liquid electrolyte. The electric double layer, which
determines the characteristics of the interface at the catalytic centers, depends on
the electrolyte. In PEC cells, concentrated electrolyte solutions are used to mini-
50 mize internal resistance, but in a EL-PEC cell approach the electrolyte is virtually
absent. However, a thin liquid film may be present over the electrocatalysts.

1 Although the ionic transport (to close the circuit) can be realized by surface
transport over the electrocatalysts and then through the membrane (without thus
the need of a liquid film over the electrode), a surface aqueous acid thin layer may
eventually be present as well as the occurrence of capillary condensation in
5 micropores, depending on the temperature and pressure of operations. Never-
theless, the interface between the electrocatalysts and a bulk electrolyte is clearly
different from that when the electrocatalysts are in direct contact with the gas
phase (CO₂), even when a thin aqueous film may be present. The concentration of
CO₂ at the surface of the electrocatalyst is thus expected to be different. However,
10 the different type of electrodes used in conventional and EL hemi-cells for the
electrocatalytic reduction of CO₂ do not allow for clarification of above question
or to obtain better insight into the motivation for the different behaviours
between conventional and EL-cells in the electrocatalytic conversion of CO₂.

15 The aim of this contribution is thus to utilize the same type of electrodes and
reaction conditions, except for the presence of the liquid bulk electrolyte, in order
to compare conventional and EL approaches, determine more precisely the
differences in the productivity and type of products, and obtain indications about
possible differences in the reaction mechanism.

20 **Electrochemical cells for the reduction of CO₂**

In electrochemistry, attention is typically focused on the electrode and operative
conditions, while cell design is often not considered, except in engineering terms
25 for the realization of optimal charge transport, homogeneous flow and electron
distribution in large cells, *etc.* The possibility to operate without a liquid elec-
trolyte is not typically considered for the electrocatalytic reduction of CO₂,
although PEM (proton exchange membrane) fuel cells may be considered an
example of EL operations. We will compare here two different approaches for the
30 electrochemical reduction of CO₂: (1) gas phase (EL-cell approach) and (2) liquid
phase, *e.g.* the conventional one, although using the same type of electrocatalysts
as the gas-phase approach. The two devices show common aspects:

35 (i) the two electrodic compartments are separated by a proton selective
membrane, which allows the migration of protons from the anode to the cathode
side;

(ii) the electrocatalyst (metal nanoparticles supported over a functionalized
carbon nanotube – CNT) is located at the cathode side, supported over a
conductive net (carbon paper) and in close contact with the membrane, while the
40 external part, which is in contact with the gas or liquid phase, is coated with
Teflon to realize a gas diffusion electrode (GDE) (Fig. 1) as in PEM fuel cells;

(iii) CO₂ continuously flows to the cathode of the electrocatalytic cell as 100%
CO₂ at a rate of 10–20 ml min⁻¹;

(iv) the currents/potentials applied are similar (1–2 V; 10–100 mA).

45 These cells are the CO₂ reduction hemi-cells of PEC solar cells, where a photo-
anode is also present. The latter is a photo-active material able to absorb sunlight
to create charge-separation, with the holes utilized at suitable catalytic centers for
the reaction of water oxidation to produce O₂ and protons, the latter being
transported to the electrocatalyst through the membrane. The electrons are
50 instead collected and transported externally (through a wire) to the conductive
electrocatalyst. We have studied the photo-anode behaviour by preparing TiO₂

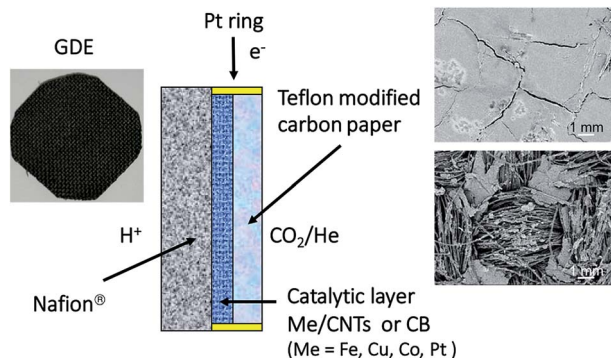


Fig. 1 Schematic illustration of the GDE-type electrodes utilized for CO_2 electrochemical reduction. The image on the left shows the full gas-diffusion electrode (GDE), while the images on the right are scanning electron microscopy images of the side in contact with the membrane and of the side in contact with the gas phase (CO_2) or the electrolyte in which the CO_2 is bubbled.

nanostructured electrodes,³³ doped with noble (Pt, Au)⁴¹ and non-noble nanoparticles (Cu)⁴² to enhance their visible response. Electrolyte and EL operations for the photoanode side (indicated as liquid and gas phase operations, respectively) were both investigated. In water photoelectrolysis and ethanol dehydrogenation processes, higher performances (in terms of H_2 production) of the gas phase with respect to liquid-phase configuration were observed.^{42,43} Therefore, a full EL-PEC cell may be developed, both for the anodic and cathodic parts. However, discussion will be focused here only on the electrocatalytic reduction of CO_2 , thus on the cathodic part of the PEC cell.

Experimental

Synthesis of the electrode materials

The working electrode for the electrochemical cells for CO_2 reduction consists of a carbon substrate on which the metal nanoparticles are deposited. This electrocatalyst is then deposited on a gas diffusion layer (GDL 25 BC Sigracet®), on the side not modified with Teflon. The carbon substrates are commercial carbon black (CB, Vulcan® XC-72) and carbon nanotubes (CNTs, PR-24-XT-PS Pyrograf®).

PR-24-XT-PS CNTs have an average diameter of about 100 nanometers. The inner part shows well-ordered graphitic layers aligned along the main axis, but the external surface displays a turbographic structure. The CNTs were pyrolyzed at $750\text{ }^\circ\text{C}$ to remove polyaromatic hydrocarbons from their surface. Due to the turbographic structure, these CNTs offer a large amount of sites for functionalization of the external surface.

The nature of the functional groups on the carbon surface plays a key role in the catalytic activity of the electrocatalysts. Thus, CNTs were functionalized by direct oxidative treatment in concentrated HNO_3 , introducing oxygen functionalities on the carbon surface. In detail, 1 g of CNTs (or CB) was suspended in 50 ml HNO_3 (65% Sigma Aldrich) and treated in reflux at $100\text{ }^\circ\text{C}$ for 3 h, followed by rinsing until at a neutral pH, filtering, and drying overnight. Different types of

oxygen functionalities were introduced by this treatment. The total quantity and relative distribution can vary as a function of the annealing post-treatment in an inert atmosphere, as shown from synchrotron radiation XPS data.²³

The main properties of a commercial GDL and CNTs are reported in Table 1.

Before depositing the carbon substrates on the GDL, metal (M = Cu, Co, Fe or Pt) nanoparticles (NPs) were deposited on CB and CNTs by an incipient wetness impregnation method using an ethanolic solution containing the proper metal precursor [Cu(NO₃)₂·3H₂O; Co(NO₃)₂·6H₂O; Fe(NO₃)₃·9H₂O; H₂PtCl₆·xH₂O]. After drying at 60 °C for 24 h, the samples were reduced for 2 h at 350 °C under a slow H₂ flow. The total amount of metal loaded onto the carbon substrate was 10 wt%. This amount was chosen in order to have an amount comparable to the metal loading in the electrocatalysts for PEM fuel cells (usually 10–20 wt%), which corresponds to a small metal loading in the final catalyst (about 0.5 mg cm⁻²).

The as-prepared carbon substrates with the deposited nanoparticles were then deposited on the GDL using a similar impregnation in anhydrous ethanol and after joining the GDL with the Nafion membrane, the samples were tested as working electrodes both in liquid and gas phase cell configurations. While in the liquid-phase cell the electrode is in contact with the electrolyte solution saturated with CO₂, in the gas-phase cell the electrode is absent and ionic conductivity is guaranteed from the contact with the proton-conducting membrane (Nafion®). Before use, the Nafion® membrane was pre-treated with hydrogen peroxide to eliminate organic impurities and finally activated with H₂SO₄.

Characterization

Surface area of the samples (BET method) was determined by the physical adsorption of N₂ at liquid nitrogen temperatures by using a Micrometrics ASAP 2010 system.

Transmission electron microscopy (TEM) images were acquired by using a Philips CM12 microscope (resolution 0.2 nm) with an accelerating voltage of 120

Table 1 Properties of the as-produced commercial materials used to prepare the electrocatalyst

Properties of GDL 25 BC Sigracet®	
Thickness	235 μm
Areal weight	86 g m ⁻²
Porosity	80%
Air permeability	1.0 cm ³ (cm ² s ⁻¹)
Electrical resistance (through plane)	<12 mΩ cm ²
Properties of CNTs PR-24-XT-PS Pyrograf®	
Fiber diameter (average)	100 nm
Surface area	45 m ² g ⁻¹
Dispersive surface energy	85 mJ m ⁻²
Moisture	<5 wt%
Iron	<14 000 ppm
Polyaromatic hydrocarbons	<1 mg PAH per g fiber

1 kV, while SEM images were recorded with a Philips XL-30-FEG scanning electron microscope.

5 Liquid-phase cell

The electrochemical cell, made in Plexiglas® to allow visual inspection, has a three-electrode configuration and is schematically illustrated in Fig. 2. The working electrode (about 3 cm²) is located at the cathode side, at a small distance (0.5 cm) from a saturated Ag/AgCl electrode (working as the reference electrode) to reduce the solution resistance. The electric contact with the working electrode is maintained with a Pt wire. The counter-electrode is a commercial Pt rod (Amel) immersed in the anode compartment. A potentiostat/galvanostat (Amel mod. 2049A) is employed to supply a constant current/bias between the electrodes.

The anode compartment is physically separated from the cathode side by a proton-conducting membrane (Nafion® 117, Ion Power). A 0.5 M aqueous solution of KHCO₃ was used as the electrolyte solution in both the cathode and anode compartments. The volume of the electrolyte solution at the anode was about 9–10 ml. The electrochemical cell was designed in order to have a large surface area of the electrode and to minimize the electrolyte solution in direct contact with the electrocatalyst. A continuous flow of pure CO₂ (10 ml min⁻¹) was introduced into an external reservoir to saturate the electrolyte solution. This prevents interference from gas bubbles striking the electrode surface in the cathode compartment. The electrolyte solution is continuously circulated between the cathode compartment and the external container by using a peristaltic pump. The total amount of solution (cathode + external container) was 20 ml.

The liquid products were analysed by sampling the liquid in the external container and determining the composition of the solution using ¹H nuclear magnetic resonance spectroscopy (NMR, Varian NMR 500) and gas chromatography-mass spectrometry (GC-MS, Thermo Trace 1310, ISQ Single Quadrupole MS, column Stabilwax MS). The gas products were detected by sampling the gaseous stream leaving the external container at regular intervals and analysing using gas-chromatography (GC-TCD, Agilent 7890A, column 5A Plot).

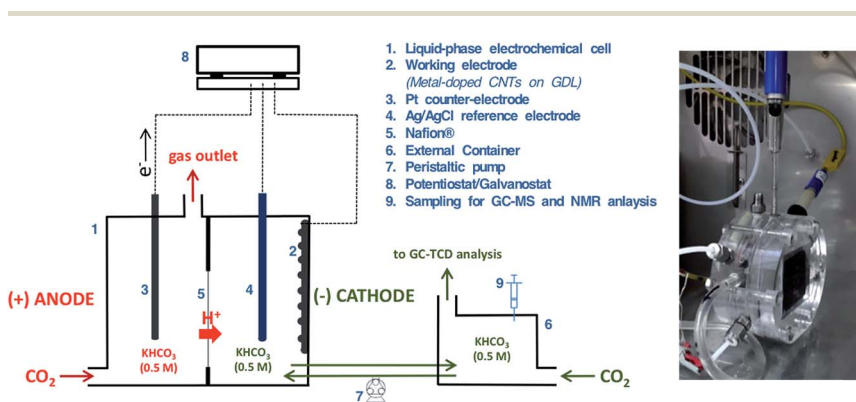


Fig. 2 Schematic drawing of the experimental apparatus for electrocatalytic tests of CO₂ reduction in liquid phase, e.g. in the presence of a liquid electrolyte.

Gas-phase cell (EL conditions)

The electrochemical cell for CO₂ reduction working in the gas-phase (electrolyte-less – EL – conditions) was designed to operate under a continuous flow of CO₂ diffusing through the GDL to arrive at the surface of the electrocatalyst. The cell was made in Plexiglas® and it is located within an oven to work eventually at higher temperatures, up to about 70–80 °C, although all the tests reported here were carried out at room temperature to be comparable to those in the liquid cell, which do not allow operations at temperatures above about 40 °C. Fig. 3 reports a schematic drawing of the experimental apparatus.

The cell has a three-electrode configuration, with a Pt wire as the counter-electrode and a saturated Ag/AgCl electrode as the reference electrode, both immersed in the anode compartment. A membrane electrode assembly (MEA) separates the two cell compartments. The MEA consists of: (i) a proton-conducting membrane (Nafion® 117) and (ii) the electrocatalyst deposited on the GDL. These two samples were assembled together by hot pressing at 80 atm and 130 °C for 90 s. The electrocatalyst is located at the interface with the membrane. The anode side, to be more comparable with the liquid cell, works in the liquid phase and is used to provide the protons (through the Nafion membrane) needed for the CO₂ reduction process. The anode side is filled with an electrolyte aqueous solution (KCl 0.5 M) and it is in direct contact with one side of the Nafion® membrane. A gas flow of pure CO₂ (10 ml min⁻¹) is continuously fluxed into the cathodic compartment.

A potentiostat/galvanostat (Amel mod. 2049A) was used to supply a constant current (10–20 mA) between the electrodes. The voltage increased as a function of time-on-stream during the first hour stabilizing to a value of around 1.4 to 1.5 V. At the end of the reaction (typically 1 h), the current polarity was inverted to facilitate desorption of the products from the working electrode. The liquid products were collected in a cold trap from the flux leaving the cathodic part of the cell. They were analyzed using a gas chromatograph equipped with a mass detector (Thermo Scientific GC Trace 1310 – ISQ MS).

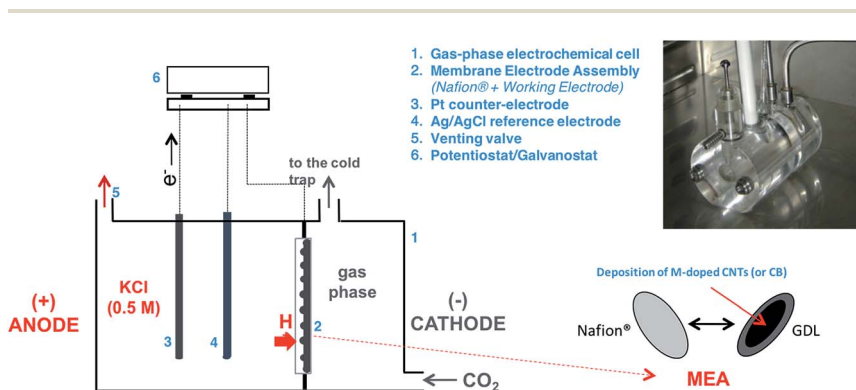


Fig. 3 Schematic drawing of the experimental apparatus for electrocatalytic tests of CO₂ reduction in gas phase, e.g. in electrolyte-less (EL) conditions.

Results and discussion

Characterization of the electrodes

The BET characterization of the electrocatalysts is reported in Table 2. An increase in the surface area and pore volume after the addition of Cu, Co, Fe nanoparticles is observed, but not for Pt, although no relevant changes in the average pore volume were observed in all cases. The effect may thus be interpreted as a reduced sticking between the CNTs, due to the change in the surface properties of functionalized CNTs during the process of addition of the metallic nanoparticles. On the contrary, the samples based on CB (carbon black) as the support (only an iron sample is reported in Table 2, with the results for the other samples being quite similar) have a significantly larger BET surface area and pore volume.

Fig. 4 reports an image by TEM of a Fe-CNT sample. It may be observed that there is presence of a good dispersion of iron particles, preferentially located on the external surface of the CNT. The average size is between 3 and 5 nm, with a relatively narrow distribution. A similar distribution of the metal nanoparticles is observed in the other samples. Pt allows for obtaining a slightly lower average size for the metal particles, centred around 1–3 nm. A good dispersion is also observed in the samples based on a CB support, without determining relevant differences in terms of dispersion and average metal nanoparticle size. It may thus be concluded that in spite of the different surface areas, both CNT_{s_{ox}} and CB allow a good dispersion of the metal nanoparticles and an analogous average size to be obtained.

CO₂ electrocatalytic reduction in a liquid phase cell

The main products detected in the liquid electrolyte on the cathode side are reported in Table 3 for all the electrocatalysts tested in the liquid-phase cell. As a reference, (i) metal Cu foil and (ii) CNT_{ox} alone (*e.g.* without metal particles, but deposited on the GDL) were analysed.

The main products detected in the liquid electrolyte solution were: formic acid, acetic acid and methyl formate. The pure Cu foil electrode also formed methanol in traces. The main other product of the reaction, detected in the gas stream leaving the cell (see Fig. 2) is H₂, while CO, CH₄ or C₂ hydrocarbons were not detected in all the samples.

The first interesting observation is that CNT_{ox} itself is able to form H₂ (from protons and electrons), as well as some products of CO₂ conversion. In the

Table 2 Characterization of the textural characteristics of the electrocatalysts using a BET method

Electro-catalyst	$a_{\text{BET}}, \text{m}^2 \text{g}^{-1}$	$V_{\text{m}}, \text{cm}^3 \text{g}^{-1}$	Average pore diameter, nm
CNT _{ox}	23, 1	5, 3	11, 4
Cu-CNT _{ox}	48, 3	11, 1	10, 8
Co-CNT _{ox}	72, 6	16, 7	14, 9
Fe-CNT _{ox}	63, 8	14, 6	9, 2
Fe-CB	221, 2	50, 8	12, 2
Pt-CNT _{ox}	23, 6	5, 4	11, 3

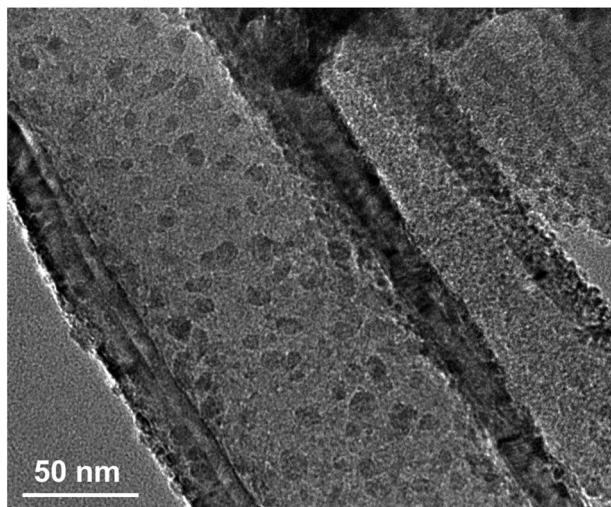


Fig. 4 Transmission electron microscopy (TEM) image of a Fe-CNT sample.

absence of CNTs, the products of CO_2 conversion were instead not detected. Thus, the CNT itself (without metal particles) is able to convert CO_2 electrocatalytically. It is worth noting that without the oxidative pretreatment, the CNT is inactive, thus the behaviour observed cannot be attributed to residual traces of metal utilized for the synthesis of the CNT itself (by catalytic chemical vapour deposition). The activity has to be related to the oxygen functional groups created during the CNT pretreatment (see the Experimental part).

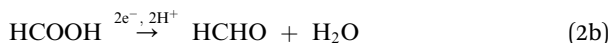
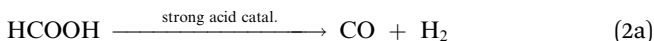
Formic acid formation may be explained as deriving from the reaction of H_2 (formed by the catalytic electroreduction of the protons diffusing through the membrane) with the CO_2 present in the electrolyte. However, bubbling together H_2 and CO_2 in the absence of a potential/current applied to the electrode did not result in the formation of products of CO_2 conversion. Reasonably, the functional groups present on CNT_{ox} , likely chetonic groups as observed for other catalytic reactions,⁴⁴ are able to reduce CO_2 to formic acid according to a mechanism tentatively outlined in Scheme 1.

Table 3 Main products formed in 1 h of reaction in the CO_2 electrochemical reduction in the liquid phase

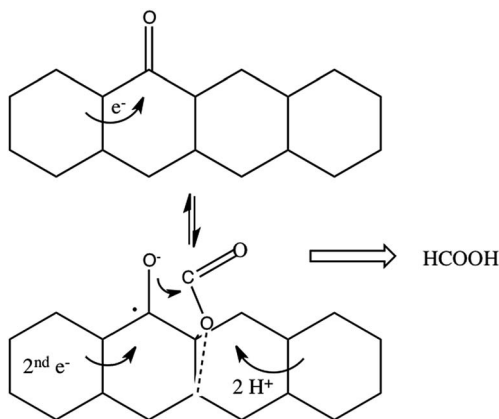
Electrode	Formic acid [M]	Acetic acid [M]	Methyl formate [M]
Cu foil	6.1×10^{-4}	4.0×10^{-4}	—
Cu-CB/GDL	3.6×10^{-5}	1.4×10^{-5}	1.7×10^{-4}
Fe-CB/GDL	4.6×10^{-5}	5.4×10^{-5}	6.0×10^{-6}
Co-CB/GDL	8.1×10^{-5}	9.5×10^{-5}	7×10^{-6}
Cu- CNT_{ox} /GDL	1.2×10^{-4}	8.4×10^{-5}	1.5×10^{-5}
Fe- CNT_{ox} /GDL	1.8×10^{-5}	2.1×10^{-5}	1.2×10^{-5}
Pt- CNT_{ox} /GDL	2.3×10^{-4}	1.8×10^{-4}	—
CNT_{ox} /GDL	2.2×10^{-5}	1.4×10^{-5}	—

Chetonic groups present at the edges or defects of CNTs may act as trapping sites for electrons, forming resonance species as outline in Scheme 1. The presence of an electron localized on the carbon activates the nearby C–C bond, becoming able to coordinate the oxygen in CO₂, breaking the molecule from linearity. The activation of nearby C–C bonds, making it susceptible for O₂ activation, is the mechanism proposed for N-doped CNTs active in the oxygen reduction reaction (ORR).^{44,45}

Acetic acid is the other main product observed using a CNT_{ox}/GDL electrocatalyst (Table 3). It is not easy to explain the formation of this product. A preliminary hypothesis is that the further reduction of formic acid, with a mechanism similar to that outlined in Scheme 1, leads to the formation of formaldehyde. Formaldehyde may selectively transform with even 100% selectivity to acetic acid in relatively mild conditions (100 °C, 500 psi CO) in the presence of a strong acid (HI).⁴⁶ Formic acid in strong acid conditions (as present near the electrocatalyst surface, being located close to the Nafion membrane) decomposes to CO and H₂O. Carbon monoxide may react with formaldehyde in the presence of a strong acid to selectively give acetic acid (a variation of the Kock–Haaf reaction).⁴⁶ It is reasonable that a similar mechanism occurs in our case during the electrochemical reduction of CO₂:

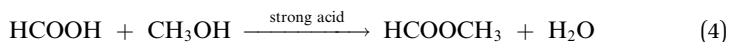


This may also explain why methanol, the further product of formaldehyde reduction, is not observed.



Scheme 1 Tentative reaction mechanism of CO₂ at chetonic groups present on the surface of CNT_{ox}.

1 The presence of a metal nanoparticle leads to an increase in the productivity in
the conversion of CO₂ and the presence of methyl formate in some cases (Table 3).
The latter reasonably derives from the reaction of formic acid esterification with
methanol under acid conditions:



Methyl formate may thus be associated with the formation of methanol and its
fast conversion under the reaction conditions present in our experiments.

10 Various other observations can be made on the results evidenced in Table 3.
Copper-based electrodes have been tested in three types of forms: as Cu foil (as a
reference, being one of the type of electrodes often utilized in the electrocatalytic
reduction of CO₂), and in the form of copper nanoparticles supported over CNT_{ox}
15 or CB. It may be observed that methyl formate is observed in both cases using CB
or CNT_{ox} as a support for copper nanoparticles, but not when copper foil is used.
This result indicates that the presence of copper metal nanoparticles supported
on carbon materials rather than copper itself (as suggested often in literature)
promotes the formation of methanol. In terms of productivity, a Cu-CB/GDL has a
20 formation of methyl formate nearly one order of magnitude higher than a Cu-
CNT_{ox}/GDL, although the copper amount and size of the copper nanoparticles is
analogous. The higher surface area of CB with respect to CNT_{ox} (Table 2) may thus
not be the reason for the different behaviour, as the dispersion of copper in the
two supports is relatively similar. We may also note in Table 3 that formic and
25 acetic acid formation is instead higher in a Cu-CNT_{ox}/GDL in comparison to a Cu-
CB/GDL. Thus the main difference between the two samples is in the rate of the
further reduction of formaldehyde to methanol:



with methanol then further reacting according to eqn (4). CB (Vulcan XC-72)
contains about 0.3% S, present as sulphonic groups (-SO₃H) on the surface.
These acid groups, stronger than the -COOH groups present on CNT_{ox} as a
consequence of the oxidative pretreatment, reasonably favour a better surface
35 transport of protons coming from the membrane. Probably the difference in the
behaviour observed between the CNT_{ox}/GDL and Cu-CB/GDL is associated with
the different concentration of protons at the electrocatalytic centers, although
this hypothesis should have better proof. A higher proton concentration favours
the further reduction up to methanol, reducing the rate of side reactions. In fact,
40 Table 3 shows that productivity to acetic acid (which can be considered a side
reaction with respect to methanol formation) is about six times higher in the
CNT_{ox}/GDL with respect to the Cu-CB/GDL, which parallels the strong decrease in
methyl formate productivity.

45 A comparison of the results of the Cu-foil electrode with those of the Cu-CB/
GDL and Cu-CNT_{ox}/GDL electrodes provides some further interesting indica-
tions. To estimate the amount of copper present in the two types of samples, it
may be considered that in the Cu-CB/GDL or Cu-CNT_{ox}/GDL the total amount of
copper in the 3 cm² electrode is about 1.5 mg. To estimate the amount of copper
50 active in copper foil, it is not possible to just have the weight of the foils, but it
may be assumed that a foil of the same electrode size (3 cm²) having a 10 nm

1 thickness would have a comparable thickness to the size of copper nanoparticles
in the samples over the carbon support.

5 Considering for copper a density of 8.9 g cm^{-3} , this estimated amount of
“surface” copper in the copper foil is about 0.03 mg, thus significantly lower than
that present in the “3D-like” electrodes based on a carbon support. Alternatively,
it may be considered as the surface area of metal copper. For copper-foil, it is
10 simply the geometrical electrode area of the copper foil, *e.g.* 3 cm^2 . For copper
nanoparticles, the surface area can be estimated assuming round-shaped copper
nanoparticles of 10 nm size. With this simplification, the surface area for a total
amount of 1.5 mg of copper in the electrode results to be about $0.5 \times 10^6 \text{ cm}^2$, *e.g.*
15 much larger than that of the geometrical surface of the copper foil electrode. It
may be argued that the real surface of the copper foil is not flat, but some
roughness is present as well as some porosity. Also for metal nanoparticles, the
part of the surface in contact with the carbon is not accessible (lowering the
electrocatalytic active surface), but also particles smaller than 10 nm are present,
20 increasing the overall metal surface. However, the differences estimated for the
two types of electrodes (copper foil and copper nanoparticles on a carbon support)
are so large indicating that the issue is not related to a too simple model to
calculate the active surface area of copper.

Therefore, the electrocatalytic active copper is much lower in copper-foil than
in samples supported over carbon. Nevertheless, the productivity in conversion of
25 CO_2 is about five times higher in Cu-foil than that of the Cu-CB/GDL sample and
even more with respect to the Cu-CNT_{ox}/GDL (Table 3). This indicates that
transport of protons/electrons as well as CO_2 diffusion to the active electro-
catalytic centers is dominating the behaviour and productivity is not related to the
metal active surface area in our experimental conditions.

This conclusion may also explain why notwithstanding some differences, the
behaviour of other metal nanoparticles, namely iron and cobalt, is not signifi-
30 cantly different from that observed for copper nanoparticles (Table 3). However,
copper, particularly when on a CB support, allows significantly higher methyl
formate formation with respect to iron nanoparticles on the same support. Pt
nanoparticles, on the contrary, do not form methyl formate but, as for Cu foil,
they give larger quantities of formic acid as well as acetic acid.

35 The change of production rate with time during liquid-phase cell experiments
is shown in Fig. 5 for Cu-CB/GDL and Cu-CNTs/GDL electrodes. Formic acid
formation decreases after 3 h of reaction, while the concentration of acetic acid
increases in both the cases in agreement with the reaction mechanism discussed
before. The methyl formate concentration in the liquid phase is higher after 1 h
40 for the Cu-CB/GDL, strongly decreasing after 3 h, due to its high volatility (methyl
formate boiling point = $32 \text{ }^\circ\text{C}$). Traces of methyl formate were found in the gas
outlet from the external container.

It should also be commented that pH changes greatly influence the perfor-
45 mance, in agreement with the discussion on the possible reaction mechanism.
The aqueous electrolyte used for liquid phase experiments is KHCO_3 (0.5 M).
When CO_2 is bubbled into the hemi-cell compartments, an acid–base equilibrium
between CO_2 and HCO_3^- establishes in solution:



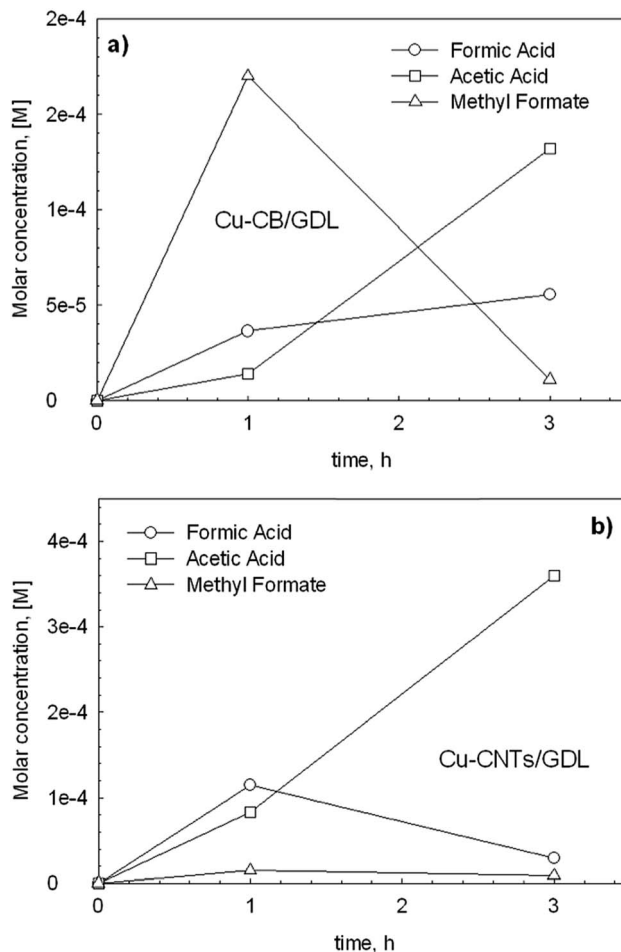


Fig. 5 Time dependence of formic acid, acetic acid and methyl formate formation for liquid-phase testing experiments with (a) Cu-CB/GDL and (b) Cu-CNT_{ox}/GDL electrocatalysts.

The pH of the fresh electrolyte is about 12, but decreases to about 9 when CO₂ is bubbled in it. A small flow of pure CO₂ (10 ml min⁻¹) was also fluxed directly into the anode compartment to favour desorption of O₂ and oxygen species on the Pt counter-electrode surface which may increase the overpotential of the cell.⁴⁷ The flux of CO₂ in both compartments of the cell also avoids the creation of pH gradients related to the solubilisation of CO₂, as indicated in eqn (6). However, the pH in the anodic section varies as a consequence of the reaction. The pH of the electrolyte solution at the anode compartment is initially 6. It maintains stable during the first 30–60 min, depending on the electrocatalyst in the cathodic part. During this initial time, the voltage and current given to the electrochemical cell remain stable (Fig. 6). Then, a sharp decrease of both the current and potential is observed, due to the following reaction at the anode, which decreases the pH inhibiting the half-reaction at the anode:

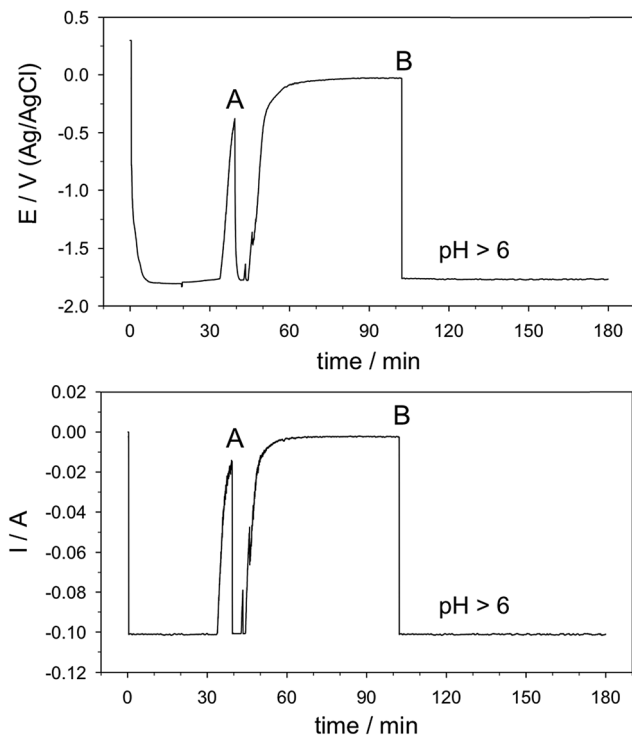
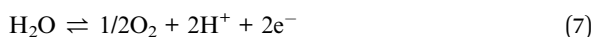


Fig. 6 Profiles of voltage (E) and current (I) as a function of time in experiments in the liquid-phase. (A) addition of some drops of fresh electrolyte solution (0.5 M KHCO_3); (B) addition of some drops of 1 M NaOH aqueous solution to maintain pH in the anode part at $\text{pH} > 6$.



By adding some drops of 1 M NaOH aqueous solution, the pH increased to values above 6 and the current rapidly returned back to the set-point value. In order to have stable performances, it is thus necessary to maintain a $\text{pH} > 6$ in the anodic part by adding a base.

This corroborates that the transport of protons across the membrane is the rate limiting process in our case, because otherwise they should be transported to the cathodic part where they are consumed to generate H_2 and reduce CO_2 .

The comparison of these results with those reported in the literature in terms of TOF (turnover frequency) is not easy, because the cell/electrodes and cell operation conditions are different and TOF values are typically not reported in the literature for the electrocatalytic reduction of CO_2 . Kuhl *et al.*³⁵ have not only made a quite detailed investigation of this reaction, but have also reported the TOF values for each of the products determined (in the supplementary part). Due to the different types of electrode (a copper foil mechanically polished) and reaction conditions, they observed different types of products in the reduction of CO_2 (CH_4 , formate, CO, methanol, ethylene, ethanol, glycolaldehyde,

1 acetaldehyde, acetate, ethylenglycol, *n*-propanol, allyl alcohol, acetone). It is thus
 possible to compare the total TOF in products of CO₂ reduction, rather than for
 the single species. The results are reported in Table 4. A potential of -1.1 V (*vs.*
 5 RHE), corresponding to the maximum formation of products of CO₂ reduction in
 the Kuhl *et al.*³⁵ results, was chosen for this comparison. TOF data are reported as
 $\mu\text{mol s}^{-1} \text{cm}^{-2}$, *e.g.* the same unit used by Kuhl *et al.*³⁵ They also reported in
 parallel the TOF values expressed as molecules s⁻¹ surface Cu atoms⁻¹. However,
 10 this estimate requires a series of assumptions on the number of Cu atoms which
 are even less valid in our case, due to the different types of electrodes. As Kuhl
*et al.*³⁵ used only a Cu foil electrode, we report the TOF data in Table 4 only for the
 Cu-based electrode, for a more homogeneous comparison. TOF results may be
 easily derived for the other electrodes, being proportional to the total amount of
 product formed. Having not detected in our case CO formation, the results of
 15 Kuhl *et al.*³⁵ are differentiated to or not to include the amount of CO formed.
 However, the differences are limited.

As shown in Table 4, TOF data in our electrodes are from three times higher
 (for dispersed Cu nanoparticles on a carbon support) to 13 times higher (for Cu
 foil).

CO₂ electrocatalytic reduction in a gas phase cell (EL operations)

20 Experiments made in the gas-phase electrochemical cell on the same electrodes
 used for the liquid-phase cell show relevant differences, regarding both the types
 of products formed and the productivity. However, a common aspect in both cells
 25 is the relevant formation of H₂. Hydrogen is an undesired product, because it
 reduces the Faradaic efficiency to the products of CO₂ reduction. This indicates
 that in our experimental conditions the use of electrons/protons for the reduction
 of CO₂ is a slower process with respect their recombination to form H₂. Inhibiting
 the last reaction is thus a requirement to improve the performances in the elec-
 30 trocatalytic reduction of CO₂. On the other hand, these results also show that the
 formation of H₂ is a facile reaction not specifically requiring dedicated catalysts.

There are main differences in the type of products of reaction between liquid-
 and gas-phase cell operations, *e.g.* the presence or absence of the bulk electrolyte.
 35 In the gas outlet stream leaving the cathodic part of the cell, together with H₂, CO
 and in a small amount CH₄ are also detected in the case of EL operations. The two
 last products are not detected in liquid phase operations. Although CO may form
 from formic acid decomposition (eqn (2a)) in liquid-phase operations, it imme-
 40 diately reacts and CO is not detected in the product stream leaving the cell, at
 least up to the detection limit. On the contrary, CO is a main product of CO₂

Table 4 TOF values ($\mu\text{mol s}^{-1} \text{cm}^{-2}$) on copper-based electrodes, in comparison with
 TOF values reported by Kuhl *et al.*³⁵ (*) for Cu foil electrode

Electrode	TOF (all products)	TOF (all products, except CO)	TOF (all products)
Cu foil	9.35×10^{-2}	—	—
Cu-CB/GDL	2.04×10^{-2}	—	—
Cu-CNT _{ox} /GDL	2.03×10^{-2}	—	—
Cu foil (*)		6.66×10^{-3}	6.96×10^{-3}

1 electrocatalytic reduction in gas-phase cell operations, indicating a different
 mechanism of formation, with probably CO being the primary product of CO₂
 5 reduction, rather than a secondary product, as observed in liquid-phase opera-
 tions. This may explain why methane, deriving from the catalytic reduction of CO
 on copper, iron and cobalt metal nanoparticles, is observed even if in small
 amounts in experiments with gas-phase cells, but not in those with liquid-phase
 cells.

The type of liquid products formed, detected in the electrolyte or condensed in
 10 the cold trap from the gaseous stream leaving the gas-phase cell, are also different
 in the two cases. Table 5 summarizes the behaviour of the different types of tested
 electrodes in gas-phase cells (EL conditions). A first observation is that different
 types of products are observed:

(i) methanol, rather than formic acid as the C1 main product (together with
 15 CO);

(ii) acetaldehyde and ethanol together with acetic acid as C2 products, while
 only the latter was observed together with methyl formate in some
 electrocatalysts;

(iii) acetone and isopropanol as C3 products, while no C3 products were
 20 detected in liquid phase operations.

This different type of products clearly suggests a different type of mechanism
 of CO₂ electrocatalytic conversion, in agreement with what is commented earlier.
 Table 6 summarizes the difference observed in the type of products of reduction
 of CO₂ between gas-phase and liquid-phase cell operations.

25 It may be observed that not only is the productivity different between gas-
 phase (Table 5) and liquid-phase (Table 3) operations, but also the relative
 order of activity. In gas-phase cells, the best productivity to products of CO₂
 reduction is shown by a Fe-CNT_{ox}/GDL (around 4.8×10^{-4} mmol h⁻¹). The same
 electrode in liquid phase operations, considering the total volume of electrolyte,
 30 has a productivity of about 0.3×10^{-4} mmol h⁻¹, *e.g.* about one order of

Table 5 Products obtained in the CO₂ electrochemical reduction in gas-phase

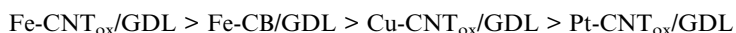
Electrode	Methanol, mmol h ⁻¹	Acetaldehyde, mmol h ⁻¹	Ethanol, mmol h ⁻¹	Acetone, mmol h ⁻¹	Isopropanol, mmol h ⁻¹	Acetic acid, mmol h ⁻¹	H ₂ , mmol h ⁻¹	CO, mmol h ⁻¹
40 Co- CNT _{ox} / GDL	1.2×10^{-4}	4.5×10^{-5}	2.0×10^{-4}	1.3×10^{-6}	—	3.4×10^{-5}	2.0×10^{-1}	3.2×10^{-2}
Cu- CNT _{ox} / GDL	4.8×10^{-5}	1.1×10^{-5}	6.7×10^{-5}	1.0×10^{-7}	9.3×10^{-6}	—	1.7×10^{-1}	9.6×10^{-3}
45 Fe-CB/ GDL	1.1×10^{-4}	2.9×10^{-5}	1.1×10^{-4}	1.2×10^{-6}	1.1×10^{-6}	1.5×10^{-5}	3.2×10^{-1}	3.6×10^{-2}
Fe- CNT _{ox} / GDL	1.4×10^{-4}	6.7×10^{-5}	9.4×10^{-5}	1.8×10^{-7}	8.4×10^{-5}	9.2×10^{-5}	3.6×10^{-1}	6.5×10^{-2}
50 Pt- CNT _{ox} / GDL	1.0×10^{-5}	1.7×10^{-5}	3.6×10^{-5}	1.7×10^{-7}	2.4×10^{-5}	1.4×10^{-5}	4.5×10^{-1}	3.5×10^{-2}

Table 6 Comparison of types of products obtained in liquid and gas phase operations in CO₂ electrocatalytic reduction

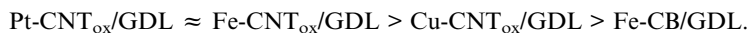
Gas phase	Liquid phase
Methanol	Formic acid
Acetaldehyde	Acetic acid
Ethanol	Methanol (in traces)
Acetone	
Isopropanol	
Hydrocarbons C4–C9 (in traces)	

magnitude lower. For the Cu-CTN_{ox}/GDL catalyst, productivity in gas-phase operations is about 1.4×10^{-4} mmol h⁻¹, while in liquid-phase operations about 0.15×10^{-4} mmol h⁻¹. Thus again a difference of about one order of magnitude is observed.

Also the relative order of productivity to products of CO₂ reduction is different, being:



in gas-phase cells (Table 5) while for liquid-phase cells (Table 3):



This observation further remarks that different aspects may determine the productivity in the reduction of CO₂, and can be reasonably associated to the different reaction mechanisms.

Differences in the reaction mechanism

Clarification of the above question requires a more in depth analysis of the reaction mechanisms, with operando techniques, which, however, are not simple to apply to electrochemical tests under relevant environmental conditions. We may thus advance only some initial considerations, which help in setting the scene for more detailed mechanistic studies.

As earlier commented, the mechanism in the liquid-phase may be associated (on the specific carbon-based electrocatalysts we utilize) with the activation mechanism of CO₂ at specific carbon sites, such as the carbonyl groups formed by oxidation pretreatment. One electron transfer to this site generates a C–O⁻ center, with the charge localized on the carbon activating the nearby C–C bond making it susceptible of activating the oxygen in the O=C bond of carbon dioxide, thus generating a δ+ charge on the C of CO₂, facilitating the electron transfer from a C–O⁻ center. In a different paper on the reactivity of carbon nanotubes (modified by a specific surface nitrogen doping mechanism), we showed that the amount of nitrogen in CNTs influences performance in the electrocatalytic reduction of CO₂. The behaviour linearly correlated with the change of work function in these materials. The latter aspect influences the electronic coupling between the electron donor/acceptor and in turn the rate of electron transfer.

1 This can provide an explanation of the role of metal nanoparticles in our
electrocatalysts. It may be noted, in fact, that there are differences in the behav-
5 iour and productivity, but limited with respect to the very relevant change in the
type of metal nanoparticles, from Pt to Cu, Fe and Co. If the reaction occurs only
at the metal surface, much greater differences are expected. On the other hand,
metal nanoparticles may change locally the work function of carbon, thus facil-
10 itating the electron transfer. It may be also facilitate the electron transfer to
protons, generating H⁺ species, which are more reactive in reacting with oxygen of
CO₂ or with the products of its reduction. The metal will thus act as co-catalyst
with the functional groups present on activated carbon, rather than as unique
catalytic sites. The sites will thus be mainly located at the perimetral edge between
15 carbon and metal particles, in agreement with previous studies using calorimetry
on this type of electrocatalysts for the reduction of CO₂.⁴⁹ Although clearly further
demonstrations are necessary to support this mechanism, it can provide
preliminary indications on the aspects investigated, as being different from the
actual mechanisms proposed for CO₂ electrocatalytic conversion, which are
20 focused only on the role of the metal surface.

Reasonably the intermediate generated in this mechanism of reduction of CO₂
25 requires a solvent to be stabilized. On the other hand, metal nanoparticles are
easy passivated, because CO₂ dissociation at the electrocatalyst metal surface
generates CO and an O species, both remain strongly bound to the metal surface.
In the absence of the bulk electrolyte, both the absence of the solvent (electrolyte)
and the higher CO₂ concentration at the surface of the electrocatalyst reasonably
30 contribute in inhibiting one side of the mechanism of electron transfer/
hydrogenation of CO₂ (*via* formic acid and formaldehyde), and on the other
hand, promoting the mechanism of CO₂ dissociation to CO at the metal surface or
reasonably at the metal-carbon perimetral region. The further reaction of adsor-
bed species on the metal surface leads to C–C bond formation and to the products
35 being observed experimentally.

Although speculative, this change in the type of mechanism of CO₂ reduction
may explain the differences observed in the productivity, type of products and
relative rates of reactions between different electrodes. These observations show
40 how a more complex surface chemistry in the electrocatalytic reduction of CO₂
may exist with respect to what is previously suggested in the literature. A better
understanding of these aspects opens new possibilities in controlling the type of
products formed and their productivity, as evidenced from the comparison
between liquid- and gas-phase operations on the same electrodes. On the other
45 hand, the results also remark that carbon may not only be a support, but also
plays a relevant role in understanding the chemistry of the reduction of CO₂. This
also opens new possibilities in the design of electrocatalysts for the reduction of
CO₂ and of the critical elements to consider for their improvement.

45 Conclusions

The comparison of the same electrodes for the electrocatalytic reduction of CO₂ in
operations in the presence (liquid-phase) or absence (gas-phase) of a bulk elec-
50 trolyte provide a series of interesting indications both on the limiting steps of the
process and on the reaction mechanism.

1 It is demonstrated that under electrolyte-less (EL) operations, the productivity
in the reduction of CO₂ is about one order of magnitude larger, and different types
of products are formed. This is related to differences in the reaction mechanism,
5 which were discussed, although further studies are needed to better clarify the
reaction mechanism and the influence of the presence of the electrolyte.

In liquid-phase operations it is suggested that the mechanism involves step
reduction *via* intermediate formation of formic acid and formaldehyde and finally
methanol, although the latter step is observed only in some electrodes. In fact,
10 due to the strong acidic conditions present at the electrocatalyst, located at the
interface with Nafion membrane, formic acid decomposes to generate CO, which
reacts with formaldehyde to form acetic acid. Methanol also reacts further in
these strong acid conditions to form methyl formate.

In gas-phase operations, this mechanism is no longer effective and the
15 conversion of CO₂ involves its dissociation to CO, which remains strongly
chemisorbed, giving rise to further transformation reactions and the formation of
C–C bonds that produce a different spectrum of products of that observed in
liquid-phase operations.

The electrocatalysts utilized here are based on metal nanoparticles (Fe, Cu, Co,
20 Pt) deposited on two types of conductive carbon supports: carbon nanotubes
functionalized by oxidation treatment (CNT_{ox}) and Vulcan XC-72 carbon black
(CB). CNTs_{ox} without metal particles are active both in producing H₂ from
protons/electrons and in the reduction of CO₂. The possible mechanism and the
25 role of carbonyl groups, formed during the oxidative treatment, is outlined. It is
commented on why in general and also when metal nanoparticles are present, the
carbon does not act only as a support or to transport charges, but has also an
active role in the reaction mechanism. It is suggested that the active sites for the
electrocatalytic reduction of CO₂ are located at the perimetral edge between metal
30 nanoparticles and the carbon. The nature of the latter, in particular the type of
surface functional groups, thus determine considerably the performance, as
experimentally observed.

As commented, these results are the start, not the end of the analysis of the
35 mechanism of reaction in the type of electrodes investigated here. However, we
believe that these results provide evidence on how a more complex surface
chemistry than typically supposed in the literature is present in the electro-
catalytic reduction of CO₂ in the type of electrodes we investigated. It should be
noted that their performances are better than that of various other electrodes
40 reported in the literature for the conversion of CO₂, even if the different reaction
conditions and the way data are reported do not often allow for a precise
comparison.

There is thus the need of a better understanding of the performance and
45 reaction mechanism of these electrocatalysts (based on metal nanoparticles on
conductive, functionalized carbon supports) for the reduction of CO₂. They may
open new possibilities in controlling the type of products formed and their
productivity in this challenging reaction.

Acknowledgements

50 The authors acknowledge the PRIN10-11 project “Mechanisms of activation of
CO₂ for the design of new materials for energy and resource efficiency” and the EU

1 project ECO²CO₂ (“Eco-friendly biorefinery fine chemicals from CO₂ photo-
catalytic reduction”), which have partially supported this work. C. Marepally also
thanks the European Doctoral Programme on Sustainable Industrial Chemistry
(SINCHEM) for supporting his PhD programme.
5

Notes and references

- 1 G. A. Ozin, *Adv. Mater.*, 2015, **27**, 1957.
2 G. Centi and S. Perathoner, in *Green Carbon Dioxide*, ed. G. Centi and S.
Perathoner, Wiley & Sons, 2014, ch. 1, p. 1.
3 M. D. Kaerkaes, O. Verho, E. V. Johnston and B. Aakermark, *Chem. Rev.*, 2014,
114, 11863.
4 S. Protti, A. Albinì and N. Serpone, *Phys. Chem. Chem. Phys.*, 2014, **16**, 19790.
5 C. van der Giesen, R. Kleijn and G. J. Kramer, *Environ. Sci. Technol.*, 2014, **48**,
7111.
6 J. M. Thomas, *Energy Environ. Sci.*, 2014, **7**, 19.
7 S. Bensaid, G. Centi, E. Garrone, S. Perathoner and G. Saracco, *ChemSusChem*,
2012, **5**, 50.
8 G. Centi and S. Perathoner, *Greenhouse Gases: Sci. Technol.*, 2011, **1**, 21.
9 G. Centi and S. Perathoner, *ChemSusChem*, 2010, **3**, 195.
10 D. G. Nocera, *Acc. Chem. Res.*, 2012, **45**, 767.
11 C. Ampelli, S. Perathoner and G. Centi, *Philos. Trans. R. Soc., A*, 2015, **373**, 1.
12 P. Lanzafame, G. Centi and S. Perathoner, *Chem. Soc. Rev.*, 2014, **43**, 7562.
13 S. Perathoner and G. Centi, *ChemSusChem*, 2014, **7**, 1274.
14 G. Centi, E. A. Quadrelli and S. Perathoner, *Energy Environ. Sci.*, 2013, **6**, 1711.
15 S. Perathoner and G. Centi, *J. Chin. Chem. Soc.*, 2014, **61**, 719.
16 G. Centi and S. Perathoner, Artificial leaves, in *Kirk-Othmer Encyclopedia of
Chemical Technology*, 2014.
17 J. Albo, M. Alvarez-Guerra, P. Castano and A. Irabien, *Green Chem.*, 2015, **17**,
2304.
18 P. Kang, Z. Chen, M. Brookhart and T. J. Meyer, *Top. Catal.*, 2015, **58**, 30.
19 Q. Lu, J. Rosen and F. Jiao, *ChemCatChem*, 2015, **7**, 38.
20 E. S. Rountree, B. D. McCarthy, T. T. Eisenhart and J. L. Dempsey, *Inorg. Chem.*,
2014, **53**, 9983.
21 J. Qiao, Y. Liu, F. Hong and J. Zhang, *Chem. Soc. Rev.*, 2014, **43**, 631.
22 E. V. Kondratenko, G. Mul, J. Baltrusaitis, G. O. Larrazabal and J. Perez-
Ramirez, *Energy Environ. Sci.*, 2013, **6**, 3112.
23 C. Genovese, C. Ampelli, S. Perathoner and G. Centi, *J. Energy Chem.*, 2013, **22**,
202.
24 G. Centi and S. Perathoner, in *Chemical Energy Storage*, ed. R. Schlögl, De
Gruyter, 2013, p. 379.
25 K. S. Joya, Y. F. Joya, K. Ocakoglu and R. van de Krol, *Angew. Chem., Int. Ed.*,
2013, **52**, 10426.
26 J. Barber and P. D. Tran, *J. R. Soc., Interface*, 2013, **10**, 20120984.
27 M. D. Kaerkaes, O. Verho, E. V. Johnston and B. Aakermark, *Chem. Rev.*, 2014,
114, 11863.
28 S. Fukuzumi and Y. Yamada, *ChemSusChem*, 2013, **6**, 1834.
29 D. K. Bora, A. Braun and E. C. Constable, *Energy Environ. Sci.*, 2013, **6**, 407.

- 1 30 C. Ampelli, G. Centi, R. Passalacqua and S. Perathoner, *Catal. Today*, 2015, submitted.
- 31 C. Ampelli, C. Genovese, S. Perathoner, G. Centi, M. Errahali, G. Gatti and L. Marchese, *Chem. Eng. Trans.*, 2014, **41**, 13; C. Ampelli, C. Genovese, R. Passalacqua, S. Perathoner and G. Centi, *Theor. Found. Chem. Eng.*, 2012, **46**, 651.
- 5 32 C. Genovese, C. Ampelli, S. Perathoner and G. Centi, *J. Catal.*, 2013, **308**, 237; C. Ampelli, S. Perathoner and G. Centi, *Chin. J. Catal.*, 2014, **35**, 783.
- 10 33 C. Ampelli, G. Centi, R. Passalacqua and S. Perathoner, *Energy Environ. Sci.*, 2010, **3**, 292.
- 34 G. Centi, S. Perathoner, G. Wine and M. Gangeri, *Green Chem.*, 2007, **9**, 671.
- 35 K. P. Kuhl, E. R. Cave, D. N. Abramc and T. F. Jaramillo, *Energy Environ. Sci.*, 2012, **5**, 7050.
- 15 36 P. Hirunsit, W. Soodsawang and J. Limtrakul, *J. Phys. Chem. C*, 2015, **119**, 8238.
- 37 Q. Shen, Z. Chen, X. Huang, M. Liu and G. Zhao, *Environ. Sci. Technol.*, 2015, **49**, 5828.
- 38 J. Albo, M. Alvarez-Guerra, P. Castano and A. Irabien, *Green Chem.*, 2015, **17**, 2304.
- 20 39 S. Back, H. Kim and Y. Jung, *ACS Catal.*, 2015, **5**, 965.
- 40 S. Rasul, D. H. Anjum, A. Jedidi, Y. Minenkov, L. Cavallo and K. Takanahe, *Angew. Chem., Int. Ed.*, 2015, **54**, 2146.
- 41 C. Ampelli, C. Genovese, P. Lanzafame, S. Perathoner and G. Centi, *Chem. Eng. Trans.*, 2014, **39**, 1627.
- 25 42 C. Ampelli, R. Passalacqua, C. Genovese, S. Perathoner, G. Centi, T. Montini, V. Gombac and P. Fornasiero, *Chem. Eng. Trans.*, 2013, **35**, 583; C. Ampelli, R. Passalacqua, C. Genovese, S. Perathoner, G. Centi, T. Montini, V. Gombac, J. J. Delgado and P. Fornasiero, *RSC Adv.*, 2013, **3**, 21776.
- 30 43 C. Ampelli, C. Genovese, R. Passalacqua, S. Perathoner and G. Centi, *Appl. Therm. Eng.*, 2014, **70**, 1270.
- 44 D.-W. Wang and D. S. Su, *Energy Environ. Sci.*, 2014, **7**, 576.
- 45 G. Centi, S. Perathoner and D. S. Su, *Catal. Surv. Asia*, 2014, **18**, 149; D. S. Su, S. Perathoner and G. Centi, *Chem. Rev.*, 2013, **113**, 5782.
- 35 46 L. Kaplan, *J. Org. Chem.*, 1985, **50**, 5376.
- 47 J. K. Nørskov, J. Rossmeisl, A. Logadottir, L. Lindqvist, J. R. Kitchin, T. Bligaard and H. Jónsson, *J. Phys. Chem. B*, 2004, **108**, 17886.
- 48 J. Xu, R. Huang, X. Sun, B. Zhang, Y. Lin, Q. Li, D. Su and G. Centi, *ACS Catal.*, 2015, submitted.
- 40 49 R. Arrigo, M. E. Schuster, S. Wrabetz, F. Girgsdies, J.-P. Tessonier, G. Centi, S. Perathoner, D. S. Su and R. Schlögl, *ChemSusChem*, 2012, **5**, 577.
- 45
- 50

PAPER

Catalytic dehydrogenation of propane by carbon dioxide: a medium-temperature thermochemical process for carbon dioxide utilisation

X. Du,^a B. Yao,^b S. Gonzalez-Cortes,^a V. L. Kuznetsov,^a
Hamid AlMegren,^c T. Xiao^{*a} and P. P. Edwards^{*a}

Received 5th May 2015, Accepted 27th May 2015

DOI: 10.1039/c5fd00062a

The dehydrogenation of C₃H₈ in the presence of CO₂ is an attractive catalytic route for C₃H₆ production. In studying the various possibilities to utilise CO₂ to convert hydrocarbons using the sustainable energy source of solar thermal energy, thermodynamic calculations were carried out for the dehydrogenation of C₃H₈ using CO₂ for the process operating in the temperature range of 300–500 °C. Importantly, the results highlight the enhanced potential of C₃H₈ as compared to its lighter and heavier homologues (C₂H₆ and C₄H₁₀, respectively). To be utilised in this CO₂ utilisation reaction the Gibbs free energy ($\Delta_r G_m^0$) of each reaction in the modelled, complete reacting system of the dehydrogenation of C₃H₈ in the presence of CO₂ also indicate that further cracking of C₃H₆ will affect the ultimate yield and selectivity of the final products. In a parallel experimental study, catalytic tests of the dehydrogenation of C₃H₈ in the presence of CO₂ over 5 wt%–Cr₂O₃/ZrO₂ catalysts operating at 500 °C, atmospheric pressure, and for various C₃H₈ partial pressures and various overall GHSV (Gas Hourly Space Velocity) values. The results showed that an increase in the C₃H₈ partial pressure produced an inhibition of C₃H₈ conversion but, importantly, a promising enhancement of C₃H₆ selectivity. This phenomenon can be attributed to competitive adsorption on the catalyst between the generated C₃H₆ and inactivated C₃H₈, which inhibits any further cracking effect on C₃H₆ to produce by-products. As a comparison, the increase of the overall GHSV can also decrease the C₃H₈ conversion to a similar extent, but the further cracking of C₃H₆ cannot be limited.

^aKing Abdulaziz City of Science and Technology (KACST) – Oxford Centre of Excellence in Petrochemicals, Inorganic Chemistry Laboratory, Department of Chemistry, University of Oxford, Oxford, OX1 3QR, UK. E-mail: peter.edwards@chem.ox.ac.uk; Fax: +44(0) 1865 272690; Tel: +44(0) 1865 272660

^bSINOPEC Shanghai Petrochemical Company LTD., Shanghai, 200540, China

^cPetrochemicals Research Institute (PRI), King Abdulaziz City of Science and Technology (KACST), P. O. Box 6086, Riyadh 11442, Saudi Arabia

1. Introduction

In an attempt to ameliorate the burgeoning growth in greenhouse gas emissions, there are currently intense world-wide efforts aimed at the utilisation of CO₂, particularly in its conversion to fuels and high-value chemical products.^{1–7} Chemical processes aimed at the utilisation and conversion of CO₂ are, of course, driven in a thermodynamic sense by the difference in Gibbs free energy between the resulting final chemical products, and CO₂ and the targeted reactants under the relevant experimental conditions. However, CO₂ being a highly stable molecule will require a substantial amount of energy, effective catalysts and effective reaction conditions for any chemical conversion processes into fuels or high-value chemical products.

Thus probably all chemical reactions for CO₂ conversion and utilisation are endothermic and will consume considerable amounts of energy. If such energy is provided by fossil fuels, the net effect based on any well-to-wheels analysis of the process will invariably result in a net production of CO₂; this situation could only be deemed beneficial from a climate mitigation perspective if the necessary input process energy is provided from renewable or sustainable sources.

The motivation behind this work, therefore, is to identify and develop specific chemical utilisation processes for CO₂ that can be achieved by the application of relatively easily-accessible solar thermal energy and associated thermochemical processes, using so-called “Low and Medium Temperature Thermochemical Processes”, typically operating for temperature ranges of $T \sim 250$ °C and $T \sim 250$ –500 °C, respectively.⁸

Utilising solar thermal energy at these lower temperatures rather than the widely-utilised high temperature process regime⁹ ($T \sim 1000$ °C) for thermochemical processes, creates highly interesting and important challenges for catalysis science. Coupling and optimising the catalyst chemistry of CO₂ chemical reactions in the temperature/energy range of *ca.* 300–500 °C with the engineering challenges of cheap, solar thermal collectors may allow the prospect of accessible, sustainable CO₂ utilisation. These coupled challenges therefore provide a high level of opportunity for modern catalysis science and engineering.

As an “improved” reaction of the dehydrogenation of C₃H₈, the dehydrogenation of C₃H₈ in the presence of CO₂ ($C_3H_8 + CO_2 \rightarrow C_3H_6 + H_2O + CO$) has been heavily studied over the last decade.^{10–15} In this promising reaction, CO₂ acts as a mild oxidant to combine the dehydrogenation of C₃H₈ with a reverse water gas shift ($H_2 + CO_2 \rightarrow H_2O + CO$), and hence, the equilibrium of the dehydrogenation of C₃H₈ can be shifted to the product side. Moreover, CO₂ may also reduce the coking effect of the catalyst by coke gasification ($C + CO_2 \rightarrow 2CO$). Competitive adsorption among C₃H₈, CO₂ and generated gaseous water can also explain the relatively lower initial conversion of C₃H₈, the reduced coking effect, and the higher stability of catalysts in the CO₂ atmosphere.¹⁶

In this paper, the advantages of specifically selecting C₃H₈ as the feedstock for CO₂ utilisation are advanced for the lower temperature requirements, as compared to both its lighter and heavier alkane homologues, C₂H₆ and C₄H₁₀, respectively. Furthermore, in seeking the possibility to convert alkanes with the energy source from accessible solar heating technology, the temperature range to be targeted in thermodynamic calculations has been localised in the range 300–

500 °C which can be easily achieved, for example, by high pressure steam from a solar heating system.

The shift of the equilibrium state by CO₂ in the dehydrogenation of C₃H₈ has been identified from a thermodynamic analysis.^{17–19} However, the reaction systems modelled previously rarely take into consideration the competing side reactions and by-products. The dehydrogenation of C₃H₈ in the presence of CO₂ can be significantly affected by various competing side reactions which are deleterious to the targeted C₃H₆ yield, selectivity and indeed to the stability of the operating catalyst. Hence in this paper, the thermodynamic analysis was operated across a more comprehensive reaction system which covered all the possible by-products together with the generation of carbon – particularly important when considering catalyst operating lifetimes.

When considering the side reactions for the dehydrogenation of C₃H₈ in the presence of CO₂, the major cause of by-products is the further cracking effect on C₃H₆,²⁰ and the competitive adsorption from CO₂ is claimed to be an effective way to inhibit that process.¹⁶ Our analysis reveals that the availability of active sites on the catalyst surface does indeed play a critical role in the reaction system. To observe the different performance properties of a catalyst when the reactants are saturated, to the availability of active sites, the reactions were operated over a ZrO₂-supported Cr₂O₃ catalyst with careful control of the various partial pressures of C₃H₈ but keeping a constant C₃H₈/CO₂ ratio. The reaction results exhibited high C₃H₆ selectivity by inhibiting the selectivity of the by-products, which is a promising result if these processes are to be applied in any larger scale industrial process.

2. Thermodynamics and (selected) chemical reactions of carbon dioxide

In Fig. 1 we illustrate the underlying thermodynamic considerations for the chemical utilisation of CO₂, where the Gibbs free energy of formation of CO₂ and various related substances are shown for comparison. Any attempt at utilising CO₂ as a chemical reactant must therefore take into account the relative stability

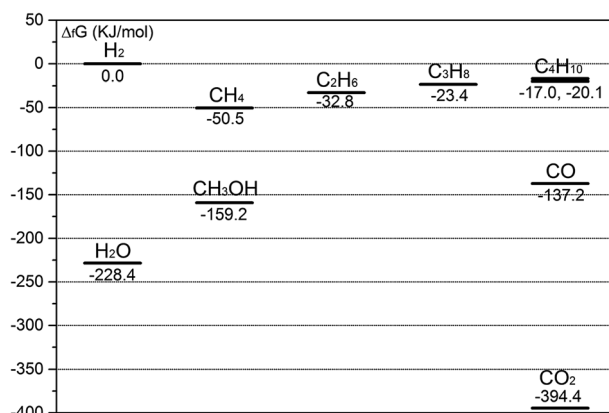


Fig. 1 $\Delta_f G_m^0$ of CO₂ and related substances at normal temperature and pressure (NTP).

(Gibbs free energy) of the CO₂ utilisation reaction products, as compared to CO₂ and the other reactant(s).

Both contributing terms (ΔH and $T\Delta S$) for the Gibbs free energy are not favourable in converting CO₂ to other molecules. The carbon–oxygen bonds are strong and substantial energy is needed for their dissociation and subsequent reduction. Similarly, the entropy term ($T\Delta S$) typically makes little or no contribution to the thermodynamic driving force for any CO₂ utilisation reaction.

The resulting Gibbs free energy of the CO₂ chemical utilisation reaction, ΔG , provides information as to the ultimate yield of the reaction products at equilibrium, through the relationship $\Delta_r G_m^0 = -RT \ln(K^0)$.

From Fig. 2, however, the attractive option that the Gibbs free energy changes of CO₂ reaction becomes increasingly favourable by moving to higher members of the alkane homologous series. One notes, of course, that a ready solution for CO₂ utilisation is its conversion to the more reactive CO *via* the reverse water gas shift reaction ($H_2 + CO_2 \rightarrow H_2O + CO$), and subsequent use of syngas chemistry to yield the desired products. However, this attractive route clearly needs a ready source of H₂ and ideally a source of sustainable H₂ derived from non-fossil fuel routes. In the absence of hydrogen from low cost, low (zero) carbon sources, this process will yield a net CO₂ emission for the total wheel-to-wheel analysis.

Our research therefore looks in detail at the thermodynamics of the dehydrogenation of C₃H₈ by CO₂ as a potential prospect for CO₂ utilisation in temperature and reaction conditions where the ultimate application of solar thermal energy may be a promising technology. This is a specific example of the broader challenge facing *any* CO₂ utilisation technology; namely due to the inevitable input energy required to convert CO₂ to useful products, reducing CO₂ emissions through CO₂ utilisation will only be possible if the energy inputs are from renewable sources. We believe that Low-to-Medium Temperature Solar Thermochemical processes offer considerable opportunities in that regard and the research outlined here — setting out the complete thermodynamic analysis

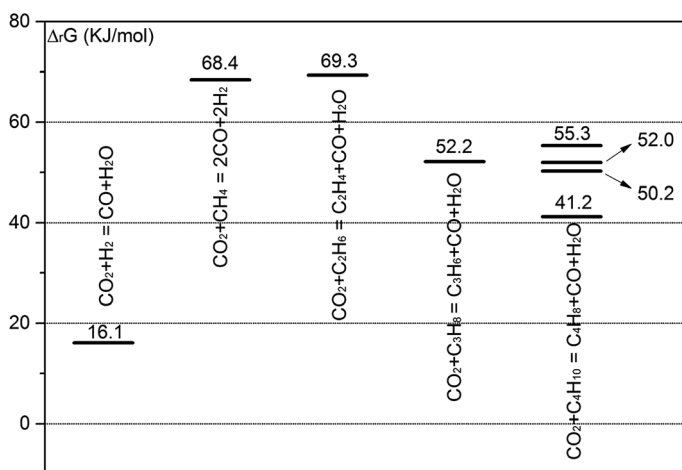


Fig. 2 $\Delta_r G_m^0$ of the reactions between CO₂ and other substances at 400 °C and normal pressure.

1 together with a catalytic chemistry study — may present a way forward for CO₂ utilisation.

3. Thermodynamic calculations and simulations

3.1 Methods

10 In order to fully understand the thermodynamic basis of the dehydrogenation of C₃H₈ in the presence of CO₂, in connecting also with the solar thermal technology which is normally set close to 500 °C in the form of a high pressure steam, the standard change of reaction in Gibbs free energy, $\Delta_r G_m^0$, of the dehydrogenation of C₂–C₄ alkanes with CO₂ utilisation ($C_n H_{2n+2} + CO_2 \rightarrow C_n H_{2n} + H_2O + CO$, $n = 2, 3, 4$) were calculated in the temperature range of 300–500 °C. The cracking of C₁–C₄ alkanes and olefins to form carbon ($C_n H_m \rightarrow nC + \frac{m}{2} H_2$, $n = 1, 2, 3, 4$) were also included in these calculations, in this temperature range, to indicate the potential coking ability on operating catalysts of each substances.

15 Here, the $\Delta_r G_m^0$ of each single reaction in the temperature range of 300–500 °C were calculated as following:

$$\Delta_r H_m^0(298.15 \text{ K}) = \sum_j v_j \Delta_f H_m^0(298.15 \text{ K}, j) \quad (1)$$

$$\Delta_r H_m^0(T) = \Delta_r H_m^0(298.15 \text{ K}) + \sum_j v_j \int_{298.15}^T C_{p,m} dT \quad (2)$$

$$\Delta_r S_m^0(298.15 \text{ K}) = \sum_B v_B S_m^0(298.15 \text{ K}) \quad (3)$$

$$\Delta_r S_m^0(T) = \Delta_r S_m^0(298.15 \text{ K}) + \sum_j v_j \int_{298.15}^T \frac{C_{p,m}}{T} dT \quad (4)$$

$$\Delta_r G_m^0 = \Delta_r H_m^0 - T \Delta_r S_m^0 \quad (5)$$

25 In the functions above, $\Delta_f H_m^0$ is the standard molar enthalpy of formation, S_m^0 is the standard molar entropy, while $C_{p,m}$ is the parameters of molar heat capacity at constant pressure. The property parameters can be looked up in the chemical properties hand books, and these parameters for the related substances are list in Table 1 below.

3.2 Thermodynamic advantages of the dehydrogenation of C₃H₈ in the presence of CO₂

35 Fig. 3 exhibits the standard change of reaction in Gibbs free energy ($\Delta_r G_m^0$) of the reactions being compared. In the temperature range of 300–500 °C, all dehydrogenation reactions show a similar trend. The highest $\Delta_r G_m^0$ is found for the process to dehydrogenate C₂H₆ with CO₂, indicating that it is much harder to operate this reaction as compared to other low- n alkanes at 300–500 °C. Importantly, $\Delta_r G_m^0$ does not keep falling as the carbon number of alkane increases, and the dehydrogenation of C₃H₈ with CO₂ appears to be more feasible than some C₄ reactions, for example.

Table 1 Standard thermodynamic properties of chemical substances: standard molar enthalpy of formation ($\Delta_f H_m^\theta$),²⁵ standard molar entropy (S_m^θ)²⁵ and parameters of molar heat capacity at constant pressure ($C_{p,m}$)²⁶

Substance	$\Delta_f H_m^\theta$ (298.15 K) (kJ mol ⁻¹)	S_m^θ (298.15 K) (J K ⁻¹ mol ⁻¹)	$C_{p,m} = A + BT + CT^2 + DT^3 + ET^4$				
			A($\times 10^0$)	B($\times 10^{-3}$)	C($\times 10^{-5}$)	D($\times 10^{-8}$)	E($\times 10^{-11}$)
H ₂	0	130.684	2.883	3.681	-0.772	0.692	-0.213
CO	-110.53	197.67	3.912	-3.913	1.182	-1.302	0.515
CO ₂	-393.51	213.74	3.259	1.356	1.502	-2.374	1.056
H ₂ O	-241.82	188.83	4.395	-4.186	1.405	-1.564	0.632
CH ₄	-74.81	186.26	4.568	-8.975	3.631	-3.407	1.091
C ₂ H ₄	52.26	219.56	4.221	-8.782	5.795	-6.729	2.511
C ₂ H ₆	-84.68	229.6	4.178	-4.427	5.660	-6.651	2.487
C ₃ H ₆	20.42	267.05	3.834	3.893	4.688	-6.013	2.283
C ₃ H ₈	-103.85	269.91	3.847	5.131	6.011	-7.893	3.079
1-C ₄ H ₈	-0.13	305.71	4.389	7.984	6.143	-8.197	3.165
<i>cis</i> -2-C ₄ H ₈	-6.99	300.94	3.689	19.184	2.230	-3.426	1.256
<i>trans</i> -2-C ₄ H ₈	-11.17	296.59	5.584	-4.890	9.133	-10.975	4.085
<i>i</i> -C ₄ H ₈	-17.10	295.29	3.231	20.949	2.313	-3.949	1.566
<i>n</i> -C ₄ H ₁₀	-126.15	310.23	5.547	5.536	8.057	-10.571	4.134
<i>i</i> -C ₄ H ₁₀	-134.73	291.82	3.351	17.883	5.477	-8.099	3.243
C (graphite) ^a	0	5.74	-0.977	9.458	-1.118	0.739	-0.207

^a The parameters of $C_{p,m}$ are calculated by regressing the molar heat capacity at various temperatures in handbook.²⁷

The $\Delta_r G_m^\theta$ of alkane and olefin cracking to generate carbon and H₂ are shown in Fig. 4. The C₄ alkanes have multiple curves because of their constituent isomers. In general, a lower value of $\Delta_r G_m^\theta$ indicates a higher possibility of cracking. The olefins therefore show a much higher cracking possibility than any

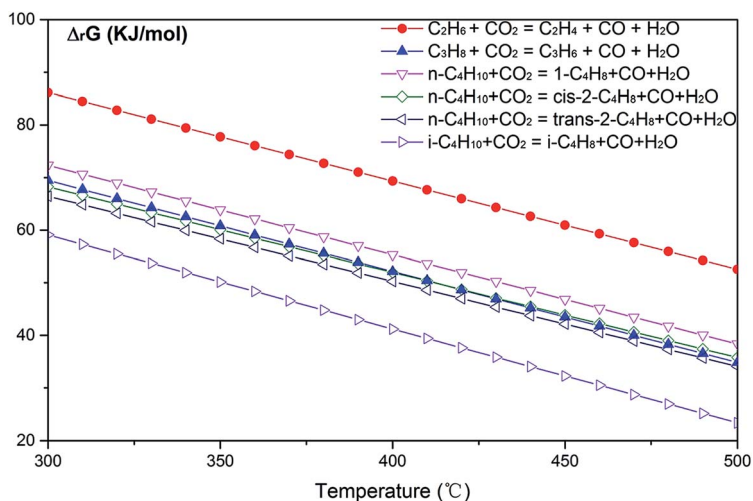


Fig. 3 $\Delta_r G_m^\theta$ of the dehydrogenation of light alkane in the presence of CO₂ at 300–500 °C.

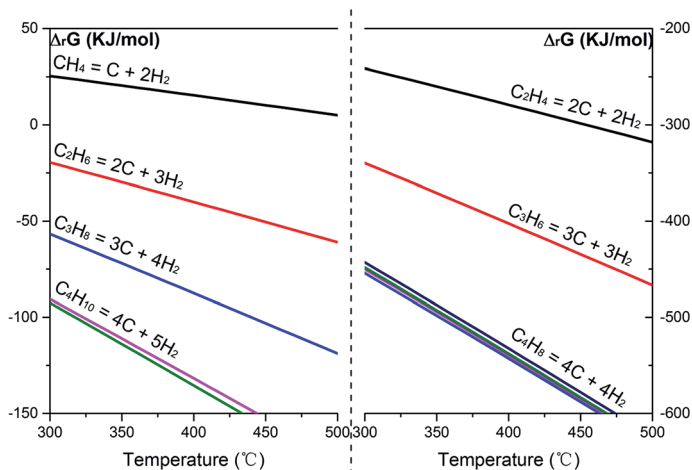


Fig. 4 $\Delta_r G_m^\ominus$ of the alkanes (left) and olefins (right) cracking to generate carbon and H_2 at 300–500 °C.

alkanes, which implies that the selectivity of the target products will be greatly affected by further cracking of the olefins. For instance, C_3H_6 will be further cracked to lower level hydrocarbons or even carbon, so the selectivity will be reduced. It is also obvious that CH_4 has the highest resistance to coking, and as a sequence of stepwise mechanisms of hydrocarbon decomposition, it will be a major by-product in these reaction systems when looking at olefins only. Furthermore, it is obvious that the carbon number is the most important indicator of the cracking possibility. With a similar $\Delta_r G_m^\ominus$ of dehydrogenation of alkane with CO_2 , C_3H_6 has a much higher resistance to cracking than any isomers of butene. Although C_2H_4 has even higher resistance to subsequent cracking, it is even more difficult for C_2H_6 to be activated with CO_2 when the temperature is kept below 500 °C. From this analysis, the dehydrogenation of C_3H_8 in the presence of CO_2 is recognisably the best alkane to be targeted for a chemical utilisation process for CO_2 operating in this temperature range, a range specifically chosen for the ready-availability of solar heating technology for these conditions.

3.3 Modelled calculations of the dehydrogenation of C_3H_8 in the presence of CO_2

In reality, of course, the dehydrogenation of C_3H_8 in the presence of CO_2 is not a simple single reaction but a multiple reaction system, as shown in Table 2, mainly coupling the traditional dehydrogenation of C_3H_8 (reaction (1)) and reverse water gas shift (reaction (2)).

In this system, (1) and (2) are the main reactions considered; (3) and (4) are the further cracking of C_3 species where lighter by-products are formed; (5) is the reaction to gasify the carbon deposition.

The $\Delta_r G_m^\ominus$ of reaction (1)–(3) and (5) are shown in Fig. 5, while the $\Delta_r G_m^\ominus$ of hydrocarbons cracking (reaction (4)) are already displayed in Fig. 4. From 300–500 °C, only the cracking of C_2 and C_3 , including reaction (3), can reach a negative value of $\Delta_r G_m^\ominus$, which means these reactions are thermodynamically favoured. On

Table 2 Modelled reaction system for the dehydrogenation of C_3H_8 in the presence of CO_2

Reaction number	Reaction formula
(1)	$C_3H_8 \rightarrow C_3H_6 + H_2$
(2)	$H_2 + CO_2 \rightarrow H_2O + CO$
(3)	$C_3H_8 \rightarrow C_2H_4 + CH_4$
(4)	$C_nH_m \rightarrow nC + \frac{m}{2}H_2$
(5)	$C + CO_2 \rightarrow 2CO$

the contrary, the decomposition of CH_4 is not favoured in this temperature range. Considering C_3H_8 is the feedstock in this system, and the stepwise mechanism of the hydrocarbons to be decomposed, the generation of CH_4 can be an important indicator to measure the degree and extent of side reactions during the reaction process. CO_2 , as a mild oxidant, is not favoured to gasify the formed carbon deposition. Hence, CO_2 is always applied in order to shift the equilibrium without increasing the temperature. It is obvious that all other reactions in this system depend strongly on the conversion of C_3H_8 in reaction (1). Thus, when considering only reaction (1), this is a decomposition reaction which is favoured under a lower partial pressure of C_3H_8 . With the equilibrium constants calculated from $\Delta_r G_m^\theta$ at the temperature range of 300–500 °C, the conversions of C_3H_8 under a different partial pressure are calculated as shown in Fig. 6.

$$K^\theta = \exp \left[\frac{-\Delta_r G_m^\theta}{RT} \right]$$

The C_3H_8 conversion is observed to be significantly affected by the partial pressure of C_3H_8 within the temperature range of 300–500 °C, it is for this reason that the dehydrogenation of C_3H_8 in the presence of CO_2 should be operated with a very low partial pressure of C_3H_8 when designing experiments.

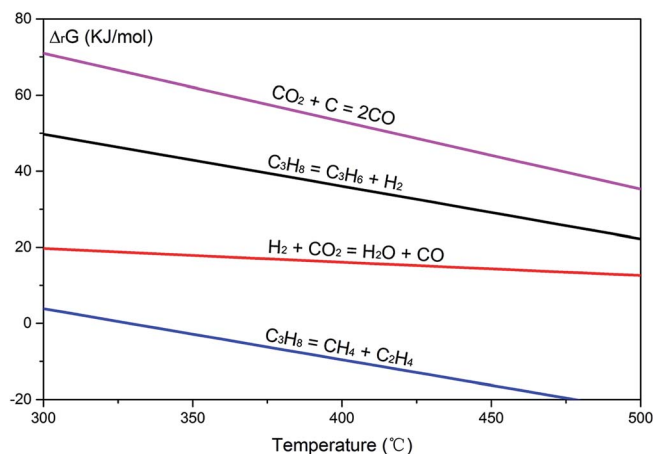


Fig. 5 $\Delta_r G_m^\theta$ of reactions (1)–(3) and (5) in the modelled system, at 300–500 °C.

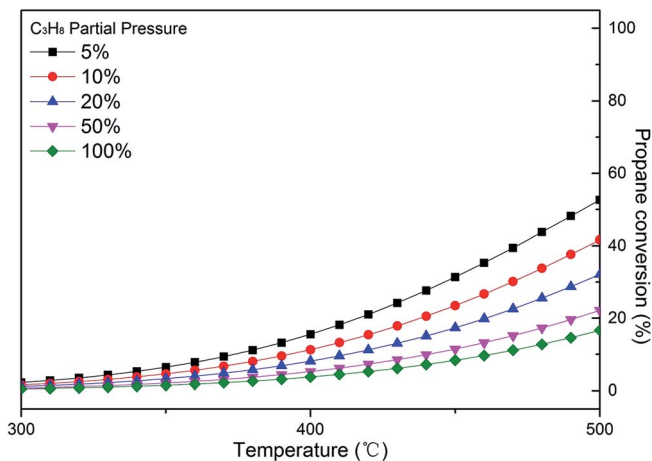


Fig. 6 Calculated C₃H₈ conversions (mol%) at equilibrium state, considering reaction (1) only; various C₃H₈ partial pressure; 300–500 °C.

Apart from the improvement of catalysts, higher C₃H₆ selectivity can also be achieved by changing the conditions of reaction. A general way to inhibit the reaction extent is to limit the contact time of reactants on a catalyst surface by increasing the space velocity of gas flow.²¹ As a comparison we model this and also increase the partial pressure of reactants operating under these conditions.

4. Experimental

4.1 Catalyst preparation

To prepare the 5 wt% of the Cr₂O₃/ZrO₂ catalyst by a precipitation method, ZrO₂ (Alfa-Aesar, 90 m² g⁻¹, 99%) was pre-heated at 600 °C for 6 hour before being ground and sieved to <125 μm in particle size. Subsequently, the Cr(NO₃)₃·9H₂O precursor (99%, Sigma-Aldrich) was dissolved in distilled water, and this solution was mixed with the ground ZrO₂ support and stirred at room temperature for 24 hours. To achieve Cr₂O₃-ZrO₂, the as prepared suspension was dried to obtain a slurry or paste, which was finally calcined at 600 °C for 6 hours in a muffle furnace using a heating ramp of 10 °C min⁻¹. The solid sample was ground to obtain fine particles <125 μm.

4.2 Catalyst characterisation

All the samples, including the ZrO₂ support, were characterized with high resolution X-ray Diffraction (XRD) using a PANalytical X'Pert PRO diffractometer with CuKα radiation (45 kV, 40 mA). When being scanned, the samples were flat loaded in the custom-built sample holders and scanned from 20° to 30° 2θ with a step size of 0.0084° and a scanning speed at 0.017778° s⁻¹.

The amount of carbon deposition on the spent catalyst was measured *via* thermal gravimetric analysis (TGA). The instrument employed was a TA Instrument, SDT Q-600, using flowing air at 100 ml min⁻¹ from 50 °C to 1000 °C with a

ramp rate of 10 °C min⁻¹. The TGA curves were also derived as D-TGA to show the rate of weight loss of the samples.

4.3 Catalyst testing

The stability test of C₃H₈ dehydrogenation in the presence of CO₂ was operated in an M-R-10A micro-reactor (KUNLUN YONGTAI Company, China) over the Cr-based catalyst prepared as above. All tests were operated under atmospheric pressure and 500 °C for 5 hours, and the C₃H₈/CO₂ mixture, whose mole ratio was kept at C₃H₈/CO₂ = 1 : 2. As shown in Table 3, the conditions of tests differed from each other by two variables, the mole fractions of C₃H₈ (and CO₂) and overall gas hourly space velocity (GHSV). N₂ balance was applied to dilute the gas mixture. Considering that the reactions were operated under atmospheric pressure, the partial pressure of C₃H₈ in “R-4800 × 2” and “R-4800 × 3” was increased, and the GHSV of C₃H₈ was changed to the same level as “R-9600” and “R-14 400” respectively.

The composition of outlet gas was tested by online Gas Chromatography (Perkin-Elmer, Clarus 580 GC), and the conversions of C₃H₈ and CO₂, the selectivity of products, and the carbon balance in the gaseous products can be determined using the following equations:

$$\text{Conversion (\%)} = C_i = 1 - \frac{X_i^{\text{outlet}} \times X_{\text{N}_2}^{\text{inlet}}}{X_i^{\text{inlet}} \times X_{\text{N}_2}^{\text{outlet}}} \times 100 \quad (i = \text{C}_3\text{H}_8 \text{ or } \text{CO}_2)$$

Flow of gas in product (ml min⁻¹) =

$$F_j^{\text{outlet}} = \frac{X_j^{\text{outlet}} \times \text{flow of N}_2}{X_{\text{N}_2}^{\text{outlet}}} \quad (j = \text{H}_2, \text{CO}, \text{CO}_2, \text{CH}_4, \text{C}_2\text{H}_4, \text{C}_2\text{H}_6, \text{C}_3\text{H}_6, \text{C}_3\text{H}_8)$$

$$\text{Selectivity of Hydrocarbon (\%)} = S_{\text{C}_n\text{H}_m} = \frac{n \times F_{\text{C}_n\text{H}_m}^{\text{outlet}}}{3 \times F_{\text{C}_3\text{H}_8}^{\text{inlet}} \times C_{\text{C}_3\text{H}_8}} \times 100$$

$$\text{Yield of CO (\%)} = Y_{\text{CO}} = \frac{F_{\text{CO}}^{\text{outlet}}}{2 \times F_{\text{CO}_2}^{\text{inlet}}} \times 100$$

Table 3 Mole fractions of C₃H₈ (X_{C₃H₈}), overall GHSV and C₃H₈ GHSV of the coded reactions

Reaction code	X _{C₃H₈} (mol%)	GHSV (ml h ⁻¹ g _{cat} ⁻¹)	GHSV of C ₃ H ₈ (ml h ⁻¹ g _{cat} ⁻¹)
R-4800	5	4800	240
R-4800 × 2	10	4800	480
R-4800 × 3	15	4800	720
R-9600	5	9600	480
R-14 400	5	14 400	720

Carbon Balance (%) =

$$B_C = \frac{F_{\text{CH}_4}^{\text{outlet}} + 2 \times F_{\text{C}_2\text{H}_4}^{\text{outlet}} + 2 \times F_{\text{C}_2\text{H}_6}^{\text{outlet}} + 3 \times F_{\text{C}_3\text{H}_6}^{\text{outlet}} + 3 \times F_{\text{C}_3\text{H}_8}^{\text{outlet}} + F_{\text{CO}}^{\text{outlet}} + F_{\text{CO}_2}^{\text{outlet}}}{3 \times F_{\text{C}_3\text{H}_8}^{\text{inlet}} + 3 \times F_{\text{CO}_2}^{\text{inlet}}} \times 100$$

$$\text{Oxygen Balance (\%)} = B_O = \frac{2 \times F_{\text{CO}_2}^{\text{outlet}} + F_{\text{CO}}^{\text{outlet}}}{2 \times F_{\text{CO}_2}^{\text{inlet}}} \times 100$$

5. Results and discussion

5.1 Catalytic test results

The C_3H_8 conversion and C_3H_6 selectivity of the reaction under different C_3H_8 partial pressures and overall GHSV are shown in Fig. 7. The results reveal effective C_3H_8 conversions at each specified condition while the C_3H_6 selectivity drops at the beginning of reactions. The results with different mole fractions of C_3H_8 were displayed with solid symbols and the conclusion drawn from the data in these figures is an inhibition of C_3H_8 conversion, but also an improvement in C_3H_6 selectivity. However, with the same increase in C_3H_8 fractional GHSV (by increasing the overall GHSV), the C_3H_8 conversion was inhibited to a similar extent while the C_3H_6 selectivity also decreased. These comparative results indicate that even though the C_3H_8 conversion was similarly inhibited *via* the two routes to increase the C_3H_8 fractional GHSV, the underpinning mechanisms were fundamentally different.

Fig. 8 exhibits the production of CH_4 , the main by-product. The initial selectivity of CH_4 was decreased from 6% to 3% as an increase of C_3H_8 fractional GHSV. The CH_4 selectivity can roughly indicate the cracking capability of the

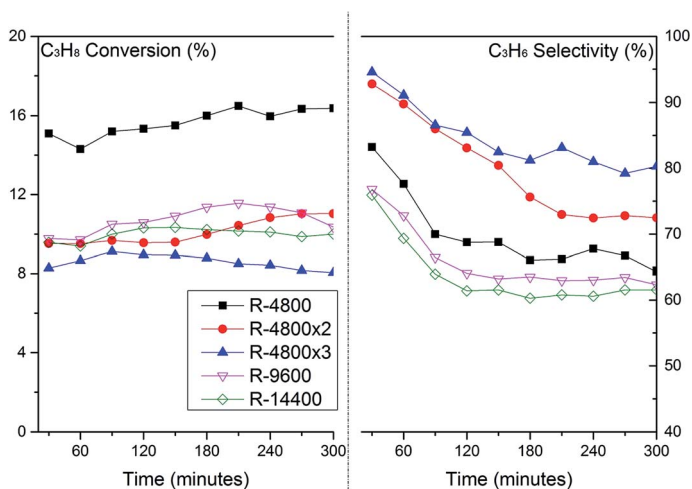


Fig. 7 C_3H_8 conversion and C_3H_6 selectivity over 5 wt%– $\text{Cr}_2\text{O}_3/\text{ZrO}_2$ upon operation times at various C_3H_8 partial pressures and overall GHSV; 500 °C and $\text{C}_3\text{H}_8/\text{CO}_2 = 0.5$.

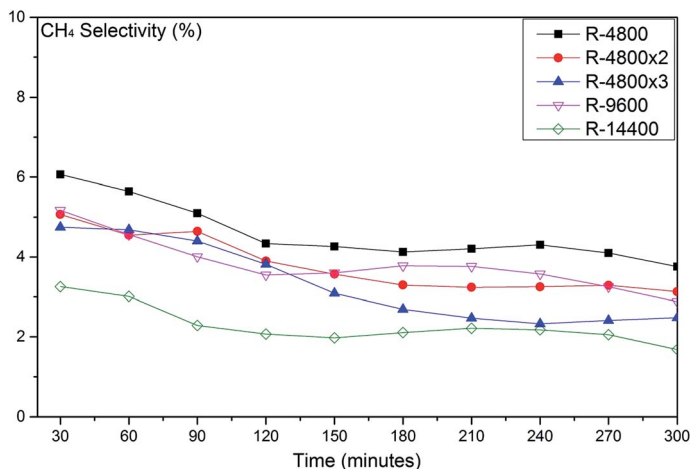


Fig. 8 Dependence of the CH₄ selectivity with time on stream over 5 wt%-Cr₂O₃/ZrO₂ at various C₃H₈ partial pressures and overall GHSV; 500 °C and C₃H₈/CO₂ = 0.5.

catalyst on higher level hydrocarbons, which indirectly exhibits the extent of further cracking effects on C₃H₆ during the reaction.

5.2 Discussion on the changes of C₃H₆ selectivity

The conversion of reactants and the mass balances of carbon and oxygen elements are shown in Table 4. In contrast to the high stability of the C₃H₈ conversion, the CO₂ conversions dropped drastically over the first 5 hours. This may be due to the various and different sites for C₃H₈ and CO₂ to be adsorbed on the catalyst surface respectively; C₃H₈ is usually attached to Cr species while CO₂ can be adsorbed at the interface between the Cr₂O₃ dopant and ZrO₂ support.²² The high level of C-balance indicates the low generation of solid and liquid C-containing products; this confirms the high stability of C₃H₈ conversions in each test. The O-balance, which was higher than 100% at the end of the test, indicates additional, extraneous oxygen must have entered into the gaseous phase during the reaction, and the oxygen source can be attributed to the reduction of high valance state chromium species (Cr⁶⁺/Cr⁵⁺) on the catalyst surface.²³

Table 4 Conversion of reactants (C_{C₃H₈}, C_{CO₂}) and balance of elements (B_C, B_O, B_H) in gaseous products over 5 wt%-Cr₂O₃/ZrO₂ at various C₃H₈ partial pressures and overall GHSV; 500 °C and C₃H₈/CO₂ = 0.5

C ₃ H ₈ partial pressure (atm)	C _{C₃H₈} (%)		C _{CO₂} (%)		B _C (%)		B _O (%)	
	0 h	5 h	0 h	5 h	0 h	5 h	0 h	5 h
R-4800	15.09	16.37	6.95	1.80	99.27	99.17	96.64	103.80
R-4800 × 2	9.52	11.03	4.62	2.79	99.90	99.30	97.80	103.16
R-4800 × 3	8.28	8.05	3.29	1.78	99.99	99.91	99.04	101.45
R-9600	9.77	10.35	5.15	1.51	98.65	98.87	96.93	102.42
R-14 400	9.57	10.00	4.50	1.19	98.55	98.80	97.30	101.78

Table 5 Yield of CO (Y_{CO}) and selectivity of hydrocarbons (S_i) over 5 wt%-Cr₂O₃/ZrO₂ at various C₃H₈ partial pressures and overall GHSV; 500 °C and C₃H₈/CO₂ = 0.5

C ₃ H ₈ partial pressure (atm)	Y_{CO} (%)		S_{CH_4} (%)		$S_{C_{2H_6}}$ (%)		$S_{C_{3H_6}}$ (%)	
	0 h	5 h	0 h	5 h	0 h	5 h	0 h	5 h
R-4800	3.59	3.54	6.06	3.76	1.32	1.00	83.23	64.30
R-4800 × 2	2.43	2.42	5.07	3.13	1.52	1.36	92.75	72.47
R-4800 × 3	1.94	1.89	4.74	2.48	1.66	1.88	94.56	80.30
R-9600	2.08	1.80	5.17	2.88	1.50	1.33	76.81	62.31
R-14 400	1.80	1.57	3.26	1.68	1.46	1.35	75.91	61.53

Weckhuysen *et al.*²⁴ claimed that Cr⁶⁺ plays as a precursor for the Cr dehydrogenation centres, and the reduction of Cr species is assumed to be one of the primary deactivation mechanisms.

Table 5 is a compilation of the selectivity of gaseous products. The reduced level of C₂H_x production as compared to that of the selectivity of CH₄ was observed. This experimental trend matched the prediction (highlighted in Fig. 4) that it is much more difficult to thermally crack CH₄ at 500 °C than corresponding C₂ molecules. The decrease in CO yield was not as much as the trend of CO₂ conversion; we believe that this is due to the carbon gasification by reducing the chromium species (Cr⁶⁺/Cr⁵⁺) on the catalyst surface, which matches the observed increasing O-balance.

The XRD patterns of 5 wt%-Cr₂O₃/ZrO₂ before and after the catalytic tests are displayed in Fig. 9, and the pattern of the ZrO₂ support is also shown here as a reference. The peak at $2\theta = 36.18^\circ$ corresponds to the 1-1-0 phase of Cr₂O₃ with rhombohedral crystal symmetry. No peak shift or new peaks were observed from the post-reaction catalyst, which indicated that no phase change occurred during

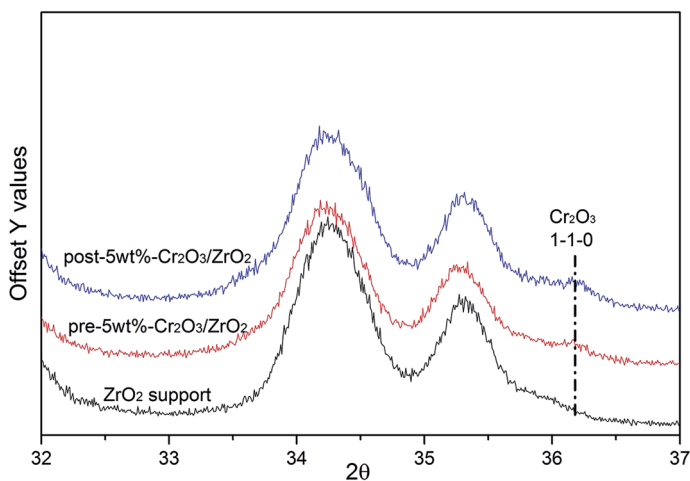


Fig. 9 X-ray diffraction (XRD) results over the catalysts both before (pre-5 wt%-Cr₂O₃/ZrO₂) and after (post-5 wt%-Cr₂O₃/ZrO₂) the catalytic tests, with ZrO₂ support as the reference.

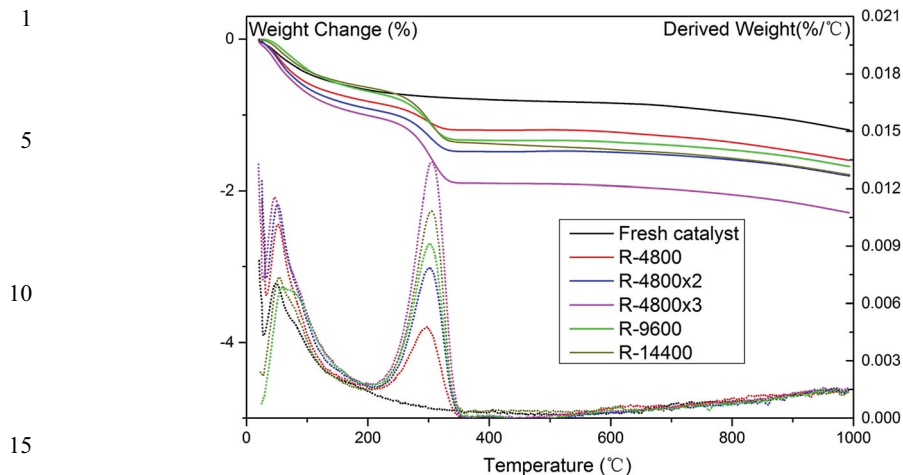


Fig. 10 TGA (solid lines) and D-TGA (dot lines) results over 5 wt%-Cr₂O₃/ZrO₂ at various C₃H₈ partial pressure and overall GHSV; 500 °C and C₃H₈/CO₂ = 0.5.

the catalytic test. Importantly, this also matched the high stability of C₃H₈ conversions, as shown in Fig. 7.

Thermal gravimetric analysis (TGA) results and the corresponding derivative weight-to-temperature (D-TGA) plots are displayed in Fig. 10. We attribute the weight loss, starting from 200 °C, to the combustion of amorphous carbon in air. The integrated area of the derivative weight equals the weight loss, which displayed more coke formed with an increase of the C₃H₈ fractional GHSV.

In general terms, the mechanism of C₃H₈ dehydrogenation in the presence of CO₂ involves the primary activation of C₃H₈ on the catalyst surface, while CO₂ provides a contribution to the reaction equilibrium shift by oxidising H₂ generated from the C₃H₈ dehydrogenation (*via* the reverse water gas shift reaction, H₂ + CO₂ → H₂O + CO). From the macro perspective, the average contact time for each C₃H₈ molecule is shortened with the higher C₃H₈ fractional GHSV, and this is the cause of a decreased C₃H₈ conversion by optimising both methods to modify the C₃H₈ fractional GHSV. However, the observed changes of C₃H₆ selectivity indicate that only increasing the partial pressure of reactants can effectively inhibit the further cracking of C₃H₆. This arises because the competitive adsorption between C₃H₆ and other substances are strengthened from the micro perspective.

6. Conclusions

With the aim of attempting to (ultimately) correlate the dehydrogenation of C₃H₈ in the presence of CO₂ with the energy source from solar heating technology, thermodynamic calculations were operated for chemical processes operating in the temperature range 300–500 °C. An important outcome is the great potential of C₃H₈ as compared to its lighter and heavier homologues (C₂H₆ and C₄H₁₀, respectively) from both the perspective of CO₂ activation and also coking resistance across this temperature range. The Δ_rG_m⁰ of each reaction in our thermodynamic modelling of the dehydrogenation of C₃H₈, in the presence of CO₂, also

1 indicated that neither the reverse water gas shift nor the coke gasification with
CO₂ are favoured at 300–500 °C.

2 A series of catalytic tests were carried out over 5 wt%-Cr₂O₃/ZrO₂ at various
3 C₃H₈ partial pressures and overall GHSV. It was shown that the increase in C₃H₈
4 partial pressure is highly beneficial for the enhancement of C₃H₆ selectivity.
5 Meanwhile, the C₃H₈ conversion was sacrificed due to the competitive adsorption
6 between the produced C₃H₆ and inactivated C₃H₈ molecules, which was the major
7 reason for the inhibition of further cracking of C₃H₆. As a comparison, the
8 increase of the overall GHSV can also decrease the C₃H₈ conversion to a similar
9 extent. However, the further cracking of C₃H₆ cannot be limited as only the
10 contact time of C₃H₈ on the catalyst surface was shortened from this micro
perspective.

11 With respect to the ultimate application of this particular CO₂ utilisation
12 process, we believe that the enhancement of selectivity of the (target) C₃H₆
13 product, whilst sacrificing some of the reactants' ultimate conversion, is accept-
14 able. The efficiency can be improved by a cycle system involving the reuse of the
unconverted feedstock by separating it from the outlet mixture and subsequently
15 cycling it back to the inlet mixture. It is recognised that this kind of cycle system is
16 beneficial to the reactions with low conversion but very high selectivity. The high
17 thermo-stability of the present catalyst makes it attractive to scale-up to a moving
18 bed or even a fluid bed reactor for catalyst regeneration.

19 We believe that the results presented here are promising in terms of the
20 underpinning catalyst science for establishing the potential industrialisation of
21 the process of CO₂ utilisation through C₃H₈ dehydrogenation. This type of CO₂
22 utilisation, operating in the relatively low temperature range of 300–500 °C, and
23 easily accessible by solar thermochemical routes, could help shift the focus of CO₂
24 interest from the disposal of an inconvenient by-product – typified by the process
25 of Carbon Capture and Storage (CCS) – towards the production and use of CO₂ as
26 a commodity chemical in Carbon Capture and Utilisation (CCU). However, one
27 must stress again that in order for any proposed CCU process to be realistic for
28 emission reduction potential, it can only be beneficial if any necessary energy
29 input is from renewable sources. As noted here, our view is that solar thermal
30 chemical processes for CO₂ utilisation, accessible across these temperature
31 ranges, offer considerable potential in this regard.

32 Acknowledgements

33 We thank the China Scholarship Council (CSC) for financial support to X. Du and
34 KACST and EPSRC for their continued support.

35 References

- 36 1 C. Song, *Catal. Today*, 2006, **115**, 2–32.
- 37 2 F. Schierbaum, *Carbon dioxide as chemical feedstock*, ed. Michele Aresta, 2010.
- 38 3 Z. Jiang, T. Xiao, V. L. Kuznetsov and P. P. Edwards, *Philos. Trans. R. Soc., A*,
39 2010, **368**, 3343–3364.
- 40 4 F. T. Zangeneh, S. Sahebdehfar and M. T. Ravanchi, *J. Nat. Gas Chem.*, 2011, **20**,
41 219–231.

- 1 5 S. J. Bennett, D. J. Schroeder and S. T. McCoy, *Energy Procedia*, 2014, **63**, 7976–7992.
- 6 Presented in part at the ADP technical Expert meetings, Bonn, Germany, 2014.
- 7 C. Ampelli, S. Perathoner and G. Centi, *Philos. Trans. R. Soc., A*, 2015, **373**, 1–35.
- 5 8 P. Phelan, T. Otanicar, R. Taylor and H. Tyagi, *J. Therm. Sci. Eng. Appl.*, 2013, **5**, 021003.
- 9 G. Maag, G. Zanganeh and A. Steinfeld, *Int. J. Hydrogen Energy*, 2009, **34**, 7676–7685.
- 10 D. B. Fox, E. H. Lee and M.-H. Rei, *Ind. Eng. Chem. Prod. Res. Dev.*, 1972, **11**, 444–446.
- 11 P. Michorczyk and J. Ogonowski, *React. Kinet. Catal. Lett.*, 2003, **78**, 41–47.
- 12 K. Takehira, Y. Ohishi, T. Shishido, T. Kawabata, K. Takaki, Q. Zhang and Y. Wang, *J. Catal.*, 2004, **224**, 404–416.
- 15 13 A. L. Lapidus, N. A. Gaidai, Y. A. Agafonov, N. V. Nekrasov, D. V. Trushin, A. V. Makashov, M. A. Botavina, G. Martra and S. Coluccia, *DGMK Tagungsber.*, 2008, **2008-3**, 275–282.
- 14 M. Chen, J.-L. Wu, Y.-M. Liu, Y. Cao, L. Guo, H.-Y. He and K.-N. Fan, *Appl. Catal., A*, 2011, **407**, 20–28.
- 20 15 P. Michorczyk, P. Kustrowski, A. Kolak and M. Zimowska, *Catal. Commun.*, 2013, **35**, 95–100.
- 16 T. Shishido, K. Shimamura, K. Teramura and T. Tanaka, *Catal. Today*, 2012, **185**, 151–156.
- 25 17 L. Liu, H. Liu, C.-y. Li and S.-f. Ji, *Beijing Huagong Daxue Xuebao, Ziran Kexueban*, 2005, **32**, 9–13.
- 18 R. Shanguan, X. Ge, J. Wang and J. Shen, *Shiyou Yu Tianranqi Huagong*, 2002, **31**, 5–7.
- 19 K. Mueller, A. Baumgaertner, L. Mokrushina and W. Arlt, *Chem. Eng. Technol.*, 2014, **37**, 1261–1264.
- 30 20 F. Solymosi and P. Tolmascov, *Catal. Lett.*, 2002, **83**, 183–186.
- 21 H. Liu, Z. Zhang, H. Li and Q. Huang, *J. Nat. Gas Chem.*, 2011, **20**, 311–317.
- 22 S. Naito, M. Tsuji and T. Miyao, *Catal. Today*, 2002, **77**, 161–165.
- 23 S. Deng, S. Li, H. Li and Y. Zhang, *Ind. Eng. Chem. Res.*, 2009, **48**, 7561–7566.
- 35 24 B. M. Weckhuysen and R. A. Schoonheydt, *Catal. Today*, 1999, **51**, 223–232.
- 25 P. Atkins and J. de Paula, *Atkins' Physical Chemistry*, 7th edn, 2002.
- 26 J. Kunesh, *The Properties of Gases and Liquids*, ed. B. Poling, J. Prausnitz and J. O'Connell, 5th edn, 2002.
- 40 27 W. M. Haynes, *CRC Handbook of Chemistry and Physics on DVD, Version 2012*, 2011.

45

50

PAPER

New catalysts for carboxylation of propylene glycol to propylene carbonate *via* high-throughput screening†

José A. Castro-Osma,^a James W. Comerford,^a Richard H. Heyn,^{*b} Michael North^a and Elisabeth Tangstad^b

Received 4th May 2015, Accepted 28th May 2015

DOI: 10.1039/c5fd00061k

High throughput methodologies screened 81 different metal salts and metal salt combinations as catalysts for the carboxylation of propylene glycol to propylene carbonate, as compared to a 5 mol% Zn(OAc)₂/*p*-chlorobenzene sulfonic acid benchmark catalyst. The reactions were run with added acetonitrile (MeCN) as a chemical water trap. Two new catalysts were thereby discovered, zinc trifluoromethanesulfonate (Zn(OTf)₂) and zinc *p*-toluenesulfonate. The optimal reaction parameters for the former catalyst were screened. Zn(OTf)₂ gave an overall propylene carbonate yield of greater than 50% in 24 h, twice as large as the previous best literature yield with MeCN as a water trap, with 69% selectivity and 75% conversion of propylene glycol at 145 °C and 50 bar CO₂ pressure.

Introduction

Research on carbon dioxide (CO₂) utilization (CDU) has been gaining momentum over the past decade. While the motivation for this surge in interest may well be a response to the increasing levels of CO₂ in the atmosphere and the need for mitigating CO₂ emissions, the sheer volumes of CO₂ emitted¹ and relatively modest contribution CDU can make toward mitigation of these emissions, at least in terms of chemical production volumes, strongly suggest that a greater motivation is the development of CO₂ as a sustainable C₁ source for the chemical industry. CO₂ is renewable, easily handled and stored, and essentially non-toxic. The challenge in its use arises from its thermodynamic and kinetic inertness. Advances in catalysis and process engineering are therefore necessary in order to overcome these barriers. Some of these issues can be and have been addressed by the use of high energy chemical reactants, as exemplified by the production of

^aUniversity of York, Department of Chemistry, Green Chemistry Center of Excellence, York YO10 5DD, North Yorkshire, England, UK

^bSINTEF Materials and Chemistry, P. O. Box 124 Blindern, 0314 Oslo, Norway. E-mail: rhh@sintef.no

† Electronic supplementary information (ESI) available: ¹H NMR spectrum of a typical PG to PC product mixture; list of all HT screened catalyst formulations. See DOI: 10.1039/c5fd00061k

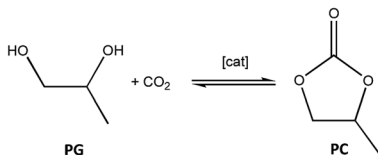
1 aliphatic polycarbonates from CO₂ and epoxides, which is on the cusp of industrial implementation.²

5 One class of compounds that have generated considerable interest as products for CDU is the organic carbonates, both open, linear carbonates such as dimethylcarbonate (DMC) and closed, cyclic carbonates such as propylene carbonate (PC). These molecules can be synthesized from CO₂ with two equivalents of an alcohol (methanol, for DMC) or one equivalent of a diol (1,2-propanediol, for PC). The latter can also be prepared from CO₂ and propylene oxide using the appropriate choice of catalyst, and the cyclic carbonates can be undesired by-products

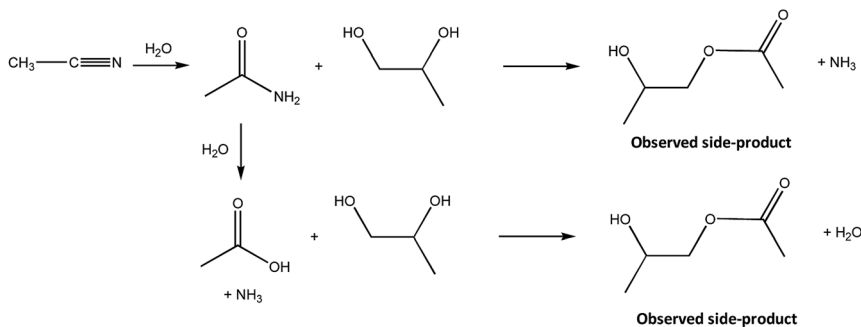
10 in the production of aliphatic polycarbonates.³ The reaction between CO₂ and alcohols or diols is thermodynamically unfavorable,⁴ with water as the other reaction product (see Scheme 1). Without any added water trap, the yield of PC from 1,2-propanediol (propylene glycol, PG) is 0.5% at 130 °C with CeO₂·ZrO₂ as a heterogeneous catalyst.⁵ The addition of physical or chemical water traps will pull the equilibrium toward products, and this has most recently been successful with a CeO₂/2-cyanopyridine system (20 mol% CeO₂ and 10-fold excess 2-cyanopyridine based on PG), which is able to provide a nearly quantitative yield of PC from PG and CO₂ within 1 h at 130 °C and 50 bar CO₂, with 2-acetamidopyridine as the by-product from the chemical trapping of the co-produced water.⁶

15 The effect of water traps on the synthesis of organic carbonates from CO₂ and alcohols or diols has recently been reviewed.⁷ The majority of the other investigations into this reaction have used acetonitrile (MeCN) as the chemical water trap. One drawback with MeCN is the formation of a number of by-products from the water-trapping reaction, including acetamide, acetic acid, and acetylated glycols (see Scheme 1). The most efficient catalytic system (as based on time-yield)

30 **Primary reaction**



35 **Side reactions**



40
45
50 **Scheme 1** Primary reaction and formation of the observed side products. Only the 2-hydroxypropyl acetate side-product is shown. 1-Hydroxypropyl acetate and 1,2-propyl diacetate side-products were also observed.

reported thus far is 2.5 mol% Zn(OAc)₂ with a 1.8 fold excess of MeCN at 160 °C and 30 bar CO₂, which provided a 12% yield of PC with a 64% selectivity after 2 h.⁸ A second report also indicates Zn(OAc)₂ as the best M(OAc)₂ catalyst (M = Co, Ni, Cu, Mn, Mg, Ca), but the reported time-yield is poorer (24% yield and 62% selectivity within 12 h at 170 °C and 100 bar CO₂).⁹ In addition to Zn(OAc)₂, inorganic carbonates (K₂CO₃ and Cs₂CO₃/(NH₄)₂CO₃),¹⁰ organic bases (TBD = 1,5,6-triazabicyclo[4.4.0]dec-5-ene)¹¹ and modified ZnO (KI/ZnO)¹² have been identified as the best catalysts in individual studies.

Direct comparison between these catalysts is difficult since there is always variation in the reported reaction pressures, temperatures, times and catalyst loadings.

Considering the relatively limited number of compounds that have been tested for this reaction, we undertook a high throughput (HT) screening of 81 different metal salts and salt combinations. This contribution describes the selection of the benchmark catalyst for the HT studies, trends gleaned from the HT studies, and a parameter screening for an improved catalyst system found during the HT screening.

Results and discussion

Catalyst pre-screening and choice of benchmark

This study started with a small catalyst pre-screening for determination of a suitable benchmark catalyst for the carboxylation of PG into PC at 145 °C and 60

Table 1 Synthesis of PC from PG and CO₂ with different catalysts^a

Entry	Catalyst	Solvent	Yield PC ^b (%)
1	[SalenAl] ₂ O ^c	MeCN	0
2 ^d	[SalenAl] ₂ O + TBAB	MeCN	0
3	Tetrabutylammonium bromide	MeCN	0
4	K ₂ CO ₃	MeCN	0
5	Bu ₂ Sn(OAc) ₂	MeCN	<1
6	Mn(OAc) ₂	MeCN	7
7	Mn(OAc) ₂	MeOH	0
8	Fe(OAc) ₂	MeCN	<1
9	Fe(OAc) ₂	MeOH	0
10	Co(OAc) ₂	MeCN	8
11	Ni(OAc) ₂	MeCN	0
12	Cu(OAc) ₂	MeCN	5
13	Cu(OAc) ₂	MeOH	0
14	ZnBr ₂	MeCN	<1
15	ZnI ₂	MeCN	<1
16	ZnI ₂	MeOH	0
17	Zn(acac)·H ₂ O	MeCN	15
18	Zn(OAc) ₂	MeOH	<1
19 ^e	Zn(OAc) ₂	MeOH	0
20 ^e	Zn(OAc) ₂	MeCN	1
21	Zn(OAc) ₂	MeCN	27

^a Reactions carried out at 145 °C and 60 bar CO₂ pressure for 16 hours using 2.5 mol% of catalyst and 10 ml MeCN or MeOH. ^b Yield of PC determined by ¹H NMR spectroscopy of the crude reaction mixture (see ESI). ^c See ref. 13. ^d 2.5 mol% tetra-butylammonium bromide (TBAB) used. ^e 13X molecular sieves added (200 mg).

bar CO₂. Reactions were carried out in the presence of either methanol or MeCN as the solvent for 16 hours using 2.5 mol% of catalyst (Table 1). These conditions were chosen as an average between the conditions provided in the two previous papers reporting the catalytic activity of Zn(OAc)₂.^{8,9} As shown in Table 1, zinc salts displayed higher catalytic activity than other metal salts, and Zn(OAc)₂ was, perhaps unsurprisingly, the most active catalyst. Additionally, reactions carried out in MeCN showed higher conversions than those carried out in methanol, which supports previous results showing that MeCN not only acts as a solvent but also as a dehydrating agent, shifting the reaction to the formation of products. As a catalyst, Zn(OAc)₂ showed some problems with reproducibility; a series of 6 runs gave a 39 ± 7% conversion of PG and a 18 ± 5% yield of PC with a 41 ± 4% selectivity.

One of the main routes for the synthesis of cyclic carbonates is the transesterification reaction between DMC and diols.¹⁴ Similarly, the synthesis of diphenyl carbonate (DPC) can be carried out by a transesterification reaction between DMC and phenol,¹⁵ and it was found that using sulfonic acids as co-catalysts improved both the conversion of DMC and the isolated yield of DPC.¹⁶ Therefore, the addition of a sulfonic acid as a co-catalyst for the synthesis of PC from PG was investigated. As shown in Table 2, the addition of 5 mol% *p*-chlorobenzene sulfonic acid (*p*-CBSA) gave higher PC yields and larger PG conversions. The yields of PC in Table 2 were the highest overall yields that have been reported in the literature for systems that employ MeCN as a water trap. The 5 mol% Zn(OAc)₂/*p*-CBSA system was therefore chosen as the benchmark catalyst for the high throughput screening.

High throughput screening

The high throughput (HT) screening experiments included a total of 81 different metal salts, combinations of metal salts and combinations of metal salts and strong acids. These screening experiments also included some metal salts tested in the pre-screening activity, as an additional check of the reproducibility of the HT system. The screened catalyst systems can be loosely grouped into four categories: simple Zn salts, other late transition metal salts, combinations of Zn salts with other reagents, and Lewis acidic triflate salts. The first three categories

Table 2 Synthesis of PC from PG and CO₂ with Zn(OAc)₂ and sulfonic acids as catalysts^a

Entry	Sulfonic acid	Yield PC (%)	Conversion PG (%)	Selectivity (%)	Isolated PC yield ^b (%)
1 ^c	<i>p</i> -CH ₃ C ₆ H ₄ SO ₃ H	22	48	44	—
2 ^d	<i>p</i> -CH ₃ C ₆ H ₄ SO ₃ H	28	69	41	18
3	C ₆ H ₅ SO ₃ H	29	72	40	17
4	<i>p</i> -ClC ₆ H ₄ SO ₃ H	33	73	45	25
5 ^e	<i>p</i> -ClC ₆ H ₄ SO ₃ H	35	84	42	34
6 ^f	<i>p</i> -CH ₃ C ₆ H ₄ SO ₃ H	26	63	41	27

^a Reactions carried out with 5 mol% Zn(OAc)₂ and 5 mol% sulfonic acid, at 145 °C and 60 bar CO₂ for 16 h. Product distributions based on ¹H NMR spectra of the crude reaction mixtures. ^b Yield of PC isolated by flash chromatography. See Experimental section.

^c Used 2.5 mol% Zn(OAc)₂ and 2.5 mol% *p*-CH₃C₆H₄SO₃. Average values for 3 runs.

^d Average of three runs. ^e Dry MeCN. ^f 64 h reaction time.

1 included combinations with strong acids. In addition to the *p*-CBSA and *p*-toluene
 sulfonic acid (*p*-TSA) used in the pre-screening, the HT studies also used 4-
 5 nitrobenzene sulfonic acid and dibzenesulfonimide, as acids with different pK_a
 values (from 6.60 for 4-nitrobenzene sulfonic acid to 11.34 for dibzenesulfon-
 imide) in MeCN.¹⁷ The Lewis acids and other reagents were chosen as they have
 been shown to be effective transesterification catalysts. Specifically, lanthanide
 triflates have been shown to catalyze the transesterification of DMC with
 ethanol.¹⁸ The other reagents, KI, KOH, K₂CO₃ and NEt₄Br, have been shown to be
 10 catalysts or co-catalysts in the synthesis of DMC from CO₂, MeOH and epoxides.¹⁹
 The results from the catalysts tested in the pre-screening compared well with the
 results from the same catalysts tested in the HT experiments. Table 3 compares
 the PC yield of five catalysts studied both in the pre-screening and the HT
 experiments. The qualitative comparison as based on the yield of the benchmark
 15 catalyst is good, providing support of the validity of the results from the HT
 screening experiments. The larger differences for Co(OAc)₂ and Zn(acac)₂·H₂O
 may be attributed to the different catalyst loadings in the different experiments.

All 81 screened catalyst formulations are provided in the ESI.† For HT
 screening experiments, an important decision point is the definition of a “hit”.
 20 For this study, any screened catalyst formulation that gave a better PC yield than
 that of the benchmark was deemed a “hit” and worth potential follow-up in a
 bench-top reactor. It must be emphasized that the HT experiments are designed
 simply to identify potential lead catalyst candidates. The absolute PC yield for any
 one screened catalyst formulation was considered as merely suggestive. The list of
 25 catalyst formulations considered as lead candidates is shown in Table 4. These 16
 catalyst formulations represent 20% of all screened catalysts. It is likely that the
 hits for zinc trifluoromethanesulfonate (Zn(OTf)₂) and zinc *p*-toluenesulfonate
 hydrate (Zn(Tos)₂·H₂O) with acids are simply due to the Zn salts, and therefore
 these successful catalyst combinations can essentially be reduced to four lead
 30 candidates: Zn(OTf)₂, Zn(Tos)₂·H₂O, zinc hexafluoroacetylacetate dihydrate,
 and Zn(OAc)₂ with Lewis acidic triflate salts. On the basis of performance and the
 preference for a single-component catalyst, Zn(OTf)₂ and Zn(Tos)₂·H₂O were
 chosen for bench-top validation experiments.

35 The data for the carboxylation of PG to PC using 5 mol% Zn(OTf)₂ and
 Zn(Tos)₂·H₂O are shown in Table 5. In particular, Zn(OTf)₂ showed a significantly

40 Table 3 Comparison of selected catalysts in the pre-screening and HT experiments^a

Catalyst	PC yield relative to benchmark	
	Pre-screening	HT
Co(OAc) ₂	24%	48%
Cu(OAc) ₂	15%	10%
Zn(acac) ₂ ·H ₂ O	45%	81%
Zn(OAc) ₂	82%	97%
Zn(OAc) ₂ + <i>p</i> -TSA ^b	85%	89%

50 ^a Pre-screening data with 2.5 mol% catalyst, HT data with 5 mol% catalyst. Entry 4 in Table 2
 used as the benchmark catalyst yield. HT results based on HeadSpace GC analyses. ^b 5 mol%
 catalyst in the pre-screening experiment.

Table 4 Lead catalyst candidates from the HT screening^a

Catalyst	Relative % PC yield ^b	Catalyst	Relative % PC yield
Zn(OTf) ₂ + 4-NO ₂ -benzenesulfonic acid	1.01	Zn(OAc) ₂ + Sm(OTf) ₃	1.11
ZnI ₂ + <i>p</i> -TSA ^d	1.02	Zn(OTf) ₂ + <i>p</i> -TSA	1.11
Zn(F ₆ -acac) ^c	1.03	Zn(OTf) ₂ + dibenzenesulfonimide	1.12
Zn(F ₆ -acac) + <i>p</i> -CBSA	1.07	Zn(OAc) ₂ + LiOTf	1.18
Zn(OTf) ₂ + <i>p</i> -CBSA	1.08	Zn(OAc) ₂ + Mg(OTf) ₂	1.25
Zn(OTf) ₂	1.08	Zn(OAc) ₂ + Yb(OTf) ₃	1.30
Zn(Tos) ₂ · H ₂ O + <i>p</i> -TSA	1.09	Zn(Tos) ₂ · H ₂ O	1.31
Zn(OAc) ₂ + <i>p</i> -TSA ^d	1.09	Zn(OAc) ₂ + Ca(OTf) ₂	1.35

^a HT reaction conditions: 145 °C, 50 bar CO₂, 16–18 h reaction time. ^b Data based on comparison to benchmark data, as determined from GC HeadSpace data. ^c F₆-acac = hexafluoroacetylacetonate. ^d 10 mol%.

Table 5 Lead candidate validation results^a

Catalyst	Time (h)	<i>p</i> (CO ₂) bar	PC yield (%)	PG conversion (%)	Selectivity (%)
Zn(OTf) ₂	24	53	52	75	69
Zn(Tos) ₂ · H ₂ O	25	47	48	77	62

^a Conditions: 20.7 g (2.72 mmol) PG, 31.45 g (766 mmol) MeCN, 145 °C, time from start of heating, product ratios from integration of ¹H NMR spectra.

improved catalytic performance over previously studied catalysts. Over 50% yield with nearly a 70% selectivity was observed for the Zn(OTf)₂ catalyst. The observed PC yield for Zn(OTf)₂ is double the best reported overall yield in the literature for those systems that used MeCN as the chemical water trap.

Parameter screening for Zn(OTf)₂

Given the superior catalytic performance of Zn(OTf)₂ in the HT screening and validation studies, this catalyst was chosen for a parameter optimization. The effect of the reaction parameters of pressure and temperature and the amount of Zn(OTf)₂ on the conversion to PC and the overall selectivity of the reaction were screened in a bench-top pressure reactor, and the results are presented in Fig. 1–3, respectively.‡ There is very little effect of a change in pressure from 30 to 70 bar CO₂ on the product distribution. The yield of PC is essentially constant above 40 bar, and there is a slight increase in the side products with increasing pressure, as

‡ Note that the amount of MeCN and the reaction time in the parameter screening experiments are less than those for the validation experiments. These differences, in addition to differences in protocol and reactor set-up, are the likely reasons for the slightly poorer overall results in the parameter screening experiments, as compared to those in the validation experiments.

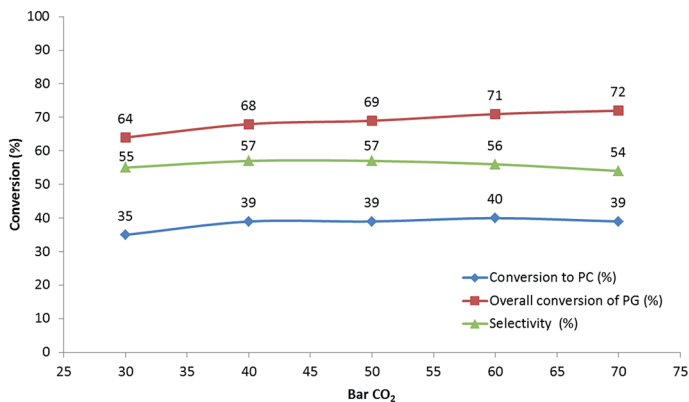


Fig. 1 Effect of different pressures on the yield of PC with 5 mol% Zn(OTf)₂ as the catalyst.

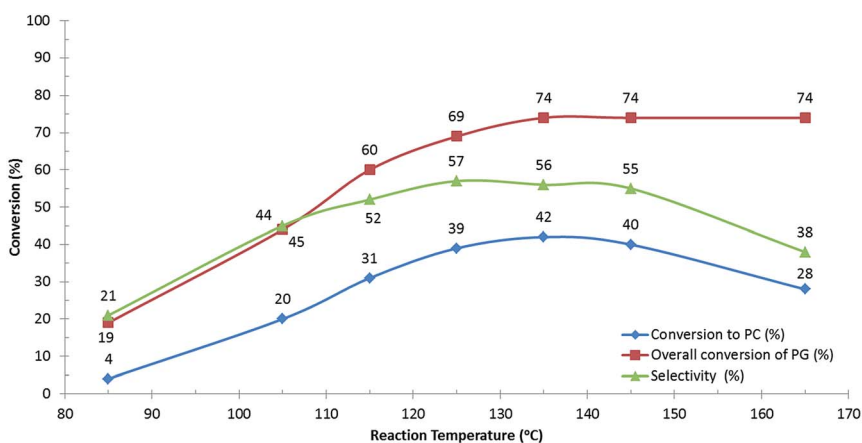


Fig. 2 Effect of different temperatures on the yield of PC with 5 mol% Zn(OTf)₂ as the catalyst.

indicated by the increase in the overall conversion of PG and the decrease in selectivity.

The effect of temperature is more profound. At 85 °C, the yield of PC is only 4%. The yield increases monotonically with an increase in temperature up to 135 °C; at this temperature the yield of PC, the overall selectivity and the conversion of PG are at their maximum values. Higher reaction temperatures show a decrease in PC yield and selectivity, while the conversion of PG remains constant, indicating that reaction temperatures higher than 135 °C only increase side product formation. Similarly, an increase in the mol% catalyst from 1 mol% to 5 mol% provides a monotonic increase in the PC yield, from 17% to 42%. There is a concomitant increase in PG conversion, while the selectivity remains essentially constant. Increasing the catalyst amount from 5 to 10 mol% does not appreciably increase the PC yield. The overall conversion of PG does slightly increase, but this is mainly due to a greater increase in the formation of side products, as shown by the decrease in selectivity.

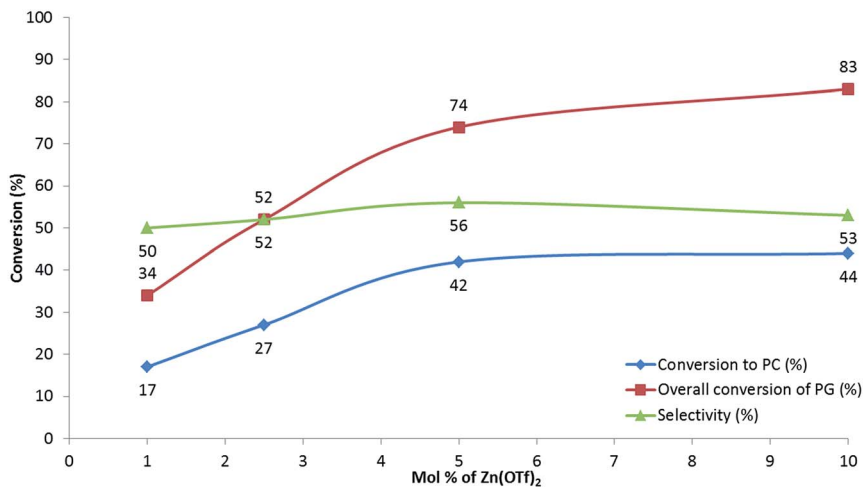


Fig. 3 Effect of different amounts of the catalyst Zn(OTf)₂ on the yield of PC.

Discussion

On the basis of the many different catalyst formulations that have been screened, either in a bench-top reactor or in a HT system, certain trends can be identified in this work. One, transition metal salts, apart from the Zn salts, are not very good catalysts for this reaction. None of the Ni or Cu salts showed any significant catalytic activity, even in the presence of strong acids. Salts of Mn, Fe and Co showed better activities, while the screened salts did not fare as well as the Zn salts; examples with different coordination spheres may prove to be viable candidates. Two, Lewis acidic triflate salts, based on group 1, 2 and lanthanide metals, are also very poor catalysts, although some of these salts showed promise in combination with Zn(OAc)₂ and are under further study. Three, the pK_a of the added acid had in general no effect on catalytic activity. Four, a strong acid than they did alone. For example, both ZnBr₂ and ZnI₂ when combined with either *p*-CBSA or *p*-TSA, showed much better catalytic activities in the HT screening experiments than the simple salts did in the pre-screening experiments.

One hypothesis for the improved catalytic activity of Zn(OTf)₂ and Zn(Tos)₂·H₂O over the benchmark system is that they do not need other reagents to produce open metal coordination sites. The activity of the benchmark catalyst (and other Zn salts) in combination with sulfonic acids may well be attributed to the formation of HOAc and some Zn²⁺ species with a labile coordination sphere. That other Zn salts with ostensibly poorly coordinating anions such as Zn(BF₄)₂ fail to show appreciable catalytic activities, even in the presence of strong acids, suggests that Zn(OTf)₂ and Zn(Tos)₂·H₂O may impart other, as-yet unknown, benefits towards the catalysis of this reaction.

Experimental

General considerations

All reagents were commercially available (Alfa Aeser, Sigma-Aldrich, Fluka, TCI or Acros) and were used as received. Metal salts for the high throughput studies were

1 in general anhydrous. See ESI† for further information. The bimetallic
aluminium salen complex was prepared as previously reported.¹³ Carbon dioxide
was purchased from BOC or Yara and used without further purification. ¹H and
5 ¹³C NMR spectra were recorded on a Jeol Oxford 400 spectrometer or on a Bruker
UltraShield 400 spectrometer at resonance frequencies of 400 and 100 MHz,
respectively.

Initial screening

10 Reactions were magnetically stirred in a 300 mL stainless steel pressure reactor
heated in an oil bath. Product compositions were then analysed using ¹H NMR
spectroscopy without any purification to determine the conversion and selectivity,
as based on the integration of the Me signals of PC, side products and PG (see
ESI.†)

15

Representative procedure for the synthesis of PC catalysed by Zn(OAc)₂ and *p*-chlorobenzene sulfonic acid

20 PG (7.35 mL, 100 mmol), Zn(OAc)₂ (0.917 g, 5 mmol), *p*-CBSA (1.07 g, 5 mmol) and
MeCN (10 mL, 191 mmol) were placed in a 300 mL stainless steel pressure reactor
heated in an oil bath. The reaction mixture was magnetically stirred and heated to
145 °C. Then, the reactor was pressurized to 60 bar of carbon dioxide and the
reaction mixture was stirred for 16 h. The conversion of PG to PC was then
25 determined by analysis of a sample using ¹H NMR spectroscopy. The remaining
sample was evaporated *in vacuo* to give a mixture of PC, PG, propylene glycol
acetate and propylene glycol diacetate. The mixture was purified by flash chroma-
tography, using dichloromethane as the eluent, to give the pure PC.

High throughput screening

30 The high throughput experiments were conducted in an in-house constructed HT
reactor featuring four rows of six reactor wells, with each row of reactors having a
common gas feed. Each well was 9 cm high and had an inner diameter of 1.5 cm,
with an effective reactor volume of approximately 11 mL. All wells were closed
35 during the reaction to avoid well-to-well contamination. On a bench-top, the
catalyst formulation (metal salts, acids, ligands) was added to each well of the
reactor. The amount of catalyst was kept to *ca.* 5 mol% of the amount of PG. A 1
mL aliquot of PG (13.6 mmol) and a 2 mL aliquot of MeCN (38.3 mmol) were then
added by autopipette. Three steel balls (5 mm diameter) were added to each well
40 to ensure proper mixing. The set of 24 reactor wells was then attached to the gas
inlet portion of the reactor under a CO₂ flow, placed in an oven and warmed up to
145 °C under 2–3 bar CO₂ pressure. After reaching the reaction temperature, the
CO₂ pressure in each row of 6 reactors was sequentially increased to 50 bar.
Mixing was accomplished with the help of a variable speed vortex (shaker).
45 Reactions were run overnight, usually between 16–18 h from the time of pres-
surizing the reactors to 50 bar CO₂ until cooling was initiated. Approximately two
hours were required to cool the reactor sufficiently before the CO₂ pressure could
be released. Once the reactors reached a sufficiently low temperature, the pres-
sure was carefully released overnight to a holding container. The initial HT
50 experiment contained the benchmark catalyst system in each of the 24 reactor
wells. No significant internal variation was observed, apart from a small,

1 reproducible decrease in benchmark catalyst yields in the row of 6 reactors closest
to the oven door. Comparison of PC yields for the screened catalysts were
therefore made on a row-by-row basis, and in order to ensure reproducibility of
each high-throughput experiment, the benchmark catalyst was placed in one
5 randomly chosen well in each row of 6 reactors. The placement of the 20 other
catalyst formulations in each high throughput experiment was also randomized.

Product analysis was conducted on a Teledyne Tekmar HT3 HeadSpace
analyzer coupled to a Agilent 6890 gas chromatograph, using a DB-WAX column
10 (30 m × 0.320 mm × 0.5 μm) and flame ionization detector. Samples were sub-
jected to a 140 °C, 15 minute temperature profile. Analyses were conducted on two
10 μL samples withdrawn from the high-throughput reactor wells.

Validation experiments

15 Results from selected catalysts from the high throughput experiments were
validated in a 300 mL Parr reactor with mechanical stirrer and heating jacket. On
a bench top, a glass liner for the reactor was charged with the chosen catalyst
formulation (*ca.* 5 mol% based on PG), PG (*ca.* 20.7 g, 0.272 mol) and MeCN (*ca.*
20 31.5 g, 0.767 mol). The reactor top was mounted under a flow of CO₂. After the
reactor had been assembled, it was flushed with CO₂ three times, and the
temperature was raised to 145 °C under a slight pressure of CO₂ (2–3 bar). Finally,
the pressure was raised to *ca.* 50 bar and the CO₂ feed was closed. The reaction
was stopped by simply removing the heating jacket and allowing the reactor to
25 cool to room temperature, followed by a slow release of CO₂. The reactor was
cleaned with hot isopropanol and dried between runs. Product distributions were
determined by the established ¹H NMR method.

Parameter screening for Zn(OTf)₂

30 The reactor was dried at 100 °C under vacuum for a minimum of one hour and
cooled to <40 °C before use. The reactor was then charged with anhydrous
Zn(OTf)₂ and 10 mL (191 mmol) of dry MeCN stored under Ar. 60 mmol PG and a
magnetic stirring bar was subsequently added. The reactor was then sealed,
pressurized to 20 bar with CO₂ and heated to the desired temperature. Once this
35 temperature had been reached, the CO₂ pressure was increased to the desired
value. After 16 hours, the reactor was cooled in a bath of liquid nitrogen or dry ice/
acetone until the internal temperature dropped below 30 °C, at which time the
reactor was depressurized. Yields and selectivities were determined from inte-
gration of the ¹H NMR spectra of the products.
40

Conclusions

45 Due to its thermodynamic stability and kinetic sluggishness, CO₂ needs catalysts
in order to be transformed into useful chemical products. In this study, we have
endeavored to apply high throughput techniques so as to more rapidly screen a
host of different metal salts as catalysts for the carboxylation of propylene glycol
to propylene carbonate. Our initial pre-screening results found an improved
catalyst system –5 mol% Zn(OAc)₂/*p*-chlorobenzene sulfonic acid – that showed
50 an improvement in PC yield over data reported in the literature. With this
benchmark catalyst system in hand, 81 different metal salts and metal salt

1 combinations were screened. This resulted in the discovery of two new catalysts
for this reaction, $\text{Zn}(\text{OTf})_2$ and $\text{Zn}(\text{Tos})_2 \cdot \text{H}_2\text{O}$, the activities of which were vali-
dated using a bench-top reactor. The $\text{Zn}(\text{OTf})_2$ system underwent further bench-
top screening, in order to establish the optimal reaction parameters. The $\text{Zn}(\text{OTf})_2$
5 catalyst showed an overall PC yield at least twice as large as the best catalyst
system hitherto reported in the literature, using MeCN as a water trap. The activity
of the new catalyst is still inferior to that obtained with CeO_2 and 2-
cyanopyridine.⁶

10 We are continuing our studies into these new Zn catalyst systems, and varia-
tions on the basic $\text{Zn}(\text{OTf})_2$ catalyst and investigations into the mechanism of the
reaction will be reported in due course.

Acknowledgements

15 The authors would like to thank the European Union Seventh Framework
program (FP7/2007–2013) project “CyclicCO2R”, under grant agreement number
309497, for financial support. R.H.H. and E.T. would like to thank Kari Anne
Andreassen, Anne Andersen, Aud M. Bougza, Dr Silje F. Håkonsen and Ruth
20 Elisabeth Stensrød for experimental assistance.

Notes and references

- 1 G. M. Bond, J. Stringer, D. K. Brandvold, F. A. Simsek, M.-G. Medina and
25 G. Egeland, *Energy Fuels*, 2001, **15**, 309–316.
- 2 J. Langanke, A. Wolf, J. Hofmann, K. Böhm, M. A. Subhani, T. E. Müller,
W. Leitner and C. Gürtler, *Green Chem.*, 2014, **16**, 1865–1870;
A. M. Chapman, C. Keyworth, M. R. Kember, A. J. J. Lennox and
C. K. Williams, *ACS Catal.*, 2015, **5**, 1581–1588.
- 3 For a recent review, see C. Martin, G. Fiorani and A. Kleij, *ACS Catal.*, 2015, **5**,
30 1353–1370.
- 4 The standard Gibbs energy of reaction in the ideal gas state $\Delta_{\text{R}}G^{\text{IG}}$ is
calculated to be $\approx +37 \text{ kJ mol}^{-1}$ for synthesis of open carbonates such as
DMC from CO_2 and 2 equiv. of an alcohol. K. Müller, L. Mokrushina and
35 W. Arlt, *Chem. Ing. Tech.*, 2014, **86**, 497–503.
- 5 K. Tomishige, H. Yasuda, Y. Yoshida, M. Nurunnabi, B. Li and K. Kunimori,
Green Chem., 2004, **6**, 206–214.
- 6 M. Honda, M. Tamura, K. Nakao, K. Suzuki, Y. Nakagawa and K. Tomishige,
ACS Catal., 2014, **4**, 1893–1896.
- 7 M. Honda, M. Tamura, Y. Nakagawa and K. Tomishige, *Catal. Sci. Technol.*,
2014, **4**, 2830–2845.
- 8 X. Zhao, N. Sun, S. Wang, F. Li and Y. Wang, *Ind. Eng. Chem. Res.*, 2008, **47**,
1365–1369. After 6 h reaction, the yield of PC had increased to 19%, while
45 the selectivity had decreased to 51%.
- 9 S. Huang, S. Liu, J. Li, N. Zhao, W. Wei and Y. Sun, *J. Fuel Chem. Technol.*, 2007,
35, 701–705.
- 10 S. Huang, S. Liu, J. Li, N. Zhao, W. Wei and Y. Sun, *Catal. Lett.*, 2006, **112**, 187–
191.
- 50 11 S. Huang, J. Ma, J. Li, N. Zhao, W. Wei and Y. Sun, *Catal. Commun.*, 2008, **9**,
276–280.

- 1 12 S. Huang, S. Liu, J. Li, N. Zhao, W. Wei and Y. Sun, *Catal. Lett.*, 2007, **118**, 290–294.
- 13 J. Meléndez, M. North and R. Pasquale, *Eur. J. Inorg. Chem.*, 2007, 3323–3326; M. North and R. Pasquale, *Angew. Chem., Int. Ed.*, 2009, **48**, 2946–2948;
- 5 J. A. Castro-Osma, M. North and X. Wu, *Chem.–Eur. J.*, 2014, **20**, 15005–15008.
- 14 J. R. Ochoa-Gomez, O. Gomez-Jimenez-Aberasturi, B. Maestro-Madurga, A. Pesquera-Rodriguez, C. Ramirez-Lopez, L. Lorenzo-Ibarreta, J. Torrecilla-Soria and M. C. Villaran-Velasco, *Appl. Catal., A*, 2009, **366**, 315–324; A. Kumar, K. Iwatani, S. Nishimura, A. Takagaki and K. Ebitani, *Catal. Today*, 2012, **185**, 241–246.
- 10 15 M. Fuming, *J. Mol. Catal. A: Chem.*, 2002, **184**, 465–468.
- 16 H. Lee, S. J. Kim, B. S. Ahn, W. K. Lee and H. S. Kim, *Catal. Today*, 2003, **87**, 139–144.
- 15 17 A. Kütt, I. Leito, I. Kaljurand, L. Sooväli, V. M. Vlasov, L. M. Yagupolskii and I. A. Koppel, *J. Org. Chem.*, 2006, **71**, 2829–2838; F. Eckert, I. Leito, I. Kaljurand, A. Kütt, A. Klamt and M. Diedenhofen, *J. Comput. Chem.*, 2009, **30**, 799–810. The pK_a 's for *p*-CBSA and *p*-TSA in MeCN are 7.16 and 8.01.
- 18 F. M. Mei, E. X. Chen and G. X. Li, *Kinet. Catal.*, 2009, **50**, 666–670.
- 20 19 N. A. M. Razali, K. T. Lee, S. Bhatia and A. R. Mohamed, *Renewable Sustainable Energy Rev.*, 2012, **16**, 4951–4964.
- 25
- 30
- 35
- 40
- 45
- 50

PAPER

Extraction of $\text{Mg}(\text{OH})_2$ from Mg silicate minerals with NaOH assisted with H_2O : implications for CO_2 capture from exhaust flue gas

Silvia Madeddu,^{*a} Michael Priestnall,^{†b} Erik Godoy,^c R. Vasant Kumar,^d Sugat Raymahasay,^e Michael Evans,^f Ruofan Wang,^a Seabelo Manenye^a and Hajime Kinoshita^a

Received 1st May 2015, Accepted 5th June 2015

DOI: 10.1039/c5fd00047e

The utilisation of $\text{Mg}(\text{OH})_2$ to capture exhaust CO_2 has been hindered by the limited availability of brucite, the $\text{Mg}(\text{OH})_2$ mineral in natural deposits. Our previous study demonstrated that $\text{Mg}(\text{OH})_2$ can be obtained from dunite, an ultramafic rock composed of Mg silicate minerals, in highly concentrated NaOH aqueous systems. However, the large quantity of NaOH consumed was considered an obstacle for the implementation of the technology. In the present study, $\text{Mg}(\text{OH})_2$ was extracted from dunite reacted in solid systems with NaOH assisted with H_2O . The consumption of NaOH was reduced by 97% with respect to the NaOH aqueous systems, maintaining a comparable yield of $\text{Mg}(\text{OH})_2$ extraction, *i.e.* 64.8–66%. The capture of CO_2 from a CO_2 – N_2 gas mixture was tested at ambient conditions using a $\text{Mg}(\text{OH})_2$ aqueous slurry. $\text{Mg}(\text{OH})_2$ almost fully dissolved and reacted with dissolved CO_2 by forming $\text{Mg}(\text{HCO}_3)_2$ which remained in equilibrium storing the CO_2 in the aqueous solution. The CO_2 balance of the process was assessed from the emissions derived from the power consumption for NaOH production and $\text{Mg}(\text{OH})_2$ extraction together with the CO_2 captured by $\text{Mg}(\text{OH})_2$ derived from dunite. The process resulted as carbon neutral when dunite is reacted at 250 °C for durations of 1 and 3 hours and CO_2 is captured as $\text{Mg}(\text{HCO}_3)_2$.

^aDepartment of Materials Science and Engineering, The University of Sheffield, Sheffield, UK. E-mail: mtq11sm@sheffield.ac.uk

^bInnovate UK, Swindon, UK

^cPolarcus DMCC, Dubai, United Arab Emirates

^dDepartment of Materials Science and Metallurgy, University of Cambridge, Cambridge, UK

^eWRK Design & Engineering Ltd, Birmingham, UK

^fCambridge Carbon Capture Ltd, Cambridge, UK

[†] Previously, Cambridge Carbon Capture Ltd.

Introduction

Carbon Capture and Storage (CCS) is a portfolio of technologies developed for the abatement of anthropogenic CO₂ emissions *via* permanent isolation of CO₂ from the atmosphere.¹ CCS includes the separation of CO₂ from exhaust flue gases and its storage either underground, in seawater or through the fixation into stable mineral carbonates *via* mineral carbonation.¹

Mg(OH)₂ can capture CO₂ in a wide range of conditions: it can permanently and safely store CO₂ into solid Mg carbonate minerals upon exposure to gaseous or supercritical CO₂ or *via* dissolution in H₂O with purged CO₂.^{2–4} Mg(OH)₂ aqueous slurries have been successfully tested to separate CO₂ from gas mixtures *via* liquid–gas scrubbing, and the technology has been proposed to separate CO₂ from exhaust flue gases.⁵ Mg(OH)₂ and CO₂ dissolved in H₂O can react to form Mg(HCO₃)₂ which remains in solution as a soluble phase under a controlled pH.^{5,6} This chemistry is suited to industrial applications such as in the coastal industry and power plants or ships, where CO₂ can be separated from exhaust flue gases using Mg(OH)₂ slurries and permanently stored in seawater as dissolved Mg(HCO₃)₂.⁷ This technology combines the separation and storage of CO₂ into a single stage, which is favourable because it avoids the capture and conversion of CO₂ into a pure CO₂ stream, as well as the compression and transport operations, all of which are expensive and energy demanding.^{8,9} Despite the wide range of possible applications and potential advantages, Mg(OH)₂ utilisation for CO₂ capture has been hindered due to its rare occurrence in natural outcrops.^{1,10}

Mg silicate minerals, on the other hand, in particular serpentine and forsterite have been the preferred feedstock materials for CO₂ sequestration due to their vast availability in natural deposits which provide large storage capacity.^{1,11,12} The main challenge of Mg silicate mineral carbonation is the slow kinetics of the carbonation reaction which requires acceleration through mechanical and chemical pre-treatment of the materials and the application of high pressure and temperatures.^{1,13}

The extraction of Mg(OH)₂ from Mg silicate minerals *via* chemical processing benefits from the large availability of Mg silicate minerals. The overall efficiency of the process is also improved as Mg(OH)₂ has faster kinetics in carbonation than these Mg silicate minerals and allows greater flexibility in the design of the CCS technologies.⁴ There are technologies currently available to obtain Mg(OH)₂ from Mg silicate minerals, *e.g.* a solid state reaction with ammonium salts at 400–500 °C or dissolution with HCl at 150 °C.^{4,14} These technologies involve a second step where the pH of the system is increased by introducing another reactant to favour the precipitation of Mg(OH)₂ under alkaline conditions.^{4,14}

In a previous study we investigated the alkaline digestion of Mg silicate minerals to obtain Mg(OH)₂ using highly concentrated NaOH aqueous systems.¹⁵ The alkali digestion of dunite, an ultramafic rock composed of Mg silicate minerals, at 180 °C for 6 hours, resulted in the near-complete digestion and formation of Mg(OH)₂. The technology is advantageous because it is a one-step reaction and involves a single reactant, although the high consumption of NaOH was identified as a possible obstacle for the implementation.¹⁵

The present study proposes a new technique for the extraction of Mg(OH)₂ from Mg silicate minerals, aiming to reduce the NaOH consumption by

1 introducing NaOH into the system in the solid state. After studying the basic
reaction of the system at 180 °C with the aid of thermodynamic consideration, the
investigation focused on the effect of H₂O on the efficiency of Mg(OH)₂ extraction
5 from the dunite–NaOH solid mixtures. The effects of temperature and duration of
reaction were also studied for a dunite–NaOH–H₂O system with a fixed compo-
sition reacted at 130, 180 or 250 °C for 1, 3 and 6 hours. The obtained results are
compared with those from the alkaline digestion of dunite with NaOH aqueous
systems previously investigated. The feasibility of CO₂ sequestration using
10 Mg(OH)₂ was also demonstrated using a Downflow Gas Contactor (DGC) reactor.
CO₂ was separated from a flow of CO₂–N₂ mixture at ambient conditions using an
aqueous slurry of reagent grade Mg(OH)₂, and the implications of using Mg(OH)₂
derived from dunite for CO₂ sequestration are discussed.

15 Materials and methods

Dunite

The dunite mined in Åheim, Norway, was provided by Sibelco Ltd. The material
was analysed *via* X-ray fluorescence (XRF) and was composed of 48.3 wt% MgO,
20 45.35 wt% SiO₂, and 6.16 wt% Fe₂O₃, while other oxides were present at <1 wt%.
The X-ray diffraction (XRD) analysis revealed that dunite was mainly composed of
forsterite, Mg₂SiO₄, the Mg-rich member of the olivine group. The minor
components were also Mg-bearing minerals, *i.e.* clinocllore, serpentine, ensta-
tite, talc, hornblende and spinel. The Rietveld Refinement Quantitative Phase
25 Analysis (QPA) conducted on the XRD pattern estimated the amount of forsterite
to be 73 ± 2 wt%. Thermogravimetric analysis (TGA) detected the presence of
Mg(OH)₂ at 0.42 wt% in the dunite.

The powdered dunite was sieved to <63 µm and analysed by laser diffraction
30 with dry dispersion, which showed an average distribution of the particle size to
be around 25 µm, with 90% of the particles <58 µm. These results were confirmed
via SEM analysis.

35 Extraction of Mg(OH)₂

NaOH pearl, reagent grade provided by Fisher Chemical, was mixed with
powdered dunite, with or without addition of distilled H₂O, in an agate mortar
with a pestle. The mole ratio of the reactants in the samples used in the present
study is summarised in Table 1. Three series were prepared at different duni-
40 te : NaOH mole ratios, *i.e.* 1 : 1, 1 : 1.5, and 1 : 2, which are referred to as Series 1,

Table 1 Normalised mole of reactants in samples

	Dunite ^a (mole)	NaOH (mole)	H ₂ O ^b (mole)				
Series 1	1	1	—	0.25	0.5	1	2
Series 1.5	1	1.5	—	0.375	0.75	1.5	3
Series 2	1	2	0	0.5	1	2	4

^a Approximate mole of dunite was estimated based on the chemical formula of forsterite,
50 Mg₂SiO₄. ^b Different amounts of H₂O were tested at NaOH : H₂O mole ratios of 4 : 1, 2 : 1,
1 : 1 or 1 : 2 for each series. Series 2 also includes a *dry* system without H₂O.

1 Series 1.5, and Series 2, respectively. The moles of dunite were estimated based on
the chemical formula of forsterite, Mg_2SiO_4 . For all series, the samples were
prepared at different $\text{NaOH} : \text{H}_2\text{O}$ mole ratios of 4 : 1, 2 : 1, 1 : 1, and 1 : 2. Series
2 also includes a sample reacted without H_2O addition.

5 When the reactants were well-blended, the mixture was transferred in a steel
vessel lined with Teflon which was sealed and heated at 180 °C for 6 hours in a
Carbolite electric oven, series PF30. The system with dunite : $\text{NaOH} : \text{H}_2\text{O}$ mole
ratio of 1 : 2 : 0.5 was replicated at different durations of reaction, *i.e.* 1 and 3
10 hours, and different temperatures, *i.e.* 130 and 250 °C.

After the reaction, the products were ground and washed with distilled water
and the solid component was separated from the liquid phase *via* vacuum
filtration. The solid filtrate was dried for 1 hour at 90 °C and then analysed *via*
XRD and TGA.

15 CO_2 capture with $\text{Mg}(\text{OH})_2$ suspension

A Downflow Gas Contactor (DGC) reactor, designed by WRK Design & Engineering
Ltd, with a liquid volume capacity of 10 litres was used as the liquid–gas reactor to
capture CO_2 from a flowing gas-mixture. In this reactor, the gas-mixture at
20 atmospheric pressure enters at the top of the bubble column, is entrained (at 0.8
atm) in the downward circulating liquid flow, and exits at 1 atm from the bottom
of the column after reaction and separation from the recirculating liquid phase.
The DGC reactor provides a large interfacial area between the gas bubbles and
liquid which enhances the reactivity of the phases involved. The rate of liquid
25 recirculation was typically 10 L minute^{-1} to maintain a stable bubble–liquid
interface.

A gas-mixture of N_2 and 4–5% CO_2 was injected at the top of the column at a
fixed flow-rate of 2.25 ± 0.07 L minute^{-1} and bubbled through the column at
30 approximately 10 °C and under ambient pressure. When the solution was satu-
rated with CO_2 , *i.e.* the concentration of CO_2 in the outlet gas became the same in
the inlet gas, 50.8 g of powdered $\text{Mg}(\text{OH})_2$ was added to the circulating H_2O .

The $\text{Mg}(\text{OH})_2$ with 98% purity used in the study was provided by Lehmann &
Voss & Co. The material had an average particle size of 7 μm , and also contained
35 0.5% CaO and smaller amounts of SiO_2 and Fe_2O_3 as impurities.

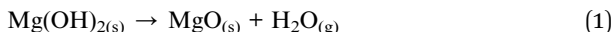
The CO_2 concentration in the inlet and outlet gas was periodically monitored
using a calibrated inline infrared data logger, and the monitoring continued until
the concentration of CO_2 in the outlet gas had increased and become equal to that
in the inlet gas, indicating that no further reaction was occurring. The experiment
40 took approximately 12 hours to complete and was run over the course of two days
with an overnight shut-down. Samples of the circulating liquid were also taken
periodically to monitor the change in pH.

45 Products and data analysis

XRD was conducted for phase analysis of the reaction products using a Siemens
D5000 with $\text{Cu K}\alpha$ X-ray source, $\lambda = 1.54 \text{ \AA}$. The powdered samples were placed in
a plastic sample holder, and the scans were run from 10° to 70° 2θ with a step size
of 0.05° 2θ .

50 TGA of the reaction products was also conducted using a Perkin Elmer Pyris 1.
The samples were placed in an alumina crucible and heated at a rate of 10 °C

minute⁻¹ from room temperature to 1000 °C under a N₂ flow. The first derivative of the TG curve, DTG, was also determined to assist the analysis. The amount of Mg(OH)₂ was calculated based on the dehydroxylation of Mg(OH)₂ (reaction (1)) taking place at 350–450 °C.¹⁶



The analysis was also assisted with the thermodynamic consideration. The change in the Gibbs free energy and enthalpy for the possible reactions were calculated using the SGTE Substances Database (SSUB5) in Thermo-Calc.¹⁷ The calculation was also performed for the minor mineral phases in the dunite. The calculation was not performed for clinocllore and hornblende due to the lack of available data in the SSUB5.

The carbon content in the solid residue recovered from the CO₂ capture test was determined using a Perkin Elmer 2400 CHNS/O Series II Elemental Analyser. The sample was combusted at 975 °C under an oxygen environment. The gases released were reduced by copper and separated through a chromatographic column. The amount of carbon was obtained from the gases eluting off the column based on their thermal conductivity, which were converted into CO₂ wt% to assess the CO₂ captured in the solid phase.

Results and discussion

Extraction of Mg(OH)₂

The reaction of dunite with NaOH usually resulted in the formation of brucite, Na₂SiO₃ and natrite, *i.e.* Na₂CO₃, together with the mineral components from the unreacted dunite and remaining NaOH. Fig. 1 shows the XRD patterns of selected reaction products from the solid systems with a dunite : NaOH mole ratio of 1 : 2 and a dunite : NaOH : H₂O mole ratio of 1 : 2 : 0.5, before and after being washed with distilled H₂O, respectively. The by-products, Na₂SiO₃ and natrite are usually detected before washing the reaction products as demonstrated in Fig. 1. These

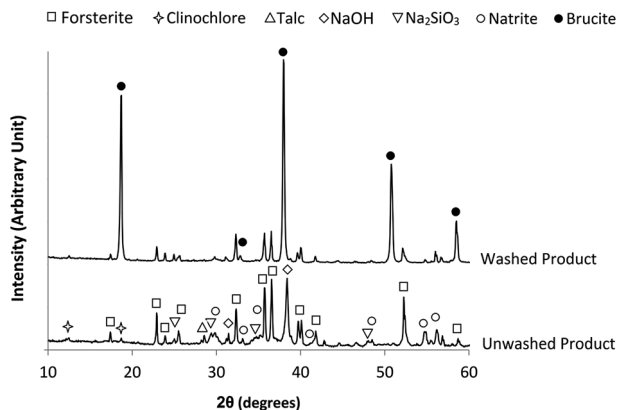
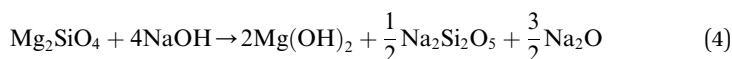
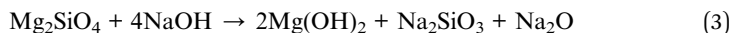
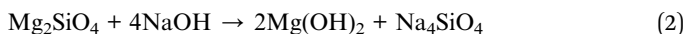


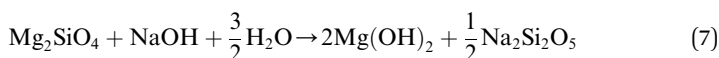
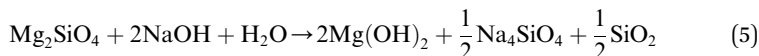
Fig. 1 XRD patterns of selected reaction products from solid systems with a dunite : NaOH mole ratio of 1 : 2 and a dunite : NaOH : H₂O mole ratio of 1 : 2 : 0.5 before and after washing, respectively.

by-products are soluble in water and can be removed together with the remaining NaOH by washing the reaction products. After washing and successive filtration, the samples are typically left with a solid fraction composed of $\text{Mg}(\text{OH})_2$ and remaining dunite components (Fig. 1).

It is expected to be difficult to obtain Na_2SiO_3 from the reaction of dunite and NaOH. Reactions (2)–(4) are examples of reactions for Mg_2SiO_4 and NaOH which assume Na_4SiO_4 , Na_2SiO_3 and $\text{Na}_2\text{Si}_2\text{O}_5$ as reaction products, respectively. Mg_2SiO_4 was chosen as a representative of dunite because it is the main mineral component. The calculation of the Gibbs energy change (ΔG°) for reactions (2)–(4) showed that only the formation of Na_4SiO_4 is thermodynamically favoured, as indicated by the negative ΔG° of the reaction in Fig. 2, whereas, the formation of Na_2SiO_3 or $\text{Na}_2\text{Si}_2\text{O}_5$ is not possible because $\Delta G^\circ > 0$.



However, when H_2O is involved in the reactions (reactions (5)–(7)), the formation of these Na silicate species becomes possible because their ΔG° are all negative, as shown in Fig. 2.



It should be noted that the formation of Na_2SiO_3 in the presence of H_2O becomes thermodynamically more favourable than that of Na_4SiO_4 in a *dry*

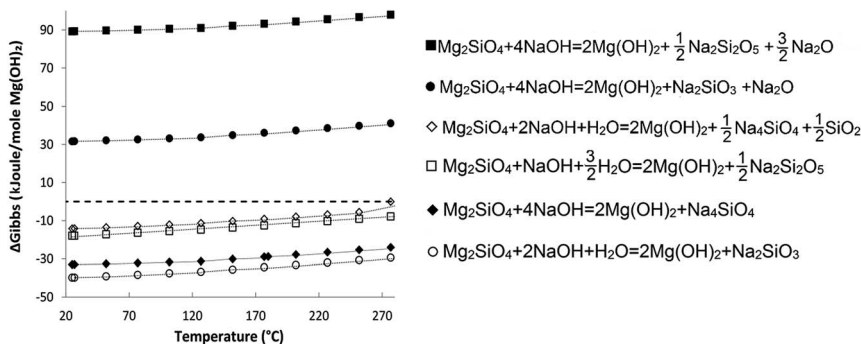
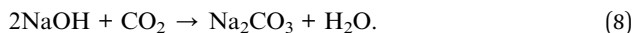


Fig. 2 ΔG° per 1 mole of $\text{Mg}(\text{OH})_2$ produced calculated for possible reactions for Mg_2SiO_4 and NaOH. Closed data points are for the *dry* reactions, and open data points for those involving H_2O .

1 reaction. These data suggest the involvement of H₂O in the studied reaction and
 its thermodynamical advantage over the *dry* reaction. The carbonation of NaOH
 could also aid the involvement of H₂O in the reaction. As seen in the XRD data in
 5 Fig. 1, natrite has been formed in the system. Because the samples are in contact
 with air during the preparation and the reaction (in a closed vessel with trapped
 air), some of the NaOH in the system can be carbonated, and this reaction
 releases H₂O through the following reaction:

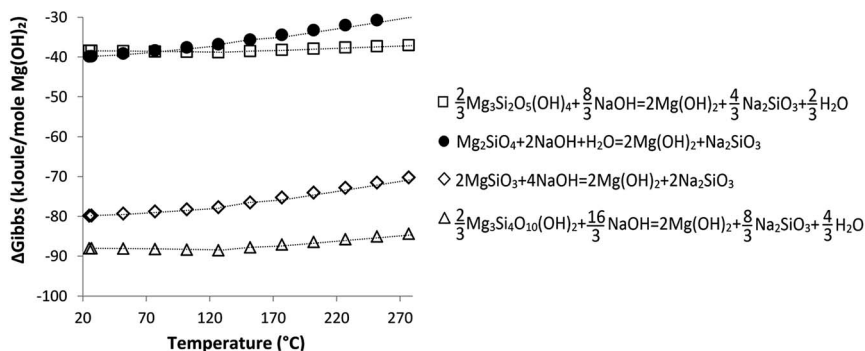


10 The ΔG° for the reactions of NaOH and minor phases in the dunite *i.e.*,
 serpentine (Mg₃Si₂O₅(OH)₄), talc (Mg₃Si₄O₁₀(OH)₂), and enstatite (MgSiO₃)
 are shown in Fig. 3 and suggests that the formation of Mg(OH)₂ and Na₂SiO₃ from
 15 these Mg silicate minerals is also thermodynamically possible ($\Delta G^\circ < 0$). The
 thermodynamical feasibility of Mg(OH)₂ extraction from serpentine with NaOH is
 particularly relevant because serpentine is widely available in natural deposits
 and contains a high wt% of Mg which makes it a suitable alternative feedstock
 material to dunite.⁴

20 The enthalpy change (ΔH°) for the possible reactions occurring in the dunite–
 NaOH system was also calculated at the temperatures of reaction investigated in
 this study, *i.e.* 130, 180 and 250 °C. All the reactions showed negative ΔH° in the
 temperature range of interest and the lowest was found at 250 °C. The values of
 25 ΔH° at this temperature are shown for each reaction in Table 2. These reactions
 are all exothermic and although their balance is not known, overall the extraction
 of Mg(OH)₂ from dunite should be energetically favoured.

Effect of added H₂O

30 The introduction of H₂O into the system had a significant effect on the extraction
 of Mg(OH)₂. Fig. 4 compares the XRD patterns of the reaction products from the
dry reaction and the reaction with added H₂O in Series 2. These samples were
 washed with distilled water and Na₂SiO₃, Na₂CO₃ had been removed. The
 extraction of brucite (Mg(OH)₂), in the *dry* dunite–NaOH system appeared to be



45 Fig. 3 ΔG° per 1 mole Mg(OH)₂ produced calculated for possible reactions for serpentine
 (Mg₃Si₂O₅(OH)₄), talc (Mg₃Si₄O₁₀(OH)₂), and enstatite (MgSiO₃) with NaOH in comparison
 with that for forsterite (Mg₂SiO₄).

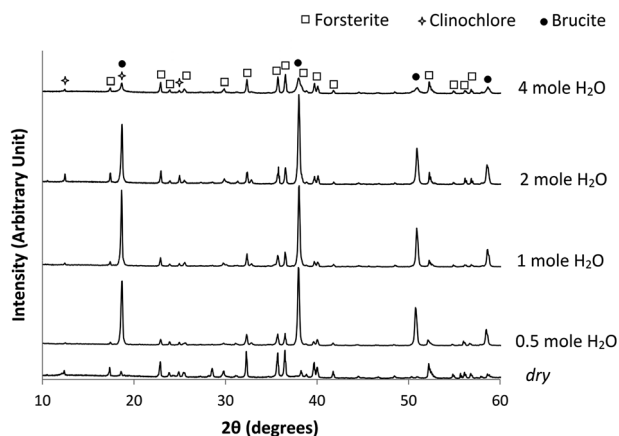
Table 2 Standard enthalpy change per 1 mole of Mg(OH)₂ produced at 250 °C

Reactions	ΔH° (kJ) ^a
$\text{Mg}_2\text{SiO}_4 + 2\text{NaOH} + \text{H}_2\text{O} \rightarrow 2\text{Mg}(\text{OH})_2 + \text{Na}_2\text{SiO}_3$	-58
$\frac{2}{3}\text{Mg}_3\text{Si}_2\text{O}_5(\text{OH})_4 + \frac{8}{3}\text{NaOH} \rightarrow 2\text{Mg}(\text{OH})_2 + \frac{4}{3}\text{Na}_2\text{SiO}_3 + \frac{2}{3}\text{H}_2\text{O}$	-44
$2\text{MgSiO}_3 + 4\text{NaOH} \rightarrow 2\text{Mg}(\text{OH})_2 + 2\text{Na}_2\text{SiO}_3$	-98
$\frac{2}{3}\text{Mg}_3\text{Si}_4\text{O}_{10}(\text{OH})_2 + \frac{16}{3}\text{NaOH} \rightarrow 2\text{Mg}(\text{OH})_2 + \frac{8}{3}\text{Na}_2\text{SiO}_3 + \frac{4}{3}\text{H}_2\text{O}$	-99
$2\text{NaOH} + \text{CO}_2 \rightarrow \text{Na}_2\text{CO}_3 + \text{H}_2\text{O}$	-176

limited. The only reflection peaks identified are for the mineral components present in the dunite, while the reflection peaks for brucite were not observed. On the other hand, the systems with added H₂O all indicated the presence of brucite. The two main reflection peaks for the brucite, were detected at 18.6° and 38° 2θ. These peaks partially overlap with those for clinocllore and forsterite, respectively, but are distinguishable based on the proportion of the other peaks intensity. The introduction of H₂O is beneficial and the intensity of the reflection peaks for brucite considerably increases in systems with 0.5, 1 and 2 moles of H₂O, although, the intensity significantly decreases in the system with 4 moles of H₂O. A similar trend was observed also in Series 1.5 and 1.

The TGA and DTG curves of the reaction products from Series 2 are shown in Fig. 5(A) and (B), respectively. The sample reacted in *dry* conditions had a small weight loss between 300 and 450 °C for the dehydroxylation of Mg(OH)₂, whereas those reacted in the presence of water showed a larger weight loss in this temperature region, indicating that more Mg(OH)₂ was produced when H₂O was added to the system.

The calculated concentration of Mg(OH)₂ in the reaction product was 19 wt% for the *dry* dunite–NaOH mixture, and 57.6, 55.4, 51.2 and 28 wt% with 0.5, 1, 2 and 4 moles of H₂O added per 1 mole of dunite, respectively. Thus, the amount of Mg(OH) in the products decreases with the increase in H₂O content.

Fig. 4 XRD patterns of reaction products from Series 2 with different amounts of H₂O.

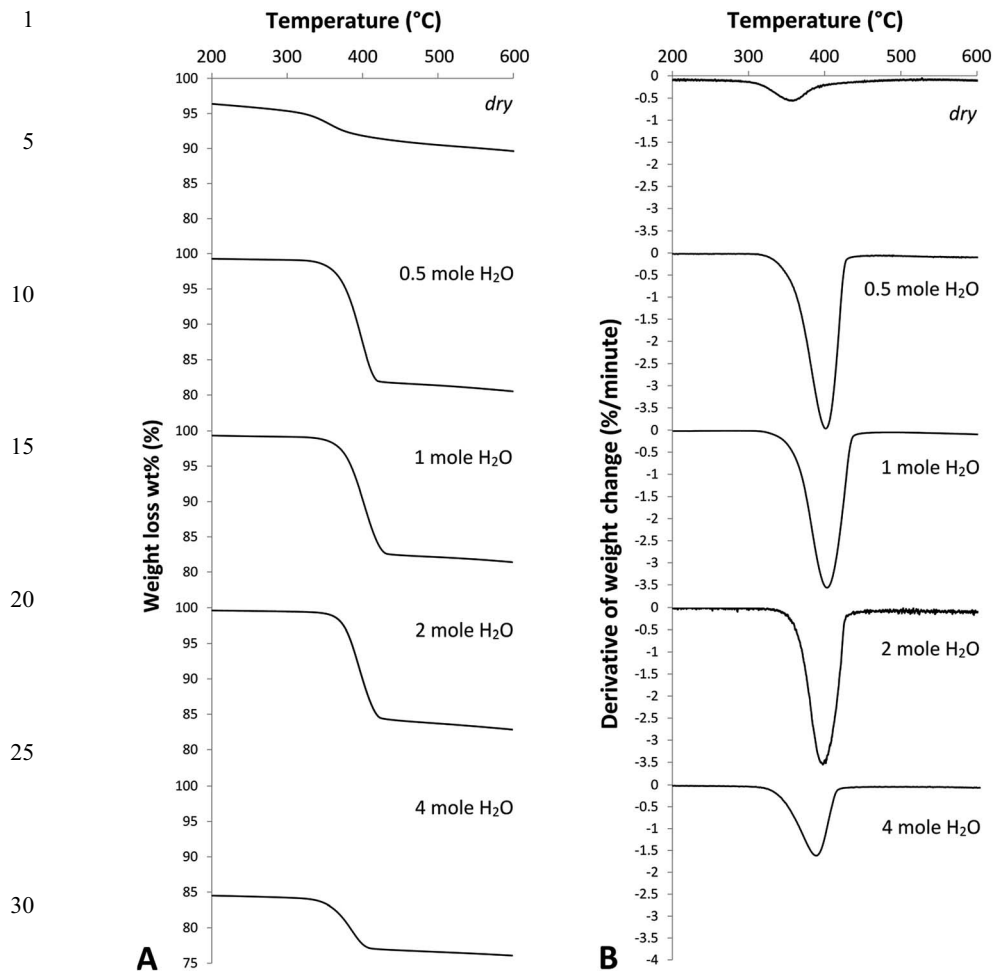


Fig. 5 (A) TGA and (B) DTG curves of the reaction products from Series 2.

The TGA results are in agreement with the XRD data and indicate that the addition of H₂O was beneficial compared to *dry* conditions, which is likely because the dissolution of NaOH in H₂O favoured the ion exchange and the diffusivity of materials involved in the reaction.^{18,19} The addition of smaller amounts of H₂O, *i.e.* a higher NaOH : H₂O mole ratio, was a more preferable condition for Mg(OH)₂ formation, which suggests that the concentration of NaOH in H₂O played a decisive role for the extraction of Mg(OH)₂ from dunite.

Effect of NaOH concentration

The Mg(OH)₂ content in the reaction products were estimated *via* TGA for Series 2, 1.5 and 1, and are compared in Fig. 6. The data are plotted against the NaOH : H₂O mole ratio to study the effects of NaOH concentration in H₂O.

The reaction products from Series 2 showed the highest concentration of Mg(OH)₂, followed by those from Series 1.5 and 1, indicating the advantage of

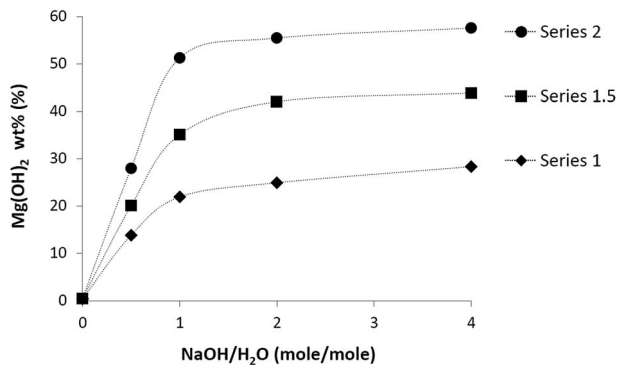


Fig. 6 $\text{Mg}(\text{OH})_2$ concentrations estimated via TGA in reaction products from Series 1, 1.5, and 2.

having a higher NaOH content in the system. The three series showed the same trend in the presence of H_2O , and the wt% of $\text{Mg}(\text{OH})_2$ in the reaction products increased with the increase of the NaOH : H_2O mole ratio. However, this effect becomes less significant at a higher NaOH : H_2O mole ratio. In fact, at higher NaOH : H_2O mole ratios the concentration of NaOH in H_2O is higher but the amount of H_2O in the system is lower, and thus the positive effect of H_2O , such as the improvement of the reactants diffusion is reduced.

The data shown in Fig. 6 are also plotted against the amount of H_2O added to the system in Fig. 7(A), grouped by the same NaOH : H_2O mole ratio.

The gradients of the linear fitting for these data sets are proportional to the NaOH : H_2O mole ratio as shown in Fig. 7(B). Based on these results, it is possible to estimate the approximate wt% of $\text{Mg}(\text{OH})_2$, $\text{Mg}(\text{OH})_2$ (%), expected in the reaction product under the conditions studied, using the following empirical equation with the amount of NaOH (X_{NaOH}) and H_2O ($X_{\text{H}_2\text{O}}$):

$$\text{Mg}(\text{OH})_2 \text{ (%) } = 30.79(X_{\text{NaOH}}) - 7.34(X_{\text{H}_2\text{O}}). \quad (9)$$

These data together with those previously discussed for Series 2, indicate that the extraction of $\text{Mg}(\text{OH})_2$ from dunite in NaOH– H_2O solid systems is the result of a combined effect of NaOH concentration in H_2O and the amount of liquid phase present in the system. At 180 °C, the NaOH in the system should be fully dissolved at a NaOH : H_2O mole ratio of 1 : 2 and 1 : 1, or constitute a solid system with partially dissolved NaOH at a NaOH : H_2O mole ratio of 2 : 1 and 4 : 1.²⁰ The optimal conditions for the extraction of $\text{Mg}(\text{OH})_2$ appears to be found when H_2O is present in a sufficient quantity to help the diffusion of the reactants but not in excess to reduce the relative concentration of NaOH in the liquid.

Effect of temperature and time

Amongst the compositions investigated, the system with a mole ratio of dunite : NaOH : H_2O = 1 : 2 : 0.5 gave the highest $\text{Mg}(\text{OH})_2$ extraction. The effect of the reaction conditions was further investigated for this system, using three durations of reaction, *i.e.* 1, 3 and 6 hours, at different temperatures, *i.e.* 130, 180

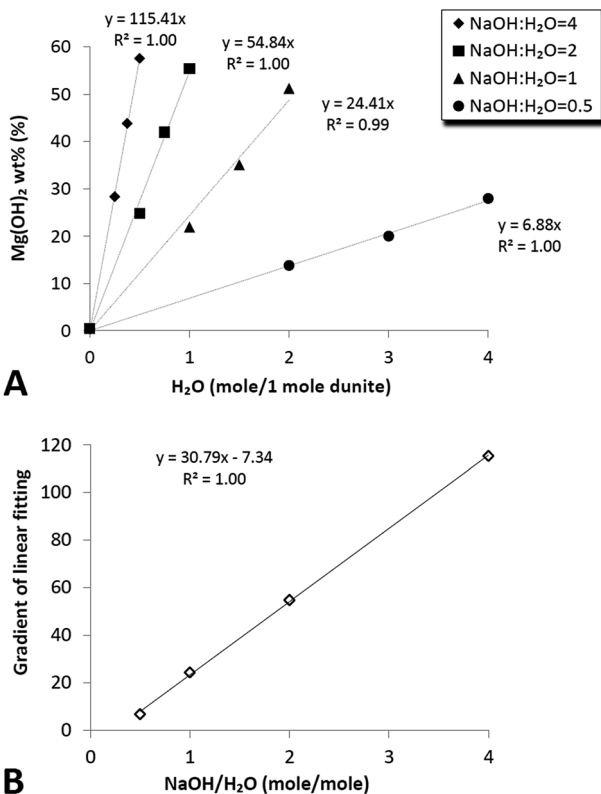


Fig. 7 Mg(OH)_2 concentrations estimated *via* TGA of the reaction products: (A) effect of H_2O content for different $\text{NaOH} : \text{H}_2\text{O}$ mole ratios, and (B) the gradient of the linear fitting for the datasets shown in (A).

and 250°C . The reaction products were analysed *via* TGA, and the wt% of Mg(OH)_2 in the reaction products are compared in Fig. 8.

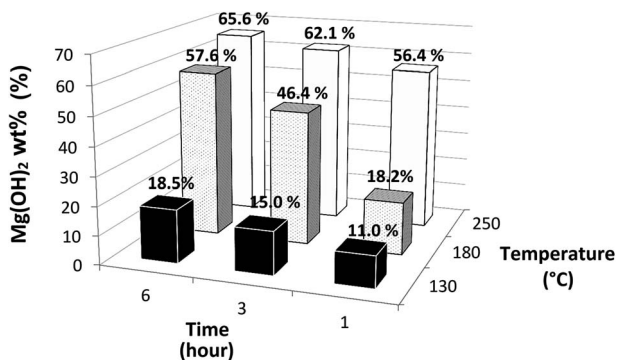


Fig. 8 Mg(OH)_2 concentration estimated *via* TGA in the reaction products of dunite : $\text{NaOH} : \text{H}_2\text{O}$ systems with a 1 : 2 : 0.5 mole ratio at different temperatures and times of reaction.

As expected, increasing the duration and temperature of the reaction was beneficial for the extraction of $\text{Mg}(\text{OH})_2$. At $130\text{ }^\circ\text{C}$ the formation of $\text{Mg}(\text{OH})_2$ was limited, achieving only 18.5 wt% after 6 hours which is comparable with 18.2 wt% obtained at $180\text{ }^\circ\text{C}$ in 1 hour. The reaction conducted at $180\text{ }^\circ\text{C}$ resulted in a significant $\text{Mg}(\text{OH})_2$ extraction of 46.4 wt% after 3 hours of reaction. Increasing the temperature to $250\text{ }^\circ\text{C}$ significantly improved the extraction of $\text{Mg}(\text{OH})_2$, and a concentration of 56.4 wt% $\text{Mg}(\text{OH})_2$ was achieved after 1 hour, which increased to 65.6 wt% in 6 hours. The $\text{Mg}(\text{OH})_2$ extraction obtained within 1 hour at $250\text{ }^\circ\text{C}$ is comparable with the 57.6 wt% attained at $180\text{ }^\circ\text{C}$ over 6 hours of reaction. The reaction at $250\text{ }^\circ\text{C}$ is faster than at the other temperatures, and the majority of the reaction appears to have taken place in the first hour. This is highly advantageous for the industrial application of the process, as it would allow a reduction of the reaction time from 6 hours to 1 hour to achieve the same degree of $\text{Mg}(\text{OH})_2$ extraction obtained at $180\text{ }^\circ\text{C}$.

Fig. 9 shows the $\text{NaOH}\text{-H}_2\text{O}$ phase diagram.²⁰ The diagram has been adapted to show the temperatures and NaOH concentration used in this study. The $\text{NaOH} : \text{H}_2\text{O}$ mole ratio of 4 : 1 corresponds to a NaOH concentration in H_2O of approximately 90% by weight. The diagram shows that there could be a solid portion remaining at 130 and $180\text{ }^\circ\text{C}$ in the $\text{NaOH}\text{-H}_2\text{O}$ system at 90 wt% NaOH whereas, only liquid or gas can be present at $250\text{ }^\circ\text{C}$, similar to molten salt systems.²⁰ Consequently, at $250\text{ }^\circ\text{C}$ dunite reacted with a highly alkaline melt instead of a solid system with a limited amount of NaOH dissolved in H_2O , which should have favoured the diffusion of reactants,²¹ contributing to the much faster kinetics of $\text{Mg}(\text{OH})_2$ extraction observed within the first hour of reaction at this temperature. Although the increase of pressure in the closed vessel at higher temperatures may shift the melting temperature, based on the obtained results it appears to be still below $250\text{ }^\circ\text{C}$.

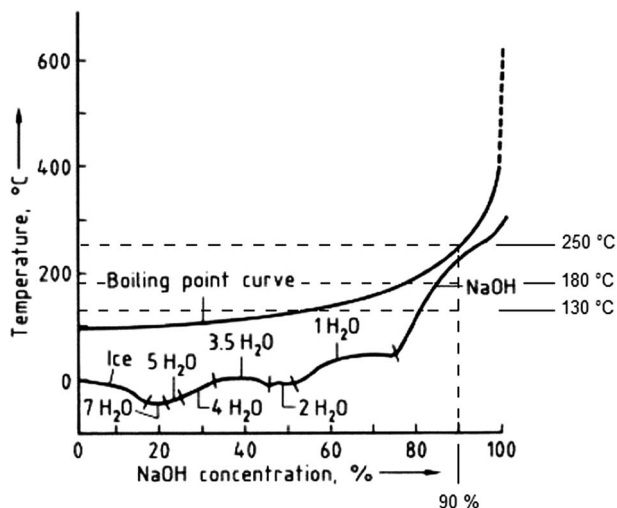


Fig. 9 $\text{NaOH}\text{-H}_2\text{O}$ phase diagram, modified from Kurt and Bittner, 2003.²⁰

Efficiency of the reaction

The efficiency of $\text{Mg}(\text{OH})_2$ extraction is estimated through the yield of the reaction which calculates the percentage of $\text{Mg}(\text{OH})_2$ produced with respect to the maximum amount of $\text{Mg}(\text{OH})_2$ theoretically producible from dunite.^{15,22} The procedure adopted for the yield calculation is described by Madeddu *et al.*¹⁵ In the present study, the yield was calculated using eqn (10) and (11) from which the amount of $\text{Mg}(\text{OH})_2$ extracted from dunite was obtained, based on the wt% estimated *via* TGA.

The wt% of $\text{Mg}(\text{OH})_2$ in the reaction products determined *via* TGA, $\text{Mg}(\text{OH})_2$ (%), can be expressed according to eqn (10), where $\text{Mg}(\text{OH})_{2(\text{rp})}$ and $\text{dunite}_{(\text{rp})}$ are the amount of $\text{Mg}(\text{OH})_2$ and dunite in the reaction products, respectively. Eqn (11), on the other hand calculates the amount of MgO involved in the reaction. $\text{Dunite}_{(\text{i})}$ is the initial feed of dunite, and 48.3 is the wt% of MgO in $\text{dunite}_{(\text{i})}$. 48.21 is the wt% of MgO in dunite excluding the MgO initially presented as 0.42 wt% of $\text{Mg}(\text{OH})_2$, and 40.3 and 58.3 are the molecular weights of MgO and $\text{Mg}(\text{OH})_2$, respectively.

$$\text{Mg}(\text{OH})_2(\%) = \frac{100\text{Mg}(\text{OH})_{2(\text{rp})}}{\text{Mg}(\text{OH})_{2(\text{rp})} + \text{dunite}_{(\text{rp})}} \quad (10)$$

$$\frac{48.3 \times \text{dunite}_{(\text{i})}}{100} = \frac{48.21 \times \text{dunite}_{(\text{rp})}}{100} + \frac{40.3 \times \text{Mg}(\text{OH})_{2(\text{rp})}}{58.3} \quad (11)$$

With the values of $\text{Mg}(\text{OH})_2$ (%) and $\text{dunite}_{(\text{i})}$, it is possible to obtain $\text{Mg}(\text{OH})_{2(\text{rp})}$ and $\text{dunite}_{(\text{rp})}$ by solving the system of eqn (10) and (11).

For the three series tested at 180 °C in the present investigation, a highest yield of 66% for the reaction was achieved in the reaction product of Series 2, with a NaOH : H₂O mole ratio of 4 : 1 reacted for 6 hours. The same yield was obtained from the alkaline digestion of dunite with NaOH 50 mol kg⁻¹ aqueous system at the same temperature and same duration of reaction.¹⁵ The NaOH consumed in the solid system reaction was 0.57 g per 1 g of dunite, whereas 20.6 g of NaOH was demanded in the aqueous system to process 1 g of dunite, which corresponds to the reduction of NaOH usage by 97%.¹⁵ The H₂O consumed was also reduced by 99%.¹⁵ When the system was reacted at 130 °C, the yield of the reaction was 24% after 6 hours, whereas, at 250 °C the yield was 64.8, 70 and 73% after 1, 3, and 6 hours, respectively. As expected the yield achieved after a 1 hour reaction at 250 °C is comparable with that achieved at 180 °C after 6 hours.

The NaOH was reduced by 97.9% in Series 1.5 and 98.6% in Series 1, although the yield of the reaction was reduced to 53% and 36%, respectively, after a 6 hour reaction at 180 °C.

These results show that the extraction of $\text{Mg}(\text{OH})_2$ *via* the reaction of dunite with NaOH in a solid system is preferable to the alkaline digestion with NaOH aqueous systems as the amount of NaOH required can be significantly reduced while maintaining the same efficiency of $\text{Mg}(\text{OH})_2$ extraction.

Feasibility of CO₂ capture with $\text{Mg}(\text{OH})_2$

Fig. 10 shows the CO₂ concentration in the flow gas measured at the inlet and outlet of the GDC reactor during the experiment. The CO₂ concentration at the

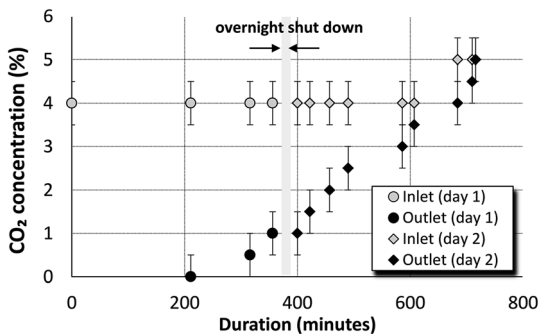


Fig. 10 CO₂ concentration in the flow gas at the inlet and outlet of the DGC reactor.

outlet was initially negligible, and all CO₂ in the flow gas appeared to be retained in the circulating solution by reacting with Mg(OH)₂ in the system. The CO₂ concentration started increasing after approximately 200 minutes due to the consumption of Mg(OH)₂ in the system, and became equal to that in the inlet gas at 720 minutes where the system no longer captures CO₂. The overnight shut down period did not cause any obvious change in the system. The obtained results clearly show the CO₂ capture capability of this system.

The amount of CO₂ captured from the flow gas was estimated using eqn (12) where CO_{2*i*} % and CO_{2*o*} % are the concentration of CO₂ in the inlet and outlet gas, respectively. The volume of gas under atmospheric pressure at 10 °C was estimated as 23.2 L mole⁻¹.

$$\text{CO}_2(\text{mole}) = \frac{2.25 (\text{L minute}^{-1})}{23.2 (\text{L mole}^{-1})} \times \frac{\text{CO}_{2i}(\%) - \text{CO}_{2o}(\%)}{100} \times \text{time (minute)} \quad (12)$$

The amount of captured CO₂ is plotted in Fig. 11 together with the pH of the circulating solution. CO₂ was steadily captured up to around 400 minutes, and

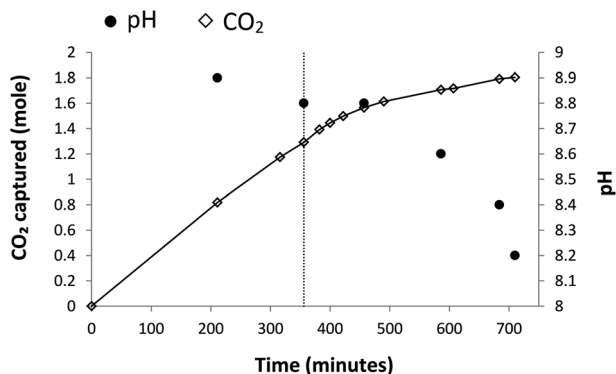


Fig. 11 Amount of CO₂ captured and pH of the circulating solution in the liquid–gas scrubbing with Mg(OH)₂–H₂O slurry.

1 then the rate of capture slightly decreased. The significant reduction in pH at this
2 period suggests the exhaustion of the dissolved $\text{Mg}(\text{OH})_2$ available for reaction.

3 In total, 1.80 ± 0.19 moles of CO_2 were sequestered over the 2 days of the
4 experimental run.

5 Since the circulating solution used in the present study contained approxi-
6 mately 0.85 mole of $\text{Mg}(\text{OH})_2$, the maximum CO_2 to be captured is 1.71 mole (1.72
7 mole if CaO presented as an impurity is also counted) assuming the reaction
8 product is $\text{Mg}(\text{HCO}_3)_2$, and 0.86 mole of MgCO_3 was produced. Although our
9 estimation, 1.80 ± 0.19 mole, contains a significant deviation, it is clear that the
10 reaction product in the tested system was mainly $\text{Mg}(\text{HCO}_3)_2$. It is known that the
11 formation of $\text{Mg}(\text{HCO}_3)_2$ is favoured when the pH of the solution is around 8.4
12 where HCO_3^- ions are the predominant species of CO_2 dissolution, whereas
13 MgCO_3 preferentially forms when the pH of the solution is above 10 as the CO_3^{2-}
14 ions are the predominant species.^{5,23,24} The obtained results confirm that
15 $\text{Mg}(\text{HCO}_3)_2$ can form at a pH ranging between 8.2 and 8.9.

16 The amount of solid material collected upon completion of the experiment was
17 2 g. The XRD analysis showed that the solid residue constituted of brucite and
18 poorly crystalline hydromagnesite ($\text{Mg}_5(\text{CO}_3)_4(\text{OH})_2 \cdot 4\text{H}_2\text{O}$) and another poorly
19 crystalline phase which was not identified. The amount of CO_2 in the collected
20 solid was determined *via* CHN analysis and estimated as 0.01 mole. These results
21 indicate that $\text{Mg}(\text{OH})_2$ almost fully dissolved and captured CO_2 by forming
22 $\text{Mg}(\text{HCO}_3)_2$ which remained in equilibrium in solution while only a small fraction
23 reacted forming Mg carbonate phases.

24 The exact quantification of CO_2 captured by the reaction with $\text{Mg}(\text{OH})_2$ is
25 challenging and requires further analysis. Nevertheless, these preliminary results
26 suggest that at least 93.6% of CO_2 potentially capturable by the $\text{Mg}(\text{OH})_2$
27 suspension was effectively captured.

30 Implications of $\text{Mg}(\text{OH})_2$ extraction for CCS

31 The consumption of NaOH was identified as one of the major drawbacks for the
32 extraction of $\text{Mg}(\text{OH})_2$ in the NaOH aqueous system¹⁵ because the production of
33 NaOH involves significant energy consumption and thus CO_2 emissions. There-
34 fore, the reduction in NaOH achieved in the present study is significant and it
35 would reduce the environmental impact of the process.

36 In the present study, the CO_2 balance was evaluated based on the emissions
37 associated with the NaOH , $\text{Mg}(\text{OH})_2$ extraction and the sequestration potential of
38 $\text{Mg}(\text{OH})_2$ derived from dunite. The assessment is based on the mass balance of
39 the materials used assuming that 1 kg of dunite is processed with the corre-
40 sponding amount of NaOH used for Series 1, 1.5 and 2. The amount of $\text{Mg}(\text{OH})_2$
41 extracted was estimated from the yield of reaction achieved. The CO_2 emission
42 from NaOH production was calculated assuming that 2.9 k W h of electricity is
43 required to produce 1 kg of NaOH , which corresponds to the emission of at least
44 250 g of CO_2 per 1 k W h, when natural gas is used.^{25,26} The CO_2 emission from the
45 extraction of $\text{Mg}(\text{OH})_2$ is based on the use of an electric oven with a capacity of 28
46 litres to process 1 kg of dunite. The oven consumes 0.17, 0.26 and 0.385 k W h of
47 energy to operate at 130, 180 and 250 °C, respectively, according to the manu-
48 facturer's specification.²⁷ The CO_2 sequestration was calculated based on the full
49 conversion of $\text{Mg}(\text{OH})_2$ into either MgCO_3 or $\text{Mg}(\text{HCO}_3)_2$.

Fig. 12 compares the CO₂ potentially captured by the Mg(OH)₂ extracted at 180 °C in 6 hours for Series 1, 1.5, and 2, together with that achievable at a 100% yield of the reaction. The dotted lines represent the sum of the CO₂ emissions from the NaOH production and Mg(OH)₂ extraction. The graph shows that the potential CO₂ capture naturally increases with the improvement of the yield of Mg(OH)₂ extraction, but the estimated CO₂ emission from NaOH production and Mg(OH)₂ extraction is still larger, indicating the importance of process optimisation. The achievement of a 100% yield at 180 °C in 6 hours would effectively reduce CO₂ emission for all series when Mg(OH)₂ is fully converted into Mg(HCO₃)₂. On the other hand, the CO₂ captured into MgCO₃ would not be sufficient to offset the CO₂ emission even at the maximum yield of Mg(OH)₂ extraction. According to reaction (6), 1 mole Mg(OH)₂ requires the consumption of 1 mole NaOH, and from the amount of Mg(OH)₂ in the reaction products it was estimated that only 55, 59 and 60% NaOH reacted with dunite in Series 2, 1.5 and 1, respectively, suggesting that there is still a wide margin for improvement of Mg(OH)₂ extraction.

Fig. 13(A)–(C) show the CO₂ balance for Series 2 extracted at 130, 180 and 250 °C, respectively. As shown in Fig. 13(A), the yield of Mg(OH)₂ extraction at 130 °C is too low and the CO₂ emission from the power consumption is considerably larger. Fig. 13(B) shows that the CO₂ balance is significantly improved at 180 °C. In fact, at this temperature the potential CO₂ capture comes close to the CO₂ produced in the case of 3 hours of extraction, when CO₂ is captured as Mg(HCO₃)₂. Thus, a small improvement of the extraction conditions could result in a carbon neutral process. Extending the duration of the reaction to 6 hours is not energetically beneficial as more CO₂ is emitted. The CO₂ balance for the extraction at 250 °C is much better. As shown in Fig. 13(C), at 1 and 3 hours extraction, the CO₂ capture exceeds the CO₂ produced from the NaOH production and Mg(OH)₂ extraction, and CO₂ is successfully reduced. At this temperature, a shorter duration is clearly more beneficial. It should be noted that the CO₂ capture exceeds the CO₂ emission only when Mg(HCO₃)₂ is produced as a reaction product. The achievement of a 100% yield of extraction at 130, and 180 °C would

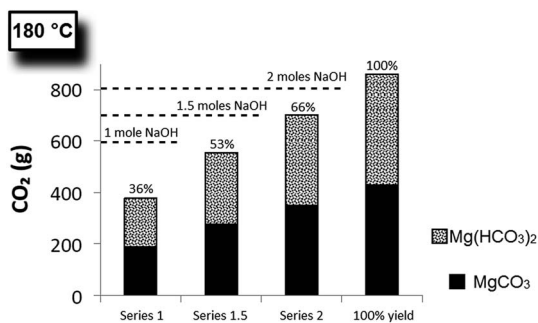


Fig. 12 Potential CO₂ capture by Mg(OH)₂ conversion into MgCO₃ or Mg(HCO₃)₂ (columns). The estimated CO₂ emission associated with the NaOH production and Mg(OH)₂ extraction at 180 °C for 6 hours are also shown (dotted lines) for Series 1, 1.5 and 2 for comparison. The yield of Mg(OH)₂ extraction is reported on top of the columns for each series.

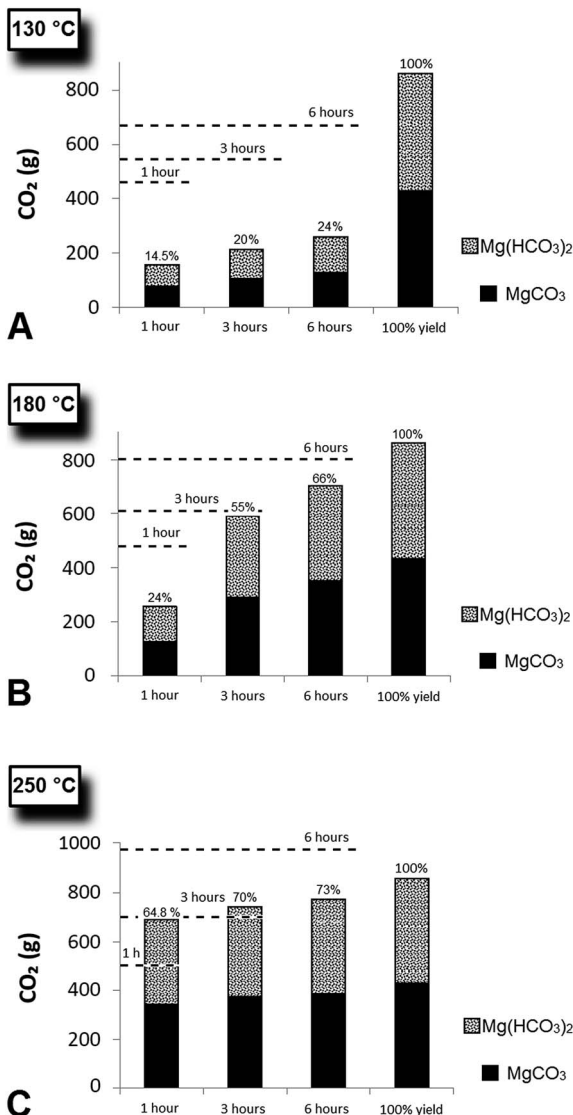


Fig. 13 Potential CO₂ capture by Mg(OH)₂ conversion into MgCO₃ or Mg(HCO₃)₂ (columns) for Series 2 at (A) 130 °C, (B) 180 °C and (C) 250 °C. The estimated CO₂ emission associated with the NaOH production and Mg(OH)₂ extraction for 1, 3 and 6 hours are also shown (dotted lines) for comparison. The yield of Mg(OH)₂ extraction is reported on top of the columns for each series.

reduce CO₂ under the studied conditions when Mg(HCO₃)₂ is formed, while at 250 °C, this occurs only for the extraction at 1 and 3 hours, and with 6 hours CO₂ is emitted. When MgCO₃ is produced as the reaction product, the amount of CO₂ to be captured is less than the CO₂ produced during the process, even at 100% yield, and thus the production of Mg(HCO₃)₂ is a key factor to offset the CO₂ produced during the extraction.

Conclusions

The present study demonstrated that the NaOH required to extract $\text{Mg}(\text{OH})_2$ from dunite can be reduced to a stoichiometric ratio with the reaction in the solid system assisted with H_2O .

H_2O considerably improved the extraction of $\text{Mg}(\text{OH})_2$ compared with the reaction in *dry* conditions, favouring the diffusion of the reactants involved. Both NaOH concentration in H_2O and the amount of liquid phase in the system played a significant role in the extraction of $\text{Mg}(\text{OH})_2$ from dunite and the best results were achieved in systems with a dunite : NaOH : H_2O 1 : 2 : 0.5 mole ratio. Decreasing the NaOH below the stoichiometric ratio resulted in less $\text{Mg}(\text{OH})_2$ extraction.

At 180 °C, the maximum yield of $\text{Mg}(\text{OH})_2$ extraction was 66% over 6 hours reaction for solid systems with a dunite : NaOH : H_2O 1 : 2 : 0.5 mole ratio. The NaOH consumption was reduced by 97% without affecting the efficiency of extraction with respect to the NaOH aqueous systems used in the previous study reacted at the same temperature and time. The H_2O consumption was also reduced by 99%. At 250 °C, the extraction of $\text{Mg}(\text{OH})_2$ was significantly accelerated and a 64.8% yield was achieved in 1 hour for solid systems with a dunite : NaOH : H_2O mole ratio of 1 : 2 : 0.5.

CO_2 was successfully separated from a gas mixture composed of 4–5% CO_2 and N_2 *via* liquid–gas scrubbing using a $\text{Mg}(\text{OH})_2$ aqueous slurry and stored in the solution as $\text{Mg}(\text{HCO}_3)_2$. At least 93.6% capture efficiency was achieved over 12 hours at ambient conditions. This technology integrates the separation and capture of CO_2 in one single step and may improve the efficiency of the overall CCS process.

The CO_2 balance of the process was estimated from the emission associated with the power consumed for NaOH production and $\text{Mg}(\text{OH})_2$ extraction together with the CO_2 captured by $\text{Mg}(\text{OH})_2$ derived from dunite. At 130 and 180 °C, the process is carbon neutral only at yields of reaction higher than those achieved in the present study when $\text{Mg}(\text{OH})_2$ is converted into $\text{Mg}(\text{HCO}_3)_2$. The CO_2 balance becomes negative when dunite is processed at 250 °C for 1 or 3 hours and CO_2 is captured as $\text{Mg}(\text{HCO}_3)_2$. This is promising for the possible application of $\text{Mg}(\text{OH})_2$ derived from dunite for CO_2 separation from flue gases and storage in H_2O .

Acknowledgements

The authors thank Regione Autonoma della Sardegna, Agenzia Regionale per il Lavoro, Italy, and the EU-European Social Fund for their contribution to the work presented which is part of the PhD project funded by the Master and Back Programme 2011, Percorsi di Alta Formazione, P.O.R. FSE 2007–2013.

References

- 1 IPCC: *IPCC Special Report on Carbon Dioxide Capture and Storage*, ed. B. Metz, O. Davidson, H. C. De Coninck, M. Loos and L. A. Meyer, Prepared by Working Group III of the Intergovernmental Panel on Climate Change, Cambridge University Press, Cambridge, United Kingdom and New York, NY, USA, 2005.

- 1 2 L. Zhao, L. Sang, J. Chen, J. Ji and H. H. Teng, *Environ. Sci. Technol.*, 2010, **44**,
406–411.
- 3 H. T. Schaef, C. F. Windisch Jr, B. P. McGrail, P. F. Martin and K. M. Rosso,
Geochim. Cosmochim. Acta, 2011, **75**, 7458–7471.
- 5 4 J. Fagerlund, E. Nduagu, I. Romão and R. Zevenhoven, *Energy*, 2012, **41**, 184–
191.
- 5 K. S. Jung, T. C. Keener, S.-J. Khang and S.-K. Lee, *Clean Technol. Environ.
Policy*, 2004, **6**, 201–212.
- 10 6 H. K. Bharadwaj, J.-Y. Lee, X. Li, Z. Liu and T. C. Keener, *J. Hazard. Mater.*, 2013,
250–251, 292–297.
- 7 P. Renforth and T. Kruger, *Energy Fuels*, 2013, **27**, 4199–4207.
- 8 A. Sanna, M. R. Hall and M. Maroto-Valer, *Energy Environ. Sci.*, 2012, **5**, 7781–
7796.
- 15 9 X. Wang, M. Maroto-Valer, G. Shiwang and X. Shisen, *Energy Procedia*, 2013, **37**,
2529–2535.
- 10 G. J. Simandl, S. Paradis and M. Irvine, *Geosci. Can.*, 2007, **34**, 57–64.
- 11 K. S. Lackner, C. H. Wendt, D. P. Butt, E. L. Joyce and D. H. Sharp, *Energy*, 1995,
20, 1153–1170.
- 20 12 M. G. Best, *Igneous and metamorphic petrology*, Blackwell Science Ltd, Oxford,
UK, 2nd edn, 2003.
- 13 W. J. J. Huijgen and R. N. J. Comans, *Carbon dioxide sequestration by mineral
carbonation, literature review update 2003-2004*, 2005, ECN-C-05-022, ECN.
- 25 14 P.-C. Lin, C.-W. Huang, C.-T. Hsiao and H. Teng, *Environ. Sci. Technol.*, 2008,
42, 2748–2752.
- 15 S. Madeddu, M. Priestnall, H. Kinoshita and E. Godoy, *Miner. Eng.*, 2014, **59**,
31–38.
- 16 M. Földvári, *Handbook of thermogravimetric system of minerals and its use in
geological practice*, Occasional Papers of the Geological Institute of Hungary,
Geological Institute of Hungary, Budapest, 2011, p. 213.
- 30 17 *Thermo-Calc Software User's Guide, Version 5*, ed. P. Shi and B. Sundman, Royal
Institute of Technology, Sweden, 1995.
- 18 H. B. Boubaker, M. Mhamdi, E. Marceau, S. Khaddar-Zine, A. Ghorbel, M. Che,
Y. B. Taarit and F. Villain, *Microporous Mesoporous Mater.*, 2006, **93**, 62–70.
- 35 19 J. Zhang, M. Huang, K. Yanagisawa and S. Yao, *Ceram. Int.*, 2015, **41**, 5439–
5444.
- 20 C. Kurt and J. Bittner, Sodium Hydroxide, in *Ullmann's Encyclopedia of
Industrial Chemistry*, Wiley-VCH, Weinheim, Germany, 2003.
- 40 21 A. R. West, *Solid state chemistry and its applications*, Wiley, 2nd edn, 2014.
- 22 K. W. Whitten, R. E. Davis, M. L. Peck and G. G. Stanley, *Chemistry*, Brooks/
Cole, Cengage Learning, Belmont, USA, 9th edn, 2010.
- 23 W. Stumm and J. J. Morgan, *Aquatic Chemistry, Chemical Equilibria and Rates in
Natural Waters*, John Wiley & Sons, 3rd edn, 1970.
- 45 24 M. A. Shand, *The chemistry and technology of magnesia*, John Wiley & Sons Inc.,
Hoboken, New Jersey, USA, 2006.
- 25 Y. Kiros and M. Bursell, *Int. J. Electrochem. Sci.*, 2008, **3**, 444–451.
- 26 Parliamentary Office of Science and Technology, Carbon footprint of electricity
generation, postnote, October 2006, Number 268, United Kingdom.
- 50

1 27 Carbolite, Installation, operation & maintenance instructions, Ovens Peak
Series, MF15 – 3.14, available at: [http://www.carbolite.com/downloads/
operating-manuals/](http://www.carbolite.com/downloads/operating-manuals/).

5

10

15

20

25

30

35

40

45

50

PAPER

Carbon dioxide capture and utilization: using dinuclear catalysts to prepare polycarbonates†

N. Yi, J. Unruangsri, J. Shaw and C. K. Williams

Received 12th May 2015, Accepted 18th May 2015

DOI: 10.1039/c5fd00073d

The copolymerization of epoxides, including cyclohexene oxide and vinyl-cyclohexene oxide with carbon dioxide are presented. These processes are catalyzed using a homogeneous di-zinc complex that shows good activity and very high selectivities for polycarbonate polyol formation. The polymerizations are investigated in the presence of different amounts of exogenous reagents, including water, diols and diamines, as models for common contaminants in any carbon dioxide capture and utilization scenario.

Introduction

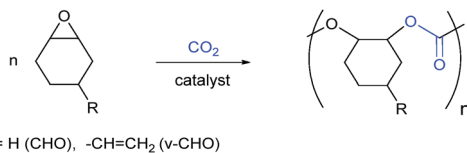
Using carbon dioxide to make useful products, including chemicals and fuels, is an attractive way to add value to a common waste gas and could be a useful method to reduce pollution.^{1–4} From a practical, implementation focused perspective, there are two primary considerations for any carbon capture and usage process: (1) the overall carbon dioxide emission must be reduced, which sounds obvious but requires careful consideration of the overall energies of both the process and embedded in the preparation of co-reagents; and (2) the product must be needed and viable, both in terms of the potential market volume and value.

Amongst the myriad of possible carbon dioxide transformations, the production of polymers offers significant potential.^{5–10} Such polymers are prepared by the ring-opening copolymerization (ROCOP) of carbon dioxide and epoxides (Scheme 1), a process which requires a catalyst. The reaction has attracted considerable attention, with a number of different catalysts and processes being reported by both academic and industrial researchers worldwide.^{5–18}

The products of the reaction are aliphatic polycarbonates; at low molecular weights these polymers are suitable replacements for petrochemical polyols used in polyurethane manufacturing.^{19,20} In the context of carbon dioxide reduction, the replacement of polyether polyols by poly(ether carbonate) polyols leads to

Department of Chemistry, Imperial College London, London, SW7 2AZ, UK

† Electronic supplementary information (ESI) available. See DOI: 10.1039/c5fd00073d



Scheme 1 Illustrates the ring opening copolymerizations using cyclohexene oxide (CHO) and vinyl-cyclohexene oxide (v-CHO).

10 significant reductions in greenhouse (GHG) emissions ($\sim 20\%$).²¹ By selecting the correct catalyst, it is possible to substitute $>40\%$ of the epoxide with carbon dioxide. Such a substitution is attractive both economically and environmentally as it may further reduce GHG emissions. Thus, the first criterion can be met by

15 the production of polymers from carbon dioxide.

The second criterion, that the products are valuable and needed/used on a large-scale, is also met by polymer production. Considering only polyols, there are currently >8 Mt of polyurethanes produced globally requiring 3–4 Mt of polyols in their manufacture.^{19,20} Therefore, the production of polymers from CO_2 has the potential to offer a viable industrial route to add value to waste emissions. The process is critically dependent on the selection of the catalyst, with a range of very promising heterogeneous and homogeneous catalysts having been reported.^{5–18} However, so far there remain far fewer studies on the tolerance of such catalysts to a range of impurities, which are likely to be present in any carbon capture and usage scenario.^{22,23} We recently reported that our dinuclear metal catalysts are tolerant to a wide range of impurities found in captured carbon dioxide, including nitrogen, oxygen, oxides of carbon, NO_x and SO_x .²³ Furthermore, using di-magnesium catalysts a wide-ranging study of common contaminants was undertaken which revealed remarkable catalyst stability, even in the presence of large amounts of contaminants.²³ In that study, carbon dioxide captured from a UK power station was applied and showed near-equivalent performance compared to pure carbon dioxide.²³

25

30

Our group have reported a series of homogeneous catalysts for CO_2 /epoxide copolymerization, based on dinuclear complexes of Zn(II) , Mg(II) , Co(II/III) and Fe(III) .^{24–35} This discussion paper will focus on a di-zinc bis(trifluoroacetate) complex²⁸ and the influence of the addition of known quantities of water, alcohols and amines to the polymerizations. The additives and monomers are investigated both to test tolerance of the catalyst and also to target particular polymer chain functionalities (end-groups, side-chain substituents) so as to widen the scope, and ultimately the scale, of future applications.

35

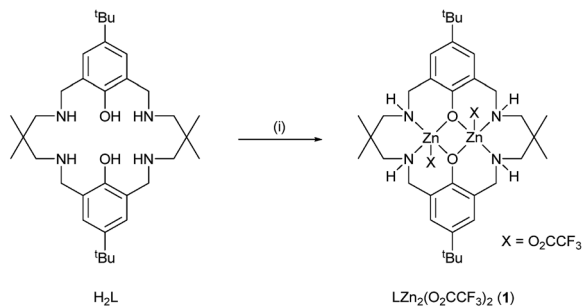
40

45 Results and discussion

The preparation and structure of catalyst **1** is shown in Scheme 2.²⁸

The catalyst was synthesized from the ancillary ligand, H_2L , which can itself be prepared in high yield (82%) from commercial materials in 3 steps. Its purity was assessed by ^1H NMR spectroscopy (Fig. S1†) and by elemental analysis, which showed results in line with the literature.²⁸

50



Scheme 2 Synthesis of the dizinc complex (LZn₂(O₂CCF₃)₂, **1**). Reagents and conditions: (i) 2 equiv. Zn(O₂CCF₃)₂·xH₂O, MeOH, 25 °C, 16 h.

Catalyst **1** was applied in the copolymerization of cyclohexene oxide (CHO) or vinyl cyclohexene oxide (vCHO) and carbon dioxide (Table 1 and Scheme 2). It showed a good performance using both monomers, with the TOF for CHO being 25 h⁻¹ and for v-CHO being 24 h⁻¹, at 1 bar CO₂ pressure, 0.1 mol% catalyst loading and 80 °C. The activity for CHO is in-line with the value reported in the literature.²⁸ The activity using v-CHO has not previously been reported and is more difficult to quantify precisely due to significant overlap of resonances associated with monomer and polymer in the crude ¹H NMR spectrum (Fig. S2 and S3[†]). For both monomers, the polycarbonates produced show a very high selectivity for carbonate linkages (≥99%) and there is ≤1% formation of a cyclic carbonate by-product.

The alternating polymers show moderate molecular weights, with values typically being lower than 10 000 g mol⁻¹, and narrow dispersities (*D* < 1.20). Copolymerizations using **1** show a linear evolution of molecular weight vs. CHO conversion and narrow dispersities: both are features of well-controlled/living polymerizations. Such behaviour is indeed typical of this class of dinuclear catalyst and indicates good polymerization control.³⁰

Controlled polymerizations are defined as exhibiting rapid and quantitative initiation leading to all chains propagating at the same rate and limited/no

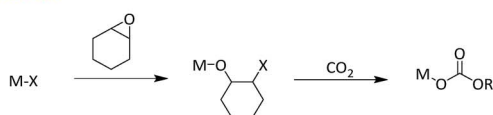
Table 1 Epoxide/CO₂ copolymerization using **1**^a

Entry	Monomer	Catalyst	Temp. (°C)	TOF ^c TON ^b (h ⁻¹)	% carbonate ^d	% cyclic carbonate ^d	<i>M</i> _n ^e (g mol ⁻¹)	<i>M</i> _w / <i>M</i> _n ^e (<i>D</i>)	
1 ^f	CHO	1	80	608	25	99	3	1500	1.08
2	CHO	1	80	502	25	99	1	6600	1.18
3 ^g	v-CHO	1	80	429	20	>99	<1	5900	1.30
4	v-CHO	1	80	389	24	>99	<1	6700	1.18

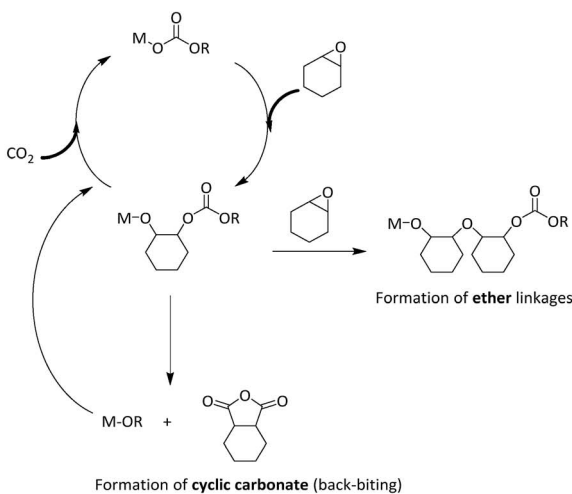
^a Polymerization conditions: 0.1 mol% catalyst, in neat epoxide, for 6–24 h, 1 bar research grade CO₂ unless stated otherwise. ^b TON = number of epoxide consumed per mole of catalyst. ^c TOF = TON per hour. ^d Determined by comparing the integrals of resonances at 4.65 ppm (PCHC) or 4.75–4.90 ppm (PVCHC), at 4.0 ppm (cyclic carbonate by-product) and at 3.45 ppm (ether linkages). ^e Determined by SEC, in THF using narrow *M*_w polystyrene standards. ^f Unpurified CHO. ^g Unpurified v-CHO.

1 termination or chain transfer reaction. In such a polymerization, the molecular
 weight of the polymer should be predictable from the monomer conversion and
 catalyst/initiator concentration. However, the polymerizations using catalyst **1**
 5 result in the production of polymers that have molecular weights, determined by
 size exclusion chromatography, which are substantially lower than predicted;
 indeed the values obtained suggest that chain transfer reactions occur, and that
 approximately 8 chains grow per equivalent of catalyst. Thus, the polymerizations
 appear to be occurring under immortal conditions, whereby chains are rapidly
 10 being exchanged or transferred between the catalyst and a chain transfer agent
 (often an alcohol). Fig. 1 illustrates the key processes occurring during polymer-
 ization. It is proposed that 1,2-diols are present in the polymerizations and
 function as the chain transfer agents. Such chain transfer processes are
 commonly observed in this field using a range of different catalysts.^{14,27,30,36–38}

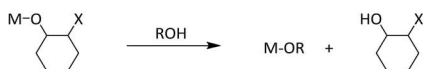
Initiation



Propagation



Chain transfer reaction



X = Halide, carboxylate

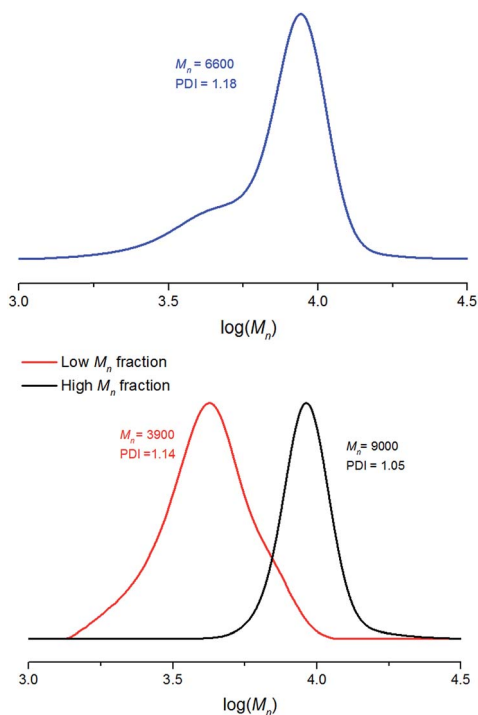
OR = OCH₂CH₂X

ROH = water, alcohol

Fig. 1 The proposed catalytic cycle for the copolymerization of CO₂ and epoxides.⁸

1 A further consideration is that bimodal molecular weight distributions are
commonly observed, but seldom explained, for a wide range of catalysts in the
literature.^{27,29,30,37,39} Indeed, catalyst **1** also shows a distinctly bimodal M_w distribution for both PCHC and PvCHC (Fig. 2, blue trace, Fig. S4 and S5†). In order to
5 study the observed bimodality, two fractions of PCHC containing the higher and
lower M_n distributions were isolated by SEC, according to a preparative separation
by elution time (see Experimental section). These fractions were analysed by ^1H
NMR spectroscopy, MALDI-ToF and SEC. For both fractions, the ^1H NMR spectra
10 are identical, indicating PCHC end-capped with hydroxyl groups (Fig. S6†).
Furthermore ^{19}F NMR spectroscopy does not show any signals consistent with a
lack of trifluoroacetate end-groups on the polymer chains. The MALDI-ToF
spectra show that both fractions contain a single series attributed to poly-
carbonates having di-hydroxyl end groups. SEC analyses showed a clear separation
15 into two molecular weight distributions: the lower fraction has M_n of 3900 (D :
1.14), whilst the higher fraction has M_n of 9000 (D : 1.05). Based on these obser-
vations, it appears that catalyst **1** leads to the production of PCHC with narrow but
bimodal molecular weight distributions, where all detectable chains are di-
hydroxyl terminated (Fig. 3).

20 We have previously observed bimodal M_w distributions, due to chains end-
capped by the initiating group (lower M_n series) and by the di-hydroxyl groups
(high M_n series, Fig. S3†).³⁰ Based on this previous data, it would be expected that
catalyst **1** would show chains end-capped by both trifluoroacetate (from the



50 Fig. 2 Top: molecular weight distribution of the isolated (crude) PCHC polymer (Table 1 entry 2) and bottom: the separation of PCHC into two fractions of low and high M_w .

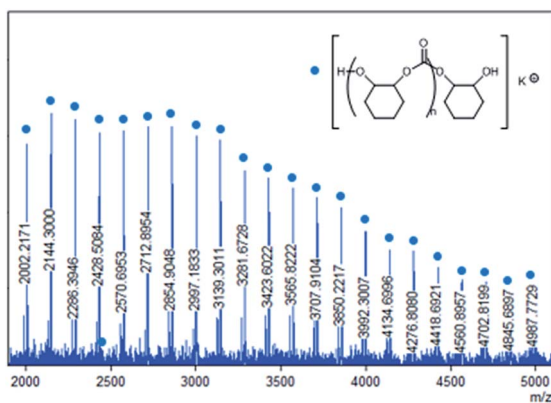


Fig. 3 MALDI-ToF spectrum of the low M_n fraction of PC (Table 1 entry 2), a single series is observed corresponding to: $[\text{HO}(\text{C}_7\text{H}_{10}\text{O}_3)_n\text{C}_6\text{H}_{11}\text{O}_2]\text{K}^+ = [(142.15)_n + 116.16 + 39.1]$.

catalyst) and di-hydroxyl groups (from 1,2-diols). As the polymerizations are well-controlled, it is expected that the chains propagate at the same rate, therefore the molecular weight of the polymer from the telechelic diol would be expected to be double that of polymers initiated from the trifluoroacetate group. Thus, the bimodality can be generally attributed to the two types of initiating group. In order to rationalize the lack of a trifluoroacetate end-group (by spectroscopy and MALDI-ToF), it is proposed that those chains are susceptible to end-group (trifluoroacetate) hydrolysis during work-up due to the strongly electron-withdrawing substituents on the carboxylate group. The hydrolysis would lead to a bimodal M_w distribution where both series of chains are end-capped by hydroxyl groups, in line with the experimental observations. Darensbourg and co-workers observed that salen-chromium(trifluoroacetate) catalysts also lead to di-hydroxyl terminated polycarbonates.⁴⁰ They confirmed that the trifluoroacetate end-group was present during polymerization, using anhydrous electrospray mass spectrometry, but was hydrolysed during termination/work-up to selectively produce the polyol.⁴⁰

The important outcome is that catalyst **1** leads to the highly selective formation of dihydroxyl end-capped polymers or polyols. This is potentially beneficial for further application in polyurethane manufacture or in the production of higher polymers. We have previously demonstrated that such polyols are viable initiators for lactide ring-opening polymerizations, upon addition of a ROP catalyst, so as to produce ABA type triblock copoly(ester-carbonate-esters).²⁸ Given that selective production of polyols is feasible using catalyst **1**, it is of interest to investigate its tolerance to the presence of various other chain transfer agents and also the potential to prepare mono-modal M_w distributions.

Polymerizations with added water

Chain transfer reactions are known to occur during these polymerizations if protic compounds are present. These reactions serve to 'swap' the growing polymer chain on/off the metal centre and result in more than one polymer chain growing per equivalent of catalyst (Fig. 1). Given that there is good control of the

M_w and the dispersities are narrow, it is proposed that the chain transfer reactions occur more rapidly than propagation. Thus, it should be possible to control the molecular weights *via* the addition of chain transfer agents, the simplest and most cost-effective of these is probably water. Furthermore, water is of interest as it is a common contaminant of carbon dioxide and would be expected to be present in any gases captured from industrial processes. In order to investigate the tolerance of catalyst **1** to water, a series of copolymerizations were run with increasing quantities of water being added (Table 2).

In all cases where water was added, the polymerizations were nearly as active and selective as polymerizations in the absence of any additive (Table 2). It is feasible to add large quantities of water to the polymerizations, including from ~90–5700 ppm by weight, and still maintain effective polymerization. This is particularly notable as typical pipeline specifications for captured CO₂ water content are approximately 100–1000 ppm.²³

For the polymerizations using water as the chain transfer agent, the polymer MWs reduce as increasing quantities of water are added. Furthermore, monomodal M_w distributions are observed when excess water is added (Fig. 4). A representative MALDI-ToF spectrum (Fig. 4) confirms that only a single series of polycarbonate polyol chains is formed in all cases.

Polymerizations with added alcohols

It has been proposed that water reacts with epoxides to produce cyclohexane-1,2-diol (CHD), such a process likely occurs immediately and may be metal catalyzed.^{27–30} Cyclohexane-1,2-diol would be expected to function as a chain transfer agent (CTA), leading to propagation from both of its secondary hydroxyl groups.⁴¹ Thus, it is of interest to investigate polymerizations in the presence of various equivalents of exogenous CHD (Table 3, entry 1–4). Using either CHO or vCHO resulted in successful polymerizations, and all the polymers contained high carbonate linkage contents (>99%) and low quantities of cyclic carbonates (~5% for PCHC and <1% for PvCHC). Using a 5-fold excess of CHD, *vs.* catalyst, with CHO or v-CHO led to polymerizations occurring at near equivalent activity to those run in the absence of additives (Table 1, entries 2 and 4). Increasing the

Table 2 Data obtained for polymers produced by the ring opening copolymerization (ROCO) of CHO and CO₂ with the addition of water as a chain transfer agent (CTA)^a

Entry	Amount of water added (mol equiv.)	ppm H ₂ O ^b (by weight)	M_n^c (g mol ⁻¹)	M_w/M_n^c (\bar{D})
1	0.5	91	5700	1.17
2	1	182	5200	1.15
3	2	364	4600	1.12
4	4	728	3300	1.11
5	8	888	2500	1.10
6	16	2904	1800	1.10
7	32	5792	800	1.09

^a Polymerization conditions: 0.1 mol% of **1**, 18 h reaction time, 1 bar research grade CO₂, 80 °C. ^b The quantity of water (as ppm weight fraction) added, based on the overall quantities of catalyst **1**, epoxide and additive. ^c Determined by SEC, in THF, using narrow molecular weight polystyrene standards to calibrate the instrument.

1

5

10

15

20

25

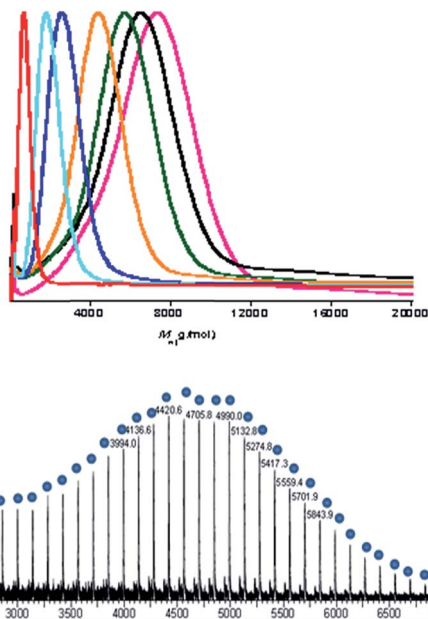
30

35

40

45

50



amount of CHD to a 10-fold excess also enabled successful polymerization with the selectivity remaining very high.

As would be expected, increased quantities of CHD led to a decrease in polycarbonate M_n due to multiple polymer chains resulting per metal centre. As stated earlier, bimodal molecular weight distributions were observed for both PCHC and PvCHC. In contrast, the addition of an excess of CHD suppressed this bimodality and produced polycarbonates with monomodal molecular weight distributions (Fig. 5 and S8†).

Based on the successful results using CHD (a bifunctional alcohol) as a chain transfer agent, it was of interest to investigate the addition of a tri-functional alcohol to produce branched polycarbonates (Table 3). The efficient copolymerization of CO_2 and CHO was undertaken in the presence of 20 mol equiv. *vs.* catalyst **1**, of triethanolamine ($\text{N}(\text{CH}_2\text{CH}_2\text{OH})_3$, TEA) (Table 3, entry 5). The polycarbonate was analysed by ^1H and $^{31}\text{P}\{^1\text{H}\}$ NMR spectroscopy, MALDI-ToF and SEC; all of which confirmed the formation of a perfectly alternating copolymer. The synthesis of tri-functional, or branched, PCHC was confirmed from the ^1H NMR spectrum (Fig. S9†), where the ethylene protons of the NCH_2 and OCH_2 groups of the TEA segment were observed at 2.86 and 4.17 ppm, respectively.

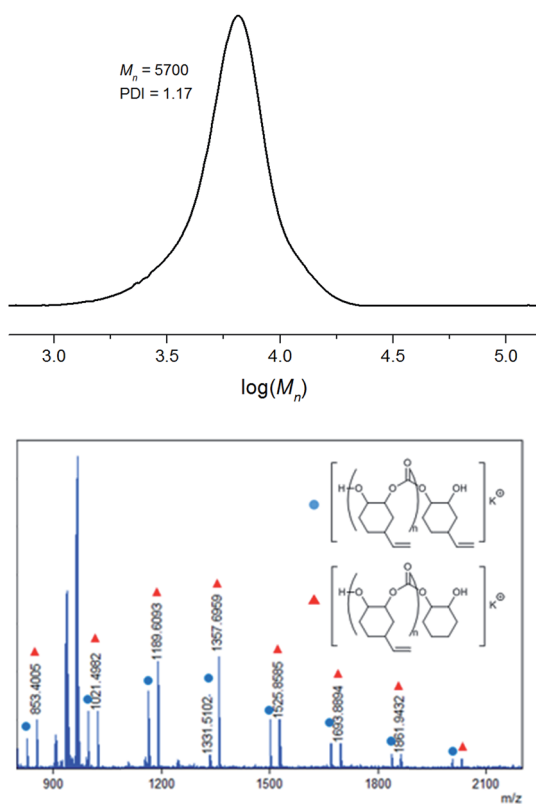
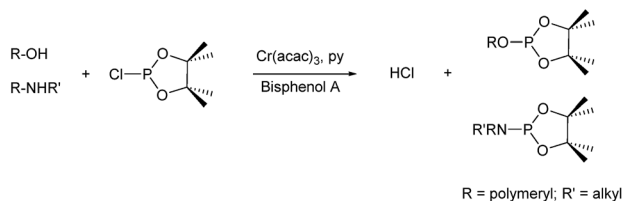


Fig. 5 Top: the monomodal molecular weight distribution of PvCHC (Table 3 entry 4), as determined by SEC, using 10 equiv. of CHD in the polymerization. Bottom: MALDI-ToF spectrum of the PvCHC produced in Table 3 entry 4, using 10 equiv. of CHD.



10
11
12
13
14
15
16
17
18
19
20
21
22
23
24
25
26
27
28
29

Scheme 3 The reaction between alcohol or amine and 2-chloro-4,4,5,5-tetramethyl dioxaphospholane.

Furthermore, only secondary alcohol groups (145.5 ppm) were identified using a $^{31}\text{P}\{^1\text{H}\}$ NMR spectroscopic analysis method (Fig. S10†). The method involves reacting a sample of the polymer with 2-chloro-4,4,5,5-tetramethyl dioxaphospholane, using bis(phenol)A as an internal standard (Scheme 3).^{42–44} It indicates that, within the detection limits of the technique, all polymerizations were successfully initiated from all the hydroxyl functionalities of TEA as all the primary alcohol groups were consumed and only secondary hydroxyl groups, due to cyclohexanol end groups were observed. The MALDI-ToF spectrum (Fig. S11†) showed a major series corresponding to the dihydroxyl end-capped PCHC. The absence of the expected series, corresponding to PCHC initiated from TEA, is proposed to be due to difficulties in branched chains. In this case, the rate of polymerization was relatively slower ($\text{TOF} = 7 \text{ h}^{-1}$), yielding a polymer with M_n of 1500 g mol^{-1} ($D = 1.23$).

30 31 32 33 34 35 36 37 38 39

Polymerizations with added amines

Amine based post combustion capture of CO_2 has recently received much attention as a promising method for the reduction of atmospheric CO_2 emissions.⁴⁵ Approximately, 0.2 ppm of amine, namely methanolamine (MEA) and methylamine, in conjunction with 20 ppm ammonia are found as common contaminants. Denitrification is required to remove the amine-based contaminants in the production of reclaimed CO_2 .^{46,47}

It has already been established that the successful ROCOP of CHO and reclaimed CO_2 occurs using analogous a di-magnesium catalyst (Table 1, entry 6).²³ It was, therefore, of interest to establish whether $\text{LZn}_2(\text{O}_2\text{CCF}_3)_2$ (**1**) can successfully catalyze ROCOP in the presence of amine additives.

40
41
42
43
44
45
46
47
48
49
50
51
52
53
54
55
56
57
58
59
60

The polymerizations of CHO and CO_2 with primary (H_2NBn) and secondary (HNBn_2) amine additives occurred successfully (Table 3, entries 6 and 7, respectively). Slightly lower polymerization rates ($\text{TOF} < 20 \text{ h}^{-1}$) were obtained in both cases compared to the polymerizations in the absence of any additives ($\text{TOF} = 25 \text{ h}^{-1}$, Table 1, entry 2), whereas in all cases the polymerization selectivities were high. The ^1H NMR spectra of the isolated PCHC clearly indicate the incorporation of the amine reagents into the polymer chains. A representative ^1H NMR spectrum of the PCHC from Table 3, entry 7 is shown in Fig. 6, illustrating the key resonances assigned to the benzyl protons at 7.32–7.22 and 4.37 ppm, respectively. In addition, SEC analysis using a UV detector also served to confirm the incorporation of the benzyl units as end-groups to the polymers (Fig. S12†).

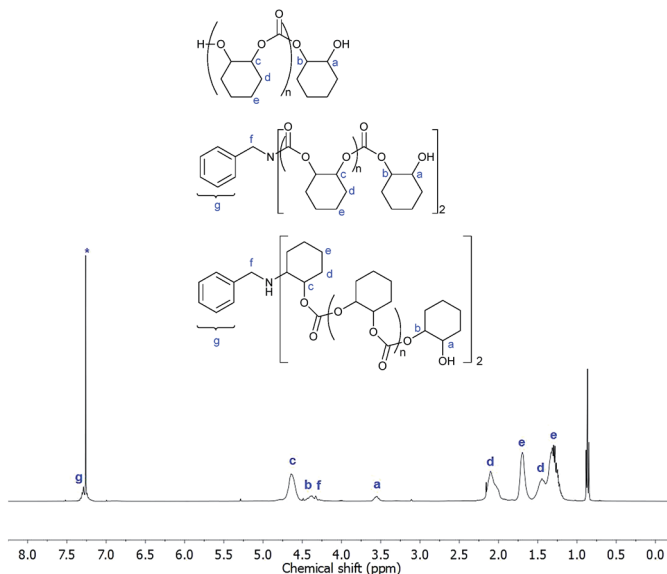


Fig. 6 ^1H NMR spectrum (400.0 MHz, $\text{CDCl}_3\text{-}d_3$, 298 K) of the isolated PCHC produced in the polymerization with H_2NBn additive (Table 3, entry 7). The asterisk denotes the residual protio-solvent.

The MALDI-ToF mass spectra showed three series attributed to polycarbonates end-capped by: (1) dihydroxy groups, (2) amine/hydroxyl groups and (3) carbamate/hydroxyl groups (Fig. 7).

The presence of both amine and amide end groups must be due to the formation of both the carbamate alcohol (a, Scheme 4) and the amino alcohol (b, Scheme 4) from the reaction between amine, CHO and CO_2 , in the presence of

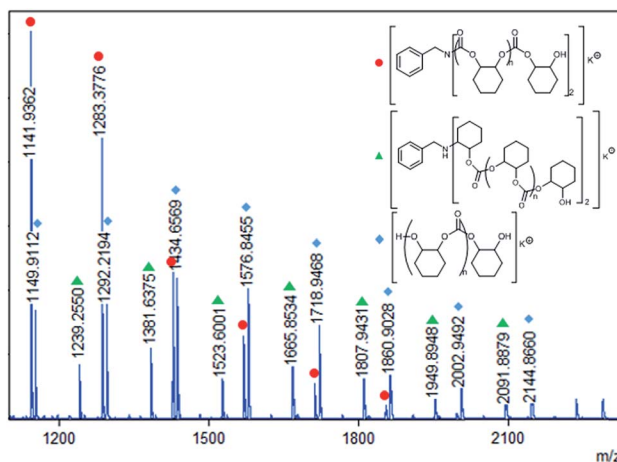
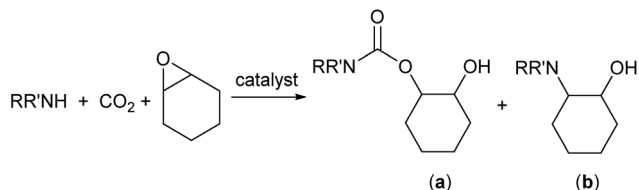


Fig. 7 MALDI-ToF spectrum of the PCHC obtained in Table 3 entry 7, using 20 equiv. of H_2NBn .



Scheme 4 The synthesis of carbamate alcohol and amino alcohol.

10 catalyst **1**. Other researchers have reported the reactions of amines, carbon dioxide and epoxides can lead to the formation of both products, although it is notable that in these cases more forcing conditions were generally required.^{48–50}

15 A control experiment was carried out to examine the behaviour of the amine reagents under the polymerization conditions which showed that polymerization only occurred in the presence of the catalyst, *i.e.* the amines themselves are not able to ‘catalyze’ polymerization. This observation reinforces the proposed metal-mediated ROCOP pathway, whereby monomers are activated through the coordination to the metal centres prior to reactions with the amines. The carbamate alcohol and amino alcohol intermediates are expected to act as chain transfer reagents in the polymerizations. These polymerizations occurred with slightly slower rates than in the absence of additives, this may be due to inhibition of monomer binding by the amines and/or slower initiation processes. The polymers were analyzed using MALDI-ToF MS and by ³¹P{¹H} NMR spectroscopy, after reaction with 2-chloro-4,4,5,5-tetramethyl dioxaphospholane. The resonances were characteristic of polycarbonates with secondary hydroxyl end-groups, with peaks at 145.5 ppm in ³¹P{¹H} NMR spectra (C and D, Fig. S10†). Whereas the reaction between dibenzylamine and the dioxaphospholane resulted in a peak at 142.5 ppm in the ³¹P{¹H} NMR spectrum (B, Fig. S10†). Thus supporting the involvement of the NH groups in the polymerizations, as illustrated in Scheme 4.

25 The scope of polymerizations in the presence of amines was expanded to include bi-functional reagents, such as, monoethanolamine (MEA) and ethylenediamine (EN). The formation of a white suspension was observed during the initial stages of polymerizations using these additives (Table 3, entries 10 and 11, respectively). Such observations are consistent with the formation of ammonium salts, as part of equilibria between amines, carbon dioxide and carbamic acid.^{48–50} The white suspension dissolved as the polymerization proceeded, and the reactions resulted in the formation of low molecular weight PCHC, with a slightly broader dispersity ($M_n = 2200 \text{ g mol}^{-1}$, $D = 1.21$ for MEA and $M_n = 2900 \text{ g mol}^{-1}$, $D = 1.21$ for EN) compared to that obtained from the control experiment ($M_n = 6600 \text{ g mol}^{-1}$, $D = 1.18$). Once again, the polymerization activities were significantly lower (TOF = 9 h^{-1}) than that of the control experiment. The polymer chain end group analysis, using the reaction with 2-chloro-4,4,5,5-tetramethyl dioxaphospholane, showed the formation of polycarbonates with secondary alcohol end-groups (E and F, Fig. S10†), however, the MALDI-ToF spectra were highly complex and as yet cannot be fully assigned. These findings indicate that although successful polymerizations did occur in the presence of primary amines, the precise polymer structures may be complicated by carbamate formation at the chain ends.

30

35

40

45

50

Experimental section

Materials and methods

All manipulations were carried out using standard Schlenk line or dry-box techniques under an inert atmosphere of nitrogen. All glassware was dried at 160 °C for 20 h and cooled under vacuum prior to use. Solvents were dried by passing through a column of appropriate drying agent, degassed and stored under nitrogen atmosphere. Chloroform-*d*₃ was dried over CaH₂, distilled under reduced pressure and stored over 4 Å molecular sieves, under nitrogen atmosphere.

Ligand H₂L and catalyst **1** were synthesised according to the previously published literature. Cyclohexene oxide and vinyl cyclohexene oxide were purchased from Acros and Sigma-Aldrich, respectively, and fractionally distilled from CaH₂. Cyclohexene diol was recrystallised from ethyl acetate and stored under nitrogen atmosphere. Benzylamine (99%), dibenzylamine (97%), monoethanolamine (99.5%), ethylenediamine (99.5%) and triethanolamine (98%) were purchased from Sigma-Aldrich, degassed and stored under nitrogen atmosphere. High-purity CO₂ was obtained by passing research grade CO₂ (99.99995%) purchased from BOC (Linde Gas) through a high performance purifier (Drierite column).

¹H, ¹³C{¹H}, ³¹P{¹H} NMR spectra were recorded using a Bruker AV400 MHz spectrometer at ambient temperature (unless stated otherwise). ¹H, ¹³C{¹H} NMR spectra were referenced internally to residue proteo-solvent (¹H) or solvent (¹³C) resonances, and are reported relative to tetramethylsilane. SEC data were determined by a Shimadzu LC-20AD instrument using MALLS detector (Wyatt Dawn 8+), with THF as the eluent, at a flow rate of 1.0 mL min⁻¹ at 30 °C. Two Mixed Bed PSS SDV linear S columns were used in series. The MALLS detector was calibrated using a polystyrene standard. MALDI-ToF MS experiments were carried out on Waters/Micromass MALDI micro MX spectrometer, using a dithranol matrix in THF at a 1 : 1 loading with potassium trifluoroacetate (KO₂CCF₃) as the cationizing agent. Elemental analyses were carried out using the Elemental Analysis Service at London Metropolitan University.

Synthetic procedures

General polymerization protocol

Copolymerization of cyclohexene oxide or vinyl cyclohexene oxide and carbon dioxide. Cyclohexene oxide (1.67 mL, 17 mmol) or vinyl cyclohexene oxide (2.15 mL, 17 mmol) and LZn₂(O₂CCF₃) (**1**, 15.0 mg, 0.017 mmol) were added into a Schlenk tube. The epoxide was degassed, before being left stirring under 1 atm CO₂ at 80 °C for a pre-determined time period. The crude reaction mixture was dried *in vacuo* to remove unreacted epoxide. The polymer was purified by repeat precipitations from methylene chloride using methanol.

Separation of poly (cyclohexene carbonate) (PCHC) with a bimodal molecular weight distribution. 100 mg of PCHC in THF (1.5 mL) was analysed using the previously stated SEC equipment. The delay time of the instrument was calculated based on the flow rate and the column length. Different fractions were collected manually according to the pre-determined time (elution and delay time).

1 *Polymerizations in the presence of chain transfer agents.* The general procedure
stated above was followed, whereby multi-equivalents of chain transfer agents
were added to the reaction mixture prior to the degassing process.

5 Conclusions

In conclusion, a di-zinc trifluoroacetate catalyst was investigated for the copoly-
merization of cyclohexene oxide or vinyl-cyclohexene oxide and carbon dioxide.
The catalyst shows moderate/good activity and productivity and very high selec-
tivity for carbonate linkage formation. It also selectively produces polycarbonate
polyols, with bimodal molecular weight distributions. The catalyst functions well
in the presence of additives, including water, diols and amines. These added
reagents lead to good catalytic performances and enable control over the
molecular weight of the polymers and the production of polyols with monomodal
molecular weight distributions. The catalyst shows a high tolerance to such
contaminants, including the ability to selectively prepare polyols in the presence
of >5000 ppm of water.

20 Acknowledgements

The authors acknowledge the Engineering and Physical Sciences Research
Council (EPSRC grants: EP/K035274/1, EP/L017393/1, EP/H046380) for funding.

25 Notes and references

- 1 P. Markewitz, W. Kuckshinrichs, W. Leitner, J. Linssen, P. Zapp, R. Bongartz,
A. Schreiber and T. E. Muller, *Energy Environ. Sci.*, 2012, **5**, 7281–7305.
- 2 N. MacDowell, N. Florin, A. Buchard, J. Hallett, A. Galindo, G. Jackson,
C. S. Adjiman, C. K. Williams, N. Shah and P. Fennell, *Energy Environ. Sci.*,
2010, **3**, 1645–1669.
- 3 M. Mikkelsen, M. Jorgensen and F. C. Krebs, *Energy Environ. Sci.*, 2010, **3**, 43–
81.
- 4 D. J. Darensbourg, *Inorg. Chem.*, 2010, **49**, 10765–10780.
- 5 D. J. Darensbourg and A. D. Yeung, *Polym. Chem.*, 2014, **5**, 3949–3962.
- 6 M. I. Childers, J. M. Longo, N. J. Van Zee, A. M. LaPointe and G. W. Coates,
Chem. Rev., 2014, **114**, 8129–8152.
- 7 X.-B. Lu and D. J. Darensbourg, *Chem. Soc. Rev.*, 2012, **41**, 1462–1484.
- 8 M. R. Kember, A. Buchard and C. K. Williams, *Chem. Commun.*, 2011, **47**, 141–
163.
- 9 D. J. Darensbourg, *Chem. Rev.*, 2007, **107**, 2388–2410.
- 10 S. Paul, Y. Zhu, C. Romain, R. Brooks, P. K. Saini and C. K. Williams, *Chem.*
Commun., 2015, **51**, 6459–6479.
- 11 K. Nakano, K. Kobayashi, T. Ohkawara, H. Imoto and K. Nozaki, *J. Am. Chem.*
Soc., 2013, **135**, 8456–8459.
- 12 M. W. Lehenmeier, S. Kissling, P. T. Altenbuchner, C. Bruckmeier,
P. Deglmann, A.-K. Brym and B. Rieger, *Angew. Chem., Int. Ed.*, 2013, **52**,
9821–9826.
- 13 J. K. Varghese, D. S. Park, J. Y. Jeon and B. Y. Lee, *J. Polym. Sci., Part A: Polym.*
Chem., 2013, **51**, 4811–4818.

- 1 14 W. C. Ellis, Y. Jung, M. Mulzer, R. Di Girolamo, E. B. Lobkovsky and
G. W. Coates, *Chem. Sci.*, 2014, 5, 4004–4011.
- 15 G.-P. Wu, D. J. Darensbourg and X.-B. Lu, *J. Am. Chem. Soc.*, 2012, **134**, 17739–
17745.
- 5 16 Y. Liu, W. M. Ren, M. Wang, C. Liu and X. B. Lu, *Angew. Chem., Int. Ed.*, 2015,
54, 2241–2244.
- 17 L. Pena Carrodegua, J. Gonzalez-Fabra, F. Castro-Gomez, C. Bo and
A. W. Kleij, *Chem.–Eur. J.*, 2015, **21**, 6115–6122.
- 18 P. K. Saini, C. Romain and C. K. Williams, *Chem. Commun.*, 2014, **50**, 4164–
4167.
- 19 S. H. Lee, A. Cyriac, J. Y. Jeon and B. Y. Lee, *Polym. Chem.*, 2012, **3**, 1215–1220.
- 20 J. Langanke, A. Wolf, J. Hofmann, K. Bohm, M. A. Subhani, T. E. Muller,
W. Leitner and C. Gurtler, *Green Chem.*, 2014, **16**, 1865–1870.
- 15 21 N. Von der Assen and A. Bardow, *Green Chem.*, 2014, **16**, 3272–3280.
- 22 D. J. Darensbourg, W.-C. Chung, K. Wang and H.-C. Zhou, *ACS Catal.*, 2014, **4**,
1511–1515.
- 23 A. C. Chapman, C. Keyworth, M. R. Kember, A. J. J. Lennox and C. K. Williams,
ACS Catal., 2015, 1581–1588.
- 20 24 M. Winkler, C. Romain, M. A. R. Meier and C. K. Williams, *Green Chem.*, 2015,
17, 300–306.
- 25 C. Romain, A. Thevenon, P. K. Saini and C. K. Williams, in *Topics in
Organometallic Chemistry: Carbon Dioxide and Organometallics*, ed. X. B. Lu,
Springer DE, 2015.
- 25 26 P. K. Saini, C. Romain, Y. Zhu and C. K. Williams, *Polym. Chem.*, 2014, **5**, 6068–
6075.
- 27 M. R. Kember and C. K. Williams, *J. Am. Chem. Soc.*, 2012, **134**, 15676–15679.
- 28 M. R. Kember, J. Copley, A. Buchard and C. K. Williams, *Polym. Chem.*, 2012, **3**,
1196–1201.
- 30 29 A. Buchard, F. Jutz, M. R. Kember, A. J. P. White, H. S. Rzepa and
C. K. Williams, *Macromolecules*, 2012, **45**, 6781–6795.
- 30 F. Jutz, A. Buchard, M. R. Kember, S. B. Fredrickson and C. K. Williams, *J. Am.
Chem. Soc.*, 2011, **133**, 17395–17405.
- 35 31 A. Buchard, M. R. Kember, K. G. Sandeman and C. K. Williams, *Chem.
Commun.*, 2011, **47**, 212–214.
- 32 M. R. Kember, A. J. P. White and C. K. Williams, *Macromolecules*, 2010, **43**,
2291–2298.
- 33 M. R. Kember, A. J. P. White and C. K. Williams, *Inorg. Chem.*, 2009, **48**, 9535–
9542.
- 40 34 M. R. Kember, P. D. Knight, P. T. R. Reung and C. K. Williams, *Angew. Chem.,
Int. Ed.*, 2009, **48**, 931–933.
- 35 M. R. Kember, F. Jutz, A. Buchard, A. J. P. White and C. K. Williams, *Chem. Sci.*,
2012, **3**, 1245–1255.
- 45 36 Y. Liu, W. M. Ren, K. K. He and X. B. Lu, *Nat. Commun.*, 2014, **5**.
- 37 R. K. Dean, L. N. Dawe and C. M. Kozak, *Inorg. Chem.*, 2012, **51**, 9095–9103.
- 38 M. W. Lehenmeier, C. Bruckmeier, S. Klaus, J. E. Dengler, P. Deglmann,
A.-K. Ott and B. Rieger, *Chem. – Eur. J.*, 2011, **17**, 8858–8869.
- 39 K. Nakano, M. Nakamura and K. Nozaki, *Macromolecules*, 2009, **42**, 6972–6980.
- 50 40 D. J. Darensbourg and G.-P. Wu, *Angew. Chem.*, 2013, 10796–10800.

- 1 41 F. Jutz, A. Buchard, M. R. Kember, S. B. Fredriksen and C. K. Williams, *J. Am. Chem. Soc.*, 2011, **133**, 17395–17405.
- 42 Y. Zhu, C. Romain, V. Poirier and C. K. Williams, *Macromolecules*, 2015, **48**, 2407–2416.
- 5 43 E. Hatzakis, E. Archavlis and P. Dais, *J. Am. Oil Chem. Soc.*, 2007, **84**, 615–619.
- 44 A. Spyros, D. S. Argyropoulos and R. H. Marchessault, *Macromolecules*, 1997, **30**, 327–329.
- 45 N. MacDowell, N. Florin, A. Buchard, J. Hallett, A. Galindo, G. Jackson, C. S. Adjiman, C. K. Williams, N. Shah and P. Fennell, *Energy Environ. Sci.*, 2010, **3**, 1645–1669.
- 10 46 IEAGHG, Gaseous emissions from amine based PCC processes and their deep removal, May, 2012.
- 47 I. Hauser, A. Einbu, H. F. Stevendsen and K. Ostgaard, *J. Exp. Clin. Med.*, 2014, **1**, 1–5.
- 15 48 Y. Yoshida and S. Inoue, *J. Chem. Soc., Perkin Trans. 1*, 1979, 3146–3150.
- 49 Y. Yoshida and S. Inoue, *Chem. Lett.*, 1978, **7**, 139–140.
- 50 D. Chaturvedi, *Tetrahedron*, 2012, **68**, 15–45.
- 20
- 25
- 30
- 35
- 40
- 45
- 50

PAPER

An enriched electroactive homoacetogenic biocathode improves the microbial electrosynthesis of acetate through carbon dioxide reduction

Gunda Mohanakrishna, Jai Sankar Seelam, Karolien Vanbroekhoven and Deepak Pant*

Received 27th April 2015, Accepted 29th June 2015

DOI: 10.1039/c5fd00041f

In the direction of generating value added chemicals from CO₂ reduction through microbial electrosynthesis, considering the crucial impact of the electrode material for the biofilm development and electron delivery, an attempt was made in this study to evaluate the efficiency of two different materials as biocathodes and their respective output in terms of electrosynthesis. The electrode material is a key component in the MES (microbial electrosynthesis) process. Several electrodes such as platinum, graphite foil, dimensionally stable anode (DSA) and graphite rod, and VITO-CoRE™ electrodes were tested for their suitability for ideal electrode combination in a three electrode cell setup. Bicarbonates (the dissolved form of carbon dioxide) was reduced to acetate by a selectively developed biocathode under a mild applied cathodic potential of -400 mV (vs. SHE) in 500 mL of single chamber MES cells operating for more than four months. Among the two electrode combinations evaluated, VITO-CoRE-PL (VC-IS, plastic inert support) as the cathode and VITO-CoRE-SS (VC-SS, stainless steel metal support) as the counter electrode showed higher production efficiencies (4127 mg L⁻¹) with a volumetric production rate of 0.569 kg per m³ per d than the graphite rod (1523 mg L⁻¹) with a volumetric production rate of 0.206 kg per m³ per d. Contrary to the production efficiencies, the coulombic efficiency was higher with the second electrode combination (40.43%) than the first electrode combination (29.91%). Carbon conversion efficiency to acetate was higher for VC-IS (90.6%) than the graphite rod (82.0%).

1. Introduction

Carbon dioxide (CO₂) reduction for the generation of renewable energy and value added chemicals is one of the emerging areas of present research developments. Microbial electrosynthesis (MES) is one of the recent applications of bio-electrochemical systems (BES), that involves cathodic reduction reactions to

Separation & Conversion Technologies, VITO – Flemish Institute for Technological Research, Boeretang 200, 2400 Mol, Belgium. E-mail: deepak.pant@vito.be; pantonline@gmail.com

1 generate biofuels and speciality chemicals.¹⁻⁵ The bacteria that metabolizes on
the conductive electrode surface acts as the catalyst for the chemical conversions
in BES and are known as electroactive biocatalysts. Other forms of BES are
5 microbial fuel cells (MFCs) and microbial desalination cells (MDC) where the
biocatalyst functions on the anode⁶⁻⁹ and in microbial electrolysis cells (MEC),
where the biocatalyst functions on the cathode.¹⁰⁻¹² On the whole, the BES
processes are considered as a biotechnology with electrodes in which solid state
electrodes can provide a stable and sustainable solution.¹³ The anode serves as a
10 terminal electron acceptor for the discharge of excess/surplus microbial reducing
equivalents and the cathode provides reducing equivalents required for
biochemical processes. The applied electrode potential tunes the strength of the
electron acceptor or donor. It results in an electric current which determines the
biocatalytic performance of electroactive biofilms.¹⁴⁻¹⁸

15 CO₂ plays a key role in the eventual climate change due to its accumulation in
the atmosphere. The control of CO₂ emissions into the atmosphere requires novel
ideas that can assure future generations with sustainable growth options.
Considerable research is being carried out to convert CO₂ to various commercial
20 products by thermochemical and electrochemical technologies, which need high
energy input and but also generate a wide variety of products.¹⁹ MES is a novel
biocathode-driven production technology for the reduction of CO₂ to chemicals
and biofuels. It is characterised as a promising way for sustainable development
and new carbon-consuming technologies.^{3,20} The specificity of the product
25 formation from CO₂ is largely influenced by the bacteria and its metabolic
functions and electrical potential that drives the process.^{2,12} Acetate is the basic
intermediary product compound that is formed by the photosynthesis process
from CO₂ conversion and is the most important step to generate available carbon
forms for biological domains. Furthermore, acetate can be used as the substrate
30 for the various biological building blocks of life. Homoacetogenic bacteria are a
specialized group of bacteria that are able to produce acetate from two molecules
of carbon dioxide (CO₂) through the Wood-Ljungdahl pathway (WLP).^{21,22} Ace-
togens are facultative autotrophs that can grow by the consumption of hydrogen
(H₂) or carbon monoxide (CO) which is usually coupled to the reduction of CO₂.
35 Also, a large variety of organic substrates, including hexoses, pentoses, alcohols,
methyl groups and formic acid can be used as the substrates.^{21,23} On the whole,
acetogens are present in 23 different bacterial genera. Most acetogens are found
in phylum Firmicutes, which are Gram-positive bacteria with low GC content. The
genera *Clostridium* contains acetogenic as well as non-acetogenic species, whereas
40 other genera such as *Acetobacterium* or *Sporomusa* contain only acetogens. Most
known acetogens belong to the *Clostridium* and *Acetobacterium* genera.^{21,22} Among
the large number of acetogens, three organisms have been studied quite exten-
sively (*Moorella thermoacetica*, *Acetobacterium woodii* and *Clostridium ljungdahlii*).
These bacteria were primarily studied for biocathode driven CO₂ fixation. Another
45 advantage of acetogens for use in the MES process is their metabolic flexibility.
Acetogens are ubiquitously distributed in alkaline, high-salt and hot environ-
ments, in deep subsurface samples, the termite hindgut and in human intestines.
They are also found in terrestrial soil, in freshwater and marine sediments.²² This
metabolic flexibility can be an advantage for their application in MES which is a
50 hybrid system with biological electrochemical functions.

1 Proof of concept studies of the MES process reported by Nevin *et al.*,^{17,24}
showed the production of acetate, butyrate, oxy-buterate and formate by the
bioelectrochemical production by *Sporomusa ovata*, *Clostridium ljungdahlii*,
5 *Clostridium acetivum*, and *Moorella thermoacetica* at an applied potential of -400
mV (SHE). Later Nie *et al.*,²⁵ achieved higher acetate production rates by *Sporomusa ovata*. Besides pure cultures, few researchers were able to produce acetate
with mixed and adapted mixed cultures at various applied potentials ranging
10 from the -400 mV to -950 mV.^{18,20,26–29} Due to several obvious advantages of the
process such as low energy input and CO₂ fixation, it is gaining much global
attention. Along with whole cell biocatalysts, the use of specific enzymes in bio-
electrocatalysis for CO₂ sequestration is also finding possible application for
sustainable energy and chemicals generation.^{3,30}

15 In the present study, an attempt was made to generate a sustainable homo-
acetogenic biocathode that reduces CO₂ to acetate under mild applied potential
conditions where the hydrogen production can be completely limited. A detailed
evaluation was also performed for the selection of electrode combination for the
potential window analysis where no hydrogen can be produced and to avoid
20 interference of the fermentation process. Furthermore, a detailed discussion is
made on the benchmarking microbial electrosynthesis process with respect to the
type of bacterial catalyst, energy efficiency and production rate.

2. Experimental

2.1 Homoacetogenic electroactive bacteria

25 Homoacetogenic bacteria that have specific metabolic competence to produce
acetate from the inorganic carbon source (CO₂) were enriched from granular
activated sludge. The granular activated sludge was collected from an anaerobic
digester that treats effluents of the potato processing industry (Cargill Sas van,
30 Ghent). It contains 6% of total solid (TS) and 75% of volatile solid (VS) content
along with <1% of inorganic carbon. A four stage selective enrichment method-
ology was applied to enrich the electroactive homoacetogenic bacteria for bio-
cathode development. During the first stage the sludge collected from anaerobic
35 digester was subjected to heat treatment (90 °C for 1 hour) to eliminate the
methanogenic bacteria and to retain the acetogenic bacterial spores.³¹ In the
second stage, the heat treated sludge was subjected to heterotrophic growth using
glucose as a substrate in nutrient broth medium at pH 6.0 under 35 °C to activate
40 the metabolism of whole consortia. Heterotrophically grown active cultures of
acetogenic bacteria were shifted to autotrophic conditions by providing a mixture
of CO₂ and H₂ as a substrate, where only homoacetogenic bacteria were grown
and they were enriched by repeated culturing on a CO₂ and H₂ mixture for four
cycles. The homoacetogenic activity was confirmed through the acetate produc-
45 tion and inhibition of methane. The resultant consortia was used as inoculum for
electroactive biofilm formation.

2.2 Bioelectrochemical systems

50 **2.2.1 Design.** A MES reactor was designed with a three electrode setup (single
chamber) and fabricated with a glass bottle (total/working, 0.62/0.5 L) which
included suitable ports for the provision of electrodes and N₂ gas flushing, and

1 was used in the present study (Fig. 1). Initially, 6 different materials were screened
to use as the anode/counter electrode to select the most suitable one. As the BES is
5 single chambered, if the counter electrode evolves oxygen, the biofilm on the
working electrode cannot sustain its anaerobic properties to carry out the
reduction reaction. Henceforth, different electrode materials, *viz.*, platinum,
dimensionally stable anode (DSA made of titanium coated with iridium mixed
metal oxide, Magneto BV Netherlands), graphite foil, graphite rod, VITO-CoRE™
10 with stainless steel (VC-SS) and VITO-CoRE™ with inert plastic support (VC-IS)
were chosen against a VC-SS counter electrode in both abiotic and biotic
(enriched bacteria in suspension) conditions under -400 mV of applied cathodic
potential.

The performance of the electrodes was evaluated in terms of voltage reached
and whether the electrode showed a lower potential than water electrolysis (1.23
15 *vs.* SHE). Two MES reactors (MES1 and MES2) of similar configuration, having a
VC-SS electrode³⁴ as the anode (selected from the screening experiment), were
used in the current experiment. Two different cathode materials, *viz.*, VC-IS in

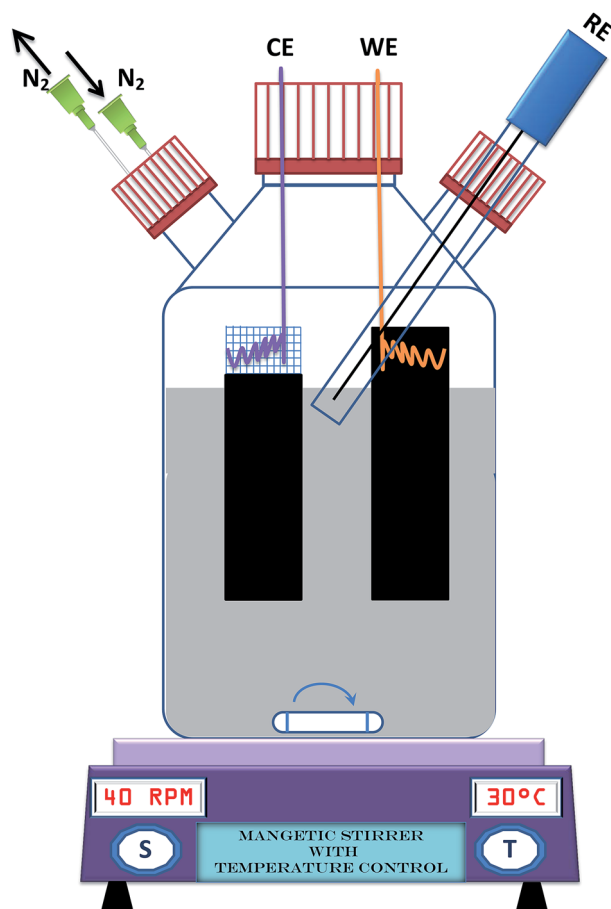


Fig. 1 Schematic diagram of the single chamber microbial electrosynthesis cell (CE, counter electrode; WE, working electrode and RE, reference electrode).

MES1 and a graphite rod in MES2, were evaluated for their efficiency of biofilm growth as well as electron uptake for the acetate synthesis. The total surface area (37.5 cm²) and the active surface area (the area in contact with the electrolyte, 30 cm²) of all the electrodes (anodes and cathodes) was kept constant, except for the DSA (6 × 2.5 cm) and platinum (surface area, 2.37 cm²) due to the unavailability of sizes. A fine stainless steel wire, weaved through the electrode and extended through the airtight passage of the reactor cap, was used as a current collector (Fig. 1). No separate current collector was used in case of platinum wire.

2.2.2 Operation. Both MES reactors were operated in batch mode at 30 °C in a temperature controlled oil bath. MES1 was operated for 127 days, while the MES2 was operated for only 47 days due to loosing biofilm on the cathode and instability of the output. The phosphate buffer media which was used during the enrichment of homoacetogenic bacteria was also used as media in MES operation. Phosphate buffer media containing NH₄Cl of 200 mg L⁻¹, MgCl₂·6H₂O of 200 mg L⁻¹, yeast extract of 10 mg L⁻¹ along with the trace elements solution (per litre, nitrilotriacetic acid, 1.5 g; MgSO₄·7H₂O, 3.0 g; MnSO₄·H₂O, 0.5 g; NaCl, 1.0 g; FeSO₄·7H₂O, 0.1 g; CoSO₄·7H₂O, 0.18 g; CaCl₂·2H₂O, 0.1 g; ZnSO₄·7H₂O, 0.18 g; CuSO₄·5H₂O, 0.01 g; KAl(SO₄)₂·12H₂O, 0.02 g; H₃BO₃, 0.01 g; Na₂MoO₄·2H₂O, 0.01 g; NiCl₂·6H₂O, 0.03 g; Na₂SeO₃·5H₂O, 0.30 mg) and vitamin solution (per litre, biotin, 2 mg; pantothenic acid, 5 mg; B-12, 0.1 mg; *p*-aminobenzoic acid, 0.5 mg; thioctic acid (alpha lipoic), 5 mg; nicotinic acid, 5 mg; thiamine, 5 mg; riboflavin, 5 mg; pyridoxine HCl, 10 mg; folic acid, 2 mg). Sodium bicarbonate was considered as the substrate for BES at a rate of 3.44 g L⁻¹ which is equivalent to 2.5 g L⁻¹ of bicarbonate (HCO₃⁻). Bromoethanesulfonic acid (BESA) was also added to the medium at a rate of 0.5 g L⁻¹ to inhibit the possible methanogenic activity.^{31–33} The final pH of the media was maintained at 7.0. During the start-up of the reactor, 10% of the enriched inoculum (50 mL) was added to the MES along with 450 mL of media. Both, MES1 and MES2 were continuously poised at -600 mV vs. Ag/AgCl (-400 mV vs. SHE) through a chronoamperometry (CA) technique using a potentiostat (BioLogic-VMP3 model, France). All the assays were performed *in situ* by considering the cathode as the working electrode and the anode as the counter electrode against an Ag/AgCl (3.0 M KCl) reference electrode. All the potentials mentioned further in the manuscript are vs. SHE unless otherwise stated.

Consumption of bicarbonates in the electrolyte (less than 0.5 g HCO₃⁻ per L) was considered as time for feed change. To avoid sudden changes in the electrolyte concentration, only 60% of feed was replaced with fresh feed using a siphon flow method. In the case of MES1, after start-up, the feed was changed on the 21st, 28th, 35th, 43rd, 50th, 60th, and 70th day of operation. Later, a constant time interval of 7 days was maintained until the 126th day of operation. In the case of MES2, feed replacement was done during the 21st, 28th, 34th, 40th and 47th day of operation. Both the reactors were continuously flushed with N₂ gas to maintain the anaerobic environment.

2.3 Analysis

Liquid samples from MES1 and MES2 were collected on every fourth day. During enrichment of the homoacetogenic bacteria, along with liquid samples, gaseous samples were also collected. The liquid samples were analysed for organic acids

(formic acid, acetic acid, propionic acid and butyric acid), ethanol and pH, whereas the gaseous samples were analysed for H₂, CO₂, CH₄ and O₂. Prior to analysis through HPLC, the samples were filtered through 0.45 μm Acrodisc syringe filters. HPLC analyses was performed using an Agilent HPLC 1200 series equipped with a RID detector (Agilent 1260) set at a wavelength of 215 nm. The column used was an Agilent Hi-Plex column 8u (3000 mm × 7.7 mm) operated at 60 °C equipped with a guard column of the same material. Phosphoric acid (0.05% in isocratic gradient) was used as the eluent at a flow rate of 1 mL min⁻¹. The injection volume of the samples and standards was 20 μL. EZchrom software provided by Agilent was used for HPLC data analysis.

Gaseous samples from the enrichment cultures and MES reactors were analysed using a Trace GC Ultra (Thermo Scientific) connected with 2 different thermal conductivity detectors. A carbosphere column (2m-1/800SS) was used for hydrogen, whereas for carbon dioxide and methane, both a Hayesep N column (1m-1/800SS) and a Molsive column A (1m-1/800SS) were used at a constant temperature of 60 °C. pH was analysed with a calibrated pH meter (WTW Multi 340i). The liquid samples from MES1 and MES2 reactors were also analyzed for bicarbonates through a TOC analyzer (Multi N/C 3100 of Analytik Jena) with an auto-sampler (APG 49 of Analytik Jena) according to the methodology developed in ISO 8245.

3. Results and discussion

3.1 Screening of electrodes for the anode

Microbial electrosynthesis is a process that proceeds with the reduction of protons and electrons that are generated from the counter electrode or anode of the cell. As the present study was carried out in single chambered configuration, it was important to avoid the abiotic water electrolysis reaction. By maintaining cells with mild electrochemical activity, oxygen and hydrogen production can be controlled. These conditions help to maintain the anaerobic system which is a prerequisite for biocatalyst activity. However, the net counter electrode (anode) potential sustained in the cell also influences the cathode potential. Theoretically, efficient electrolysis process can continue at a potential of 1.23 V (*vs.* SHE).^{35,36} However, it is also found to be influenced by the type of electrode material and the surface area considered for the electrode. Maintaining lower potentials on MES systems also warrants direct electron transfer rather than H₂ mediated electron transfer for acetate production.

To identify an efficient and suitable anode for MES, six different materials were screened under similar conditions of MES operation under both biotic and abiotic conditions (Fig. 2). Among the six different electrodes used as the counter electrode, at -400 mV of working electrode potential, three electrodes *viz.*, platinum, DSA and graphite rod, reached a potential higher than 1.23 V (*vs.* SHE), indicating the possibility of oxygen evolution. Platinum showed the highest net counter electrode potential of 5.05 V under abiotic conditions and 5.01 V under biotic conditions followed by DSA (abiotic, 2.01 V; biotic 1.87 V) and graphite rod (abiotic, 1.57 V; biotic 1.46 V). Even though graphite foil showed a lower potential of 0.78 V under abiotic conditions, a small rate of oxygen evolution was observed by the gas analysis from the reactor head space. In the case of biotic conditions, 0.51 V of counter electrode potential was observed with no visible oxygen

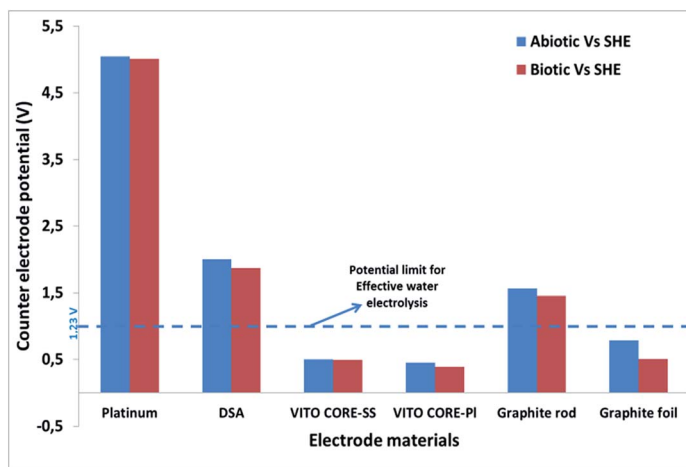


Fig. 2 Counter electrode potentials observed with various electrode materials against a VITO-CoRE electrode as the working electrode at an applied potential of -600 mV. (Surface area of all the electrodes (except platinum) was equal. It is considered as 39 cm² and effective/reactive surface area is 30 cm²). In the case of platinum, as the economic and practical applicability of the platinum is expensive, a wire surface area consisting of 2.37 cm² (effective/reactive surface area) was used.

evolution. The two types of VITO-CoRE™ electrodes (VC-SS and VC-IS) evidenced mild counter electrode potential (VC-SS, abiotic, 0.50 V and biotic 0.49 V; VC-IS, abiotic, 0.45 V and biotic 0.39 V) and no oxygen evolution was observed under both abiotic and biotic conditions. The mild electrochemical activity and similar performance under both biotic and abiotic conditions was indicated to select the VC-SS as the suitable counter electrode (anode) for further experimentation in MES towards acetate production.

3.2 Bioelectrosynthesis of acetate

Once the screening was done, two MES reactors were started up with the selected VC-SS as the anode and VC-IS and a graphite rod as the cathodes (working electrodes). During the start-up stage (first phase, 50 days) of MES1, electroactive biofilm formation from the enriched homoacetogenic bacteria and subsequent stabilization of biofilm was observed at -400 mV with bicarbonate as the carbon source and electron acceptor for the production of acetate. As the inoculum was enriched with CO₂ and H₂ for acetate production, initially MES1 showed an acetate concentration of 101.42 mg L⁻¹ which later decreased to 67.12 mg L⁻¹ on the 5th day with negligible current generation (Fig. 3). From the 8th day of operation, reduction of bicarbonate was confirmed with a reduction current as well as metabolite analysis in the electrolyte. By the end of the 20th day, the acetate concentration reached 755.67 mg L⁻¹ (Fig. 3a) with a reduction current density of -104 mA m⁻² (Fig. 3b). During the second batch the acetate production was also found to increase gradually and reached a concentration of 1231.43 mg acetate per L (30th day) with a reduction current density of -133 mA m⁻². In the first phase, a similar improvement in acetate production was observed with every feeding event and registered a maximum at the 35th day (4th cycle, 1972.86 mg

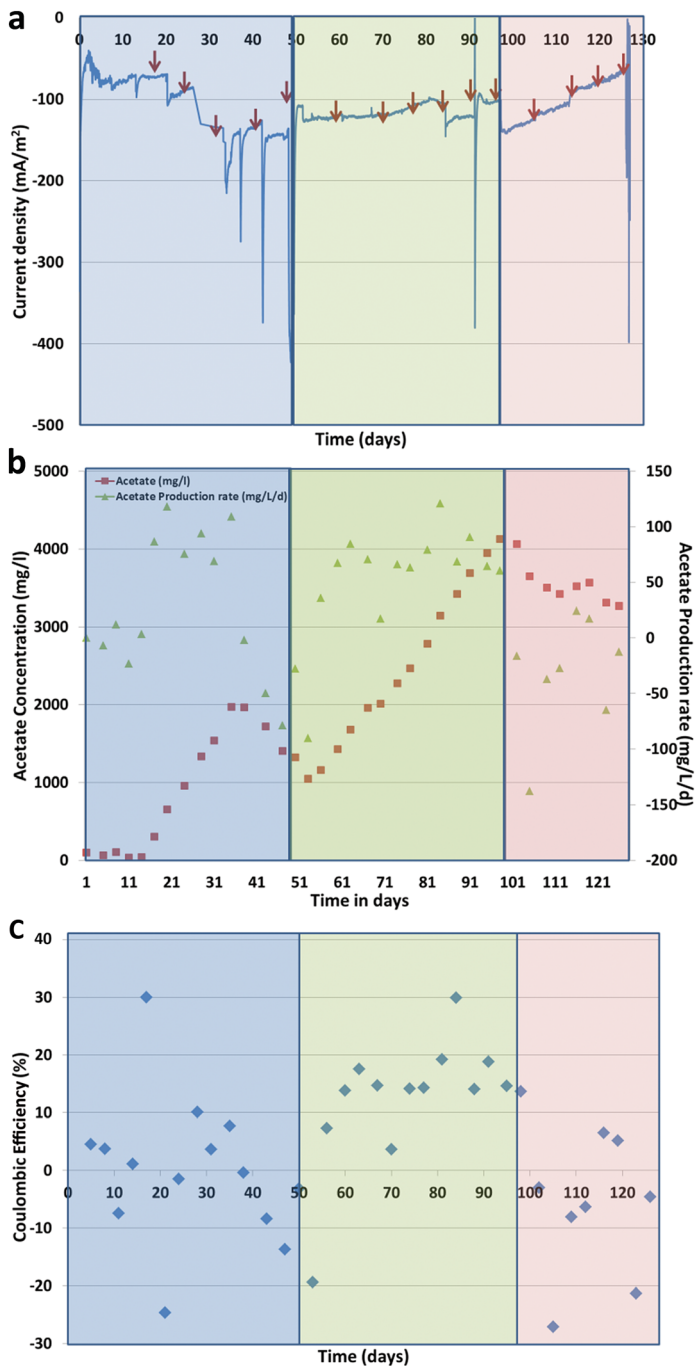


Fig. 3 The performance of the MES1 reactor during 127 days in batch mode operation with several feeding events (arrow mark depicts the feeding event). (a) Reduction current pattern during chronoamperometry (CA) used for the bicarbonate to acetate production; (b) acetate concentration and acetate production rate pattern during the 127 days of operation; (c) coulombic efficiency during the total operation time.

1 L^{-1} ; -165 mA m^{-2}). Furthermore, this phase continued for another two batch
cycles (until 50 days) to identify the optimum retention time for the 60% of feed
5 replacement. During this period, acetate production was found to fluctuate
between $1959.36 \text{ mg L}^{-1}$ (38th day, -146 mA m^{-2}) and $1320.02 \text{ mg L}^{-1}$ (50th day,
6 -128 mA m^{-2}). After continuing for another two batch cycling events, it was
identified that seven days was the optimum retention time for one batch of 60%
feeding, and the same retention time was respected to the end. From the 51st day
10 to the 98th day of operation MES1 exhibited a stable performance where the
acetate production gradually increased from $1320.02 \text{ mg L}^{-1}$ to a maximum
concentration of $4127.01 \text{ mg L}^{-1}$ (98th day, -142 mA m^{-2}) with an average
reduction current density of -117 mA m^{-2} . Later both the acetate concentration
15 and reduction current density was found to decrease until the 127th day of
operation and this period can be considered as the destabilization phase. Even
after four feeding events, a decrease in acetate concentration was observed rather
than an improvement. By the 126th day of operation, acetate concentration was
found to have decreased to $3270.26 \text{ mg L}^{-1}$. Similarly, the reduction current
20 density was also found to decrease (126th day -67 mA m^{-2}).

The acetate production rate, the amount of acetate produced during a day (mg
25 per L per d), was analysed to identify the specific bicarbonate reduction rate to
acetate. Acetate production rates were also correlated for the start-up phase,
during stable operation and the destabilization phase. During the start-up phase
the average acetate production rate was found to be $28.16 \text{ mg per L per d}$, which
later increased to $59.94 \text{ mg per L per d}$ (Fig. 3b). During the destabilization phase,
30 the average acetate production rate registered a negative value (-33.61 mg per L
per d). The observed negative rate is due to possible acetate oxidation at the anode
of the single chamber design. To support this phenomenon, a visible biofilm was
observed on the anode electrode after 90 days of operation. When the oxidation of
bio-electrochemically produced acetate at the cathode is considered, the actual
35 production rates of the start-up and stabilization phases can be higher than
visualized. As the media included was with the 0.5 g L^{-1} concentration of BESA,
the conversion of acetate to methane is completely inhibited.³¹ Along with acetate,
a negligible concentration of ethanol was also observed during the start-up phase
(10.05 mg L^{-1} , 35th day) and the final phase (8.62 mg L^{-1} , 112th day). This could be
40 due to further bioelectrochemical reduction of acetate to ethanol. Besides ethanol
production, the consumed acetate can be attributed to the biomass production of
electroactive biofilm.¹² pH is also an important factor that influences the activity
of the electroactive biofilm. Homoacetogenic bacteria favours mild acidic to
neutral pHs. The initial pH of the present MES1 was maintained at pH 7.0. It was
45 found to increase to alkaline pH with the time of operation. During the stable
phase of operation, the catholyte pH was registered between 7.8 and 8.4, whereas
in the destabilization phase, it was found to be between 8.6 and 9.3. A high
alkaline pH, that is unfavourable for homoacetogenic bacteria prevailing in the
cathodic chamber, is also one of the reasons for biofilm loss.

In the case of MES2, initially, a negligible reduction current was registered for
10 days (Fig. 4a). The acetate transferred along with the enriched inoculum
culture was (103.32 mg L^{-1}) observed degrading from day 5 (84.22 mg L^{-1}) and it
reached a minimum concentration on the 11th day (33 mg L^{-1}) (Fig. 4b). Later, an
50 increasing trend of acetate production associated with the reduction current was
observed. This depicts the electroactive biofilm formation and concomitant

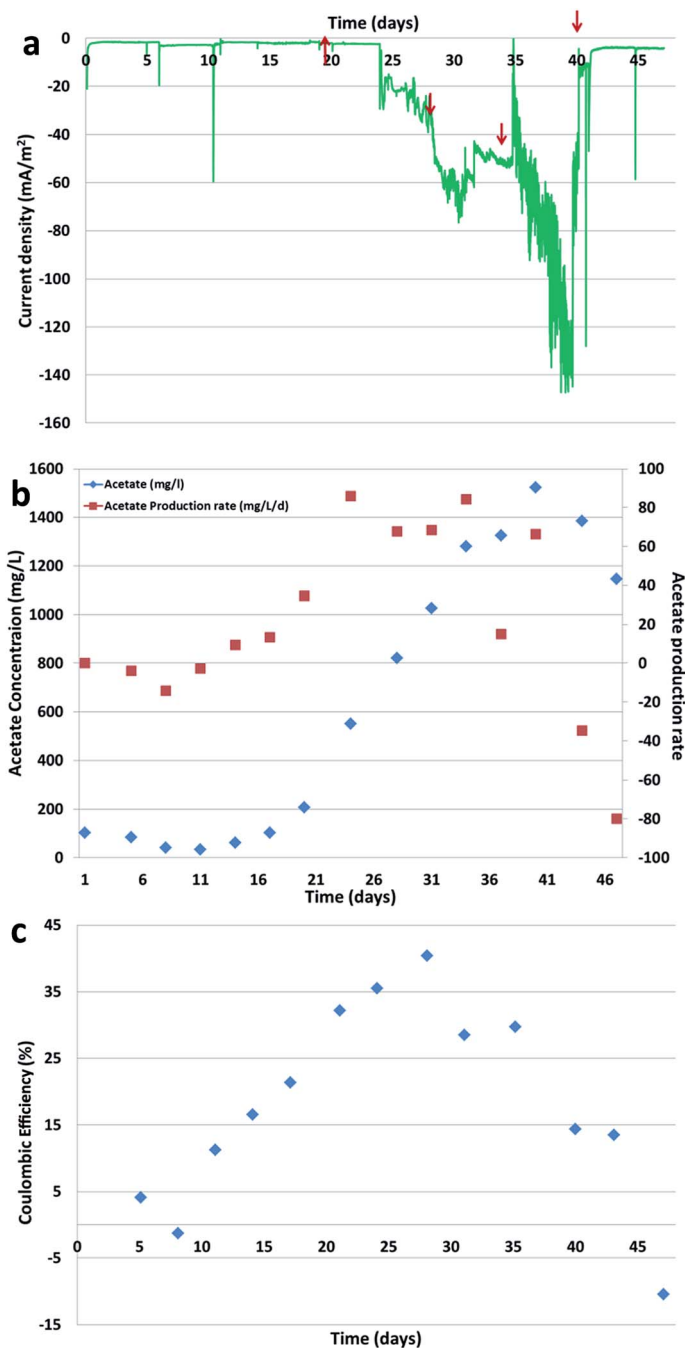


Fig. 4 The performance of MES2 reactor during 47 days in batch mode operation with several feeding events (arrow mark depicts the feeding event). (a) Reduction current pattern during chronoamperometry (CA) used for the bicarbonate to acetate production; (b) acetate concentration and acetate production rate pattern during 127 days of operation; (c) coulombic efficiency during the total operation time.

1 conversion of bicarbonate to acetate. By the end of the first feeding cycle, the
acetate production reached 206.49 mg L^{-1} with an average production rate of 5.15
5 mg per L per d . It gradually increased with every feeding event and reached 821.25
 mg L^{-1} ($75.62 \text{ mg per L per d}$) and $1279.42 \text{ mg L}^{-1}$ ($76.33 \text{ mg per L per d}$)
respectively by the end of the second and third feeding cycles. The maximum
concentration of acetate was observed on the 40th day (4th cycle, 1523.2 mg L^{-1} ;
10 $40.67 \text{ mg per L per d}$) with a current density of -53 mA m^{-2} . Among the 47 days of
operation, the reduction current density was significantly increased from the 23rd
day of operation and registered a maximum on the 39th day (-147 mA m^{-2}).

10 During this operation, no ethanol production was observed. Later, visible
detachment of biofilm was observed. It is also correlated well with the drop in
reduction current and acetate concentration in the system. At the end of this
15 cycle, the acetate concentration was decreased to $1145.25 \text{ mg L}^{-1}$ with an acetate
production rate of $-54.20 \text{ mg per L per d}$. Even after biofilm loss, the system
continued operation with regular feeding cycles for 5 consecutive cycles but no
further acetate production and no reduction current were observed confirming
20 there was no biofilm formation. As MES2 was operated for a lesser period than
MES1 and the loss of biofilm occurred immediately after reaching the maximum
acetate production and reduction current, no specific phases such as stable and
final phases were observed. Similar to MES1, the catholyte pH of MES1 was also
found to increase to alkaline conditions. By the 30th day of operation (3rd
25 cycle), the pH had increased to 7.8 and later it was found to increase at a rapid rate
and reached 8.7 by the 44th day of operation (5th cycle).

3.3 Coulombic efficiency

30 In microbial electrosynthesis, coulombic efficiency (CE%) is a relative expression
that signifies the ratio between the total charge (coulombs) consumed in the
reduction process and the actual charge contributed in the formation/production
of desired product. It can be calculated with the formula $\text{CE} (\%) = C_p/C_T$, where,
35 C_p is the product of b (number of electrons consumed for the product, for acetate
production it is 8), n (number of moles of product) and F (Faraday's constant,
 $96\,485 \text{ C mol}^{-1}$). C_T is the total coulombs consumed that can be derived from
integrating charge with the time.²⁰ Since ethanol was detected in negligible
40 concentrations and the electron demand for acetate to ethanol conversion is
lower ($4e^-$) than acetate, considering it for CE calculations do not show a
significant difference on total CE. In the case of MES1, during the stable phase of
operation, a maximum CE was registered as 29.91% and a minimum as 3.65%
with an average value of 23.52%. Whereas during the start-up phase and the
45 destabilization phase, the maximum CE was registered as 18.38% and 6.54%
respectively. Biofilm formation phase demands a high amount of energy for
biomass formation and related metabolic activities. In the start-up phase, the
electrons accepted by the cathode might be involved more in metabolic functions
to establish the biofilm on the cathode surface. The acetate was also produced as a
50 participate in the production of various molecules which also decreases the
observed acetate production in the electrolyte. So, the resultant CE is recorded
lower. A well-established electroactive biofilm requires less energy for the meta-
bolic functions that reflected in the higher CE than the start-up phase. The lowest
CE values recorded in the destabilization phase might be attributed to two events.

1 Firstly, in the destabilization phase, the biofilm observed on the anode electrode
 is involved in the oxidation of acetate produced due to a cathodic reduction
 reaction. Secondly, due to the unfavourable conditions that prevail in the system,
 the cathode electrode cannot efficiently participate in acetate production. In the
 5 case of MES2, CE increased gradually with the time of operation and reached a
 maximum of 40.42% on the 28th day (second cycle). Later a gradual drop was
 observed. During the second and third cycles of operations, it was limited to
 29.11% and 13.93% respectively. As the biofilm had detached and no acetate
 production was observed in the fifth cycle of operation, a negative value of CE was
 10 registered –10.43% (47th day). On the whole, MES2 registered an average CE value
 of 17.71%. The CE was found to be higher for the MES2 with a graphite rod as the
 cathode compared to MES1 with VC-IS. However, the formed biofilm was not
 sustained for long term operation.

15 3.4 Carbon conversion efficiency

Carbon conversion efficiency is considered as one of the crucial parameters that
 shows effective conversion of substrate to product. The efficiency of the bio-
 electrochemical reduction of bicarbonates (electron acceptors) to acetate can be
 20 found by calculating the ratio between the carbon equivalents present in the
 initial concentration of the substrate and final product in each operating cycle
 (Table 1). It should be noted that the carbon conversion efficiency calculation is
 considered not only of those products observed in the electrolyte but also in the
 biomass produced for the biofilm and suspension. In the case MES1, during the
 25 first cycle operation, it was registered as 47.08%. Gradually a steady increase in
 carbon conversion efficiency was observed with every feeding event and a
 maximum of 90.10% was registered on the 35th day (start-up phase). During the
 stable phase of operation it was registered as 90.61% on the 84th day and with an

30 **Table 1** The consolidated representation of calculated parameters from the basic results
 obtained in the present study

Parameter	Units	MES1			MES2
		Start-up	Stable phase	Final phase ^c	
Maximum acetate concentration	mg L ⁻¹	1972.86	4127.01	3568.41	1523.20
Production rate (maximum/average)	mg per L per d	117.96/ 26.97	120.90/ 56.94	24.37/—	85.96/ 20.68
Maximum current density	mA m ⁻²	–165	–142	–67	–147
Coulombic efficiency (CE)	%	29.97	29.91	6.54	40.43
Carbon conversion efficiency ^b	%	90.10	90.61	19.90	81.97
Volumetric production rate ^a	kg per m ³ per d	0.269	0.569	—	0.206
Surface based production rate	g per m ² per d	4.497	9.490	—	3.447

35 ^a Calculated from the average performance during each phase. ^b Calculated based on the
 feeding event. ^c The values of average production rate, volumetric production rate and
 50 surface based production rates were negative. So the respective values are not presented
 in the table.

1 average value of 62.38%. Due to the destabilization in the final phase, the carbon
conversion efficiency was registered very low (19.90%). The trend observed for
carbon conversion efficiency is found to be similar to CE. The carbon converted to
5 acetate is involved in the biomass production. If we consider the participation of
carbon in biomass production, the carbon conversion efficiency may be higher
than others reported. In the case of MES2, a different pattern of carbon conversion
efficiency is observed. In the first cycle only 8.25% of carbon was converted to
acetate. Then a sharp increase in carbon conversion to acetate was observed in the
10 second cycle and registered as 81.97%. It is the maximum efficiency for MES2.
During the third and fourth feeding cycles, the efficiency is limited to 61.09% and
32.50% respectively. Later due to destabilization, no significant efficiency of
carbon was converted to acetate. Compared to MES2, MES1 showed a higher
15 bioelectrocatalytic conversion of carbon to acetate and the conversion process was
sustained for a longer period of time. On the whole, the registered average values
in the stable phase of MES1 are encouraging for the early stage research on the
bio-electrochemical reduction process of CO₂ to organic molecule production
(Table 1). The difference between MES1 and MES2 is in the electrode material
20 used for the cathode (VITO CORE-PL in MES1 and a graphite rod in MES2). The
better performance of MES1 could be attributed to the high BET surface area of
the VITO CORE compared to graphite.³⁴ This also led to better biofilm growth in
MES1 which could be operated for 127 days while MES2 saw a loss of biofilm after
44 days and had to be stopped.

25 3.5 Discussion

The present study was performed with a single chambered system under mild
operation conditions at 30 °C with a continuous applied potential of -400 mV.
The thermodynamic potential required for the conversion of HCO₃⁻ to acetate is
30 found to be -280 mV (SHE)² and the present study used a still higher potential
than the thermodynamic requirement. The potential losses related to the electrode
and microbial interactions; microbial electron transfer and electrolyte
conductivity determined the required potential for the microbial electrosynthesis.
35 The design of the present study was based on characteristics that would help with
the understanding of acetogenic biocathode production at a lower cathode
potential and maintaining the biofilm for long term use in a single chamber
which also helps for the upscaling aspects of the MES process. Compared to
additional supplementation of H₂ in the reactor, direct feeding of electrons to
40 acetogens through electrodes is likely to be practically more feasible. The lower
energy input and renewable bacterial biocatalyst employment are advantageous
aspects. The standard cathodic potential for bicarbonate/acetate redox couple is
-280 mV². A biofilm of *S. ovata* that was grown on H₂, when introduced into a
cathodic chamber containing bicarbonate-based medium with no organic
45 compounds except a vitamin mixture, resulted in acetate production by directly
reducing the bicarbonate. Under an applied potential of -400 mV (*vs.* SHE) and in
the presence of a well-developed *S. ovata* biofilm, carbon dioxide or bicarbonate
acted as the sole electron acceptor and was reduced to acetate.^{17,24} Along with
acetate, 2-oxobutyrate was also produced in smaller concentrations. Current
50 consumption by *S. ovata* was found to be constant and correlated well with acetate
production with a coulombic efficiency of more than 86%. Production of both

1 compounds was stopped when current supply was stopped. Furthermore, various
acetogenic microorganisms such as *Sporomusa silvacetica*, *Sporomusa sphaeroides*,
5 *Clostridium ljungdahlii*, *Clostridium aceticum* and *Moorella thermoacetica* as pure
cultures showed their more than 88% efficiency in converting CO₂ to acetate.²⁴
Under the same applied potential of 0.4 V and with *S. ovata* as the biocatalyst, Nie
10 *et al.*, could achieve a higher acetate production rate of 1.13 mM per d.²⁵ In the
present study, MES1 showed 2.04 mM per d of maximum production rate
(average, 0.97 mM per d) during the stable operating phase.

The efficiency of the total carbon equivalents supplied to total carbon resulted
15 in the product and can be called carbon conversion efficiency. MES1 exhibited a
maximum carbon conversion efficiency of 90.61% in the stable phase followed by
the start-up phase. In the final phase, it was limited to 19.90%, which might be
due to the biofilm degeneration phase. In the case of MES2, 81.97% of carbon
conversion efficiency was registered. Carbon conversion efficiency determines the
20 carbon footprint of the system and practical applicability of the MES process on
upscaling. The use of bicarbonates, instead of CO₂ is the major advantage to
achieve higher conversion efficiencies. For direct CO₂ application, it is important
to choose a system that solubilizes the CO₂ at a higher rate or developing an
electrolyte that favours both CO₂ solubility and biocathodic functions. Various
25 reactor designs such as a continuous stirred tank reactor, hollow fiber membrane
reactor, bubble column, and airlift reactors used for the syngas fermentation can
be applied in MES design.^{37–40} As the biocatalyst of MES is electrode dwelling and
the bioelectrochemical conversion of CO₂ to acetate occurs in the electrode
vicinity designing hybrid reactors with BES and a conventional reactor design can
30 fetch these advantages, that in turn improves the bioelectrocatalytic reduction of
CO₂ to products. Biological components such as using CO₂ solubilizing enzymes
also could be considered for a higher carbon conversion efficiency. A carbonic
anhydrase enzyme system to solubilize the CO₂ and further integrate the elec-
trolyte with the acetogenic biocathode could be an interesting option for the
improved productivities.^{3,41} In the present study, the higher carbon conversion
35 efficiency can be majorly attributed to the use of bicarbonates in the system. It
also suggests that an electroactive biocathode can effectively reduce the dissolved
CO₂ to acetate. Evaluation of various approaches to improve CO₂ solubility is also
interesting to explore.

The electrodes used as the cathode, their conductive properties and the surface
40 coatings that are involved in the electron transfer mechanism also influence the
production efficiency. A detailed study was done using various types of electrodes
as cathodes that enhance the electrode and microbe-electron transfer rate for CO₂
reduction using *S. ovata*.¹³ Electron transfer rate enhancing strategies were vali-
dated by modifying the cathode surface properties which in turn resulted in
improved acetate production from CO₂ reduction. Biofilms of *S. ovata* on carbon
45 cloth functionalized with positive-charged modifications such as chitosan, cyanic
chloride, 3-aminopropyltriethoxysilane, metals and (gold and palladium)
nickel nanoparticles resulted in 3–7 folds improved acetate production than plain
carbon cloth. However, other positively charged surfaces tested with melamine or
ammonia gas did not stimulate acetate electrosynthesis.¹³ The chitosan coated
50 carbon cloth showed a maximum surface based production rate (13.8 g per m² per
day), which was higher than the VITO electrodes (9.49 g per m² per day). The VITO
CoRE™ electrode manufactured with the activated carbon functioned efficiently

for CO₂ reduction and the coulombic efficiency can be compared to other studies that employed similar mixed cultures and other economic electrode materials but at cathodic potentials higher than −400 mV (Fig. 5a).

The volume of the bioelectrochemical system is also an important parameter that determines the efficiency and the losses associated with the input energy and process efficiency. In the case of MFCs, it was clearly observed that the reactor volume is inversely proportional to the electron transfer efficiency.^{9,42} In MES, the maximum volume of the studies were limited to the 250 mL of cathodic volume in dual chambered configuration. For both MES1 and MES2, the electrolyte volume was considered as 500 mL with a single chambered configuration. The maximum acetate production achieved with the mixed culture in a dual chambered configuration at a poised potential of −590 mV, is 10.5 g L^{−1}²⁰ followed by Su *et al.*,²⁷ with 4.7 g L^{−1} at a cathodic potential of −900 mV (Fig. 5b). The present study achieved 4.13 g L^{−1} acetate with −400 mV which is almost equal to the

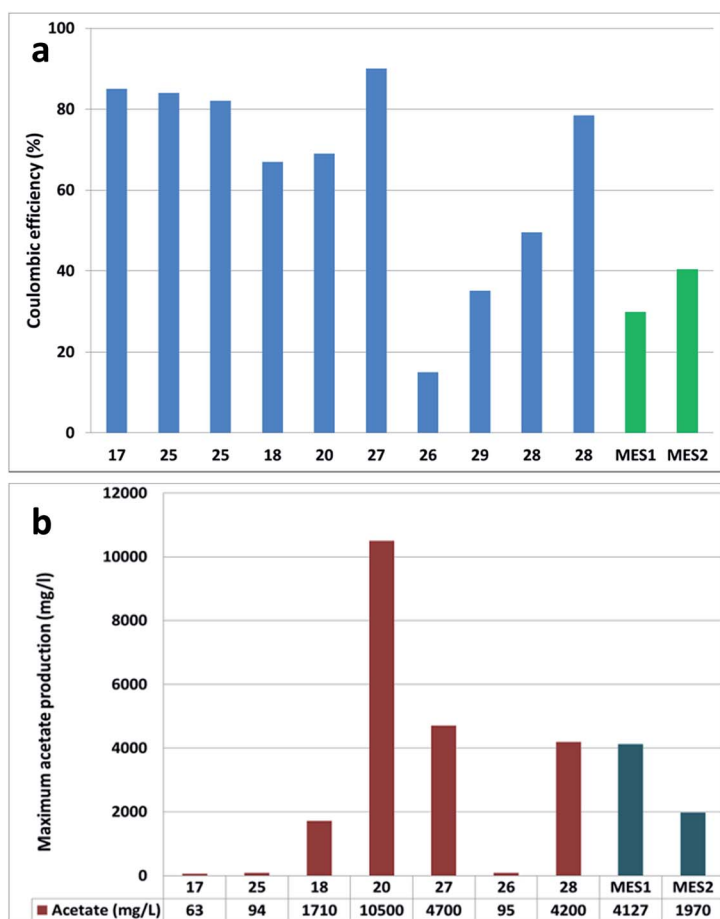


Fig. 5 Comparative evaluation of the results with the state of the art microbial electro-synthesis of acetate from CO₂ (x-axis represents studies with the references and their respective production efficiencies).

1 concentration achieved by Jourdin *et al.*,²⁸ at -850 mV. In the MES mechanism,
the reaction is also influenced by the electrode surface area and/or the biofilm
5 covered on the electrode to the bulk liquid (electrolyte), so the projected surface
area and surface based production rate (g per m^2 per d) explains MES function-
ality. Jourdin *et al.*,²⁸ achieved a highest surface based production rate of 37 g per
10 m^2 per d with nanoweb reticulated vitreous carbon at -850 mV followed by Jiang
et al.,²⁶ (19 g per m^2 per d at -800 mV) and Su *et al.*,²⁷ (10 g per m^2 per d at -700
mV) with carbon felt. The VITO CoRE™ electrode registered 9.49 g per m^2 per d at
15 -400 mV, where H_2 mediated electron transfer was completely limited and only
direct electron transfer is possible (Table 1). Maintaining higher cathodic
potentials can also lead to methane production.²⁶ MFCs were proven to sustain
the lower potentials for long term operation and the present study showed
interesting results for acetate from CO_2 and can warrant the direct integration of
stable MFCs for acetate production through the biocathodic reduction reaction.

4. Conclusions

20 Microbial electrosynthesis driven by a biocathode offers a wide range of chemicals
from inorganic carbon (CO_2). The selection of bacteria and operating conditions
influences the product and production efficiency. Formation of an electroactive
biofilm, stability and reproducibility of such biofilm delivers a commercial
25 application of this process. This is the first study that proved single chambered
operation for bicarbonate reduction with enriched bacteria and was successfully
operated for more than four months. VITO-CORE™ electrodes were found to be
effective for CO_2 to acetate production. The biofilm became fragile at higher
concentrations of acetate and identifying optimum concentrations of the biofilm
and design of the required operational conditions to improve the stability of the
30 microbial electrosynthesis process is necessary. On integration with other MES
systems where the produced acetate can be used for the synthesis of higher
organic compounds such as ethanol, butyrate, ethylene, *etc.*, will provide
sustainable competition between global warming and energy needs.

Acknowledgements

35 G. Mohanakrishna gratefully acknowledges the Marie-Curie Intra-European
Fellowship (IEF) supported project BIO-ELECTRO-ETHYLENE (Grant No.
626959) from the European Commission.

References

- 1 D. R. Lovley, *Environ. Microbiol. Rep.*, 2011, **3**, 27–35.
- 2 K. Rabaey and R. A. Rozendal, *Nat. Rev. Microbiol.*, 2010, **8**, 706–716.
- 3 S. Srikanth, M. Maesen, X. Dominguez-Benetton, K. Vanbroekhoven and
4 D. Pant, *Bioresour. Technol.*, 2014, **165**, 350–354.
- 4 R. Ganigué, S. Puig, P. Batlle-Vilanova, M. D. Balaguer and J. Colprim, *Chem.*
Commun., 2015, **51**, 3235–3238.
- 5 S. A. Patil, S. Gildemyn, D. Pant, K. Zengler, B. E. Logan and K. Rabaey,
50 *Biotechnol. Adv.*, 2015, DOI: 10.1016/j.biotechadv.2015.03.002.

- 1 6 A. ElMekawy, H. M. Hegab and D. Pant, *Energy Environ. Sci.*, 2014, 7, 3921–3933.
- 7 D. Pant, A. Singh, G. Van Bogaert, S. I. Olsen, P. S. Nigam, L. Diels and K. Vanbroekhoven, *RSC Adv.*, 2012, 2, 1248–1263.
- 5 8 G. Mohanakrishna, S. Krishna Mohan and S. Venkata Mohan, *Appl. Energy*, 2012, 95, 31–37.
- 9 G. Mohanakrishna, S. Venkata Mohan and P. N. Sarma, *J. Hazard. Mater.*, 2010, 177, 487–494.
- 10 S. Venkata Mohan, G. Velvizhi, K. V. Krishna and M. L. Babu, *Bioresour. Technol.*, 2014, 165, 355–364.
- 11 B. E. Logan, *Appl. Microbiol. Biotechnol.*, 2010, 85, 1665–1671.
- 12 M. Sharma, N. Aryal, P. M. Sarma, K. Vanbroekhoven, B. Lal, X. Dominguez Benetton and D. Pant, *Chem. Commun.*, 2013, 49, 6495–6497.
- 15 13 T. Zhang, H. Nie, T. S. Bain, H. Lu, M. Cui, O. L. Snoeyenbos-West, A. E. Franks, K. P. Nevin, T. P. Russell and D. R. Lovley, *Energy Environ. Sci.*, 2013, 6, 217–224.
- 14 L. T. Angenent and M. Rosenbaum, *Biofuels*, 2013, 4, 131–134.
- 15 D. Pant, S. Bajracharya, S. Srikanth, G. Mohanakrishna, H. de Wever, K. Vanbroekhoven and L. Diels, *Qatar Foundation Annual Research Conference 2014 (ARC'14)*, Qatar, 18–19th November 2014.
- 20 16 A. ElMekawy, H. M. Hegab, K. Vanbroekhoven and D. Pant, *Renewable Sustainable Energy Rev.*, 2014, 39, 617–627.
- 17 K. P. Nevin, T. L. Woodard, A. E. Franks, Z. M. Summers and D. R. Lovley, *mBio*, 2010, 1(2).
- 25 18 C. W. Marshall, D. E. Ross, E. B. Fichot, R. S. Norman and H. D. May, *Appl. Environ. Microbiol.*, 2012, 78, 8412–8420.
- 19 M. Aresta, A. Dibenedetto and A. Angelini, *Chem. Rev.*, 2013, 114, 1709–1742.
- 20 C. W. Marshall, D. E. Ross, E. B. Fichot, R. S. Norman and H. D. May, *Environ. Sci. Technol.*, 2013, 47, 6023–6029.
- 30 21 K. Schuchmann and V. Müller, *Nat. Rev. Microbiol.*, 2014, 12, 809–821.
- 22 H. L. Drake, A. S. Gößner and S. L. Daniel, *Ann. N. Y. Acad. Sci.*, 2008, 1125, 100–128.
- 35 23 M. R. Wilkins and H. K. Atiyeh, *Curr. Opin. Biotechnol.*, 2011, 22, 326–330.
- 24 K. P. Nevin, S. A. Hensley, A. E. Franks, Z. M. Summers, J. Ou, T. L. Woodard, O. L. Snoeyenbos-West and D. R. Lovley, *Appl. Environ. Microbiol.*, 2011, 77, 2882–2886.
- 25 H. Nie, T. Zhang, M. Cui, H. Lu, D. R. Lovley and T. P. Russell, *Phys. Chem. Chem. Phys.*, 2013, 15, 14290–14294.
- 40 26 Y. Jiang, M. Su, Y. Zhang, G. Zhan, Y. Tao and D. Li, *Int. J. Hydrogen Energy*, 2013, 38, 3497–3502.
- 27 M. Su, Y. Jiang and D. Li, *J. Microbiol. Biotechnol.*, 2013, 23, 1140–1146.
- 28 L. Jourdin, S. Freguia, B. C. Donose, J. Chen, G. G. Wallace, J. Keller and V. Flexer, *J. Mater. Chem. A*, 2014, 2, 13093–13102.
- 45 29 Z. Zaybak, J. M. Pisciotta, J. C. Tokash and B. E. Logan, *J. Biotechnol.*, 2013, 168, 478–485.
- 30 P. K. Addo, R. L. Arechederra, A. Waheed, J. D. Shoemaker, W. S. Sly and S. D. Minteer, *Electrochem. Solid-State Lett.*, 2011, 14, E9–E13.
- 50 31 E. J. Bouwer and P. L. McCarty, *Appl. Environ. Microbiol.*, 1983, 45, 1408–1410.

- 1 32 S. Venkata Mohan, G. Mohanakrishna, S. V. Raghuvulu and P. N. Sarma, *Int. J. Hydrogen Energy*, 2007, **32**, 3284–3292.
- 33 S. Venkata Mohan, G. Mohanakrishna and P. N. Sarma, *Int. J. Hydrogen Energy*,
5 2008, **33**, 2156–2166.
- 34 Y. Alvarez-Gallego, X. Dominguez-Benetton, D. Pant, L. Diels,
K. Vanbroekhoven, I. Genné and P. Vermeiren, *Electrochim. Acta*, 2012, **82**,
415–426.
- 35 D. G. Nocera, *Acc. Chem. Res.*, 2012, **45**, 767–776.
- 36 J. P. Torella, C. J. Gagliardi, J. S. Chen, D. K. Bediako, B. Colón, J. C. Way and
10 D. G. Nocera, *Proc. Natl. Acad. Sci. U. S. A.*, 2015, **112**, 2337–2342.
- 37 M. D. Bredwell, P. Srivastava and R. M. Worden, *Biotechnol. Prog.*, 1999, **15**,
834–844.
- 38 S. D. Rajagopalan, R. P. Datar and R. S. Lewis, *Biomass Bioenergy*, 2002, **23**,
15 487–493.
- 39 R. P. Datar, R. M. Shenkman, B. G. Cateni, R. L. Huhnke and R. S. Lewis,
Biotechnol. Bioeng., 2004, **86**, 587–594.
- 40 P. C. Munasinghe and S. K. Khanal, *Bioresour. Technol.*, 2012, **122**, 130–136.
- 41 X. Dominguez-Benetton, S. Srikanth, Y. Satyawali, K. Vanbroekhoven and
20 D. Pant, *Journal of Microbiology Biochemical Technology*, 2013, S6-007.
- 42 S. Srikanth, T. Pavani, P. N. Sarma and S. Venkata Mohan, *Int. J. Hydrogen
Energy*, 2011, **36**, 2271–2280.
- 25
- 30
- 35
- 40
- 45
- 50

PAPER

CO₂ capture and electrochemical conversion using super basic [P₆₆₆₁₄][124Triz]

Nathan Hollingsworth,^a S. F. Rebecca Taylor,^b Miguel T. Galante,^c Johan Jacquemin,^b Claudia Longo,^c Katherine B. Holt,^a Nora H. de Leeuw^{ad} and Christopher Hardacre^{*b}

Received 22nd May 2015, Accepted 3rd July 2015

DOI: 10.1039/c5fd00091b

The ionic liquid trihexyltetradecylphosphonium 1,2,4-triazolide, [P₆₆₆₁₄][124Triz], has been shown to chemisorb CO₂ through equimolar binding of the carbon dioxide with the 1,2,4-triazolide anion. This leads to a possible new, low energy pathway for the electrochemical reduction of carbon dioxide to formate and syngas at low overpotentials, utilizing this reactive ionic liquid media. Herein, an electrochemical investigation of water and carbon dioxide addition to the [P₆₆₆₁₄][124Triz] on gold and platinum working electrodes is reported. Electrolysis measurements have been performed using CO₂ saturated [P₆₆₆₁₄][124Triz] based solutions at −0.9 V and −1.9 V on gold and platinum electrodes. The effects of the electrode material on the formation of formate and syngas using these solutions are presented and discussed.

1 Introduction

Since the industrial revolution, the harnessing of fossil fuels by combustion for energy and transportation has seen atmospheric levels of CO₂ steadily rise.^{1,2} One concern is that the rate of growth in global CO₂ concentration in the atmosphere is associated with rising global temperatures and sea levels.³ Given the potential implications of global warming, strategies to capture and/or convert CO₂ provide the subject of much scientific endeavour.⁴

Aside from a greenhouse gas, CO₂ can be considered as an abundant, renewable and low cost C1 building block for the production of fuels, or as a feedstock for industrial chemical synthesis. The synthesis of fuels is particularly attractive given the carbon neutrality of the product.

^aDepartment of Chemistry, University College London, 20 Gordon Street, London, WC1H 0AJ, UK

^bSchool of Chemistry and Chemical Engineering, Queen's University Belfast, Belfast, N. Ireland, BT9 5AG, UK

^cInstitute of Chemistry, University of Campinas – UNICAMP, Campinas, SP, Brazil

^dSchool of Chemistry, Cardiff University, Cardiff, CF10 3XQ, UK

1 Electrochemical reduction offers a viable route to this goal due to the potential
to reduce CO₂ at high efficiencies and selectivity, as well as the ability to harness
electrical energy from renewable sources.^{5,6} The main barriers are the thermo-
dynamic stability and the kinetic inertness of CO₂, due to the fact that the first
5 electron reduction of linear CO₂ to form the bent [[•]CO₂]⁻ radical anion requires a
high reduction potential, -1.9 V vs. NHE.⁷ Attempts have been made to reduce
this potential by employing various catalysts, such as the recently reported
reductions on Fe₃S₄ surfaces.⁸

10 Ionic liquids (ILs) have been employed as CO₂ capture agents and electro-
chemical conversion mediums due to their intrinsic ionic conductivity, wide
potential windows and CO₂ solubility levels.⁹⁻¹² ILs generally physically absorb
CO₂ into the solution free volume. Reports have shown that ILs can act to stabilise
the first electron reduction of the physically absorbed CO₂ by complexation of the
15 reduction product with the IL cation.¹² This significantly reduces the energy
required to form the [[•]CO₂]⁻ radical anion. Initial CO₂ electrochemical reduction
experiments in ILs employed 1-alkyl-3-methylimidazolium ([C_nmim]⁺) based ILs
with a range of non-coordinating anions such as [BF₄]⁻, Br⁻, Cl⁻. The electro-
chemically generated anion radical, [[•]CO₂]⁻, was then reacted with alcohols
20 forming dialkyl carbonates.¹³⁻¹⁵

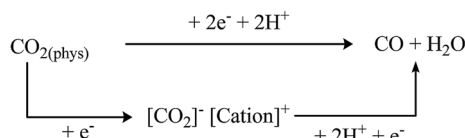
Further studies used hydrated ILs, to provide a source of H⁺. CO₂ physically
absorbed within the IL was reduced with Ag, as the working electrode, further
enabling the reduction of the IL stabilised [[•]CO₂]⁻ to CO, as shown in the Scheme
1.¹²

25 CO₂ reduced to CO in a hydrated IL [C₂mim][BF₄] on a Ag working electrode
was reported to have overpotentials as low as 0.2 V.¹² H₂ production was also
suppressed due to the cation forming a monolayer on the electrode surface.¹⁶
Further improvements have been reported by employing a MoS₂ working elec-
trode, resulting in overpotentials as low as 0.054 V.¹⁷

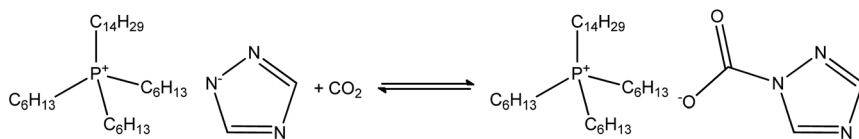
30 Product selectivity has also been observed upon altering the IL anion. For
example, using [C₂mim]⁺ based ILs on Pb electrodes, oxalate is favoured in the
presence of [NTf₂]⁻ and formate is favoured when [TFA]⁻ is used.^{9,11}

35 Recently, we have reported an alternative route for CO₂ reduction in ILs, by
using [P₆₆₆₁₄][124Triz].¹⁸ [P₆₆₆₁₄][124Triz] is able to capture significantly more CO₂
than classical ILs like [C₄mim][NTf₂] or [C₂mim][OAc], due to the chemical
reactivity of the 1,2,4-triazolide anion.¹⁹ The anion can chemically bind CO₂
allowing up to equimolar amounts of CO₂ to be captured, as illustrated in the
Scheme 2.¹⁹

40 Crucially, upon binding, the CO₂ geometry is altered from linear to bent. A
lower energy pathway to CO₂ reduction was demonstrated in this IL, which may be
related to the chemical binding of the CO₂ by the anion.¹⁸ [P₆₆₆₁₄][124Triz] is also



Scheme 1 Reduction of CO₂ to CO in an IL, which absorbs CO₂ physically.¹²



Scheme 2 CO_2 binding to the $[124\text{Triz}]^-$ anion in the IL $[\text{P}_{66614}][124\text{Triz}]$.¹⁹

able to absorb CO_2 through physical exothermic absorption in the solution free volume that is driven by an entropic process of solvation. The physically absorbed CO_2 may also undergo reduction stabilised by the $[\text{P}_{66614}]^+$ cation. Formate was produced by the lower energy route at -0.7 V vs. Ag/AgNO_3 with 95% Faradaic efficiency on the Ag electrodes. In addition, reduction of the physically absorbed CO_2 at -1.9 V vs. Ag/AgNO_3 produced CO with a 41% Faradaic efficiency.¹⁸ In comparison, on using $[\text{P}_{66614}][\text{NTf}_2]$, which does not support chemical CO_2 binding, no product was formed at -0.7 V suggesting that the reaction occurring at less negative potentials (*i.e.* -0.7 V) in $[\text{P}_{66614}][124\text{Triz}]$ is related to the reduction of chemically bound CO_2 (Scheme 2). Products were formed at -1.9 V, *i.e.* the same potential as found in $[\text{P}_{66614}][124\text{Triz}]$, indicating that they are formed from the reduction of physically absorbed CO_2 stabilised by the $[\text{P}_{66614}]^+$ cation (Scheme 1).¹⁸ Herein, the study is expanded to investigate the influence of the electrode material on the CO_2 reduction potential, product distribution and Faradaic efficiency.

2 Experimental

2.1 Materials and IL synthesis

Trihexyltetradecylphosphonium chloride ($[\text{P}_{66614}]\text{Cl}$) was received from Cytec (97.7%) and 1,2,4-triazole (98%) was purchased from Sigma-Aldrich. The Au foil (0.1 mm thick 99.9975+%) and Pt wire (0.3 mm dia., 99.99%) were purchased from Alfa Aesar. Gaseous nitrogen (99.998%) and carbon dioxide (99.99%) were obtained from BOC and passed through drying columns before contact with the IL samples. The water was purified using a Milli-Q 18.3 M Ω water system.

$[\text{P}_{66614}][124\text{Triz}]$ was prepared using a previously reported method²⁰ and a two step synthesis procedure; $[\text{P}_{66614}][\text{OH}]$ was synthesized using an anion exchange resin from $[\text{P}_{66614}]\text{Cl}$ followed by addition of the superbase. The water content of the ILs was measured using a Metrohm 787 KF Titrino Karl Fischer and was found to be <0.1 wt% for all ILs. Halide content was below the detectable limit by AgNO_3 testing.

2.2 Electrochemical experiments

Cyclic voltammograms (CVs) were recorded using an Ecochemie Autolab Potentiostat/Galvanostat (PGSTAT302) and carried out using a three-electrode arrangement with a Au or Pt working electrode (1.6 mm), a platinum coil as the counter electrode. All potentials were measured with respect to a 0.01 mol L^{-1} Ag^+/Ag reference, with AgNO_3 dissolved in $[\text{C}_4\text{mim}][\text{NO}_3]$ and separated from the bulk solution *via* a glass frit. Electrolysis experiments were carried out using a three electrode set up in a sealed 50 cm³ cell with a gas tight syringe attached. The

1 working electrodes were a coiled Pt wire or a Au foil, a Pt coil was used as the
counter electrode (contained within a counter compartment) and the potentials
were measured with respect to a 0.01 mol L⁻¹ Ag⁺/Ag reference, with AgNO₃
5 dissolved in [C₄mim][NO₃] and separated from the bulk solution *via* a glass frit. A
0.1 mol L⁻¹ [P₆₆₆₁₄][124Triz], 0.7 mol L⁻¹ H₂O in acetonitrile solution (8 cm³) was
added to the cell and bubbled with CO₂ (25 cm³ min⁻¹) for 60 min, during this
10 time the gas syringe was gradually opened. The cell was then sealed, connected up
to a potentiostat (Biologic VMP3 controlled by EC-Lab) and a potential applied to
the cell for the time required to pass 10 C of charge. It should be noted that no
ionic liquid decomposition or reaction was observed under any of the conditions
tested in this study.

2.3 Solution phase detection

15 Solution samples were analysed by obtaining ¹H NMR spectra using a Bruker
Avance III 600 with a DCH cryoprobe. Quantitative analysis was performed using
the ERETIC2 quantification tool within Topspin 3.2.

2.4 Gas phase detection

20 The gas phase of the reaction was analysed using a Perkin-Elmer Clarus 500 Gas
Chromatograph equipped with a TCD and FID (with methanizer) fitted with a
packed column (stainless steel, 30 ft, 1/8 inch OD, 2.0 mm ID packed with Haysep
DB 100/120 mesh). The gaseous products were transferred to the GC by con-
25 necting up the cell and injecting the contents of the gas tight syringe attached to
the cell into the GC. H₂ was quantified using the TCD and CO using the FID.

3 Results and discussion

3.1 Voltammetry study of CO₂ reduction in [P₆₆₆₁₄][124Triz] using various working electrodes

30 CVs have been recorded at both Au and Pt electrodes in 0.1 mol L⁻¹ [P₆₆₆₁₄]
[124Triz] in acetonitrile (MeCN). CVs were recorded at a scan rate of 100 mV s⁻¹ at
22 °C. The reference electrode was a previously reported 0.01 mol L⁻¹ Ag⁺/Ag
reference, with AgNO₃ dissolved in [C₄mim][NO₃] and separated from the bulk
35 solution *via* a glass frit.^{21,22} 0.1 mol L⁻¹ [P₆₆₆₁₄][124Triz] in MeCN was first satu-
rated with argon and a baseline CV taken. Thereafter, water was added (0.7 mol
L⁻¹), as a source of H⁺ and the influence on the CV investigated. The H⁺ is
40 required to make protonated reduction products and CO through the reaction of
reduced CO₂ and H⁺ (Scheme 1). Finally, the hydrated IL mixture was purged with
CO₂ for 30 min and a CV taken to assess CO₂ reduction processes.

3.1.1 **Au working electrode.** CVs relating to the use of a polished Au working
45 electrode (0.16 cm²) are displayed in Fig. 1. The CV, after purging with Ar, is
shown in blue. A small increase in reduction current is observed at *ca.* -1.1 V with
a rapid increase in reduction current at *ca.* -2.0 V. Upon the addition of H₂O to
the IL/MeCN mixture, a small increase in current is observed at -1.0 V and a
larger increase at *ca.* -1.75 V (Fig. 1, red). Although the small increase in current
50 observed at -1.0 V has a slight anodic shift compared with that observed in the Ar
saturated sample (-1.1 V), this feature may be attributed to the reduction of 1,2,4-
triazole formed from the reaction of the [124Triz]⁻ anion and H₂O (Scheme 3).

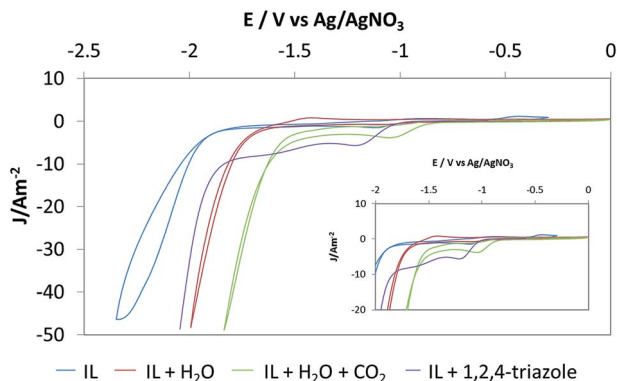


Fig. 1 Cyclic voltammograms of $0.1 \text{ mol L}^{-1} [\text{P}_{66614}][124\text{Triz}]$ (IL) in acetonitrile (MeCN) at a gold electrode; (blue) IL in MeCN; (red) IL in MeCN + $0.7 \text{ mol L}^{-1} \text{H}_2\text{O}$; and (green) IL in MeCN + $0.7 \text{ mol L}^{-1} \text{H}_2\text{O} + \text{CO}_2$, IL in MeCN + 0.5 mol L^{-1} 1,2,4-triazole; only the cathodic linear sweep is shown for clarity. Magnification is shown inset.

To test this theory, 1,2,4-triazole was deliberately added to a solution of hydrated $0.1 \text{ mol L}^{-1} [\text{P}_{66614}][124\text{Triz}]$ in MeCN. The CV showed that, upon addition of 1,2,4-triazole, the current from -1.0 V increased, supporting this proposal. The presence of the small current increase at -1.1 V in the Ar saturated sample could, therefore, either be due to adventitious water or trace 1,2,4-triazole impurities from the synthesis process of $[\text{P}_{66614}][124\text{Triz}]$, which is synthesised from the addition of 1,2,4-triazole to $[\text{P}_{66614}][\text{OH}]$.

The large reduction current at -1.8 V , observed upon the addition of H_2O , shows a large anodic shift compared to the onset of the large reduction current in the Ar saturated sample. This is proposed to be due to the reduction of H_2O to H_2 . This region also increases in current when 1,2,4-triazole is deliberately added to the electrolyte, suggesting that generation of H_2 from the reduction of 1,2,4-triazole may also contribute to this current. In addition, a small oxidative stripping peak is observed at -1.5 V , following the rapid increase of current at -1.8 V , suggesting that the product of the reduction may interact with the electrode surface. Recent reports employing $[\text{C}_4\text{mim}][\text{BF}_4]$ on Au surfaces have shown the hydrogen evolution reaction to occur at *ca.* $-2.0 \text{ V vs. Ag/Ag}^+$,²³ suggesting that the use of chemically co-ordinating IL provides a pathway to less negative reduction potentials.

Saturation of the hydrated IL mixture with CO_2 (Fig. 1 green) resulted in an increase in current at -0.9 V , followed by a rapid increase in current at -1.6 V . The peak at -0.9 V shows an increased current and greater anodic shift when compared to the hydrated sample. The large increase in current observed at -1.6 V shows an anodic shift on comparison to Ar saturated and hydrated samples. Previous reports on Ag electrodes have suggested that the reduction at less negative potentials (-0.7 V) could be assigned to the reduction of CO_2 chemically

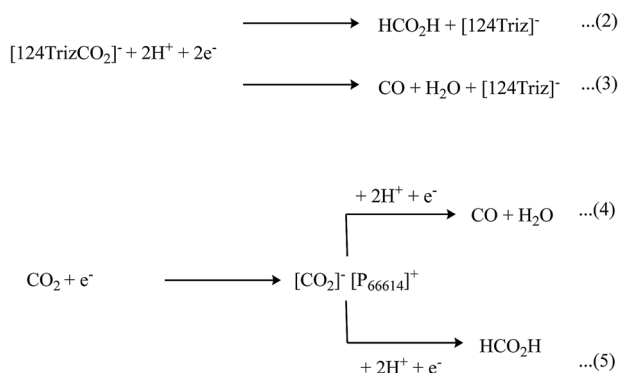


Scheme 3 H_2O reaction with the $[124\text{Triz}]^-$ anion in the $[\text{P}_{66614}][124\text{Triz}]$.

bound to the $[124\text{Triz}]^-$ anion, while reductions at more negative potentials (-1.9 V) could be assigned to the reduction of physically adsorbed CO_2 (Scheme 4 eqn (2)–(5) respectively).¹⁸ The reduction of physically adsorbed CO_2 at -1.6 V is in good agreement with CO_2 reduction reported on Au electrodes in $[\text{C}_4\text{mim}][\text{BF}_4]$. Reduction of CO_2 in $[\text{C}_4\text{mim}][\text{BF}_4]$, an IL that only exhibits physical CO_2 absorption, on the Au surface was reported at -1.8 V vs. NHE (*i.e.* -1.6 V vs. Ag/Ag^+).²³ Interestingly, the potential for the reduction of CO_2 over Au reported, herein, at -0.9 V is the lowest potential, to the best of our knowledge, reported to date using ionic liquid systems showing the potential of reactive IL to enhance the electrochemical activity.

Assuming similar mechanisms take place at the Au electrode, this suggests that chemically bound CO_2 can be reduced at less negative potentials on Ag than Au (-0.7 V compared to -0.9 V), but that the reduction of physically bound CO_2 occurs at less negative potentials on Au than Ag (-1.6 V vs. -1.9 V). One plausible explanation would be that Ag is more catalytically active than Au and, therefore, the IL is more strongly bound to the Ag electrode than the Au. This may suggest that the chemically bound CO_2 on Ag can be reduced at less negative potentials due to the increased contact with the electrode but the physically adsorbed CO_2 is blocked by the IL requiring more negative potentials for reduction. Reduced binding in the Au system suggests the physically adsorbed CO_2 has easier access to the electrode and, therefore, physically adsorbed reduction occurs at a less negative potential than on Ag, but that the reduction of the chemically adsorbed CO_2 requires a more negative potential than in the Ag system.

3.1.2 Pt working electrode. CVs relating to the use of a polished Pt working electrode (0.16 cm^2) are displayed in Fig. 2, the CV after purging with Ar is shown in blue. An increase in current is observed at -1.6 V followed by the start of a rapid current increase at *ca.* -2.1 V. Upon the addition of H_2O to the IL/MeCN mixture (Fig. 2 red), a rapid increase in current is observed at -1.5 V with no smaller current increase observed at lower potentials. The rapid increase in current at -1.5 V shows an anodic shift and enhanced current compared to the Ar saturated sample. This peak is plausibly associated with the reduction of H_2O to H_2 . On comparison with the Au electrode the reduction of H_2O to H_2 takes place at



Scheme 4 Suggested CO_2 reduction processes occurring on the working electrode.

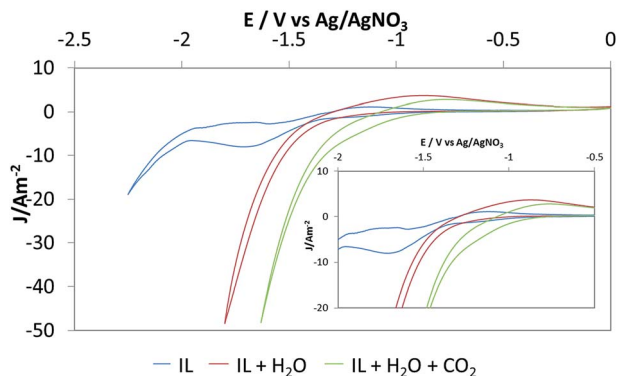


Fig. 2 Cyclic voltammograms of 0.1 mol L⁻¹ [P₆₆₆₁₄][124Triz] (IL) in acetonitrile (MeCN) at a platinum electrode; (blue) IL in MeCN, (red) IL in MeCN + 0.7 mol L⁻¹ H₂O, and (green) IL in MeCN + 0.7 mol L⁻¹ H₂O + CO₂. Magnified CVs are inset.

a less negative potential on Pt than Au (-1.5 V vs. -1.8 V). This is consistent with Pt being well known as an excellent catalyst for water splitting.

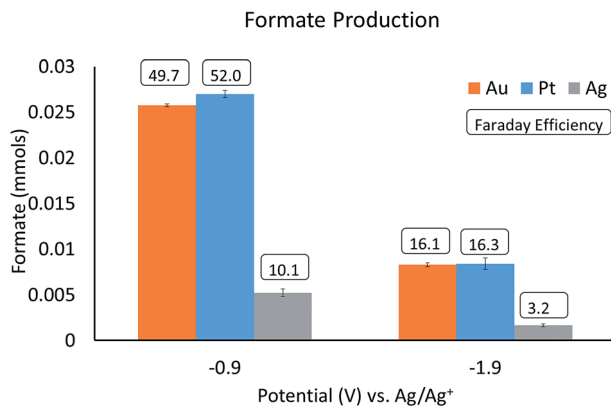
Saturating the hydrated IL mixture with CO₂ (Fig. 2 green) results in a slow increase in current at -0.9 V. The increase becomes rapid at -1.4 V. The slow increase in current is plausibly due to the reduction of CO₂ bound to the [124Triz]⁻ anion, while the rapid increase in current is associated with the reduction of physically adsorbed CO₂.

Both Au and Pt display similar reduction potentials for CO₂ bound to the [124Triz]⁻ anion (-0.9 V), which are more negative than reduction on Ag (-0.7 V). However, the reduction of physically bound CO₂ is less negative for Pt than Au (-1.4 V and -1.6 V respectively), both of which are less negative than Ag (-1.9 V). It is important to note that the Pt is more catalytically active than both the Au and Ag and, therefore, should show a higher activity. However, as a result of this increased activity Pt will also bind the IL more strongly than the Ag, therefore, the results suggest that a balance between activity and adsorption strength is required for CO₂ reduction at lower potentials. As CO is also formed during these experiments and the binding of CO to Pt will be much stronger than on Ag or Au, site blocking from the CO may also be contributing to the observed differences between the electrode performance.

3.2 Electrolysis study

Electrolysis was performed in CO₂ saturated and hydrated (0.7 mol L⁻¹ H₂O) 0.1 mol L⁻¹ [P₆₆₆₁₄][124Triz] in MeCN (8 cm³). Electrolysis was continued until a fixed charge of 10 C had passed, after which the solution phase was tested by quantitative ¹H NMR and gas phase by gas chromatography (GC). The reported values for the analogous electrolysis using Ag electrodes is displayed in Fig. 3. While Ag electrodes are reported to display Faradic efficiencies of 95% at -0.7 V, with an applied potential of 0.17 V, electrolysis on Au and Pt at this potential resulted in no detected reduction product. Therefore, electrolysis was also performed at -1.9 V and -0.9 V to test for reduction of physical and chemical absorbed CO₂, respectively, using these electrodes. The experiments were also performed at

1



5

10

15

Fig. 3 Quantitative ^1H NMR analysis of formate production at the Au, Pt, and Ag electrodes after 10 C of charge is passed. Error bars represent ± 1.5 standard deviations. Faraday efficiencies for each potential and electrode are shown in the boxes.

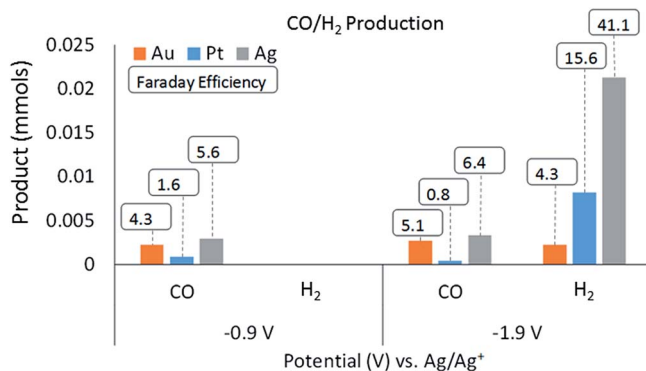
20

these potentials with Ag for comparison (Fig. 3 and 4), although it should be noted that electrolysis at -0.9 V is not the optimum potential for formate production on Ag.

25

3.2.1 Au electrode. 0.5 cm^2 of Au foil was employed as a working electrode. Quantitative ^1H NMR of the electrolyte after electrolysis showed the presence of formate for both investigated potentials (-0.9 V and -1.9 V). The formate produced at -0.9 V is proposed to be formed from the reduction of CO_2 bound to the $[\text{124Triz}]^-$ anion (Scheme 4 eqn (2)), while the formate produced at -1.9 V is proposed to be generated from the reduction of physically absorbed CO_2 stabilised by $[\text{P}_{66614}]^+$ cation (Scheme 4 eqn (5)). A greater quantity of formate was detected at -0.9 V (0.026 mmol) compared with -1.9 V (0.0083 mmol) with Faradaic efficiencies of 49.7 and 16.1%, respectively. This is in contrast to previous reports using $[\text{C}_2\text{mim}][\text{TFA}]$, whereby the Faradaic efficiency for formate production increases with potential.⁹ The open circuit potential (OCP) prior to

35



40

45

Fig. 4 GC analysis of CO and H₂ production at the Au, Pt, and Ag electrodes after 10 C of charge is passed. Faraday efficiencies (%) for each potential and electrode are shown in the boxes.

50

1 electrolysis, but after CO₂ saturation, was measured at -0.45 V, suggesting an
applied potential of -0.45 and -1.45 V for potential holds of -0.9 and -1.9 V,
5 respectively. A comparison with the reported values for the analogous electrolysis
using Ag electrodes is displayed in Fig. 3. Electrolysis on Ag resulted in consid-
erably less formate at both -0.9 and -1.9 V, and it should be noted that the
maxima for formate production is -0.7 V, at which potential considerably more
formate is produced than on the Au electrode.

GC analysis of the headspace gas mixture after electrolysis showed that both
10 CO and H₂ were formed with 0.0022 mmol and 0.0027 mmol of CO produced at
 -0.9 V and -1.9 V, respectively. This is assigned to the reduction of CO₂ bound to
the [124Triz]⁻ anion (Scheme 4 eqn (3)) and the reduction of CO₂ stabilised by the
[P₆₆₆₁₄]⁺ cation (Scheme 4 eqn (4)). In addition, hydrogen was only detected at
 -1.9 V, which is consistent with H₂O being reduced to H₂.

15 **3.2.2 Pt electrode.** Quantitative ¹H NMR of the electrolyte after electrolysis
showed a similar trend for formate production on Pt compared to Au. A greater
quantity of formate was detected at -0.9 V (0.027 mmol) compared with -1.9 V
(0.008 mmol) with Faradaic efficiencies of 52.0 and 16.3%, respectively. However,
formate production at both potentials was not significantly different from the
20 amount produced using the Au electrode. The OCP prior to electrolysis, but after
CO₂ saturation, was more negative than that previously found on Au. It was
measured at -0.60 V, giving smaller applied potentials of 0.3 and 1.3 V for elec-
trolysis at -0.9 and -1.9 V, respectively. CO was detected at both -0.9 and -1.9 V,
however, the amount of CO detected was significantly reduced at both potentials
25 compared with the analogous reductions over Au and Ag. No H₂ was detected at
 -0.9 V while significantly more H₂ was detected at -1.9 V on Pt than Au, as
expected. This corresponds well with previous reports showing that the order in
ability to catalyse the hydrogen evolution reaction is Pt > Au > Ag.²⁴ This in turn
relates to the observed reduction potentials after the addition of H₂O on the Pt, Au
and Ag electrodes (-1.5 , -1.8 and -1.9 V, respectively). However, more H₂ is
30 detected for Ag electrodes at -1.9 V than over Pt, this is surprising given that Ag
has the most negative onset potential for reduction of H₂O to H₂. Previous reports
have stated that the IL cation may suppress hydrogen production by blocking H₂O
binding. As such, the disparity in hydrogen production may indicate a differing
affinity for the cation to the three electrode surfaces, of the order Ag < Pt < Au, as
35 well as the ability of the electrode material to activate water. As such, the
production of H₂ and CO may be a balance between catalytic activity (through
onset potentials) and binding energy of the reduced species.

40 Overall, for all three electrodes (Ag, Au and Pt) the trend in the species formed
during the reduction is the same, *i.e.* less negative potentials favour formate
whereas more negative potentials favour CO and H₂. The main difference between
the electrodes is the potential at which the maxima/optimum for each species
occur. For example, for formate production, on the Ag electrode this occurs at
45 -0.7 V, which is less negative than found for the Au and Pt electrodes. In addition,
it is clear that as the potential becomes more negative the Faradaic efficiency for
the species detected decreases for all three electrodes.

4 Conclusions

We have shown that the CO₂ saturated super basic IL [P₆₆₆₁₄][124Triz] can be reduced on Au and Pt electrodes to produce formate and syngas. Two reaction pathways appear to exist at -0.9 V and -1.9 V. Formate is formed in increased quantities at -0.9 V over -1.9 V on both electrode surfaces with Faradaic efficiencies of *ca.* 50% for both electrode surfaces. The production of CO is higher on Au electrodes than Pt electrodes for both electrolysis potentials of -0.9 and -1.9 V. The production of hydrogen, only observed at -1.9 V, is *ca.* 3 times higher on Pt electrodes, enabling the ratio of CO : H₂ in the syngas mixture to be influenced by electrode choice. The reduction of physically bound CO₂ is shown to occur at similar potentials on Au electrodes to those reported for ILs that only physically absorb CO₂, such as [C₄mim][BF₄], albeit at lower Faradaic efficiencies.²³ Formate production in ionic liquids has been previously reported to occur on indium surfaces using hydrated CO₂ saturated [C₂mim][TFA].⁹ The [TFA]⁻ anion only very weakly binds to CO₂, which results in little significant activation of the CO₂ and formate production at low Faradaic efficiencies (*ca.* 10%) at 1.55 V *vs.* Ag/Ag⁺, rising to 90% efficiency at -1.95 V *vs.* Ag/Ag⁺. This behaviour is in good agreement with our proposed onset of reduction of physically bound CO₂. In the present study, the binding of CO₂ is much stronger and, thus, formate production on Au and Pt electrodes, from the chemically bound CO₂, is observed at applied potentials lower than any previously reported ILs. These results show the same trends as found over the previously reported Ag electrode, albeit with some differences. For example, the maximum formate production is found at -0.7 V over Ag at which potential no reduction was observed on Pt and Au.

5 Abbreviations

[P ₆₆₆₁₄] ⁺	Trihexyltetradecylphosphonium
[C ₂ mim] ⁺	1-Ethyl-3-methylimidazolium
[C ₄ mim] ⁺	1-Butyl-3-methylimidazolium
[124Triz] ⁻	1,2,4-Triazolide
[BF ₄] ⁻	Tetrafluoroborate
[NTf ₂] ⁻	Bis(trifluoromethylsulfonyl)imide
[TFA] ⁻	Trifluoroacetate
[OAc] ⁻	Acetate
[NO ₃] ⁻	Nitrate

Acknowledgements

This work was carried out as part of the “4CU” programme grant, aimed at sustainable conversion of carbon dioxide into fuels, led by The University of Sheffield and carried out in collaboration with The University of Manchester, Queen’s University Belfast and University College London. The authors acknowledge gratefully the Engineering and Physical Sciences Research Council (EPSRC) for supporting this work financially (Grant No. EP/K001329/1). S. F. R. Taylor and N. Hollingsworth wish to thank the ELSOL workshop, Researcher

1 Links, FAPESP and Newton fund for funding. M. T. Galante thanks the RSC and
CNPq for funding.

5 Notes and references

- 1 S. Solomon, D. Qin, M. Manning, R. B. Alley, T. Berntsen, N. L. Bindoff,
Z. Chen, A. Chidthaisong, J. M. Gregory, G. C. Hegerl, M. Heimann,
B. Hewitson, B. J. Hoskins, F. Joos, J. Jouzel, V. Kattsov, U. Lohmann,
10 T. Matsuno, M. Molina, N. Nicholls, J. Overpeck, G. Raga, V. Ramaswamy,
J. Ren, M. Rusticucci, R. Somerville, T. F. Stocker, P. Whetton, R. A. Wood
and D. Wratt, *Technical Summary, in: Climate Change 2007: The Physical
Science Basis. Contribution of Working Group I to the Fourth Assessment Report
of the Intergovernmental Panel on Climate Change*, ed. S. Solomon, D. Qin, M.
15 Manning, Z. Chen, M. Marquis, K. B. Averyt, M. Tignor and H. L. Miller,
Cambridge University Press, Cambridge, United Kingdom, New York, NY,
USA, 2007.
- 2 T. R. Karl and K. E. Trenberth, *Science*, 2003, **302**, 1719–1723.
- 3 *Climate Change and Water, Technical Paper of the Intergovernmental Panel on
Climate Change*, ed. B. C. Bates, Z. W. Kundzewicz, S. Wu and J. P. Palutikof,
20 IPCC Secretariat, Geneva, 2008, p. 210.
- 4 P. Styring, E. A. Quadrelli and K. Armstrong, *Carbon Dioxide Utilisation: Closing
the Carbon Cycle*, Elsevier Science, 2014.
- 5 D. T. Whipple and P. J. A. Kenis, *J. Phys. Chem. Lett.*, 2010, **1**, 3451–3458.
- 25 6 N. S. Spinner, J. A. Vega and W. E. Mustain, *Catal. Sci. Technol.*, 2012, **2**, 19–28.
- 7 J. Schneider, H. Jia, J. T. Muckerman and E. Fujita, *Chem. Soc. Rev.*, 2012, **41**,
2036–2051.
- 8 A. Roldan, N. Hollingsworth, A. Roffey, H. U. Islam, J. B. M. Goodall,
C. R. A. Catlow, J. A. Darr, W. Bras, G. Sankar, K. B. Holt, G. Hogarth and
30 N. H. de Leeuw, *Chem. Commun.*, 2015, **51**, 7501–7504.
- 9 J. D. Watkins and A. B. Bocarsly, *ChemSusChem*, 2014, **7**, 284–290.
- 10 M. C. Buzzeo, O. V. Klymenko, J. D. Wadhawan, C. Hardacre, K. R. Seddon and
R. G. Compton, *J. Phys. Chem. B*, 2004, **108**, 3947–3954.
- 35 11 L. Sun, G. K. Ramesha, P. V. Kamat and J. F. Brennecke, *Langmuir*, 2014, **30**,
6302–6308.
- 12 B. A. Rosen, A. Salehi-Khojin, M. R. Thorson, W. Zhu, D. T. Whipple,
P. J. A. Kenis and R. I. Masel, *Science*, 2011, **334**, 643–644.
- 13 Q. Feng, S. Liu, X. Wang and G. Jin, *Appl. Surf. Sci.*, 2012, **258**, 5005–5009.
- 40 14 X. Yuan, B. Lu, J. Liu, X. You, J. Zhao and Q. Cai, *J. Electrochem. Soc.*, 2012, **159**,
E183–E186.
- 15 F. Liu, S. Liu, Q. Feng, S. Zhuang, J. Zhang and P. Bu, *Int. J. Electrochem. Sci.*,
2012, **7**, 4381–4387.
- 16 B. A. Rosen, J. L. Haan, P. Mukherjee, B. Braunschweig, W. Zhu, A. Salehi-
Khojin, D. D. Dlott and R. I. Masel, *J. Phys. Chem. C*, 2012, **116**, 15307–15312.
- 45 17 M. Asadi, B. Kumar, A. Behranginia, B. A. Rosen, A. Baskin, N. Repnin,
D. Pisasale, P. Phillips, W. Zhu, R. Haasch, R. F. Klie, P. Král, J. Abiade and
A. Salehi-Khojin, *Nat. Commun.*, 2014, **5**, 4470.
- 18 N. Hollingsworth, S. F. R. Taylor, M. T. Galante, J. Jacquemin, C. Longo,
K. B. Holt, N. H. de Leeuw and C. Hardacre, *Angew. Chem., Int. Ed.*, 2015,
50 submitted 30/04/2015.

- 1 19 C. Wang, X. Luo, H. Luo, D.-e. Jiang, H. Li and S. Dai, *Angew. Chem., Int. Ed.*,
2011, **50**, 4918–4922.
- 20 S. F. R. Taylor, C. McCrellis, C. McStay, J. Jacquemin, C. Hardacre, M. Mercy,
R. Bell and N. de Leeuw, *J. Solution Chem.*, 2015, **44**, 511–527.
- 5 21 L. Aldous, D. S. Silvester, C. Villagran, W. R. Pitner, R. G. Compton, M. Cristina
Lagunas and C. Hardacre, *New J. Chem.*, 2006, **30**, 1576–1583.
- 22 N. S. A. Manan, L. Aldous, Y. Alias, P. Murray, L. J. Yellowlees, M. C. Lagunas
and C. Hardacre, *J. Phys. Chem. B*, 2011, **115**, 13873–13879.
- 10 23 J. H. Koh, H. S. Jeon, M. S. Jee, E. B. Nursanto, H. Lee, Y. J. Hwang and
B. K. Min, *J. Phys. Chem. C*, 2015, **119**, 883–889.
- 24 F. Zhou, S. Liu, B. Yang, P. Wang, A. S. Alshammari and Y. Deng, *Electrochem.
Commun.*, 2014, **46**, 103–106.

15

20

25

30

35

40

45

50

PAPER

Thioether-triphenolate bimetallic iron(III) complexes as robust and highly efficient catalysts for cycloaddition of carbon dioxide to epoxides†

Antonio Buonerba,^{ab} Francesco Della Monica,^a Assunta De Nisi,^{ac} Ermanno Luciano,^a Stefano Milione,^{ab} Alfonso Grassi,^{ab} Carmine Capacchione^{*ab} and Bernhard Rieger^d

Received 11th May 2015, Accepted 21st May 2015

DOI: 10.1039/c5fd00070j

The selective and effective synthesis of organic carbonates under mild conditions, starting from carbon dioxide and oxiranes, catalyzed by metal complexes is currently a focus of interest for both industrial and academic researchers. We recently developed a novel thioether-triphenolate iron(III) catalyst (C_{T-BU}) that has proven to be highly active for the coupling of CO_2 with epoxides, resulting in cyclic organic carbonates under solvent-free conditions. In the current work, the properties of this novel class of catalysts were extensively investigated. In particular, the steric properties of the ligand were modulated by changing the substituents of the aromatic rings in order to obtain a deeper knowledge of the relationship between the complex structure and catalytic performance/selectivity for these iron complexes. Notably, the less steric demanding iron(III) C_H complex synthesized shows, when activated by *n*-tetrabutylammonium bromide, an impressive turnover frequency (TOF) of 3800 h^{-1} for the formation of propylene carbonate and glycerol carbonate which are, by far, the highest reported for an iron based catalyst and compares well with the most active catalyst based on other metals.

Introduction

The possibility of converting carbon dioxide into useful chemicals has become an important area of research in both academic and industrial environments.¹ For

^aDipartimento di Chimica e Biologia, Università degli Studi di Salerno, via Giovanni Paolo II 132, 84084 Fisciano (SA), Italy. E-mail: ccapacchione@unisa.it

^bCIRCC, Interuniversity Consortium Chemical Reactivity and Catalysis, via Celso Ulpiani 27, 70126 Bari, Italy

^cDipartimento di Chimica G. Ciamician, Alma Mater Studiorum, Università di Bologna, via Selmi 2, Bologna, Italy

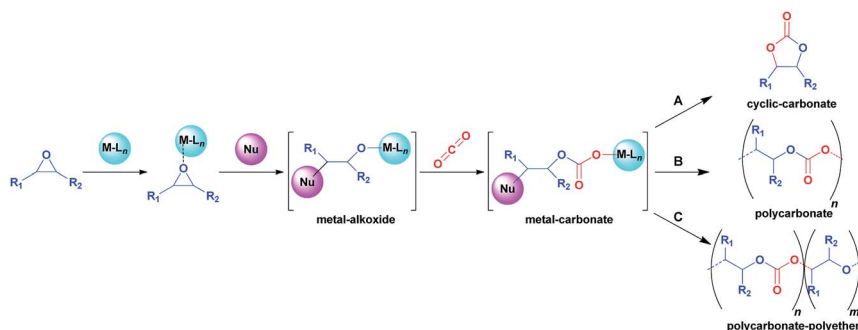
^dWACKER Lehrstuhl für Makromolekulare Chemie, Technische Universität München, Lichtenbergstrasse 4, 85748 Garching, Germany

† Electronic supplementary information (ESI) available: Further details of NMR, ESI-MS, FT-IR and UV-Vis spectroscopic characterizations. See DOI: 10.1039/c5fd00070j

example, the reduction of CO₂ by reaction with hydrogen or water to produce formic acid,² formaldehyde and methanol³ has been intensively studied for the intrinsic value of these molecules as chemical intermediates or fuel.⁴ Like other industrially relevant chemical processes, the key to overcoming the chemical sluggishness of CO₂ is the development of properly designed catalytic systems able to enhance the reactivity and selectivity of such chemical transformations. In this scenario, a prominent role is played by the coupling of CO₂ with epoxides to form cyclic organic carbonates (COCs)⁵ and polycarbonates.⁶ In particular, COCs, due their high molecular dipole moments, dielectric constants and boiling temperatures, are employed as *green* highly polar aprotic solvents and as ion-carriers for lithium-based batteries.⁷ Furthermore, they find application as valuable intermediates in organic synthesis and as monomers in the ring opening polymerization to form polycarbonates. As a result of the growing interest in using COCs in chemical synthesis, the development of efficient, selective, non-toxic and inexpensive catalytic systems able to promote the coupling between CO₂ and oxiranes or oxetanes has become a focus of the field of CO₂ chemistry.

Generally, the most active catalytic systems are based on the combination of a transition metal complex acting as a Lewis acid and a suitable nucleophile (ammonium salts and phosphonium salts).⁸ The widely accepted mechanism involves Lewis acid activation of the epoxide toward the ring opening by nucleophilic attack on the less substituted carbon atom (see Scheme 1). This reaction is followed by CO₂ insertion into the formed metal-alkoxide intermediate leading to an alkyl emi-carbonato unit which can undergo the ring closure, *via* a backbiting mechanism producing the cyclic carbonate (**A**), or by inserting additional epoxide/CO₂ molecules producing polycarbonates (**B**). The fortuitous insertion of two consecutive epoxide molecules also leads to the formation of polyether segments (**C**). Consequently, the choice of metal complex, the ratio between the Lewis acid and the nucleophile and the nature of the co-catalyst, the solvent, and the pressure and temperature are of pivotal importance for the selectivity of the reaction.^{5a}

We have recently developed a new catalytic system⁹ based on iron,¹⁰ an abundant and non-toxic metal. In particular we have reported that the dinuclear Fe(III) (C_t-Bu) (see Scheme 2) complex coordinated by dithioether-triphenolate-based ligands in combination with tetrabutylammonium bromide (TBAB) is an active and selective catalyst for the synthesis of various COCs. Notably, the



Scheme 1 Metal catalysed carbon dioxide–epoxide coupling.

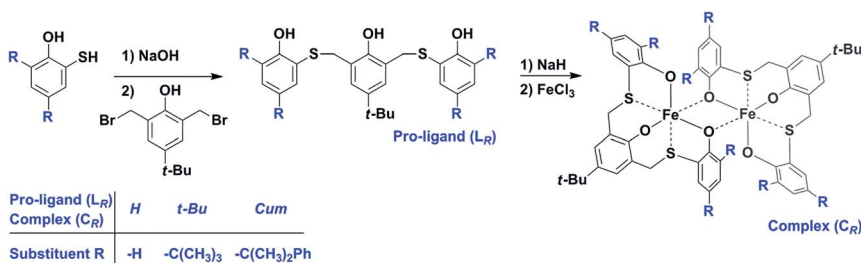
coupling of propylene oxide with CO₂, in the presence of the aforementioned catalytic system, gives the corresponding carbonate with the highest TOF (580 h⁻¹) so far reported for an iron based catalyst.¹¹

In order to establish a more refined catalyst structure–reactivity relationship for this new Fe(III) catalyst family, we report here the synthesis of two new iron(III) complexes, C_H and C_{Cum}. We report on their influence on the catalytic performance, in terms of activity and selectivity, in the CO₂/epoxide coupling reaction of the substituents on the aromatic rings in the ligands L_H–L_{Cum}.

Experimental

All manipulation involving air- and/or moisture-sensitive compounds were performed under nitrogen atmosphere using a standard Schlenk technique and a MBraun glovebox. Toluene (99.5%; Carlo Erba) and THF (99%; Sigma-Aldrich) were used as received or refluxed for 48 h over sodium and distilled before use for the moisture- and oxygen-sensitive reactions. All other reagents were used as received (Sigma-Aldrich) or distilled under reduced pressure over calcium hydride. The ligand precursor 6,6'-(((5-(*tert*-butyl)-2-hydroxy-1,3-phenylene)bis(methylene))bis(sulfanediyl))-bis(2,4-di-*tert*-butylphenol) (L_{*t*-Bu}, Scheme 2) and the corresponding iron(III) complex (C_{*t*-Bu}, Scheme 2) were synthesized according to the reported procedure.⁹ Deuterated solvents were purchased from Euriso-Top or Sigma-Aldrich and used as received.

NMR spectra were collected on Bruker Avance spectrometers (600, 400, 300 or 250 MHz for ¹H), and the chemical shifts were referenced to tetramethylsilane (TMS) as the external reference, using the residual protio signal of the deuterated solvents. Measurements of effective magnetic moments were performed on a Bruker Avance 600 MHz spectrometer at 25 °C in CD₃CN using a 5 mm Wilmad coaxial insert NMR tube. Solutions of the complex C_H (1.7 mM) and C_{Cum} (2.1 mM) in CD₃CN with 1% of TMS were prepared under a nitrogen atmosphere. The effective magnetic moment (μ_{eff}) was calculated from $\mu_{\text{eff}} = 8\chi_g M_w T$, where χ_g (cm³ g⁻¹) is the corrected molar susceptibility derived from $\chi_g = 3\Delta_f/4\pi f_o C M_w + \chi_o$,¹² Δ_f is the shift in frequency (Hz) of the signal of the solvent in the presence of the complex from the value of the pure solvent, C is the concentration of the complex (mol cm⁻³), M_w is the molecular weight of the complex (g mol⁻¹), f_o is the operating frequency of the spectrometer (Hz), and χ_o is the mass susceptibility of the pure solvent (-0.524×10^{-6} cm³ g⁻¹ for CD₃CN). The $4\pi/3$ is the shape factor



Scheme 2 Synthetic strategy for the production of the pro-ligands and of the iron(III) complexes.

1 for a cylindrical sample in a superconducting magnet. Elemental analysis was
performed on a CHNS Thermo Scientific Flash EA 1112 equipped with a thermal
conductivity detector. ESI-MS spectra were acquired on a Quattro *micro*TM API
5 triple quadrupole mass spectrometer from Waters equipped with an electrospray
ion source, using acetonitrile as the solvent. FT-IR measurements were carried out
on a Bruker Vertex 70 spectrometer equipped with a DTGS detector and a Ge/KBr
beam splitter. The samples were analysed as chloroform solutions or in the form
of KBr disks. UV-Vis acquisitions were collected on a PerkinElmer Lambda EZ 201.

10 **Synthesis of the pro-ligand 2,2'-(((5-(*tert*-butyl)-2-hydroxy-1,3-phenylene)
bis(methylene))bis(sulfanediyl))-bisphenol (L_H, Scheme 2)**

A 500 mL two-neck round-bottom flask equipped with a condenser and a
magnetic stirring bar was charged, under a nitrogen atmosphere, with 5.00 g of 2-
15 mercaptophenol (35.7 mmol) dissolved in 160 mL of ethanol, and 1.43 g of NaOH
(35.7 mmol); the mixture was refluxed for about 1 hour until complete dissolution
of the hydroxide. 6.00 g of 2,6-dibromomethyl-4-*t*-butylphenol (17.83 mmol) dis-
solved in 50 mL of ethanol were slowly added at 0 °C and the mixture was heated
to the reflux of the solvent that was kept overnight. The solvent was distilled off,
20 water was added until dissolution of the NaBr by-product and the aqueous phase
was extracted twice with methylene chloride. The combined organic phases were
dried with MgSO₄ and, after evaporation of the solvent, the product was recovered
as a white solid. Yield: 7.36 g, 96.8%. EA for C₂₄H₂₆O₃S₂ calc.: C, 67.57; H, 6.14; S
25 15.03; found: C, 67.27; H, 6.07; S, 14.93. Mass spectrum: 449.3 *m/z* (MNa⁺).

25 **Synthesis of the iron(III) complex C_H (Scheme 2)**

A 500 mL two-neck round-bottom flask, equipped with a magnetic stirring bar,
was charged with 0.51 g of sodium hydride (21.0 mmol) suspended in 130 mL of
30 THF. A solution of 2.72 g of the ligand precursor L_H (6.37 mmol) dissolved in 180
mL of THF was slowly added at room temperature under a protective nitrogen
atmosphere, and allowed to react overnight. The resulting suspension was filtered
through celite and slowly added at room temperature to 1.00 g of anhydrous
35 iron(III) chloride (6.24 mmol) dissolved in 100 mL of THF. The rapid colour
change to a deep purple was observed and the reaction was kept overnight. The
mixture was then filtered through celite and the solvent removed under reduced
pressure affording a deep purple crystalline solid. Yield: 2.80 g, 94%. EA for
40 C₄₈H₄₆Fe₂O₆S₄ calc.: C, 60.13; H, 4.84; S, 13.38; found: C, 60.33 H, 4.47; S, 13.28.
Mass spectrum: 981.2 *m/z* (MNa⁺). UV-Vis: ε₄₇₀ = 2804 L mol⁻¹ cm⁻¹.

40 **Synthesis of the pro-ligand 2,2'-(((5-(*tert*-butyl)-2-hydroxy-1,3-phenylene)
bis(methylene))bis(sulfanediyl))-bis(2,4-di-(α,α'-dimethylbenzyl)phenol) (L_{Cum},
Scheme 2)**

45 A 50 mL two-neck round-bottom flask equipped with a condenser and a magnetic
stirring bar was charged, under a nitrogen atmosphere, with 2.02 g of 2-mercapto-
4,6-bis-(α,α'-dimethylbenzyl)-2-phenol (5.56 mmol) dissolved in 25 mL of ethanol,
0.30 g of NaOH (22.2 mmol) and the mixture was refluxed for about 1 hour until
complete dissolution of the hydroxide. 0.94 g of 2,6-dibromomethyl-4-*t*-butyl-
50 phenol (2.8 mmol) dissolved in 10 mL of ethanol was slowly added at 0 °C and the
mixture was heated to the reflux of the solvent that was kept overnight. The

1 solvent was distilled off, water was added until dissolution of the NaBr by-
product, and the aqueous phase was extracted twice with methylene chloride.
The combined organic phases were dried with MgSO₄ and, after evaporation of
5 the solvent, the resulting crude solid was purified by column chromatography
(light petroleum/ethyl acetate = 95/5). Yield: 0.81 g, 33%. EA for C₆₀H₆₆O₃S₂ calc.:
C, 80.13; H, 7.40; S 7.13; found: C, 79.94; H, 7.27; S, 7.03. Mass spectrum: 899.2 *m/z*
(M⁺), 922.2 *m/z* (MNa⁺).

10 Synthesis of the iron(III) complex C_{Cum} (Scheme 2)

A 50 mL two-neck round-bottom flask, equipped with a magnetic stirring bar was
charged with 0.073 g of sodium hydride (2.60 mmol) suspended in 20 mL of THF,
and a solution of 0.78 g of the ligand precursor L_{Cum} (0.87 mmol) dissolved in 25
15 mL of THF was slowly added at room temperature under a protective nitrogen
atmosphere, and allowed to react overnight. The resulting suspension was filtered
through celite and slowly added at room temperature to 0.138 g of anhydrous
iron(III) chloride (0.85 mmol) dissolved in 20 mL of THF. A rapid colour change to
deep blue was observed and the reaction was kept overnight. The mixture was
20 then filtered through celite and the solvent removed under reduced pressure
affording a deep blue crystalline solid. Yield: 0.79 g, 97.7%. EA for
C₁₂₀H₁₂₆Fe₂O₆S₄ calc.: C, 75.69; H, 6.67; S, 6.74; found: C, 75.42; H, 6.58; S, 6.67.
Mass spectrum: 1904 *m/z* (M⁺), 1927 *m/z* (MNa⁺). UV-Vis: ε₅₈₅ = 7188 L mol⁻¹
cm⁻¹.

25 Typical procedure for CO₂/epoxide coupling to cyclic carbonates catalyzed by C_H/TBAB (referred to entry 3, Table 1)

A 60 mL stainless steel pressure reactor equipped with a magnetic stirring bar was
charged, under CO₂ atmosphere, with 17.1 mg of catalyst C_H (1.79 × 10⁻⁵ mol)
30 and 11.5 mg of TBAB (3.57 × 10⁻⁵ mol) dissolved in 5.0 mL of PO (7.15 × 10⁻²
mol). The reaction mixture was pressurized with CO₂ at 2 MPa and stirred at 120
°C for 1 h. The reactor was cooled with ice, the CO₂ was released, and mesitylene
was added as an internal standard before the mixture was analysed by ¹H-NMR
spectroscopy using CD₂Cl₂ as the solvent. Yield 49.2%.

35 Results and discussion

The ligands L_H-L_{Cum} were synthesized using the same synthetic strategy reported
40 for the synthesis of ligand L_{t-Bu} (see Scheme 2).⁹ The new ligands were purified by
recrystallization or by column chromatography, and fully characterized using
NMR, elemental analysis, MS, and FT-IR (see ESI†).

These ligands were chosen in order to study the influence of the substituents
on the aromatic rings on the catalytic activity resulting by diminishing (L_H) and
45 increasing (L_{Cum}) the steric bulk. The complexes C_H and C_{Cum} were obtained by
reaction of the corresponding sodium salt obtained by reaction with 3 equivalents
of NaH in THF with an equimolar amount of anhydrous FeCl₃ in analogy to the
procedure used for the synthesis complex C_{t-Bu}.⁹

The complexes, C_H and C_{Cum}, were recovered by crystallization in tetrahydro-
50 furofuran as small needle-shaped crystals with a red-purplish and deep-blue
colour respectively. Unfortunately, in both cases, the crystals were not suitable

1 for structural resolution by means of single crystal X-ray diffraction. Indeed the
formation of the adduct iron-ligand was initially confirmed using elemental
analysis and FT-IR spectroscopy, which revealed the disappearance of the vibra-
5 tion due to the hydroxyl of the pro-ligand as a result of the coordination of the
corresponding phenolate to the iron (see Fig. S11 and S17†). The ESI-MS spectra
of C_H and C_{Cum} show molecular ion peaks at 899 and 1927 m/z respectively, which
are consistent with the dinuclear structure observed in the case of complex C_{t-Bu} .
The Evans method¹² was applied for the determination of the solution magnetic
10 susceptibility and a value of 8.1 μB for C_H and 7.2 μB for C_{Cum} resulted at 25 °C,
which are close to the values calculated for two isolated high spin (HS) iron(III)
centres (8.37 μB)¹³ and to that observed previously for C_{t-Bu} ,⁹ confirming the
dimeric nature of the complexes and indicating some degree of ferromagnetic
coupling between the iron atoms being both in a HS ($s = 5/2$) state. Consequently,
15 the UV-Vis spectra, as expected for two HS iron(III) centres in an octahedral
environment, showed no d-d transitions but only a strong ligand-to-metal charge
transfer absorption at 470 nm (21 276 cm^{-1} ; $\epsilon_{470} = 2804 \text{ L mol}^{-1} \text{ cm}^{-1}$) for C_H and
at 585 nm (21 276 cm^{-1} ; $\epsilon_{585} = 7188 \text{ L mol}^{-1} \text{ cm}^{-1}$) for C_{Cum} . In addition, the
coordination of the sulfur atoms, necessary to ensure the octahedral geometry for
20 the iron centre, was confirmed by the shift of the vibration bands in the infrared
spectra of the complex to respect that of the free pro-ligand, respectively in the
spectral regions: 1450–1415 cm^{-1} , 1270–1220 cm^{-1} and 680–600 cm^{-1} , diagnos-
tics for the alkyl-sulphide moiety (see Fig. S12–S14 and S18–S20†).¹⁴ In particular
the shift to the red, observed for the CH_2-S-C deformation (spectral region 1450–
25 1415 cm^{-1} ; Fig. S12 and S18†) and for the C–S stretching (spectral region 680–600
 cm^{-1} ; Fig. S14 and S20†), accounts for a weakening of the C–S bond as a result of
the coordination of the sulphur to the iron, whereas the blue shift for the CH_2-S-
C wagging (spectral region 1270–1220 cm^{-1} ; Fig. S13 and S19†) indicates a
reduced conformational mobility of the moieties after coordination to the metal.

30 In order to check the catalytic performances of the iron(III) complexes, C_H and
 C_{Cum} , for the coupling of (\pm)-propylene oxide (PO) with carbon dioxide and
directly compare the results with the previously reported catalyst C_{t-Bu} , we con-
ducted several catalytic tests for the three complexes (C_H , C_{t-Bu} , C_{Cum}) under the
same reaction conditions. The main results are summarized in Table 1. Due to the
35 encouraging preliminary results obtained with catalyst C_{t-Bu} we initially decided
to use a low catalyst loading (0.025% mol) and as co-catalyst the *n*-tetrabutyl-
ammonium bromide (TBAB) (with a co-catalyst/catalyst molar ratio of 2) under a
 CO_2 pressure of 2 MPa and solvent-free conditions. The reaction time was reduced
to 1 hour in order to better evaluate the turnover frequencies (TOF) of the catalytic
40 systems. In the temperature range 80–140 °C, an increase of activity by increasing
the temperature was observed for all the titled catalysts, with the maximum
activity shown by C_H which reached a conversion of 61% with a TOF value of 2420
 h^{-1} at 140 °C (entry 4), showing that a less encumbered metal centre is more
accessible to the substrate. Notably, at a lower temperature (80–100 °C) the
45 catalytic performances of C_H are sensibly scarcer (entries 1 and 2) compared to the
more sterically demanding catalysts C_{t-Bu} and C_{Cum} (entries 5, 6 and 9, 10
respectively; see also Fig. 1). This apparent contradiction is probably due to the
lower solubility of complex C_H in the reaction medium compared to the more
soluble catalysts C_{t-Bu} and C_{Cum} . In order to support our hypothesis, we per-
50 formed the reactions using methyl ethyl ketone (MEK) as the solvent with the aim

Table 1 Synthesis of propylene carbonate through CO₂/propylene oxide coupling catalyzed by Fe(III) catalysts

Propylene oxide + CO₂ → Propylene carbonate

Entry ^a	Catalyst	Co-catalyst		PO/co-cat./ cat. (molar ratio)	Solvent	T (°C)	P _{CO₂} (MPa)	Conversion ^{bc} (%)	TOF ^d (h ⁻¹)
		(mol %)							
1	C _H	TBAB	0.05	4000/2/1	—	80	2	2.4	96
2	C _H	TBAB	0.05	4000/2/1	—	100	2	16.9	680
3	C _H	TBAB	0.05	4000/2/1	—	120	2	49.2	1970
4	C _H	TBAB	0.05	4000/2/1	—	140	2	60.5	2420
5	C _{t-Bu}	TBAB	0.05	4000/2/1	—	80	2	4.6	185
6	C _{t-Bu}	TBAB	0.05	4000/2/1	—	100	2	16.8	675
7	C _{t-Bu}	TBAB	0.05	4000/2/1	—	120	2	39.8	1595
8	C _{t-Bu}	TBAB	0.05	4000/2/1	—	140	2	57.4	2300
9	C _{Cum}	TBAB	0.05	4000/2/1	—	80	2	4.6	185
10	C _{Cum}	TBAB	0.05	4000/2/1	—	100	2	20.1	805
11	C _{Cum}	TBAB	0.05	4000/2/1	—	120	2	29.4	1175
12	C _{Cum}	TBAB	0.05	4000/2/1	—	140	2	47.5	1900
13	C _H	TBAB	0.05	4000/2/1	MEK	100	2	8.9	355
14	C _H	TBAB	0.05	4000/2/1	MEK	120	2	31.1	1245
15	C _{t-Bu}	TBAB	0.05	4000/2/1	MEK	100	2	7.8	310
16	C _{t-Bu}	TBAB	0.05	4000/2/1	MEK	120	2	20.3	810
17	C _{Cum}	TBAB	0.05	4000/2/1	MEK	100	2	8.3	330
18	C _{Cum}	TBAB	0.05	4000/2/1	MEK	120	2	21.4	855
19	C _H	TBAB	0.05	4000/2/1	—	120	0.5	35.6	1425
20	C _H	TBAB	0.05	4000/2/1	—	120	4	55.7	2230
21	C _H	TBAI	0.05	4000/2/1	—	120	2	42.3	1690
22	C _H	[PPN] Cl	0.05	4000/2/1	—	120	2	38.9	1555
23	C _H	DMAP	0.05	4000/2/1	—	120	2	0.4	16
24	C _H	TBAB	0.1	4000/4/1	—	120	2	82.4	3300
25	C _H	TBAB	0.25	4000/10/1	—	120	2	95.2	3810
26	C _{t-Bu}	TBAB	0.25	4000/10/1	—	120	2	84.6	3385
27	C _{Cum}	TBAB	0.25	4000/10/1	—	120	2	63.2	2530
28 ^e	—	TBAB	0.05	4000/2/0	—	120	2	32.6	—

^a Basic reaction conditions: propylene oxide (5 mL; 7.15×10^{-2} mol), catalyst loading = 0.025 mol% (1.79×10^{-5} mol), 1 h. ^b Determined by NMR (using mesitylene as an internal standard). ^c The selectivity for the formation of propylene carbonate was found to be >99%. ^d Turnover frequency ($\text{mol}_{\text{PC}} \text{mol}_{\text{catalyst}}^{-1} \text{reaction time}^{-1}$). ^e Control experiment in absence of catalyst: reaction time = 24 h.

of suppressing the negative effects on the catalytic activity due to the low solubility of catalyst C_H. As a matter of fact, the results obtained at both 100 and 120 °C clearly show that the catalytic activity of the more open catalyst C_H is comparable at 100 °C to those of catalysts C_{t-Bu} and C_{Cum} (entries 13, 15 and 17) and is sensibly higher at 120 °C (entries 14, 16 and 18), indicating a crucial role for temperature in determining the catalytic activity for this class of catalysts.

1 For the more active catalyst C_H , we also explored the effect of CO_2 pressure on
the catalytic activity showing that halving or doubling carbon dioxide pressure
has a small effect on the catalytic performances (compare entry 3 with entries 19
and 20).

5 In analogy to the results obtained in the presence of the complex C_{t-Bu} , the use
of other commonly employed co-catalysts such as *n*-tetrabutylammonium iodide
(TBAI), bis(triphenylphosphine)iminium chloride (PPNCl), and 4-dimethylami-
nopyridine (DMAP) resulted in a lowering of the catalytic activity (entries 21–23).
10 In particular, while the two halogen containing co-catalysts (TBAI and PPNCl)
show an activity comparable to that of TBAB, the use of DMAP results in a
dramatic reduction of the catalytic activity. Moreover, the absence of the cocata-
lyst (TBAB) or of the iron(III) catalyst C_H resulted in a complete loss of the catalytic
activity in the first case and in a conversion of only 33% (entry 28) in the second
15 case even after 24 h, highlighting a synergic effect between the catalyst and the co-
catalyst for carbonate formation.

Intriguingly, by increasing the co-catalyst/catalyst molar ratio to higher values
(4 for entry 24 and 10 for entry 25) a further increase of the catalytic activity was
observed with a conversion of 95% in 1 hour and a TOF of 3800, which is not only
20 the highest reported so far for an iron based catalyst but compares well with the
more active catalysts based on other metals.^{5a} It is worth noting that under these
conditions the order of reactivity is $C_H > C_{t-Bu} > C_{Cum}$ (entries 25–27) confirming
that a less sterically congested metal centre is more reactive in the CO_2 /epoxide
coupling.

25 Having established that catalyst C_H is a highly active and selective catalyst for
the formation of cyclic carbonates, in order to expand the scope of this catalyst we
explored the cycloaddition of CO_2 to a variety of functionalized terminal epoxides
providing organic cyclic carbonates, under similar catalytic conditions as used in
the case of propylene oxide (reaction condition of entry 3 of Table 1). The main
30 results are reported in Table 2. All the substrates were conveniently converted to

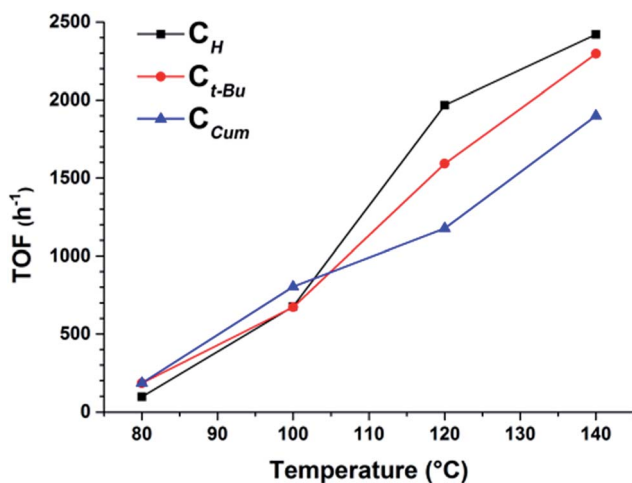


Fig. 1 TOF of the iron(III) complexes as a function of the reaction temperature (entries 1–12, Table 1).

Table 2 Synthesis of organic cyclic carbonate through CO₂/epoxide coupling catalyzed by Fe(III) catalysts


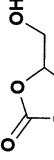

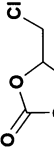
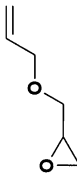
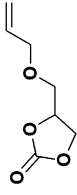
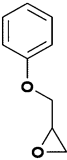
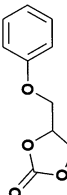
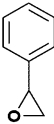
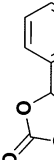

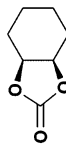

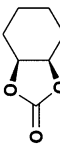

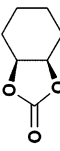
Entry ^a	Catalyst		TBAB (mol%)	Epox./co-cat./cat. (molar ratio)	Substrate	Product ^{b,c}	Time (h)	Conversion ^{b,c} (%)	TOF ^d (h ⁻¹)
	(mol%)								
29	C _H	0.025	0.05	4000/2/1			1	95.7	3830
30	C _H	0.025	0.05	4000/2/1			1	40.2	1610
31	C _H	0.025	0.05	4000/2/1			1	40	1600
32	C _H	0.025	0.05	4000/2/1			1	18.6	745
33	C _H	0.025	0.05	4000/2/1			1	16.4	655
34 ^e	C _H	0.2	0.4	500/2/1			3	62.8	105

Table 2 (Contd.)

Entry ^a	Catalyst		TBAB (mol%)	Epoxy./co-cat./cat. (molar ratio)	Substrate	Product ^{b,c}	Time (h)	Conversion ^{b,c} (%)	TOF ^d (h ⁻¹)
	(mol%)								
35 ^e	C _t -Bu	0.2	0.4	500/2/1			3	23.9	40
36 ^f	C _c um	0.2	0.4	500/2/1			3	6.8	11

^a Basic reaction conditions: epoxide = 7.15×10^{-2} mol, temperature = 120 °C, carbon dioxide pressure = 2 MPa. ^b Determined by NMR (using mesitylene as an internal standard). ^c The selectivity for the formation of cyclic carbonate was found to be >99%. ^d Turnover frequency (mol_{COC} mol_{cat}⁻¹ reaction time⁻¹). ^e A selectivity >99% for the formation of the *cis* isomer of the carbonate was observed. ^f Traces of polycarbonate were found.

1 the corresponding cyclic carbonates with good yields even at relatively short
reaction times (1 h). Notably, glycerol carbonate¹⁵ which is a very interesting target
molecule due to its properties, is easily obtained from glycidol in excellent yield
5 (96%) with a TOF of 3830 h⁻¹. These results are even superior to those observed
for propylene oxide under the same reaction conditions (compare entry 3 of Table
1 with entry 29 of Table 2) and, also in this case, it is the highest observed TOF
reported for this substrate.

10 Furthermore, we explored the synthesis of cyclic carbonates starting from the
more challenging substrate cyclohexene oxide (CHO). Actually, the formation of
the cyclic carbonate from CHO is disfavored with respect to the formation of the
corresponding polycarbonate because of the geometric strain due to the forma-
tion of two interconnected six- and five-membered cycles. In our case, we obtained
15 good conversion (63%) within 3 h with a complete selectivity toward the cyclic
product in the case of complex C_H. In this case the role of the steric bulkiness of
the substituents on the aromatic rings is even more pronounced than in the case
of PO, with the catalytic activity decreasing with steric bulk of the substituents: C_H
> C_{t-Bu} > C_{Cum} (see entries 34–36).

20 It is worth mentioning that, as already observed for other iron based catalytic
systems, the cyclic carbonates from CHO were produced selectively with *cis*-
stereochemistry, as pointed out by NMR and FT-IR analysis, that revealed strong
adsorption bands at 1802 cm⁻¹, previously assigned to the stretching of the
carbonyl, respectively for the *cis*-cyclohexene carbonate.^{11f}

25 Conclusions

In conclusion, we reported on the synthesis and characterization of two new, air
stable, dimeric iron(III) complexes bearing thioether-triphenolate ligands. When
30 activated by tetrabutylammonium bromide the title iron(III) complexes are very
effective in the coupling of CO₂ with epoxides, giving excellent results in terms of
activity, and chemo- and stereo- selectivity under solvent-free conditions. In
particular, the less sterically demanding C_H complex shows the best catalytic
performances in terms of activity and selectivity for a wide number of substrates
35 with TOF values up to 3830 h⁻¹. These results demonstrate, for this class of
catalysts, that a more accessible metal centre is crucial to increase the activity in
the cycloaddition of CO₂ to epoxide. Finally, these outcomes clearly show that this
class of iron(III) based catalysts, bearing two sulfur atoms in the ligand skeleton,
are competitive in term of activity, selectivity and substrate scope respect to other
40 catalytic systems based on more toxic and/or expensive metals, for the formation
of cyclic carbonates.

45 Acknowledgements

We gratefully acknowledge the Ministero dell'Istruzione, dell'Università e della
Ricerca (MIUR, Roma, Italy) for FARB 2014 and PRIN 2010–2011, the Regione
Campania (POR FSE, project: “Materiali e Strutture Intelligenti”, MASTRI, Code
4-17-3, CUPB25B09000010007) and the Centro di Tecnologie Integrate per la
50 Salute (Project PONA3_00138) for the 600 MHz NMR instrument time funding.
Alexander von Humboldt Foundation is deeply acknowledged for a renewal

1 fellowship (C.C.). Dr Patrizia Oliva, Dr Patrizia Iannece and Dr Ivano Immediata
from Università degli Studi di Salerno are acknowledged for technical assistance.

Notes and references

- 5
- 1 (a) M. Aresta and A. Dibenedetto, *Dalton Trans.*, 2007, 2975–2992; (b) M. Aresta, A. Dibenedetto and A. Angelini, *Chem. Rev.*, 2013, **114**, 1709–1742; (c) D. J. Darensbourg, *Inorg. Chem.*, 2010, **49**, 10765–10780; (d) I. Omae, *Coord. Chem. Rev.*, 2012, **256**, 1384–1405; (e) E. A. Quadrelli, G. Centi, J.-L. Duplan and S. Perathoner, *ChemSusChem*, 2011, **4**, 1194–1215; (f) *Activation of Carbon Dioxide*, ed. S. L. Suib, Elsevier, Amsterdam, 2013.
- 10
- 2 (a) M. Grasemann and G. Laurenczy, *Energy Environ. Sci.*, 2012, **5**, 8171–8181; (b) S. Moret, P. J. Dyson and G. Laurenczy, *Nat. Commun.*, 2014, **5**.
- 15
- 3 F. Studt, I. Sharafutdinov, F. Abild-Pedersen, C. F. Elkjær, J. S. Hummelshøj, S. Dahl, I. Chorkendorff and J. K. Nørskov, *Nat. Chem.*, 2014, **6**, 320–324.
- 4 C. Maeda, Y. Miyazaki and T. Ema, *Catal. Sci. Technol.*, 2014, **4**, 1482–1497.
- 5 (a) C. Martín, G. Fiorani and A. W. Kleij, *ACS Catal.*, 2015, **5**, 1353–1370; (b) J. W. Comerford, I. D. V. Ingram, M. North and X. Wu, *Green Chem.*, 2015, **17**, 1966–1987; (c) N. Kielland, C. J. Whiteoak and A. W. Kleij, *Adv. Synth. Catal.*, 2013, **355**, 2115–2138; (d) M. North, in *New and Future Developments in Catalysis*, ed. S. L. Suib, Elsevier, Amsterdam, 2013, pp. 379–413; (e) M. Cokoja, C. Bruckmeier, B. Rieger, W. A. Herrmann and F. E. Kühn, *Angew. Chem., Int. Ed.*, 2011, **50**, 8510–8537; (f) R. Li, X. Tong, X. Li and C. Hu, *Pure Appl. Chem.*, 2012, **84**, 621–636; (g) A. Decortes, A. M. Castilla and A. W. Kleij, *Angew. Chem., Int. Ed.*, 2010, **49**, 9822–9837.
- 20
- 6 (a) M. I. Childers, J. M. Longo, N. J. Van Zee, A. M. LaPointe and G. W. Coates, *Chem. Rev.*, 2014, **114**, 8129–8152; (b) M. Taherimehr and P. P. Pescarmona, *J. Appl. Polym. Sci.*, 2014, **131**, 41141; (c) D. J. Darensbourg and S. J. Wilson, *Green Chem.*, 2012, **14**, 2665–2671; (d) S. Klaus, M. W. Lehenmeier, C. E. Anderson and B. Rieger, *Coord. Chem. Rev.*, 2011, **255**, 1460–1479.
- 25
- 7 (a) B. Schöffner, F. Schöffner, S. P. Verevkin and A. Börner, *Chem. Rev.*, 2010, **110**, 4554–4581; (b) A.-A. G. Shaikh and S. Sivaram, *Chem. Rev.*, 1996, **96**, 951–976.
- 30
- 8 (a) D. J. Darensbourg and A. D. Yeung, *Polym. Chem.*, 2014, **5**, 3949–3962; (b) T.-T. Wang, Y. Xie and W.-Q. Deng, *J. Phys. Chem. A*, 2014, **118**, 9239–9243.
- 9 A. Buonerba, A. De Nisi, A. Grassi, S. Milione, C. Capacchione, S. Vagin and B. Rieger, *Catal. Sci. Technol.*, 2015, **5**, 118–123.
- 35
- 10 (a) I. Bauer and H.-J. Knölker, *Chem. Rev.*, 2015, DOI: 10.1021/cr500425u; (b) *Iron Catalysis Fundamentals and Applications*, ed. B. Plietker, Springer, 2011; (c) C.-L. Sun, B.-J. Li and Z.-J. Shi, *Chem. Rev.*, 2010, **111**, 1293–1314; (d) A. Correa, O. Garcia Mancheno and C. Bolm, *Chem. Soc. Rev.*, 2008, **37**, 1108–1117.
- 40
- 11 (a) M. Taherimehr, J. P. C. C. Sertã, A. W. Kleij, C. J. Whiteoak and P. P. Pescarmona, *ChemSusChem*, 2015, **8**, 1034–1042; (b) X. Sheng, L. Qiao, Y. Qin, X. Wang and F. Wang, *Polyhedron*, 2014, **74**, 129–133; (c) M. Adolph, T. A. Zevaco, C. Altesleben, O. Walter and E. Dinjus, *Dalton Trans.*, 2014, 3285–3296; (d) M. A. Fuchs, T. A. Zevaco, E. Ember, O. Walter, I. Held, E. Dinjus and M. Doring, *Dalton Trans.*, 2013, 5322–5329; (e) M. Taherimehr, S. M. Al-Amsyar, C. J. Whiteoak, A. W. Kleij and P. P. Pescarmona, *Green*
- 45
- 50

- 1 *Chem.*, 2013, **15**, 3083–3090; (f) C. J. Whiteoak, E. Martin, E. Escudero-Adán
and A. W. Kleij, *Adv. Synth. Catal.*, 2013, **355**, 2233–2239; (g) C. J. Whiteoak,
E. Martin, M. M. Belmonte, J. Benet-Buchholz and A. W. Kleij, *Adv. Synth.*
5 *Catal.*, 2012, **354**, 469–476; (h) C. J. Whiteoak, B. Gjoka, E. Martin,
M. M. Belmonte, E. C. Escudero-Adán, C. Zonta, G. Licini and A. W. Kleij,
Inorg. Chem., 2012, **51**, 10639–10649; (i) A. Buchard, M. R. Kember,
K. G. Sandeman and C. K. Williams, *Chem. Commun.*, 2011, **47**, 212–214; (j)
10 J. E. Dengler, M. W. Lehenmeier, S. Klaus, C. E. Anderson, E. Herdtweck
and B. Rieger, *Eur. J. Inorg. Chem.*, 2011, 336–343.
- 12 *Physical Methods in Bioinorganic Chemistry*, ed. J. J. J. Y. Girerd, University
Science Books, Sausalito, CA, 2000.
- 13 *Advanced Inorganic Chemistry*, ed. F. A. Cotton, G. Wilkinson, C. A. Murillo and
E. M. Bochmann, Wiley, 6th edn, 1999.
- 15 14 (a) *Interpreting Infrared, Raman, and Nuclear Magnetic Resonance Spectra*, ed. R.
A. Nyquist, Academic Press, San Diego, 2001, pp. 65–83; (b) *The Sadtler*
handbook of infrared spectra, ed. W. W. Simons, Sadtler Research
Laboratories, Philadelphia, 1978.
- 20 15 M. O. Sonnati, S. Amigoni, E. P. Taffin de Givenchy, T. Darmanin, O. Choulet
and F. Guittard, *Green Chem.*, 2013, **15**, 283–306.

25

30

35

40

45

50

PAPER

Improving the efficiency of electrochemical CO₂ reduction using immobilized manganese complexes†

James J. Walsh,‡ Charlotte L. Smith,‡ Gaia Neri, George F. S. Whitehead, Craig M. Robertson and Alexander J. Cowan*

Received 11th May 2015, Accepted 10th June 2015

DOI: 10.1039/c5fd00071h

Immobilization of [Mn(bpy)(CO)₃Br], (**1**) and [Mn(bpy(^tBu)₂)(CO)₃Br] (**2**, where (bpy(^tBu)₂) = 4,4'-di-*tert*-butyl-2,2'-bipyridine) in Nafion/multi-walled carbon nanotubes (MWCNT) on glassy carbon yielded highly active electrodes for the reduction of CO₂ to CO in aqueous solutions at pH 7. Films incorporating **2** have significantly improved selectivity towards CO₂, with CO : H₂ ~ 1 at -1.4 V vs. SCE, exceeding that for the previously reported **1**/MWCNT/Nafion electrode. Furthermore, we report the synthesis and subsequent electrochemical characterization of two new substituted Mn(II) bipyridine complexes, [Mn(bpy(COOH)₂)(CO)₃Br] (**3**) and [Mn(bpy(OH)₂)(CO)₃Br] (**4**) (where (bpy(COOH)₂) = 4,4'-di-carboxy-2,2'-bipyridine and (bpy(OH)₂) = 4,4'-di-hydroxy-2,2'-bipyridine). Both **3** and **4** were found to have some activity towards CO₂ in acetonitrile solutions, however once immobilized in Nafion membranes CO₂ reduction was found to not occur at significant levels.

1 Introduction

Carbon capture coupled with utilisation is a potentially sustainable route to useful feedstocks and fuels such as CO, HCOOH, CH₃OH and CH₄. Electro-catalytic CO₂ reduction is a particularly attractive utilisation pathway as the energetic input for CO₂ reduction can come from renewable sources of power (*e.g.* wind, solar) with the production of chemical fuels offering a solution to the intermittent nature of such renewables. Whilst the direct one electron reduction of CO₂ is extremely challenging, occurring at -2.15 V vs. SCE (pH 7),¹ the

Department of Chemistry, Stephenson Institute for Renewable Energy, The University of Liverpool, L69 7ZD, Liverpool, UK. E-mail: a.j.cowan@liverpool.ac.uk

† Electronic supplementary information (ESI) available: X-ray diffraction details and data, scan rate dependence of **3** and **4** in solution, FTIR spectra showing solvolysis, deconvoluted FTIR-SEC data, the effects of hourly gas re-purging on CPE of **2**/Nafion/MWCNT and temperature dependence on drop drying. CCDC 1061484 and 1061485. For ESI and crystallographic data in CIF or other electronic format see DOI: 10.1039/c5fd00071h

‡ These authors share equal contribution.

1 multielectron, multiproton reduction of CO₂ can be achieved at more moderate
potentials (CO₂ + 2H⁺ + 2e⁻ → CO + H₂O, -0.77 V vs. SCE, pH 7).² However in
order to achieve high Faradaic efficiencies for CO₂ reduction a suitably selective
5 electrocatalyst for CO₂ is required as the production of H₂ (2H⁺ + 2e⁻ → H₂, -0.65
V vs. SCE, pH 7) often dominates in protic solvents.

Homogenous electrocatalysts based on *fac*-[M(bpy)(CO)₃X] (where M = Re, Mn;
X = Cl⁻, Br⁻ and bpy = 2,2'-bipyridine) have been widely studied for the reduction
of CO₂ to CO due to their high selectivities and ease of synthetic modification.^{3,4}
Early studies concentrated on [Re(bpy)(CO)₃Br] and its derivatives;^{5,6} however in
10 2011 it was shown that the lower cost manganese analogue, [Mn(bpy)(CO)₃Br] **1**, is
also an excellent homogeneous electrocatalyst for the reduction of CO₂ to CO.⁷
Using **1**, CO₂ reduction was reported to occur at a potential (*ca.* -1.4 V vs. SCE)
significantly more positive than that required using the analogous rhenium
15 complex, providing that a suitable Brønsted acid such as water was present in the
organic solvent (typically CH₃CN or DMF). A range of catalysts of the form
[Mn^I(L)(CO)₃X] (L = bpy,⁷ 4,4' or 6,6'-disubstituted-2,2'-bipyridine)^{8,9} have since
been reported with the aim of improving both the turnover frequency (TOF) and
overpotential for CO₂ catalysis using **1** and amongst the most active is
20 [Mn(bpy(^tBu)₂)(CO)₃Br] (**2**, where (bpy(^tBu)₂) = 4,4'-di-*tert*-butyl-bipyridine). **2** has
been reported to have a TOF of 340 s⁻¹ at -2.2 V vs. SCE for CO production in the
presence of 1.4 M 2,2,2-trifluoroethanol (TFE), approximately 300 times higher
than that of complex **1**, although it should be noted that the onset for catalysis is
25 *ca.* 200 mV cathodic of **1**.⁸ Detailed electrochemical, spectroscopic and theoretical
studies have identified several key aspects of the mechanism of CO₂ reduction
using **1** and **2**.^{8,10-12} It is known that upon initial one-electron reduction, bromide
loss and dimerization with another reduced moiety to yield [Mn(bpy)(CO)₃]₂
rapidly occurs. Reduction of the dimer then leads to the formation of the primary
active catalyst, [Mn(bpy)(CO)₃]⁻.⁷ Using 2D-EPR measurements it has also been
30 shown that with a closely related complex, [Mn(bpy(Me)₂)(CO)₃Br] (where
(bpy(Me)₂) = 4,4'-dimethyl-2,2'-bipyridine), CO₂ reduction can also occur *via* a
second pathway involving direct CO₂ and H⁺ addition to the dimeric species
formed upon reduction.¹³ Due to the propensity of the [Mn^I(L)(CO)₃X] complexes
to dimerize upon reduction, Kubiak *et al.* developed a complex with bulky
35 bipyridine ligands, [Mn(mesbpy)(CO)₃Br] (where mesbpy = 6,6'-dimesityl-2,2'-
bipyridine),⁹ that was too sterically hindered to undergo dimerization, with the
aim of modifying the catalytic mechanism. Promisingly, such an approach led to
a large enhancement in TOF (*ca.* 5000 s⁻¹, 1.4 M TFE at *ca.* -1.8 V vs. SCE),
although no improvement in onset potential for catalysis was achieved when
40 compared to **1**. In addition to studies on the modification of the bpy ligand,
several groups have also explored the use of N-heterocyclic carbenes,^{14,15} nonar-
omatic α-diimine ligands,^{16,17} hydroxyphenol-substituted bpy¹⁸ and pentadentate
chelating¹⁹ ligands with Mn(I) centres for use as potential CO₂ reduction catalysts
with varying degrees of success.

To date, studies on [Mn^I(L)(CO)₃X] derivatives have concentrated on the
development of the homogenous catalyst in an aprotic organic solvent doped with
a proton source such as water, methanol or TFE. Here we address the develop-
ment of this class of catalysts for use in an immobilized, recyclable form in
aqueous solvents at pH 7. Nafion membranes have been used extensively as
50 catalyst supports as they are chemically stable proton conductors with high

permeability towards water. Previous examples of Nafion-supported molecular CO₂ reduction catalysts include [Re(bpy)(CO)₃Br],²⁰ [Ni(cyclam)]²⁺,²¹ and a cobalt tetramethylpyridoporphyrazine,²² however the current densities reported during sustained electrolysis were typically low (<0.1 mA cm⁻²) due to the low electrical conductivity of the Nafion support. Recently we reported on an immobilized high surface area 1/MWCNT/Nafion cathode (where MWCNT = multi-walled carbon nanotubes) that achieved CO and H₂ production in ratios suitable for use as syngas (CO : H₂ = 1 : 2) at greatly increased sustained current densities (0.7 mA cm⁻²) although with a relatively high overpotential ($\eta = 0.63$ V, -1.4 V vs. SCE) at pH 7.²³ MWCNT have been previously used as supports in a number of elegant studies on molecular catalysts for water oxidation,²⁴ water reduction,²⁵ and CO₂ reduction²⁶ where the catalysts are either directly grafted to, or modified with pyrene groups to enable interaction with, the MWCNT. In contrast, we previously employed a very simple, potentially low-cost approach where MWCNT were added to a polymer/catalyst solution before being drop-cast onto an electrode surface. It has been reported that a weak π - π interaction can occur between bpy ligands and MWCNT,^{27,28} and in our co-cast film FTIR spectroscopy indicated the presence of an interaction between the bipyridine ligand of **1** and the high surface area support,²³ although the exact nature of this MWCNT-**1** interaction remains under investigation. Critically the use of the high surface area report led to catalytic current densities an order of magnitude higher than could be achieved for the **1**/Nafion membrane alone. In this contribution, we report a **1**/MWCNT/Nafion electrode that operates at more than twice the current density (1.79 mA cm⁻², CO : H₂ \sim 0.3 at -1.4 V vs. SCE) of our previous study. We also examine a range of new [Mn(L)(CO)₃X]/MWCNT/Nafion films leading to an electrode with a high selectivity towards CO₂ over H⁺ reduction even in aqueous solutions.

We also synthesise and study, in solution, two previously unreported [Mn^I(L)(CO)₃X] complexes, modified at the 4,4'-position of the bipyridine ligand, [Mn(bpy(COOH)₂)(CO)₃Br] (**3**) and [Mn(bpy(OH)₂)(CO)₃Br] (**4**) (where (bpy(COOH)₂) = 4,4'-di-carboxy-2,2'-bipyridine and (bpy(OH)₂) = 4,4'-di-hydroxy-2,2'-bipyridine), see Fig. 1. Complex **3** is of interest as a route to overcoming the relatively high overpotential for the reduction of CO₂ by **1** ($\eta \sim 580$ mV in CH₃CN/H₂O, 95 : 5).²⁹ The addition of electron-withdrawing groups (EWGs) to the 4,4'-position of the bipyridine ligand has been shown previously to stabilise the first reduction of the analogous rhenium complex,³⁰ and it is anticipated that a similar anodic shift in the reduction potentials of **3** may occur. Conversely, complex **4** was identified due to the unique ability of the 4,4'-di-hydroxy-2,2'-bipyridine to act as a

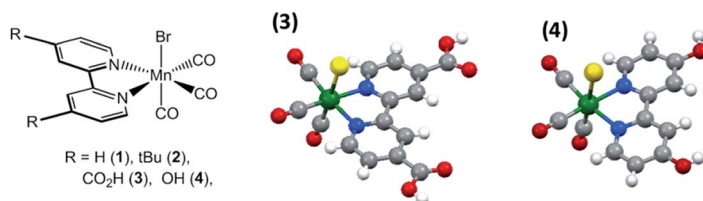


Fig. 1 [Mn^I(L)(CO)₃X] complexes under study, and single crystal X-ray structures of (**3**) [Mn(bpy(COOH)₂)(CO)₃Br] and (**4**) [Mn(bpy(OH)₂)(CO)₃Br], with solvent atoms omitted for clarity (details in the ESI†).

1 “push-pull” ligand, where deprotonation of the hydroxyl group leads to the
formation of an oxyanion bipyridine which has been shown with $[\text{Ru}(\text{bpy})_2(\text{bpy}(\text{OH})_2)]^{2+}$ to be a strong electron donor.³¹ This may be a promising approach as
5 the high catalytic activity of **2** is proposed to be related to the increased electron
density at the Mn centre due to the presence of the bulky electron-donating *t*-butyl
groups.⁸ During the preparation of this manuscript the analogous rhenium
complex, $[\text{Re}(\text{bpy}(\text{OH})_2)(\text{CO})_3\text{Br}]$ was reported to have comparable activity to
10 $[\text{Re}(\text{bpy}(\text{tBu})_2)(\text{CO})_3\text{Br}]$ for the production of CO.³² Following homogenous studies
in aprotic solvents we incorporated both the new complexes (**3** and **4**) and the
current benchmark catalysts **1** and **2**, in high surface area $[\text{Mn}(\text{L})(\text{CO})_3\text{X}]/$
MWCNT/Nafion films, leading to the report of both a new 1/MWCNT/Nafion
electrode that operates at improved current densities (1.79 mA cm^{-2} , $\text{CO} : \text{H}_2 \sim$
15 0.3 at -1.4 V vs. SCE) and a 2/MWCNT/Nafion electrode with improved selectivity
for CO_2 reduction ($\text{CO} : \text{H}_2 \sim 1$ at -1.4 V vs. SCE), compared to our previous
report.²³

2 Experimental

Materials and methods

20 Bromopentacarbonylmanganese(I), 2,2'-bipyridine, 4,4'-di-hydroxy-2,2'-bipyridine,
4,4'-di-carboxy-2,2'-bipyridine and 4,4'-di-*tert*-butyl-2,2'-bipyridine were
purchased from Sigma-Aldrich and used as received. Nafion (5% w/w in lower
25 alcohols, Sigma-Aldrich), sodium phosphate monobasic ($\geq 99\%$, Sigma-Aldrich),
sodium phosphate dibasic ($\geq 99\%$, Sigma-Aldrich), tetrabutylammonium hexa-
fluorophosphate (TBA PF₆, 99%, electrochemical grade) and multi-walled carbon
nanotubes (MWCNT > 98% carbon, 6–13 nm × 2.5–20 μm, Sigma-Aldrich) were
used as received. Acetonitrile (chromatographic grade, Sigma-Aldrich) was dried
30 over molecular sieves (3 Å) prior to use and stored under argon. Milli-Q water (18.2
MΩ) was used for all aqueous solutions. CO₂ and argon (CP and pureshield grade
respectively) were purchased from BOC.

Synthesis of complexes

35 All syntheses were carried out in the dark and under an atmosphere of Ar.
 $[\text{Mn}(\text{bpy})(\text{CO})_3\text{Br}]$ and $[\text{Mn}(\text{bpy}(\text{tBu})_2)(\text{CO})_3\text{Br}]$ were synthesized and characterized
according to literature methods (details in the ESI†).

40 **[Mn(bpy(COOH)₂)(CO)₃Br]**, **3**. A solution of 4,4'-dicarboxy-2,2'-bipyridine (180
mg, 0.74 mmol) in 8 ml of methanol was added to a solution of Mn(CO)₅Br (200
mg, 0.72 mmol) in toluene (20 ml). The mixture was refluxed for 90 minutes at 60
°C, then kept in the fridge overnight. The orange-red precipitate that formed was
45 filtered off and washed with cold diethyl ether, and the resulting red solution was
rotary evaporated to dryness to yield a bright red powder. The final product was
recrystallized from hot acetone and hexane, and dried *in vacuo* for 48 hours.
Crystals of suitable quality for diffraction studies were grown by slow vapour
diffusion of *n*-hexane into concentrated THF solutions of the complex. Yield =
50 46.84%; ¹H-NMR (300 MHz, DMSO-*d*₆): δ ppm 7.17 (br. d, *J* = 1.00 Hz, 2H), 8.09
(br. s, 2H), 9.41 (br. s, 2H), 9.68 (m, 1H); FTIR (CH₃CN/H₂O, 95 : 5): 2030, 1940,
1931 cm⁻¹; anal. calcd for C₁₅H₈BrMnN₂O₇·H₂O: C, 37.45; H, 2.10; N, 5.82.

1 Found: C, 37.30; H, 1.81; N, 5.57. m/z (ESI); 415 ($[M - Br^- + HOME]^+$), 383 ($[M - Br^-]^+$).

5 **[Mn(bpy(OH)₂)(CO)₃Br]**, **4**. A solution of 4,4'-dihydroxy-2,2'-bipyridine (140 mg, 0.74 mmol) in 8 ml of methanol was added to a solution of Mn(CO)₅Br (200 mg, 0.72 mmol) in toluene (20 ml). The mixture was refluxed for 90 minutes at 60 °C, and then placed in the fridge overnight. The orange-red precipitate that formed was filtered off and washed with cold diethyl ether, and the resulting yellow solution was rotary evaporated to dryness to yield a yellow powder. The final product was recrystallized from hot acetone and hexane, and dried *in vacuo* for 48 hours. Crystals of suitable quality for diffraction studies were grown by slow vapour diffusion of *n*-hexane into concentrated acetone solutions of the complex. Yield = 50%; ¹H-NMR (300 MHz, CD₃OD): δ ppm 7.05 (dd, $J = 1.00$ Hz, 2H), 7.70 (dd, $J = 1.00$ Hz, 2H), 8.86 (dd, $J = 1.00$ Hz, 2H); FTIR (CH₃CN): 2024, 1930, 1915 cm⁻¹; anal. calcd for C₁₃H₈BrMnN₂O₅: C, 38.36; H, 1.98; N, 6.88. Found: C, 38.20; H, 1.97; N, 6.78. m/z (ESI); 359 ($[M - Br^- + HOME]^+$), 327 ($[M - Br^-]^+$).

Electrochemical measurements

20 A PalmSens³ potentiostat, glassy carbon disc ($A = 0.0717$ cm², BASi) working electrode and a Pt basket counter electrode were used in all experiments. An Ag/AgCl (3 M KCl, BASi) or a freshly cleaned Ag wire, calibrated *vs.* Fc/Fc⁺, was used as the reference electrode in water or organic electrolytes, respectively. Bulk electrolysis measurements were carried out in a custom glass H-Cell with the Pt counter electrode separated from the working and reference electrodes by a fine glass frit. All samples were thoroughly purged with either Ar or CO₂ for 30 minutes prior to use, and kept in the dark throughout the experiments. Gas chromatography (GC) was performed using an Agilent 6890N employing N6.0 He (BOC) as the carrier gas (5 ml min⁻¹). A 5 Å molecular sieve column (ValcoPLOT, 30 m length, 0.53 mm ID) and a pulsed discharge detector (D-3-I-HP, Valco Vici) were employed. CO and H₂ peak areas were quantified by comparison to multiple calibrant gas injections (500 ppm H₂ and 200 ppm CO in helium (STG)). NMR spectra were recorded on a Bruker Advance 400 NMR spectrometer operating at 400 MHz (¹H) or 101 MHz (¹³C) or on a Bruker Advance 300 NMR spectrometer operating at 300 MHz (¹H) using an amber NMR tube. ESI-MS and elemental analyses were performed by the University of Liverpool analytical services. UV-vis spectra were recorded on a Shimadzu UV-2600 spectrophotometer using 1 cm or 1 mm pathlength quartz cuvettes. FTIR spectra were recorded on a Bruker Vertex instruments either in solution, cast on a CaF₂ plate, or using a diamond ATR crystal (Pike). Spectroelectrochemistry (SEC) was carried out using a liquid IR-SEC cell with a pathlength of approximately 0.2 mm that has been reported elsewhere.³³ The working and counter electrodes were Pt minigrids and a silver wire was used as the pseudo-reference. The concentration of the complex was approximately 0.1 mM in dry CH₃CN containing 0.1 M TBA PF₆ electrolyte, which was recrystallized from absolute ethanol and dried overnight on a Schlenk line at 70 °C prior to use.

Preparation of membrane supported catalyst electrodes

50 The membrane was prepared from a sample of complex **1–4** dissolved in 0.5 ml of acetonitrile, mixed with 0.5 ml of a Nafion/alcohol solution (5.0% w/w) in a 1 : 1

1 volume ratio in the dark to make up a 1.4×10^{-2} M solution. In a typical
 2 experiment 5 μl of this yellow solution, corresponding to 70 nmol of complex in
 3 2.5% Nafion/ CH_3CN 1 : 1, was transferred onto a polished glassy carbon electrode
 4 using an autopipette and left to dry in air in the dark for at least 2 hours at a
 5 constant temperature (maintained at 25 $^\circ\text{C}$), yielding a continuous pale yellow
 6 polymer film that completely coated the working area. It has been observed that
 7 the temperature control is critical in obtaining highly active films (see full
 8 discussion in the ESI †). Casting solutions for MWCNT/Nafion/complex films were
 9 prepared as above with the addition of MWCNT in a 1 : 1 mass ratio with the
 10 complex to the casting solution, followed by sonication in the dark for 15
 11 minutes. 5 μl of this darkly coloured casting solution was then transferred onto a
 12 polished glassy carbon electrode using an autopipette and left to dry in air in the
 13 dark for at least 2 hours. Following bulk electrolysis experiments the aqueous
 14 electrolyte was studied using UV/vis spectroscopy to confirm that complex
 15 leaching from the membrane into the electrolyte had not occurred. Morphological
 16 characterization was performed on films cast on glass slides using an Ambios
 17 Technology XP200 profilometer.

20 3 Results and discussion

Synthesis and characterisation

21 Complexes **3** and **4** are readily prepared by modification of the existing synthetic
 22 route of **1**.⁷ It is noted that complex **3** is particularly light sensitive, undergoing
 23 rapid decomposition within minutes in solution under ambient light, therefore
 24 all electrochemical experiments were carried out in the dark. Both **3** and **4** have
 25 been characterised using FTIR spectroscopy which shows three $\nu(\text{CO})$ bands
 26 corresponding to *fac*-tricarbonyl species (Table 1) in line with the single crystal
 27 structures, Fig. 1.

28 Due to the limited solubility of **3** in acetonitrile all experiments using this
 29 complex are carried out in the presence of 5% water. We observe $\nu(\text{CO})$ bands at
 30 2030, 1940 and 1931 cm^{-1} for **3** in $\text{CH}_3\text{CN}/\text{H}_2\text{O}$ (95 : 5), with the increase in the
 31 $\nu(\text{CO})$ frequencies compared to complex **1** indicating decreased electron density at
 32 the Mn centre due to the introduction of the electron withdrawing carboxylic acid
 33 group at the 4,4'-position of the bipyridine ligand.²⁷ In neat acetonitrile complex **4**
 34 has $\nu(\text{CO})$ bands at 2024, 1930 and 1915 cm^{-1} , with the decrease in frequency of

35
36
37
38
39
40
41
42
43
44
45
46
47
48
49
50
51
52
53
54
55
56
57
58
59
60
61
62
63
64
65
66
67
68
69
70
71
72
73
74
75
76
77
78
79
80
81
82
83
84
85
86
87
88
89
90
91
92
93
94
95
96
97
98
99
100
101
102
103
104
105
106
107
108
109
110
111
112
113
114
115
116
117
118
119
120
121
122
123
124
125
126
127
128
129
130
131
132
133
134
135
136
137
138
139
140
141
142
143
144
145
146
147
148
149
150
151
152
153
154
155
156
157
158
159
160
161
162
163
164
165
166
167
168
169
170
171
172
173
174
175
176
177
178
179
180
181
182
183
184
185
186
187
188
189
190
191
192
193
194
195
196
197
198
199
200
201
202
203
204
205
206
207
208
209
210
211
212
213
214
215
216
217
218
219
220
221
222
223
224
225
226
227
228
229
230
231
232
233
234
235
236
237
238
239
240
241
242
243
244
245
246
247
248
249
250
251
252
253
254
255
256
257
258
259
260
261
262
263
264
265
266
267
268
269
270
271
272
273
274
275
276
277
278
279
280
281
282
283
284
285
286
287
288
289
290
291
292
293
294
295
296
297
298
299
300
301
302
303
304
305
306
307
308
309
310
311
312
313
314
315
316
317
318
319
320
321
322
323
324
325
326
327
328
329
330
331
332
333
334
335
336
337
338
339
340
341
342
343
344
345
346
347
348
349
350
351
352
353
354
355
356
357
358
359
360
361
362
363
364
365
366
367
368
369
370
371
372
373
374
375
376
377
378
379
380
381
382
383
384
385
386
387
388
389
390
391
392
393
394
395
396
397
398
399
400
401
402
403
404
405
406
407
408
409
410
411
412
413
414
415
416
417
418
419
420
421
422
423
424
425
426
427
428
429
430
431
432
433
434
435
436
437
438
439
440
441
442
443
444
445
446
447
448
449
450
451
452
453
454
455
456
457
458
459
460
461
462
463
464
465
466
467
468
469
470
471
472
473
474
475
476
477
478
479
480
481
482
483
484
485
486
487
488
489
490
491
492
493
494
495
496
497
498
499
500
501
502
503
504
505
506
507
508
509
510
511
512
513
514
515
516
517
518
519
520
521
522
523
524
525
526
527
528
529
530
531
532
533
534
535
536
537
538
539
540
541
542
543
544
545
546
547
548
549
550
551
552
553
554
555
556
557
558
559
560
561
562
563
564
565
566
567
568
569
570
571
572
573
574
575
576
577
578
579
580
581
582
583
584
585
586
587
588
589
590
591
592
593
594
595
596
597
598
599
600
601
602
603
604
605
606
607
608
609
610
611
612
613
614
615
616
617
618
619
620
621
622
623
624
625
626
627
628
629
630
631
632
633
634
635
636
637
638
639
640
641
642
643
644
645
646
647
648
649
650
651
652
653
654
655
656
657
658
659
660
661
662
663
664
665
666
667
668
669
670
671
672
673
674
675
676
677
678
679
680
681
682
683
684
685
686
687
688
689
690
691
692
693
694
695
696
697
698
699
700
701
702
703
704
705
706
707
708
709
710
711
712
713
714
715
716
717
718
719
720
721
722
723
724
725
726
727
728
729
730
731
732
733
734
735
736
737
738
739
740
741
742
743
744
745
746
747
748
749
750
751
752
753
754
755
756
757
758
759
760
761
762
763
764
765
766
767
768
769
770
771
772
773
774
775
776
777
778
779
780
781
782
783
784
785
786
787
788
789
790
791
792
793
794
795
796
797
798
799
800
801
802
803
804
805
806
807
808
809
810
811
812
813
814
815
816
817
818
819
820
821
822
823
824
825
826
827
828
829
830
831
832
833
834
835
836
837
838
839
840
841
842
843
844
845
846
847
848
849
850
851
852
853
854
855
856
857
858
859
860
861
862
863
864
865
866
867
868
869
870
871
872
873
874
875
876
877
878
879
880
881
882
883
884
885
886
887
888
889
890
891
892
893
894
895
896
897
898
899
900
901
902
903
904
905
906
907
908
909
910
911
912
913
914
915
916
917
918
919
920
921
922
923
924
925
926
927
928
929
930
931
932
933
934
935
936
937
938
939
940
941
942
943
944
945
946
947
948
949
950
951
952
953
954
955
956
957
958
959
960
961
962
963
964
965
966
967
968
969
970
971
972
973
974
975
976
977
978
979
980
981
982
983
984
985
986
987
988
989
990
991
992
993
994
995
996
997
998
999
1000

Complex	E 1 st (V vs. SCE)	E 2 nd (V vs. SCE)	$\nu(\text{CO})$ (cm^{-1})			Solvent
1	-1.24	-1.46	2027	1933	1924	CH_3CN
2	-1.39	-1.57	2025	1930	1921	CH_3CN
3	-1.07	-1.41	2030	1940	1931	$\text{CH}_3\text{CN}/\text{H}_2\text{O}$
4	-1.38 ^a	-1.73 ^a	2024	1930	1915	CH_3CN

^a The first reductions of **4** are proposed to be primarily based on the bpy ligand (see Fig. 3 and 4).

the stretches *versus* **1** indicating that the introduction of the hydroxyl groups to the bipyridine ligand has increased the electron density at the metal centre in **4**. The magnitude of the shift of the $\nu(\text{CO})$ bands in **4** is very similar to that previously observed, and reproduced here also, for **2**.⁸ Solvolysis of the Mn–Br bonds in the case of **4** occurs rapidly in the dark leading to the formation of the solvent complex $[\text{Mn}(\text{bpy}(\text{OH})_2)(\text{CO})_3(\text{CH}_3\text{CN})]^+$ ($\nu(\text{CO})$ 2045, 1955 and 1944 cm^{-1} , Fig. S3[†]), which has been seen previously for this class of complex.^{15,34} It has been previously reported that *fac*- $[\text{Mn}(\text{bpy})(\text{CO})_3\text{Br}]$ can undergo photochemical transformation to *mer*- $[\text{Mn}(\text{bpy})(\text{CO})_3\text{Br}]$, which has $\nu(\text{CO})$ at 2043 (vw), 1948 (s) and 1903 (m) in THF.³⁵ We rule out the formation of *mer* complexes of **4** due to the relative intensities of the three new $\nu(\text{CO})$ stretches formed upon solvation, which are all of similar intensity, indicating the presence of a *fac*-tricarbonyl species.

Electrochemical characterisation of complex **3**

The electrochemistry of **1** and **2** in CH_3CN has been reported previously,^{7,8} but the cyclic voltammetry of **1** is also shown in Fig. 2(a) to allow comparison to the previously unreported complex **3**, Fig. 2(b). Initial reduction of **1** at -1.24 V in anhydrous CH_3CN results in bromide loss followed by fast dimerization to form $[\text{Mn}(\text{bpy})(\text{CO})_3]_2$ which is reduced at -1.46 V to form the catalytically active species, $[\text{Mn}(\text{bpy})(\text{CO})_3]^-$. In anhydrous CH_3CN , oxidation of $[\text{Mn}(\text{bpy})(\text{CO})_3]^-$ can occur at -1.08 V leading to dimer formation, which is oxidised at -0.21 V .⁷ In the presence of water, solvolysis of the Mn–Br bond occurs and the reduction of $[\text{Mn}(\text{bpy})(\text{CO})_3(\text{S})]^+$ to form the dimer is also observed at -1.11 V .

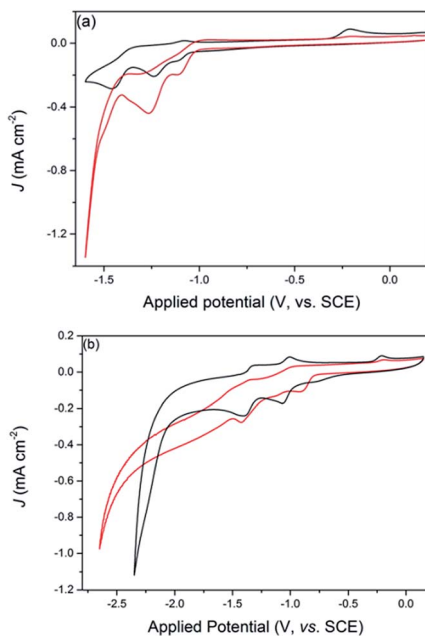


Fig. 2 (a) Solution phase CVs of the parent complex **1** under Ar (black) and CO_2 (red). (b) CVs of complex **3** under Ar (black) and CO_2 (red). The supporting electrolyte was 0.1 M TBA PF_6 in $\text{CH}_3\text{CN}/\text{H}_2\text{O}$ (95 : 5), $\nu = 100\text{ mV s}^{-1}$.

1 Spectroelectrochemical measurements which would be required to confirm
the chemical nature of the species produced in analogous experiments with **3**
were not possible due to excessive H₂ production occurring in the spectroelec-
trochemical cell (5% H₂O in CH₃CN is required to solubilise **3**). The similarities in
5 the cyclic voltammograms of **1** and **3** allow the following tentative assignments to
be made by analogy (Fig. 2(b)). Under argon, the reduction at -1.07 V is assigned
to complex **3**, with the shoulder at *ca.* -0.8 V *vs.* SCE in CH₃CN/H₂O due to
[Mn(bpy(COOH)₂)(CO)₃(SolV)]⁺, Fig. 2(b). The significant anodic shift of the
reduction potentials of both the cationic solvent complex (-0.80 V) and the
10 bromide complex (-1.07 V) of **3** compared to **1** indicates that the electron with-
drawing carboxylic acid groups are able to stabilise the reduced complex as
hypothesised. In light of the precedent for similar [Mn^I(L)(CO)₃X] complexes to
dimerize following initial reduction, it is proposed that the two-electron reduction
of the dimer [Mn(bpy(COOH)₂)(CO)₃]₂ occurs at -1.41 V to form 2
15 [Mn(bpy(COOH)₂)(CO)₃]⁻, with re-oxidation of [Mn(bpy-COOH)(CO)₃]⁻ and the
subsequently formed dimer occurring at -1.00 and -0.21 V, respectively. Our
assignment of the formation of the proposed active catalyst
[Mn(bpy(COOH)₂)(CO)₃]⁻ by dimer cleavage at -1.41 V is supported by the
enhanced current in the presence of CO₂, which is particularly pronounced at
20 slower scan rates (Fig. S8†). However we are unable to definitively rule out other
assignments, including the direct reduction of [Mn(bpy(COOH)₂)(CO)₃] in the
absence of dimerization, or the reduction of a manganese hydride species as has
been previously proposed by Gobetto *et al.* for a [Mn^I(L)(CO)₃X] complex con-
taining hydroxyl groups.³⁶ It is notable that, although present, the current
enhancement achieved under CO₂ with **3** in solution is small compared to that
25 seen for **1** (Fig. 2), indicating a low catalytic TOF.⁸ [Re(bpy(COOH)₂)(CO)₃Cl] has
previously been explored as a potential CO₂ reduction electrocatalyst, but no
current enhancement in the presence of CO₂ was observed,³⁰ and it is likely that
the reduced nucleophilic nature of the active complex here formed upon reduc-
tion of **3**, due to the presence of the EWG, is also a significant factor in decreasing
the activity towards CO₂ reduction. Nonetheless, despite the reduced activity the
promising anodic shift in reduction potentials of **4** warrants the study of the
30 complex in a polymer supported electrode.

Electrochemical characterisation of complex **4**

The cyclic voltammetry of **4** in anhydrous CH₃CN under argon at 100 mV s⁻¹ is not
40 typical of that observed for other [Mn(L)(CO)₃Br] complexes.^{7,8} The CVs in Fig. 3
show the presence of reductions at -1.38 , -2.01 and -2.20 V *vs.* SCE (labelled
processes I, III and IV in Fig. 3), in addition to a scan rate dependent feature at
 -1.73 V *vs.* SCE (II), which becomes increasingly prominent at higher scan rates
(Fig. S6†).

45 Whilst this manuscript was under preparation an IR-SEC study of the related
complex [Re(bpy(OH)₂)(CO)₃Cl] was reported, with the modified bpy ligand being
able to undergo two reductive deprotonation steps to form
[Re(bpy(OH)(O⁻))(CO)₃Cl]⁻ and [Re(bpy(O⁻)₂)(CO)₃]⁻, with assignments based
upon DFT calculations and IR analysis of chemically deprotonated complexes.³²
50 IR-SEC indicates that the behaviour of the equivalent Mn complex (**4**) is also
similar, Fig. 4. At open circuit potential (OCP), $\nu(\text{CO})$ corresponding to both

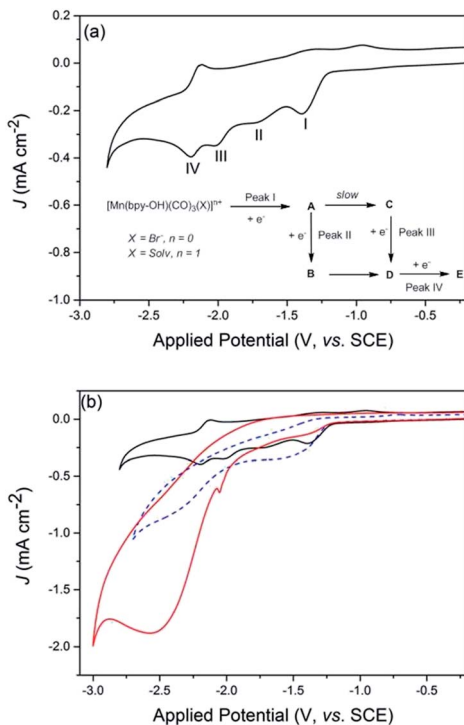


Fig. 3 (a) Cyclic voltammety of **4** (~ 1 mM) in Ar-purged CH_3CN . The inset shows the proposed electrochemical scheme. (b) Cyclic voltammety of **4** (~ 1 mM) in $\text{CH}_3\text{CN}/\text{Ar}$ (black), $\text{CH}_3\text{CN}/\text{CO}_2$ (red) and $\text{CH}_3\text{CN}/\text{H}_2\text{O}$ (95 : 5)/ CO_2 (blue). All scan rates were 100 mV s^{-1} , the supporting electrolyte was 0.1 M TBA PF_6 .

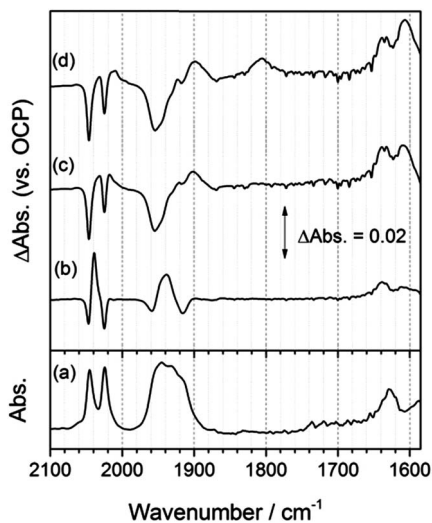


Fig. 4 IR-SEC of **4** in dry $\text{CH}_3\text{CN}/0.1 \text{ M TBA PF}_6$. (a) At OCP, difference spectrum versus OCP and (b) at reduction II, (c) reduction III and (d) reduction IV.

1 complex **4** (2024, 1930 and 1915 cm^{-1}) and the solvent complex (2044, 1955, 1944
2 cm^{-1}) are observed (Fig. 4(a), multi-Lorentzian fittings Fig. S9†). Upon initial
3 reduction (peak I) the IR difference spectrum shows the loss of **4** and its related
4 solvent complex and the growth of a new species with $\nu(\text{CO})$ that heavily overlap
5 with the starting materials, Fig. 4(b). Multi-Lorentzian curve fitting (Fig. S10†)
6 demonstrates that the product formed upon initial reduction has $\nu(\text{CO})$ at 2039,
7 1944 and 1932 cm^{-1} in addition to weaker IR modes assigned to the bipyridine
8 ligand at 1640 and 1610 cm^{-1} . By analogy to the reported spectrum of
9 $[\text{Re}(\text{bpy}(\text{OH})(\text{O}^-))(\text{CO})_3\text{Cl}]^-$, which has bpy modes at *ca.* 1630 and 1590 cm^{-1} and
10 $\nu(\text{CO})$ at 2012, 1900 and 1881 cm^{-1} corresponding to a shift of -7 to -12 cm^{-1} *vs.*
11 the parent $[\text{Re}(\text{bpy}(\text{OH})_2)\text{Cl}]$ complex,³² we assign the complex formed during IR-
12 SEC to the singly reductively deprotonated species $[\text{Mn}(\text{bpy}(\text{OH})(\text{O}))(\text{CO})_3(\text{Solv})]$.
13 Given the timescales required for bulk reduction, the process labelled II in
14 Fig. 3(a) was not identified during IR-SEC. Further reduction of $[\text{Mn}(\text{bpy}(\text{O}-$
15 $\text{H})(\text{O}^-))(\text{CO})_3(\text{Solv})]$ (peak III) leads to the formation of a complex with $\nu(\text{CO})$ at
16 2024, 1927 and 1903 cm^{-1} , in addition to a strong ligand mode at 1607 cm^{-1}
17 (Fig. 4(c) and S11†). This is assigned to the doubly reduced, doubly deprotonated
18 complex $[\text{Mn}(\text{bpy}(\text{O})_2)(\text{CO})_3(\text{Solv})]$, due to the excellent agreement with the
19 reported IR frequencies of $[\text{Re}(\text{bpy}(\text{OH})(\text{O})_2)(\text{CO})_3]^-$ (2002, 1886, 1865 and 1605
20 cm^{-1} (str.)).³² Applying increasingly negative potentials leads to the formation of
21 two new $\nu(\text{CO})$ at 1807 cm^{-1} and 1889 cm^{-1} , Fig. 4(d), with the higher frequency
22 $\nu(\text{CO})$ again masked by the bleaching of the starting material. The related Mn^0
23 complex $[\text{Mn}(\text{bpy}(\text{tBu})_2)(\text{CO})_3]^-$, formed at *ca.* -1.6 V *vs.* SCE,⁸ has $\nu(\text{CO})$ at 1907
24 and 1807 cm^{-1} and here we tentatively assign the complex with $\nu(\text{CO})$ at 1889
25 cm^{-1} and 1807 cm^{-1} to either $[\text{Mn}(\text{bpy}(\text{OH})(\text{O}))(\text{CO})_3]^-$ or $[\text{Mn}(\text{bpy}(\text{O})_2)(\text{CO})_3]^{2-}$.

26 In anhydrous acetonitrile a large current enhancement is seen in the cyclic
27 voltammetry of **4** in the presence of CO_2 , with the enhancement onset at
28 potentials cathodic of -1.79 V *vs.* SCE (Fig. 3(b)). In contrast to other
29 $[\text{Mn}(\text{L})(\text{CO})_3\text{Br}]$ complexes where the addition of a proton donor aids CO_2
30 reduction, here we find that the addition of 5% water actually decreases the
31 current density during cyclic voltammetry. Gobetto *et al.* have reported CO_2
32 reduction using a hydroxyl-substituted $\text{Mn}(\text{bpy})$ complex in the absence of an
33 additional proton source, but do not comment on the role of added water in the
34 process.³⁶ Bulk electrolysis of 0.2 mM **4** in anhydrous CH_3CN under CO_2 at -2.1 V
35 *vs.* SCE led to CO production with a Faradaic efficiency (FE) of 89% and a turnover
36 number (TON) of 0.6, with no H_2 production detected in the first four hours.
37 Sustained electrolysis (19.5 h) however led to complex degradation and the FE
38 dropped to 5% for CO . In the presence of water (5%) bulk electrolysis of **4** at -2.1
39 V shows that primarily H_2 (FE = 45%) is produced, with only low levels of CO
40 (FE = 6%). It is therefore apparent that although complex **4** is a poor CO_2
41 reduction catalyst in CH_3CN it displays markedly different electrochemical
42 behaviour in differing solvent environments, making it of interest to study in the
43 highly acidic environment of the Nafion film.

Polymer supported electrocatalytic reduction of CO_2 in water

44 To compare the catalytic behaviour of both new complexes (**3** and **4**) and the
45 known benchmark catalysts (**1** and **2**) in a polymer support for use in aqueous
46 electrolyte, complexes **1-4** were cast in Nafion films mixed with MWCNT onto a

glassy carbon working electrode and allowed to dry in the dark. We have reported on CO₂ electrocatalysis using **1**/MWCNT/Nafion previously.²³ We have optimised the drying conditions and found that the highest current densities occur when the films are dried at 25 °C and the role of drying temperature is discussed further in the ESI and Fig. S14 and S15.† In brief, there is a broad reduction at approximately –1.2 V vs. SCE which has been shown previously to be two overlapping processes: dimer formation followed by dimer reduction, Fig. 5(a) and (b). Dimer formation may seem surprising given that **1** is immobilized, but we have shown previously that clustering on the MWCNT surfaces is likely to enable the formation of bimetallic complexes.²³ The dimer reoxidation peak is observed at –0.4 V. In the presence of CO₂ there is a significant current enhancement for **1** at potentials negative of –1.2 V, indicative of CO₂ reduction (Fig. 5). Due to the optimisation of the film drying conditions we report a large improvement in sustained current densities during CPE measurements (1.8 mA cm⁻², vs. 0.7 mA cm⁻² previously reported at –1.4 V),²³ albeit with a slight loss in selectivity towards CO₂ (here 0.28, previous 0.47), see Table 1.

In contrast to electrodes of **1**/MWCNT/Nafion, equivalent experiments using complex **3** showed no significant enhancement in current density under CO₂. Square wave voltammetry (SWV) of a **3**/MWCNT/Nafion electrode under argon did show the presence of two reductions at *ca.* –0.8 and –1.25 V (Fig. 5(b)). The reduction at –0.8 V is present in films of MWCNT/Nafion without complexes **1–4** indicating that it is MWCNT-based. The reduction at –1.25 V is assigned to the reduction of a solvated [Mn(bpy(COOH)₂)(CO)₃(Solv)]⁺ complex (Solv = CH₃CN, H₂O or Nafion) indicating that a concentration of **3** was electrochemically active within the polymer. However despite the promising solution electrochemical behaviour of **3**, prolonged electrolysis of a **3**/MWCNT/Nafion electrode under CO₂ at –1.4 V in aqueous solutions at pH 7 lead exclusively to H₂ production. In a similar manner **4**/MWCNT/Nafion electrodes under argon in aqueous solutions at pH 7 showed electrochemical behaviour in line with the solution studies in

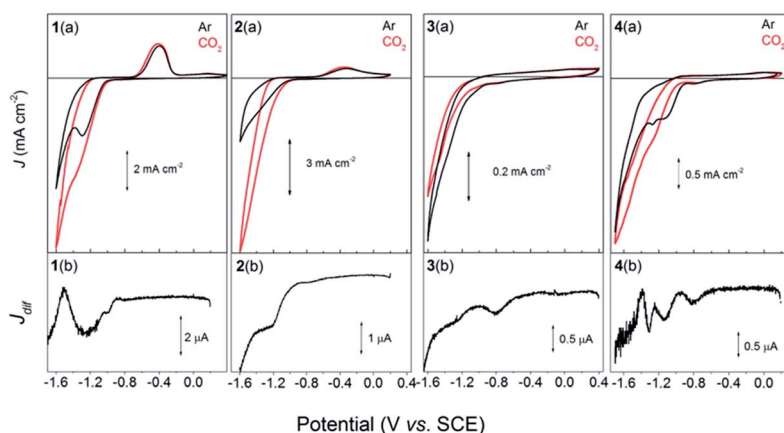


Fig. 5 Cyclic voltammograms (a) and square wave voltammograms (SWV) (b) for complexes **1–4** cast in Nafion/MWCNT on glassy carbon electrodes. Scan rates were 10 mV s⁻¹ vs. SCE in a 0.1 M phosphate buffer electrolyte. For comparison, CVs of all four complexes in solution are overlaid in Fig. S7.†

acetonitrile outlined above with two clear complex reductions assigned to the reduction of the solvated complex of **4** $[\text{Mn}(\text{bpy}(\text{OH})_2)(\text{CO})_3(\text{Solv})]^+$ at -1.15 V and of **4** at $[\text{Mn}(\text{bpy}(\text{OH})_2)(\text{CO})_3(\text{Br})]$ at -1.3 V, in addition to the MWCNT-based reduction at -0.8 V. In the presence of CO_2 a notable current increase was observed at potentials cathodic of -1.2 V, however prolonged electrolysis at -1.4 V under CO_2 indicated that the primary product formed was H_2 , Table 2.

Electrochemical studies of 2/MWCNT/Nafion electrodes are however very promising. Reductions visible by SWV at -1.28 and -1.53 V (Fig. 5(b)) are assigned to those observed in solution for the initial reduction of **2** and its subsequently formed dimer at -1.27 and -1.48 V vs. SCE in CH_3CN , Fig. S12†. A dimer reoxidation peak is also visible on the return sweep of the 2/MWCNT/Nafion electrode at ca. -0.4 V, Fig. 5. Under CO_2 a large increase in current density is measured relative to under argon (-8.8 mA cm^{-2} vs. -3.2 mA cm^{-2} at -1.6 V) that onsets at approximately -1.3 V. Bulk electrolysis measurements carried out at -1.4 V demonstrate that 2/MWCNT/Nafion electrodes are active for CO_2 reduction in pH 7 electrolyte with CO being produced with a selectivity ($\text{CO} : \text{H}_2 \sim 1.04$) exceeding that achieved with complex **1** ($\text{CO} : \text{H}_2 \sim 0.28$) under the same conditions. Based on analysis of the solution phase electrocatalysis of **2**, we postulated that films of 2/MWCNT/Nafion would operate efficiently at more negative potentials whilst maintaining high selectivity for CO_2 reduction. CPE of 1/MWCNT/Nafion at -1.5 V yielded CO with an average current density (J_{avg}) of ca. 4.38 mA cm^{-2} and a TON_{CO} of 35.9 after 4 hours, with a decreased selectivity ($\text{CO} : \text{H}_2 = 0.21$). Surprisingly CPE at -1.5 V using 2/MWCNT/Nafion for 2 hours resulted in lower average current densities (1.14 mA cm^{-2}) than for **1**, and after 2 hours the current density decreased dramatically. Accompanying this drop in current density was a concurrent loss in selectivity for CO_2 reduction, which may suggest that the 2/MWCNT/Nafion electrode is being limited by the available CO_2 concentration. Indeed, re-purging with CO_2 each hour led to recovery of the activity of the system, yielding an improved J_{avg} (2.65 mA cm^{-2}), without a loss in selectivity ($\text{CO} : \text{H}_2 = 0.33$) over 4 hours and a total TON_{CO} of over 45 at -1.5 V (Fig. S13†). It is therefore apparent the 2/MWCNT/Nafion electrode is likely to be limited by the available CO_2 concentration under typical operating conditions. Future work will explore the use of both alternative polymeric materials and electrode configurations to enhance the available CO_2 concentration at the catalytic sites. Recent examples using gas diffusion electrodes coupled to immobilized catalysts have demonstrated marked improvements in catalytic

Table 2 CPE data for Nafion/MWCNT films containing **1**, **2** or **4**

Catalyst	E (V, vs. SCE)	J_{avg} (mA cm^{-2})	Time (h)	TON_{CO} total	$\text{CO} : \text{H}_2$	FE H_2 , CO (%)
(1)/Nafion/MWCNT	-1.4	1.79	4	18.7	0.28	50, 14
(1)/Nafion/MWCNT	-1.5	4.38	4	35.9	0.21	52, 11
(2)/Nafion/MWCNT	-1.4	0.2	4	7.3	1.04	44, 46
(2)/Nafion/MWCNT ^a	-1.5	2.65	4	46.1	0.32	71, 23
(2)/Nafion/MWCNT	-1.5	1.14	2	10.6	0.33	75, 24
(4)/Nafion/MWCNT	-1.4	0.83	4	0.3	0.02	40, 1

^a Cell repurged every hour.

1 current densities.²⁶ The relatively weak interaction between the MWCNT and
complexes is also likely to be a significant limiting factor and the development of
similar complexes with aromatic functionalities better suited to π -stacking on
5 MWCNT, such as pyrene groups, is also likely to yield further improvements in
current densities.³⁷

4 Conclusions

10 Two novel Mn complexes incorporating substituted bipyridine ligands,
[Mn(bpy(COOH)₂)(CO)₃Br] (3) and [Mn(bpy(OH)₂)(CO)₃Br] (4), have been synthe-
sized and characterized with the aim of utilisation in a high surface area
[Mn(L)(CO)₃X]/MWCNT/Nafion electrode for CO₂ reduction. Detailed electro-
15 chemical studies of 3 and 4 were carried out and both complexes were found to
have some activity towards CO₂ reduction in acetonitrile solutions; however when
immobilized for use in aqueous conditions CO₂ reduction to CO was not found to
occur in significant quantities. In contrast, immobilization of the benchmark
catalyst 2 as a 2/MWCNT/Nafion electrode was found to be a highly effective
20 approach for enabling CO₂ reduction to CO in aqueous solvents at neutral pH
values, with a J_{avg} of 2.65 mA cm⁻² at -1.5 V and a selectivity towards CO₂
(CO : H₂ = 0.33) being achieved.

Acknowledgements

25 AC and JJW acknowledge the EPSRC (EP/K006851/1) for a fellowship and funding
respectively. GN thanks the University of Liverpool for funding. Thanks to Prof.
Dmitry Shchukin (SIRE) for access to the FTIR. Thanks to Prof. Ken Durose and Dr
Rob Treharne (SIRE) for access to the profilometer.

References

- 30 1 A. J. Morris, G. J. Meyer and E. Fujita, *Acc. Chem. Res.*, 2009, **42**, 1983–1994.
2 A. J. Cowan and J. R. Durrant, *Chem. Soc. Rev.*, 2013, **42**, 2281–2293.
3 C. D. Windle and R. N. Perutz, *Coord. Chem. Rev.*, 2012, **256**, 2562–2570.
4 J.-M. Savéant, *Chem. Rev.*, 2008, **108**, 2348–2478.
5 J. Hawecker, J.-M. Lehn and R. Ziessel, *J. Chem. Soc., Chem. Commun.*, 1983,
536–538.
6 J. Hawecker, J.-M. Lehn and R. Ziessel, *J. Chem. Soc., Chem. Commun.*, 1984,
328–330.
7 M. Bourrez, F. Molton, S. Chardon-Noblat and A. Deronzier, *Angew. Chem., Int.*
Ed., 2011, **50**, 9903–9906.
8 J. M. Smieja, M. D. Sampson, K. A. Grice, E. E. Benson, J. D. Froehlich and
C. P. Kubiak, *Inorg. Chem.*, 2013, **52**, 2484–2491.
9 M. D. Sampson, A. D. Nguyen, K. A. Grice, C. E. Moore, A. L. Rheingold and
C. P. Kubiak, *J. Am. Chem. Soc.*, 2014, **136**, 5460–5471.
10 C. Riplinger, M. D. Sampson, A. M. Ritzmann, C. P. Kubiak and E. A. Carter, *J.*
Am. Chem. Soc., 2014, **136**, 16285–16298.
11 C. Riplinger and E. A. Carter, *ACS Catal.*, 2015, **5**, 900–908.
12 D. C. Grills, J. A. Farrington, B. H. Layne, S. V. Lyman, B. A. Mello, J. M. Preses
50 and J. F. Wishart, *J. Am. Chem. Soc.*, 2014, **136**, 5563–5566.

- 1 13 M. Bourrez, M. Orio, F. Molton, H. Vezin, C. Duboc, A. Deronzier and
S. Chardon-Noblat, *Angew. Chem., Int. Ed.*, 2014, **53**, 240–243.
- 14 J. Agarwal, T. W. Shaw, C. J. Stanton III, G. F. Majetich, A. B. Bocarsly and
H. F. Schaefer III, *Angew. Chem., Int. Ed.*, 2014, **53**, 1–5.
- 5 15 J. Agarwal, C. J. Stanton III, T. W. Shaw, J. E. Vandezande, G. F. Majetich,
A. B. Bocarsly and H. F. Schaefer III, *Dalton Trans.*, 2015, **44**, 2122–2131.
- 16 Q. Zeng, J. Tory and F. Hartl, *Organometallics*, 2014, **33**, 5002–5008.
- 17 M. V. Vollmer, C. W. Machan, M. L. Clark, W. E. Antholine, J. Agarwal,
H. F. Schaefer III, C. P. Kubiak and J. R. Walensky, *Organometallics*, 2015,
10 **34**, 3–12.
- 18 J. Agarwal, T. W. Shaw, H. F. Schaefer III and A. B. Bocarsly, *Inorg. Chem.*, 2015,
54, 5285–5294.
- 19 T. K. Mukhopadhyay, N. L. MacLean, L. Gan, D. C. Ashley, T. L. Groy,
M.-H. Baik, A. K. Jones and R. J. Trovitch, *Inorg. Chem.*, 2015, **54**, 4475–4482.
- 15 20 T. Yoshida, K. Tsutsumida, S. Teratani, K. Yasufuku and M. Kaneko, *J. Chem.
Soc., Chem. Commun.*, 1993, 631–633.
- 21 A. Jarzebinska, P. Rowinski, I. Zawisza, R. Bilewicz, L. Siegfried and T. Kaden,
Anal. Chim. Acta, 1999, **396**, 1–12.
- 20 22 J. Zhang, W. J. Pietro and A. B. P. Lever, *J. Electroanal. Chem.*, 1996, **403**, 93–
100.
- 23 J. J. Walsh, G. Neri, C. L. Smith and A. J. Cowan, *Chem. Commun.*, 2014, **50**,
12698–12701.
- 24 F. Li, B. Zhang, X. Li, Y. Jiang, L. Chen, Y. Li and L. Sun, *Angew. Chem., Int. Ed.*,
25 **2011**, **50**, 12276–12279.
- 25 E. S. Andreiadis, P.-A. Jacques, P. D. Tran, A. Leyris, M. Chavarot-Kerlidou,
B. Jousselme, M. Matheron, J. Pécaut, S. Palacin, M. Fontecave and
V. Artero, *Nat. Chem.*, 2013, **5**, 48–53.
- 26 P. Kang, S. Zhang, T. J. Meyer and M. Brookhart, *Angew. Chem., Int. Ed.*, 2014,
30 **53**, 8709–8713.
- 27 J. Li, Y. Xu, H. Wei, T. Huo and E. Wang, *Anal. Chem.*, 2007, **79**, 5439–5443.
- 28 F. Liu, X. Yang and S. Sun, *Analyst*, 2011, **136**, 374–378.
- 29 C. Costentin, S. Drouet, M. Robert and J.-M. Savéant, *Science*, 2012, **338**, 90–94.
- 30 J. M. Smieja and C. P. Kubiak, *Inorg. Chem.*, 2010, **49**, 9283–9289.
- 35 31 S. Klein, W. G. Dougherty, W. S. Kassel, T. J. Dudley and J. J. Paul, *Inorg. Chem.*,
2011, **50**, 2754–2763.
- 32 G. F. Manbeck, J. T. Muckerman, D. J. Szalda, Y. Himeda and E. Fujita, *J. Phys.
Chem. B*, 2015, DOI: 10.1021/jp511131x.
- 40 33 M. Krejčík, M. Daněk and F. Hartl, *J. Electroanal. Chem. Interfacial Electrochem.*,
1991, **317**, 179–187.
- 34 J.-D. Compain, M. Bourrez, M. Haukka, A. Deronzier and S. Chardon-Noblat,
Chem. Commun., 2014, **50**, 2539–2542.
- 35 G. J. Stor, S. L. Morrison, D. J. Stuf and A. Oskam, *Organometallics*, 1994, **3**,
45 2641–2650.
- 36 F. Franco, C. Cometto, F. F. Vallana, F. Sordello, E. Priola, C. Minero, C. Nervi
and R. Gobetto, *Chem. Commun.*, 2014, **50**, 14670–14673.
- 37 J. D. Blakemore, A. Gupta, J. J. Warren, B. S. Brunshwig and H. B. Gray, *J. Am.
Chem. Soc.*, 2013, **135**, 18288–18291.
- 50

PAPER

Novel process and catalytic materials for converting CO₂ and H₂ containing mixtures to liquid fuels and chemicals

Nora Meiri, Yakov Dinburg, Meital Amoyal, Viatcheslav Koukouliev, Roxana Vidruk Nehemya, Miron V. Landau and Moti Herskowitz*

Received 21st April 2015, Accepted 24th June 2015

DOI: 10.1039/c5fd00039d

Carbon dioxide and water are renewable and the most abundant feedstocks for the production of chemicals and fungible fuels. However, the current technologies for production of hydrogen from water are not competitive. Therefore, reacting carbon dioxide with hydrogen is not economically viable in the near future. Other alternatives include natural gas, biogas or biomass for the production of carbon dioxide, hydrogen and carbon monoxide mixtures that react to yield chemicals and fungible fuels. The latter process requires a high performance catalyst that enhances the reverse water-gas-shift (RWGS) reaction and Fischer–Tropsch synthesis (FTS) to higher hydrocarbons combined with an optimal reactor system. Important aspects of a novel catalyst, based on a Fe spinel and three-reactor system developed for this purpose published in our recent paper and patent, were investigated in this study. Potassium was found to be a key promoter that improves the reaction rates of the RWGS and FTS and increases the selectivity of higher hydrocarbons while producing mostly olefins. It changed the texture of the catalyst, stabilized the Fe–Al–O spinel thus preventing decomposition into Fe₃O₄ and Al₂O₃, increased the content of Fe₅C₂ while shifting Fe in the oxide and carbide phases to a more reduced state and the relative exposure of carbide iron on the catalysts surface and increased the CO₂ adsorption and adsorption strength. A detailed kinetic model of the RWGS, FTS and methanation reactions was developed for the Fe spinel catalyst based on extensive experimental data measured over a range of operating conditions. Significant oligomerization activity of the catalyst was found. Testing the pelletized catalyst with CO₂, CO and H₂ mixtures over a range of operating conditions demonstrated its high productivity to higher hydrocarbons. The composition of the liquid (C₅₊) was found to be a function of the potassium content and the composition of the feedstock.

Chemical Engineering Department, Blechner Center for Industrial Catalysis and Process Development, Ben-Gurion University of the Negev, Beer-Sheva, 84105, Israel. E-mail: herskow@bgu.ac.il; Fax: +972 8 6479427; Tel: +972 8 6461482

1. Introduction

Crude oil is the dominant feedstock for the production of liquid fuels, as clearly stressed in a recent IEA report.¹ Most of the foreseen output rise over the next three decades will be produced in the Middle East. The biofuels share is currently only 8%, and is expected to remain at this level until 2040, supported by increasing subsidies. The IEA report sends a very strong message regarding the CO₂ emissions, which are expected to increase dramatically, unless low-carbon investments will increase by a factor of four beyond current values. All those projections indicate that the search for alternative, renewable and sustainable sources for the production of fungible and competitive fuels needs to be accelerated. Biomass has been the main source for renewable fuels, mainly ethanol and biodiesel. A fierce debate related to future use of biomass has been conducted over the past decade. A recent report² presents a less optimistic view of the future of bioenergy in Germany concluding that with the exception of the use of biogenic waste, the larger scale use of biomass as an energy source is limited. A proper assessment of the impact of biofuels is critical.³

Liquid fuels are mixtures of hydrocarbons that meet specific standards updated from time to time. Carbon dioxide, an environmentally damaging greenhouse gas, and water are the most abundant and low-cost sources of carbon and hydrogen needed for the production of hydrocarbons. The current scientific and technological challenge is to develop and implement environmentally-friendly processes that convert CO₂ and H₂O into commercially-viable, fungible and compatible fuels, using green energy. A viable route is the reaction of captured carbon dioxide from flue gases with hydrogen produced from water. Methods for both CO₂ capture and water splitting have been recently reviewed.⁴

Solar water splitting using photoelectrochemical cells, called artificial photosynthesis, has been extensively studied and is aimed at developing efficient, robust and scalable processes for the production of low-cost, commercially-competitive hydrogen.⁵⁻⁸ In spite of the extensive scientific effort to provide innovative solutions, the question raised in a recent publication⁸ “Will Solar-Driven Water-Splitting Devices See the Light of Day?” remains open. The solar thermochemical cycle method is another promising route being pursued, although no large scale facilities have been developed.⁹ Actually the only commercially-proven technology and operated at a large scale for water splitting is electrolysis.¹⁰ The cost of hydrogen produced by this method depends mainly on the cost of electricity, estimated to be ~\$3 kg⁻¹ at an electricity cost of <\$0.055 kW h⁻¹. This is by far higher than the cost of hydrogen¹¹ (~\$1 kg⁻¹) produced using the dominant commercial technology, steam reforming of natural gas. The projected cost of hydrogen¹¹ produced by other water splitting methods is also significantly higher (\$3.5–10 kg⁻¹).

An economic analysis¹² of the production of liquid solar fuels from carbon dioxide and water was reviewed recently. Employing a modified Fischer–Tropsch process for reacting captured carbon dioxide from flue gas with hydrogen produced by electrolysis for water (using electricity from wind energy) yielded an estimated cost of \$5.25 per gal of gasoline. The relative high cost of the fuel resulted from the high cost of hydrogen. Another study¹³ reviewed sustainable hydrocarbon fuel production by recycling CO₂ and H₂O with renewable or nuclear

1 energy and concluded that \$3 per gal gasoline could be achieved at an electricity
cost of \$0.04–0.05 kW h⁻¹. The significantly different production cost of the fuels
estimated by the two studies results from the different assumptions made in
5 estimating the cost of the electrolysis and the Fischer–Tropsch processes.

A recent paper¹⁴ reviews the catalytic CO₂ hydrogenation to hydrocarbons and
describes a novel Fe spinel catalyst coupled with a system of three packed-bed
reactors in series with interim removal of water and condensed hydrocarbons
that reached a CO₂ conversion of 89% and C₅₊ hydrocarbons productivity of >0.5
10 kg kg_{cat}⁻¹ h⁻¹. The pure-spinel catalyst displayed a significantly higher activity
and selectivity than the other Fe catalysts published in the literature. This process
produces hydrocarbon mixtures that can be readily converted to liquid fuels.

Although the CO₂ hydrogenation process is a very promising route to renew-
able and fungible fuels, its implementation is limited by the availability of low-
cost hydrogen produced from water. Only specific locations with access to
15 extremely low-cost electricity (<\$0.03 kW h⁻¹) will operate such competitive
processes unless a significantly higher-cost fuel is acceptable for specific purposes
like military use. Therefore, other sources of hydrogen should be sought like fossil
natural gas, renewable biogas or biomass. Natural gas has been applied
commercially¹⁵ as feedstock for the production of fuels through conversion to
20 syngas followed by the Fischer–Tropsch synthesis (FTS). The syngas is generated
by steam reforming, partial oxidation and autothermal reforming which produce
a mixture of hydrogen and carbon monoxide at a molar ratio close to 2. Carbon
dioxide generated in these processes is normally separated because it could be
25 detrimental to selectivity or at best is a diluent. Biomass is a potential renewable
feedstock for gasification to syngas, containing CO, CO₂ and H₂, which is fed to
the FTS process. Comprehensive reviews^{16,17} describe the potential catalysts, effect
of impurities, the economics and the challenges of such processes. A comparison
of several routes for the production of fuels from biomass, carbon dioxide and
30 electricity¹⁸ based on economical evaluation indicated that the thermochemical
route (gasification and conversion to fuels) is by far the preferred route. Biogas
is another renewable feedstock that can be readily converted to syngas. This syngas
contains a significant amount of CO₂, as pointed out in a recent review.¹⁹
Therefore, the development of suitable FTS catalysts that handle mixtures of CO₂,
35 CO and H₂ and are the basis for environmentally-acceptable and competitive
processes is a major challenge.

Iron-based catalysts^{20,21} that display significant reverse water gas shift (RWGS)
activity are employed in processes for converting CO, CO₂ and H₂ mixtures to fuels
and chemicals. Specifically, a recent paper²⁰ discusses K/Fe–Cu–Al catalyst
40 performance along with carbon deposition by variation of the CO₂/CO ratio. The
authors report that in experiments operated for 40 h at 300 °C, 20 bar,
CO₂ : CO : H₂ molar ratio of 1 : 1 : 7 and weight hourly space velocity (WHSV) of
the carbon oxides of about 0.83 h⁻¹, the conversion of CO was 96% while the
conversion of CO₂ was only 12%. The selectivity to methane was about 10% while
45 the selectivity to C₅₊ was about 60%. The significant conclusion of this study was
that operating at a high CO₂/(CO + CO₂) ratio and high pressure and temperature
prevents carbon deposition on the Fe-based catalyst. A recent patent²² extends the
information on the novel catalytic system¹⁴ from mixtures of CO₂ and H₂ to CO₂,
50 CO and H₂ mixtures.

1 Potassium was identified as an important component of the Fe-based catalysts
for the FTS. In a recent review,²³ the authors concluded that the presence of
potassium reduces the formation of CH₄ while increasing the selectivity to higher
5 hydrocarbons. A similar effect was reported in an early study²⁴ of CO₂ hydroge-
nation. This effect was related to the enhanced carburization of the Fe catalyst in
the presence of potassium. A recent study²⁵ reported the effect of potassium on
CO₂ in the hydrogenation of mixtures of CO and CO₂. Apparently, increasing the K
content did not increase the catalyst activity while the average product molecular
10 weight increased.

It is generally accepted that K acts as electronic promoter when adsorbed at the
surface of Fe⁰/FeO_x/FeC_x phase particles lowering the iron work function due to
interactions between the alkali metal valence state and conduction band states in
catalytic phases.^{26,27} Donating electron density to the vacant d-orbital of iron
enhances the dissociative adsorption of CO while lowering the H₂ adsorption
15 ability.²⁷ Depressing hydrogenation activity is associated with lower rates of CH₄
formation, higher selectivity to olefins and long-chain hydrocarbons. The oxida-
tive action of CO₂ and excessive water on Fe-carbide phases²⁸ during CO₂
hydrogenation creates more oxidized iron on the catalysts that may modify the
action of the K promoter.
20

The hydrogenation of mixtures of CO and CO₂ is a complex process that
requires optimization through modeling and simulations. A recent study²⁹
describes a simulation that includes steam reforming of natural gas with addition
of CO₂. The FTS was simulated using experimental results previously published²⁰
25 by the authors. While numerous kinetic models have been proposed for Fe-based
FT catalysts, limited information has been published on the kinetic behavior of
catalysts for the hydrogenation of CO₂. A kinetic study³⁰ of CO₂ hydrogenation
proposed two rate expressions, one for reverse WGS and the other for the FTS. The
experiments were conducted at 10 bar and a stoichiometric H₂/CO₂ ratio of 3. The
30 highest measured CO₂ conversion was 45% at 300 °C to 60% at 400 °C due to the
equilibrium limitation of the reverse WGS. Another kinetic study³¹ was conducted
at high H₂/CO₂ molar ratios of 4 and 8 that produced a light product ($\alpha = 0.2-0.3$).
A similar kinetic model that included two reactions (reverse WGS and FTS) was
used. The highest CO₂ conversion was 44% at a H₂/CO₂ molar ratio of 8.
35 Increasing the temperature and residence time did not increase the conversion.

A more detailed kinetic study of the FTS on K/Fe-Cu-Mn-Al₂O₃ catalysts has
been published.³² It includes 10 reactions of CO and H₂, nine of them to light
paraffins (C₁-C₄) and olefins (C₂-C₄). The last reaction represents the production
of C₅₊ hydrocarbons lumped in one component C₆H₁₄. The selection of hexane
40 means that the liquid product was very light and mostly paraffinic. No oxygenates
were mentioned in this study.

Potential applications of catalytic processes for converting mixtures of CO₂, CO
and H₂ to hydrocarbons and oxygenates to be readily converted to liquid fuels and
chemicals requires sustained research aimed at improving the performance of the
catalysts (selectivity to higher hydrocarbons and olefins, activity and stability) and
optimization of the processes. One of the most important components of Fe-
based catalysts is potassium. Developing a better understanding of the effects
of potassium as promoter is a key factor in improving performance. Optimization
45 of the process requires a reliable kinetic model to be implemented in modeling
and simulations. The scope of this study is to determine some of the fundamental
50

1 effects of potassium in the Fe spinel catalyst, to develop a detailed kinetic model
of the CO₂ hydrogenation on the Fe spinel catalyst and present effects of the feed
composition and operating conditions on the performance of the pelletized Fe
5 spinel catalyst in a fixed bed reactor.

2. Experimental

2.1. Catalyst preparation

10 The K-promoted, pure Fe–Al–O spinel Fe(Fe_{0.5}Al_{0.5})₂O₄ catalyst used in this study
was prepared and characterized according to procedures described elsewhere.¹⁴
Potassium was added to the dried Fe–Al–O spinel precursor by incipient wetness
impregnation with an aqueous solution of K₂CO₃, followed by overnight drying at
110 °C and calcination in air at 450 °C for 6 h. Three Fe-based spinel catalysts with
15 different K content were prepared: unpromoted 100 spinel/0 wt% K (Cat. Fe–0K),
100 spinel/2 wt% K (Cat. Fe–2K) and 100 spinel/4 wt% K (Cat. Fe–4K).

2.2. Catalyst characterization

20 The spent catalysts were characterized after He treating and passivation. After
testing, the catalysts were treated under a He flow at 300 °C for 3 h for removal of
residual adsorbed organics and passivated under a CO₂ flow at 25 °C for 1 h. The
textural properties of the catalysts, surface area, pore volume and pore size, were
calculated from N₂ adsorption–desorption isotherms using conventional BET and
25 BJH methods. The isotherms were recorded using a NOVA 3200e (Quantachrome)
at the temperature of liquid nitrogen after degassing under vacuum at 100 °C. The
phase composition of the catalysts was determined based on their X-ray diffraction
patterns. XRD measurements were conducted using a Phillips 1050/70
30 powder diffractometer fitted with graphite monochromator, at 40 kV and 28
mA using software developed by Crystal logic. The phase identification was per-
formed by using a SBDE ZDS computer search/match program coupled with the
ICDD. The relative content of iron oxide and carbide phases was obtained using
Rietveld refinement of the XRD profile by using the DBWS-9807 program. The
35 elemental composition of the catalysts was measured using the EDS method
(Quanta-200, SEM-EDAX, FEI Co instrument). The CO₂-TPD measurements were
performed using a Chemisorption Analyzer Autochem II 2920 instrument,
Micrometrics Co. The samples were saturated with CO₂ at 40 °C before recording
the desorption spectra with a heating rate of 5 °C min⁻¹ in 5% CO₂/He flow of 25
40 ml min⁻¹. XPS data were collected using X-ray photoelectron spectrometer
ESCALAB 250 ultrahigh vacuum (1 × 10⁻⁹ bar) apparatus with an Al K α X-ray
source and a monochromator. The spectral components of C and Fe signals
were found by fitting a sum of single component lines to the experimental data by
means of a non-linear least-square curve fitting. The EX05 argon gun system
45 performed controlled removal of surface layers allowing depth profile analyses of
elements.

2.3. Catalysts performance testing

50 Measurements of the catalysts activities and selectivities including data for the
kinetic model were carried out in two units:

1 1. A computer-controlled bench rig equipped with three continuous-flow fixed
bed reactors connected in series including devices for removing water and
organic liquid between reactors¹⁴ for the kinetic runs (packed with 50–200 μm
5 powder) and CO_2 , CO and H_2 mixtures (packed with 1.4–1.7 mm pellets) runs. The
pellets were prepared by pressing the powder catalyst. The catalyst was mixed with
silica powder diluent and packed in the reactors.

2. One fixed-bed reactor packed with diluted (silica) powder catalyst followed
by a cooler and a gas–liquid separator for studying the effect of potassium.

10 The hydrocarbon liquid mixture and oxygenates from aqueous products were
separated and analyzed using GC-MS (Agilent Technologies 6890N network GC
system equipped with 5973 Network mass-selective detector). CO_2 , H_2 , CO and
 C_1 – C_6 hydrocarbons were analyzed on line using a GC instrument Agilent Tech-
15 nologies, model 7890A equipped with 5 valves/7 columns (PLOT and packed)/2
TCD/FID detectors. The organic content in the aqueous product was measured
by TOC analysis (instrument TOC-V_{CPN} Shimadzu Co.).

3. Results and discussion

3.1. The effect of potassium as a promoter of the Fe-spinel catalyst

20 The catalysts were activated *in situ* by H_2/CO carburization with a stream of
 $0.03 : 0.03 : 0.14 \text{ N mL min}^{-1} \text{ g}_{\text{cat}}^{-1}$ of CO , H_2 and He , respectively, at 300°C for 3
h. The catalysts were tested at constant conditions of 20 bar, 320°C and a H_2/CO_2
25 molar ratio of 3. The WHSV of CO_2 was adjusted to reach about 30% CO_2
conversion so as to achieve differential operation of the reactor and calculate
directly the reaction rates. The catalysts reached steady state yielding constant
 CO_2 conversion/products selectivity after 120 h on stream. After the end of the
run, the catalysts were treated with He and then passivated with CO_2 before being
30 discharged from the reactor.

**The effect of potassium on the performance of the Fe–Al–O spinel catalyst in
 CO_2 hydrogenation.** The performance measured with the three catalysts, Cat. Fe–
0K, Cat. Fe–2K and Cat. Fe–4K, listed in Table 1 demonstrates a significant effect
of potassium on the catalyst activity and selectivity. The RWGS rate of reaction
35 was calculated from the differential measurements of the CO_2 conversion (30%)
and WHSV. The rate of methanation was calculated from the molar flow rate of
methane and the catalyst weight. Similarly, the rate of the FTS reaction was
calculated from the molar flow rate of all hydrocarbons (without methane) and
oxygenates and the catalyst weight.

40
45
Table 1 Effect of potassium on the performance of Fe–Al–O spinel catalyst in CO_2
hydrogenation. Testing conditions: 20 bar, 320°C , molar $\text{H}_2/\text{CO}_2 = 3$, 120 h on stream

Catalyst	Reaction rate, $\text{mmol g}_{\text{cat}}^{-1} \text{ h}^{-1}$				Product selectivity, wt%					
	RWGS	FTS	CH_4	FTS/RWGS	CO	C_2 – C_4	Olefins	Paraffins	Oxygenates	C_{5+}
Cat. Fe–0K	125	62	46	0.50	15	40	15	15	8	7
Cat. Fe–2K	179	112	34	0.63	22	23	24	11	4	16
Cat. Fe–4K	123	95	6	0.77	22	6	24	5	10	33

Adding 2 wt% potassium increased dramatically both the RWGS and FTS rates of reaction and decreased the rate of methanation. Further increasing the potassium content decreased the reaction rate of RWGS. The methanation rate displayed an extreme drop thus increasing the selectivity of the desired products. The FTS reaction rate decreased mildly. Actually, the ratio of the FTS/RWGS reaction rates increased gradually as the potassium content increased which has a very important impact on the process. The effect of potassium on selectivity was very impressive and dominant. Beyond the drop in methane selectivity, the significant increase in the selectivity to higher hydrocarbons (C_{5+}) is a substantial factor. These findings are in agreement with the results presented in other studies of Fe-catalysts in CO and CO_2 hydrogenation.^{23,33}

The effect of potassium on the texture, chemical/phase composition and surface chemistry of the Fe–Al–O spinel. The texture measurements of the spent catalysts after operation of 120 h listed in Table 2 indicate a significant decrease of the surface area, pore volume and diameter as the potassium content increased. This may be attributed to increasing crystal size or aggregation of nanoparticles of the Fe-oxide and carbide phases produced from the Fe–Al–O spinel during activation and self-organization in the presence of K as was observed in ref. 34 for other Fe-catalysts. It may also be attributed to the blocking of pores with coke or wax which was increasingly deposited as the potassium content increased.

The chemical composition of the spent catalysts expressed as the weight ratio related to Fe is shown in Table 3. The catalyst containing 2 wt% K accumulated about the same amount of total carbon as the catalyst with no K. Increasing the amount of potassium to 4 wt% increased the total carbon content from 0.23 to 0.42. In all cases, the atomic ratio C/Fe was greater than unity, much higher than in any iron carbide phases FeC_x stable under the testing conditions (*i.e.* Fe_5C_2 , Fe_7C_3). This means that the spent catalysts contained a significant amount of coke or wax carbon deposited during self-organization.

The quantitative XRD phase analysis revealed a strong effect of potassium promoter on the phase composition of the spent catalysts as illustrated by the results listed in Table 4. The calculations of the phase content and their average crystal size were conducted based on their X-ray diffraction patterns shown in Fig. 1. All catalysts contain two Fe-carbide phases: γ - Fe_5C_2 and Fe_7C_3 formed as a result of spinel activation and self-organization when part of the iron was removed from the spinel phase. This decreases the x value in the formula of the spinel phase $Fe^{II}[(Fe_x^{III}Al_{1-x})_2]O_4$ from 0.5, in fresh catalyst, to 0.2–0.3 in Fe-poor spinel residua measured according to the positions of characteristic reflections in the X-ray diffractograms.

Table 2 Effect of potassium on the texture parameters of Fe–Al–O spinel spent catalysts. Testing conditions: 20 bar, 320°C, molar $H_2/CO_2 = 3$, 120 h on stream

Catalyst	Surface area, $m^2 g^{-1}$	Pore volume, $cm^3 g^{-1}$	Average pore diameter, nm
Cat. Fe-0K	78	0.23	6.0
Cat. Fe-2K	55	0.16	5.6
Cat. Fe-4K	42	0.10	4.6

Table 3 Chemical composition of the Fe–Al–O spinel spent catalysts. Testing conditions: 20 bar, 320°C, molar H₂/CO₂ = 3, 120 h on stream

Catalyst	Chemical composition							
	wt ratio				Atomic ratio			
	Fe	Al	C	K	Fe	Al	C	K
Cat. Fe–0K	1	0.21	0.25	0.0	1	0.44	1.2	0.0
Cat. Fe–2K	1	0.22	0.23	0.05	1	0.45	1.1	0.08
Cat. Fe–4K	1	0.20	0.42	0.10	1	0.42	1.9	0.13

A very significant result is the removal of Fe from the Fe–Al–O spinel in catalyst Cat. Fe–0K that was partially decomposed into Fe-poor spinel (27 wt%), amorphous alumina whose reflections cannot be observed in the diffractogram and magnetite (18 wt%). Adding potassium prevents the formation of a magnetite phase while the content of the Fe-poor spinel increased to 41–42 wt%. Potassium also enhances carburization of the Fe–Al–O spinel precursor to the active χ -Fe₅C₂ phase.³⁵ Interestingly, the content of the χ -Fe₅C₂ phase decreased as the potassium content increased from 2 wt% to 4 wt%. A relatively little change in the crystal size of the two iron carbide phases in two potassium promoted catalysts was observed.

The XPS spectra of the spent unpromoted and K-promoted Fe–Al–O spinel catalysts, as-received and after Ar-etching, are shown in Fig. 2 and 3 respectively. The BE (binding energy) for detected peaks and surface concentrations of corresponding atoms are given in Tables 5 and 6. Two main peaks were detected in the XPS spectra of iron. The first is attributed to the iron carbides at lower binding energy around 707.1–707.5 eV corresponding to the near-metallic state of iron and the second belongs to iron ions in oxide phases with higher binding energies in the range of 710.4.5–711.5 eV. The latter peaks represent superposition of signals contributed by Fe²⁺ with a BE of 709.5 and of Fe³⁺ with a BE of 711.2 eV.^{36,37} Insertion of 2 wt% potassium shifted the BE of the carbide and oxide iron atoms to lower values: from 707.5 (707.4 after etching) to 707.3 eV and from 711.5 (710.8 after etching) to 710.8 (710.4 after etching) eV. This corresponds to formation of

Table 4 Phase composition of the Fe–Al–O spinel spent catalysts. Testing conditions: 20 bar, 320°C, molar H₂/CO₂ = 3, 120 h on stream

Catalyst	Spinel wt%	Crystal size, nm	Magnetite wt%	Crystal size, nm	χ -Fe ₅ C ₂ wt %	Crystal size, nm	Fe ₇ C ₃ wt %	Crystal size, nm	χ -Fe ₅ C ₂ / (Fe ₅ C ₂ + Fe ₇ C ₃)
Cat. Fe–0K	27	8	18	35	34	25	21	35	62
Cat. Fe–2K	41	5	0	—	47	30	12	40	80
Cat. Fe–4K	42	6	0	—	42	35	16	40	72

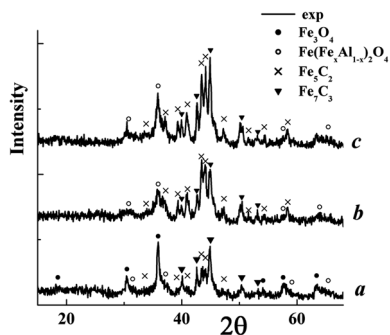


Fig. 1 XRD patterns of the Fe–Al–O spinel catalyst after reaching steady state in the catalytic testing run. (a) “Cat. Fe–0K”, (b) “Cat. Fe–2K”, (c) “Cat. Fe–4K”. Testing conditions: $P = 20$ bar, $T = 320$ °C, $H_2/CO_2 = 3$, 120 h on stream.

more reduced states of iron in carbides and in Fe-poor spinel due to electron-donation of the K-promoter.^{26,27}

Insertion of K increased the surface concentration or relative exposure of carbide iron. Deconvolution of XPS spectra recorded for the C 1s core show the coexistence of three groups of signals: peaks with BE 283.6–284.3 eV corresponding to Fe-carbide carbon, 284.8–285.1 eV belonging to C–C sp^2 and sp^3 in carbon and hydrocarbon ($-CH_2=CH$) deposits and 285.4–288.6 eV characteristic for adsorbed carbon oxygenate moieties containing C=O, C–O, CH_2-O , $O-C=O$ and other oxygen groups.^{36,38,39} Insertion of potassium increases the relative exposure of carbide carbon at the spent catalysts surface (from 11 to 19%). This is in agreement with growing of the exposure of carbide iron. Potassium also

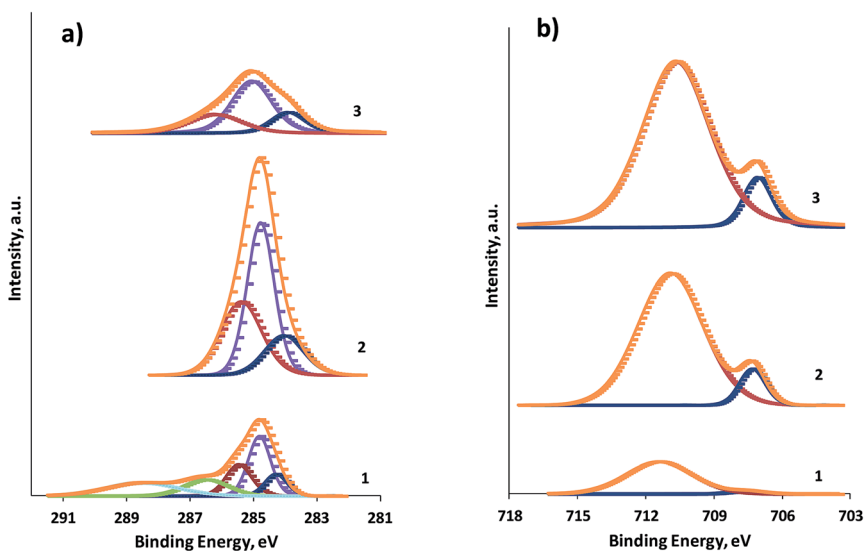


Fig. 2 XPS spectra recorded with as-received spent Fe–Al–O spinel catalysts: (a) – C 1s core; (b) – $Fe_{3/2}$ core: 1 – unpromoted catalyst; 2 – 2 wt% K; 3 – 4 wt% K.

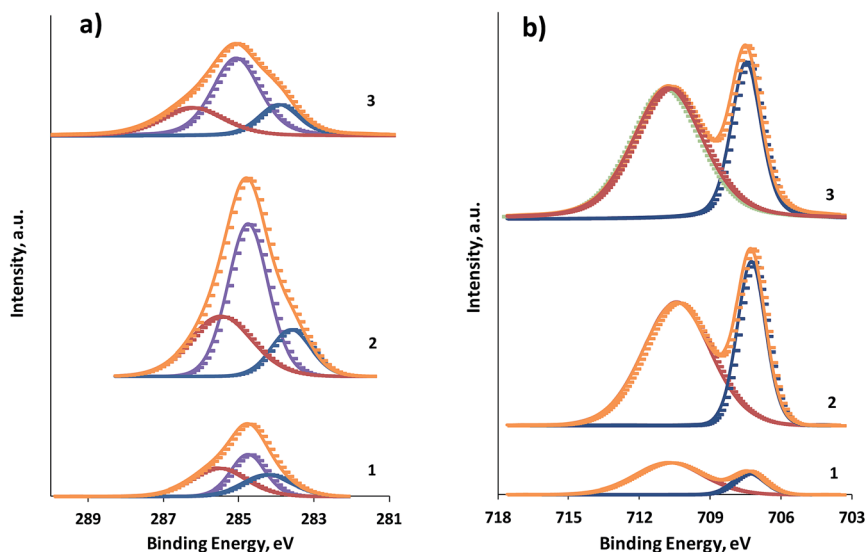


Fig. 3 XPS spectra recorded with spent Fe–Al–O spinel catalysts after Ar-etching: (a) – C 1s core; (b) – Fe_{3/2} core: 1 – unpromoted catalyst; 2 – 2 wt% K; 3 – 4 wt% K.

significantly increases the relative exposure of carbon belonging to graphite and hydrocarbon deposits from 31% (36% after etching) in the unpromoted catalyst to 48–55% in the catalysts containing 2–4 wt% K. At the same time insertion of potassium removes the oxygenated moieties with a high C 1s BE from 58% (39% after etching) in the unpromoted catalyst to 26–34% in the K-promoted catalysts.

Potassium is expected to increase the basicity of the Fe–Al–O spinel thus increasing the surface coverage with acidic CO₂ reagent molecules. The CO₂-TPD spectra illustrated in Fig. 4 indicate that the 2 wt% K catalyst displayed one CO₂ desorption peak centered at ~150 °C which represents relatively weak surface basic sites. Increasing the K content to 4 wt% further increased the weak basicity

Table 5 Binding energies and concentrations of surface atoms of the Fe–Al–O spinel spent catalyst. Testing conditions: 20 bar, 320 °C, molar H₂/CO₂ = 3, 120 h on stream

Catalyst name	C 1s core		Fe 2p _{3/2} core		Fe _{carb} /Fe _{ox}
	BE, eV	% atomic	BE, eV	% atomic	
Cat. Fe-0K	284.3	11	707.5	4	0.04
	284.8	31			
	285.5	19	711.5	96	
	286.5	17			
	288.6	22			
Cat. Fe-2K	284.1	18	707.3	10	0.11
	284.8	48	710.8	90	
	285.4	34			
Cat. Fe-4K	284.0	19	707.1	11	0.12
	285.1	55	710.7	89	
	286.3	26			

Table 6 Binding energies and concentrations of surface atoms of the Ar-etched Fe–Al–O spinel spent catalyst. Testing conditions: 20 bar, 320 °C, molar H₂/CO₂ = 3, 120 h on stream

Catalyst	C 1s core		Fe 2p _{3/2} core		Fe _{carb} /Fe _{ox}
	BE, eV	% atomic	BE, eV	% atomic	
Cat. Fe-0K	284.3	26	707.4	23	0.30
	284.8	36	710.8	77	
	285.6	39			
Cat. Fe-2K	283.6	16	707.3	36	0.56
	284.8	53	710.4	64	
	285.5	31			
Cat. Fe-4K	284.0	19	707.5	34	0.52
	285.1	55	710.8	66	
	286.3	26			

by a factor of 2.5. Furthermore, at the high K content of 4 wt% there appeared two additional CO₂ desorption peaks centered at 550 and 850 °C, corresponding to very strong basic sites. These results may be explained assuming strong interaction between Fe–Al–O spinel and potassium. At low concentrations of K, it mainly stabilizes the Fe–Al–O spinel phase, as detected by XRD. However, at the high

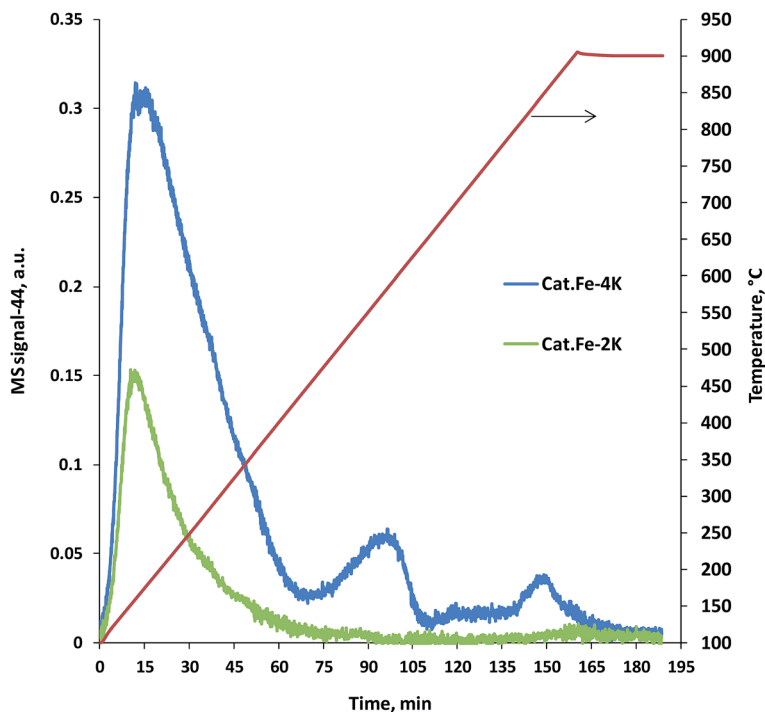


Fig. 4 CO₂-TPD spectra recorded with fresh K/Fe–Al–O spinel catalysts.

concentration of 4 wt%, potassium may exist in a free form of adsorbed K_2O , displaying strong surface basicity.

3.2. Kinetic model

Kinetic data were measured for the 4 wt% spinel Fe catalyst in a three-reactors-in-series system over a range of operating conditions (300–340 °C, 20–28 bar, molar $H_2/CO_2 = 2.9$, WHSV = 1–6 h^{-1}). In essence two processes took place in series: RWGS and FTS. Oligomerization of light olefins was also found to be important. In contrast to the recent kinetic model³² that employed power law expressions for all 10 reaction rates of FTS, our model consists of LHHW (Langmuir–Hinshelwood–Hougen–Watson) expressions that include an adsorption term in the denominator. This term contains two components: H_2O and CO_2 . The reactions were selected so as to reflect the main findings of the kinetic study: the RWGS reaction, methanation reaction, 7 FTS reactions and 4 oligomerization reactions. The 7 FT reactions (4)–(10) produce light paraffins (C_2 – C_5), four light olefins (C_2 , C_3 , C_4 and C_5), C_{6+} represented by decene and oxygenates represented by butanoic acid. The oligomerization reactions (11)–(14) convert the light olefins to C_{6+} products represented by decene. The reactions are listed in Table 7. The mass balances expressed by eqn (1) assume plug-flow with no internal or external mass and heat transfer resistances:

$$\frac{d\omega_i}{d\left(\frac{1}{\text{WHSV}}\right)} = R_i \omega_{CO_2, \text{in}} M_{w_i} \quad (1)$$

where ω_i is the mass fraction of component i , WHSV is the weight hourly space velocity of CO_2 , R_i is the rate of change in the reaction where component i is a reactant/product, $\omega_{CO_2, \text{in}}$ is the mass fraction of CO_2 at inlet and M_{w_i} is the molecular weight of component i .

The reactions and rate expressions of kinetic model are as follows:

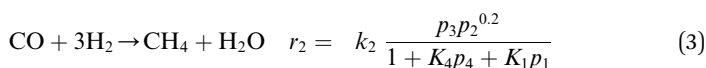
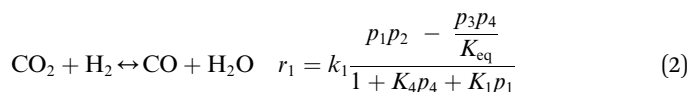
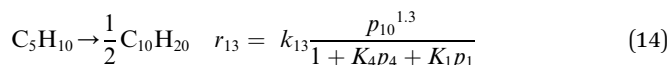
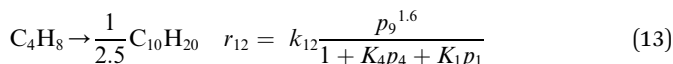
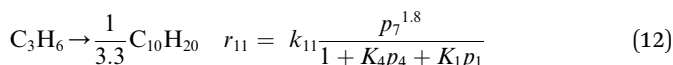
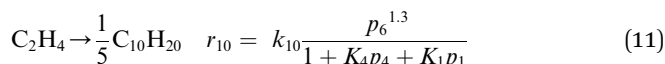
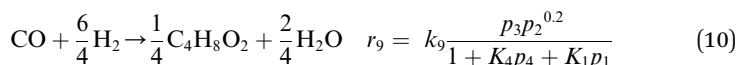
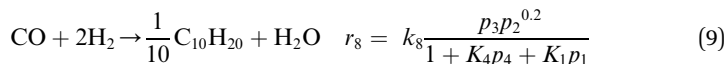
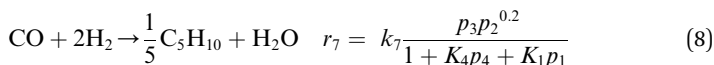
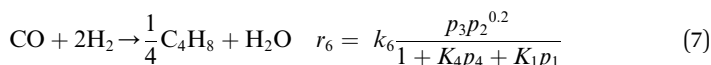
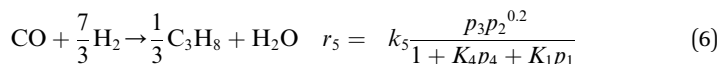
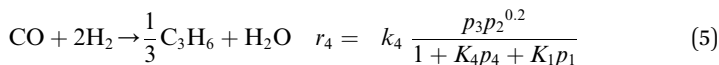
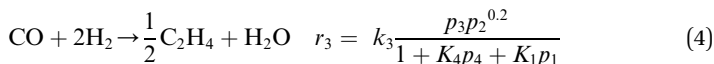


Table 7 Key components of the kinetic model

Comp.	Name	Formula	Comp.	Name	Formula
1	Carbon dioxide	CO_2	7	Propylene	C_3H_6
2	Hydrogen	H_2	8	Propane ^a	C_3H_8
3	Carbon monoxide	CO	9	1-Butene	C_4H_8
4	Water	H_2O	10	Pentene	C_5H_{10}
5	Methane	CH_4	11	Decene ^b	$C_{10}H_{20}$
6	Ethylene	C_2H_4	12	Butanoic acid ^c	$C_4H_8O_2$

^a C_2 – C_5 paraffins. ^b C_{6+} . ^c Oxygenates.



Kinetic modeling of the experimental data was conducted employing MATLAB, using 216 data points measured at the outlet of the first, second and third reactor. The MATLAB function “ode113” solved the differential equations system. Kinetic models were fitted to the data using the “fmincon” function used to find the minimum SSE value. The kinetic constants, including pre-exponent coefficient and activation energy, are listed in Table 8. The adsorption constants, including the adsorption pre-exponential factor and the heat of adsorption, are listed in Table 9. A parity plot of ω_i of all components at the outlet of each reactor that reflects the good agreement of the experimental data with values calculated with the model (R^2 calculated using regression statistics is 0.99) is depicted in Fig. 5. The predicted and experimental weight fractions of CO_2 and CO at the outlet of each one of the three reactors at 320 °C and 20 and 28 bar, depicted in Fig. 6, are in good agreement. They illustrate the significant contribution of each reactor and the relatively weak effect of total pressure.

The kinetic developed for the catalyst containing 4 wt% K will be further extended to account for the significant effect of potassium. Furthermore, it will be

Table 8 Kinetic constants of the rate expressions

k_j	k_{0j}	Units	E_j , kJ mol ⁻¹	k_j	k_{0j}	Units	E_j , kJ mol ⁻¹
k_1	$5.5 \times 10^{+6}$	mol g ⁻¹ h ⁻¹ MPa ⁻²	72.2	k_8	$4.0 \times 10^{+3}$	mol g ⁻¹ h ⁻¹ MPa ^{-1.2}	33.4
k_2	$1.0 \times 10^{+9}$	mol g ⁻¹ h ⁻¹ MPa ^{-1.2}	98.0	k_9	$3.6 \times 10^{+3}$	mol g ⁻¹ h ⁻¹ MPa ^{-1.2}	31.5
k_3	$1.2 \times 10^{+4}$	mol g ⁻¹ h ⁻¹ MPa ^{-1.2}	45.0	k_{10}	$2.7 \times 10^{+3}$	mol g ⁻¹ h ⁻¹ MPa ^{-1.3}	25.8
k_4	$1.2 \times 10^{+5}$	mol g ⁻¹ h ⁻¹ MPa ^{-1.2}	53.6	k_{11}	$1.4 \times 10^{+4}$	mol g ⁻¹ h ⁻¹ MPa ^{-1.8}	35.5
k_5	$1.8 \times 10^{+4}$	mol g ⁻¹ h ⁻¹ MPa ^{-1.2}	46.4	k_{12}	$3.7 \times 10^{+4}$	mol g ⁻¹ h ⁻¹ MPa ^{-1.6}	40.7
k_6	$1.1 \times 10^{+3}$	mol g ⁻¹ h ⁻¹ MPa ^{-1.2}	31.5	k_{13}	$6.0 \times 10^{+7}$	mol g ⁻¹ h ⁻¹ MPa ^{-1.3}	88.8
k_7	$9.0 \times 10^{+2}$	mol g ⁻¹ h ⁻¹ MPa ^{-1.2}	31.5				

employed to evaluate the effectiveness factor of the reactions in the model for pelletized catalyst. CO in the process feed will also be examined. This will facilitate the application of the kinetic model to simulate the performance of the process at operating conditions that are relevant to commercial applications.

3.3. Conversion of CO₂, CO and H₂ mixtures to higher hydrocarbons

The process described in this study was conducted with a feed containing CO₂ and H₂ and a mixture that contained CO₂, CO and H₂. The data presented here were measured with pelletized (1.4–1.7 mm) catalysts containing 3 wt% and 4 wt % K over a range of feed compositions and operating conditions to examine the potential of the process under conditions relevant for commercial applications. Furthermore, the data will be employed in the simulations of the process.

Experiments were carried out in the three-reactor system at 20 and 30 bar, 320 and 330 °C, over a range of operating conditions, including feed composition and WHSV. The results of 5 runs, 4 of them at 20 bar and run P-63-300 at 30 bar, are listed in Table 10. The oxygenates listed in Table 10 are dissolved in water. The composition of the organic liquid collected in runs P-63-164 and P-65-69 is given in Table 11. WHSV is calculated as the mass flow rate of CO₂ and CO divided by the mass of catalyst. The other parameters are defined in Table 10. sCO_x is defined so that a molar H₂/ sCO_x = 1 is stoichiometric for all feed compositions. The mass balance in all 4 runs was >94%.

Run P-63-164 was carried out with catalyst containing 4 wt% K at 20 bar with stoichiometric feed. The conversion was relatively high and the selectivity to C₅₊ was >50 wt%. P-63-300 was conducted with a sub-stoichiometric ratio. Thus the CO₂ conversion was lower than that of H₂. WHSV and the pressure were increased from 1.1 h⁻¹ and 20 bar to 1.3 h⁻¹ and 30 bar, respectively. Increasing the WHSV should lower the conversion while increasing the pressure should increase the conversion. Apparently, the two changes offset each other thus the conversion

Table 9 Adsorption constants of CO₂ and H₂O

k_i	k_{0i} , MPa ⁻¹	ΔH_{ai} , kJ mol ⁻¹
k_1	2.1×10^{-2}	33.4
k_4	2.4×10^{-2}	31.5

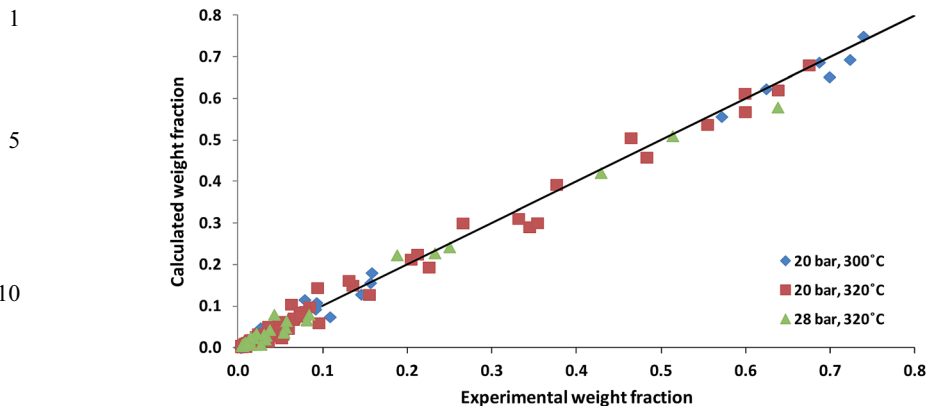


Fig. 5 Parity plot of the calculated and experimental data.

changed little. The selectivity in the runs was rather similar, although the methane selectivity in run P-63-300 was slightly lower and the C_{5+} selectivity slightly higher.

Introducing CO to the feed in the system packed with catalyst containing 4 wt% K led to a gradual deterioration of the catalyst performance as shown in run P-65 depicted in Table 10. This was rectified in Run P-66 by replacing the catalyst in the first reactor with a 3 wt% K catalyst that displayed stable performance. The performance of two reactors in series, P-66-396 R1 (after one reactor) and R2 (after two reactors) listed in Table 10, indicates that the conversion of CO is much higher than the CO_2 conversion in both reactors. The selectivity in both reactors is similar.

The composition of the organic phase in runs P-63-164 and P-66-396 is listed in Table 11. As expected, the liquid contained much more olefins (>65 wt%) than paraffins (<25 wt%). A comparison of the product distribution between naphtha and distillates in the two experiments and the data measured with the 3 wt% K catalyst published elsewhere¹⁴ is depicted in Fig. 7. Surprisingly, the first reactor

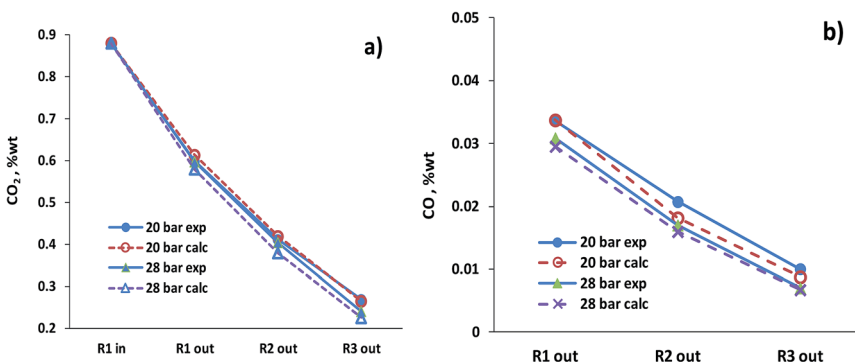


Fig. 6 Calculated vs. experimental weight fraction of CO_2 (a) and CO (b) at the outlet of the three reactors system at molar $H_2/CO_2 = 2.9$, $320^\circ C$, $WHSV = 3 h^{-1}$.

Table 10 Performance of CO₂ and CO hydrogenation process on pelletized catalyst^a

Run	WHSV h ⁻¹	Temp. °C	H ₂ / sCO _x molar	CO ₂ / CO _x molar	x ₁ %	x ₂ %	x ₃ %	S ₄ %	S ₅ %	S ₆ %	S ₇ %	S ₈ %	S ₉ %	S ₁₀ %
P-63-164	1.0	320	1.0	1.0	82	81.7	—	10.5	6.2	18.5	2.0	2.7	51.9	8.2
P-63-300	1.3	320	0.9	1.0	77.6	87.9	—	9.6	5.5	15.6	2.1	2.6	54.1	10.5
P-65-45	0.9	330	1.1	0.7	63.8	70.9	92.0	11.6	7.0	19.7	1.8	2.5	49.1	7.9
P-65-69	0.9	330	1.1	0.7	61.6	68.7	90.3	11.3	6.6	17.9	1.8	2.5	51.8	8.1
P-65-93	0.9	330	1.1	0.7	58.6	68.6	90.0	12.0	6.7	18.2	2.0	3.1	50.4	7.8
P-65-141	1.0	330	1.1	0.7	48.3	63.0	83.2	13.8	7.5	12.7	2.4	3.5	50.7	9.8
P-66-396 R1	1.0	320	0.7	0.8	20.6	33.9	48.7	12.9	7.7	22.4	1.9	2.9	45.0	7.2
P-66-396 R2	1.0	320	0.7	0.8	39.0	66.8	86.7	11.1	6.9	21.0	2.3	2.9	47.8	7.9

^a The reactants are defined as: CO₂ ≡ A₁; H₂ ≡ A₂; CO ≡ A₃ while the products are listed as: CH₄ ≡ A₄; C₂H₄ ≡ A₅; C₃H₆ + C₄H₈ ≡ A₆; C₂H₆ ≡ A₇; C₃H₈ + C₄H₁₀ ≡ A₈; C₅₊ ≡ A₉; oxygenates ≡ A₁₀; H₂O ≡ A₁₁; sCO_x = 3CO₂ + 2CO; CO_x = CO₂ + CO; x_j is the conversion of reactant j; S_j is the selectivity of product j expressed as the mass fraction of the carbon converted to that product.

packed with 3 wt% K catalyst in run P-66-396 yielded a slightly heavier product compared with the product in the second reactor of the same run and in the three combined reactors in run P-63-164, packed with 4 wt% K catalyst. This is probably

Table 11 Composition of the organic liquid in runs P-63-164 and P-66-396

		P-66-396		
		Reactor 1	Reactor 2	P-63-164
C ₅ -C ₁₀	Non α-olefins	10.8	9.2	10.1
	α-Olefins	16	19.9	21.4
	Non n-paraffins	5.1	8.4	6.1
	n-Paraffins	5	5.9	6.0
	Aromatics	2.2	2	2.6
	Oxygenates	1.6	1.7	3.3
C ₁₁ -C ₂₂	Non α-olefins	10.5	12.4	12.7
	α-Olefins	20.7	18	17.1
	Non n-paraffins	9.5	5.9	5.8
	n-Paraffins	7.8	5.8	5.4
	Aromatics	2.3	3	4.8
	Oxygenates	1.3	3.2	3.0
>C ₂₂	Non α-olefins	1	0.6	0.4
	α-Olefins	5.5	3.4	1.3
	Paraffins	0.7	0.6	0.0

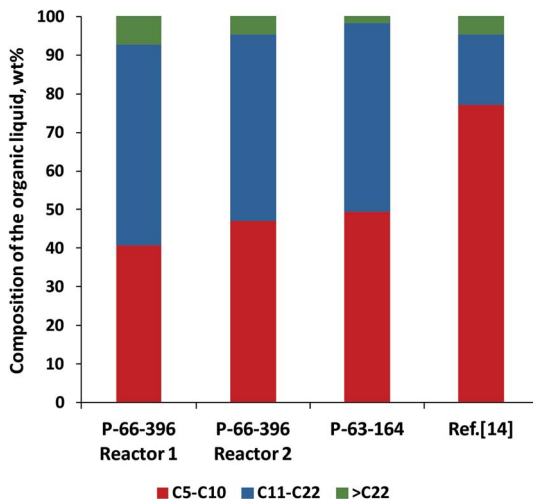


Fig. 7 A comparison of the liquid organic product between the first two reactors in run P-66-396, P-63-164 and ref. 14. First reactor in P-66-396 is loaded with 3 wt% K, second reactor in P-66-396 is loaded with 4 wt% K. P-63-164 is loaded with 4 wt% K.

due to the fact that the feed to the first reactor contained a significant concentration of CO. Furthermore, the product obtained with a stoichiometric mixture of H₂ and CO₂ in a three-reactor unit packed with a 3 wt% K catalyst¹⁴ yielded a much lighter product than produced with a 4 wt% K catalyst.

4. Conclusions

Potassium was found to be a key promoter that enhances significantly the reaction rates of RWGS and FTS and increases the selectivity to higher hydrocarbons while producing mostly olefins. The methanation rate was decreased extensively on the promoted catalysts. These effects are a result of the lower hydrogenation activity, consistent with the observation of more reduced states of iron atoms at the spent steady state Fe–Al–O catalysts surface after addition of potassium. They could be attributed to the donation of electron density to vacant d-orbitals of iron in both Fe-poor spinel and carbide phases thus enhancing the dissociative adsorption of CO while lowering the H₂ adsorption ability. The stabilization of the Fe-poor spinel phase that prevented decomposition to the magnetite phase contributed to the higher activity and selectivity of the catalyst. Furthermore, potassium enhanced the catalysts surface coverage with CO₂ as shown by CO₂-TPD data. The FTS reactions were accelerated by the enrichment of the catalyst surface with carbide iron, especially the more active Fe₅C₂ phase as established by the XRD and XPS data.

A detailed kinetic model was developed based on extensive experimental data. It includes the RWGS, methanation, 7 FTS, 4 oligomerization and oxygenates formation reactions. The fit of the kinetic model to the experimental data was very good. Specifically, the significant oligomerization activity of the catalyst that converts light olefins to higher hydrocarbons should be mentioned. Running mixtures of CO₂, CO and H₂ in a three reactor system packed with pelletized

1 catalyst yielded a high productivity of higher hydrocarbons. The composition of
the C₅₊ product was a function of the potassium content and the composition of
the feed. A heavier product was measured with a catalyst containing 4 wt%
5 potassium compared with the 3 wt% potassium catalyst and with a feed containing
CO₂, CO and H₂ compared with a feed containing only CO₂ and H₂.

Acknowledgements

10 This work was supported by the Israel – Strategic Alternative Energy Foundation
(I-SAEF), the I-CORE Program of the Planning and Budgeting Committee and The
Israel Science Foundation (grant No. 152/11) and grant No. 582/13 of the Israel
Science Foundation. The authors are grateful to Dr A. Erenburg for XRD character-
15 zation of catalysts and to Dr N. Froumin for characterization of catalysts by
XPS.

References

- 1 World Energy Outlook, IEA, 12 November, 2014.
- 2 B. Friedrich, B. Schink and R. K. Thauer, *Bioenergy – Chances and Limits*,
German National Academy of Sciences Leopoldina, 2012, pp. 1–118, <http://www.leopoldina.org>.
- 3 F. Creutzig, C. von Stechow, D. Klein, C. Hunsberger, N. Bauer, A. Popp and
O. Edenhofer, *Economics of Energy & Environmental Policy*, 2012, vol. 1, pp.
25 65–82.
- 4 J. A. Herron, J. Kim, A. A. Upadhye, G. W. Huber and C. T. Maravelias, *Energy
Environ. Sci.*, 2015, **8**, 126–215.
- 5 G. Centi and S. Perathoner, *ChemSusChem*, 2010, **3**, 195–208.
- 6 K. S. Joya, Y. F. Joya, K. Ocakoglu and R. van de Krol, *Angew. Chem., Int. Ed.*,
30 2013, **52**, 10426–10437.
- 7 B. A. Pinaud, J. D. Benck, L. C. Seitz, A. J. Forman, Z. Chen, T. G. Deutsch,
B. D. James, K. N. Baum, G. N. Baum, S. Ardo, H. Wang, E. Millere and
T. F. Jaramillo, *Energy Environ. Sci.*, 2013, **6**, 1983–2002.
- 8 J. R. McKone, N. S. Lewis and H. B. Gray, *Chem. Mater.*, 2014, **26**, 407–414.
- 9 C. Agrafiotis, M. Roeb and C. Sattler, *Renewable Sustainable Energy Rev.*, 2015,
35 **42**, 254–285.
- 10 S. P. S. Badwal, S. Giddey and C. Munnings, *WIREs Energy Environ.*, 2013, **2**,
473–487.
- 40 11 J. A. Trainham, J. Newman, C. A. Bonino, P. G. Hoertz and N. Akunuri, *Curr.
Opin. Chem. Eng.*, 2012, **1**, 204–210.
- 12 J. Newman, P. G. Hoertz, C. A. Bonino and J. A. Trainham, *J. Electrochem. Soc.*,
2012, **159**(10), A1722–A1729.
- 13 C. Graves, S. D. Ebbesen, M. Mogensen and K. S. Lackner, *Renewable
Sustainable Energy Rev.*, 2011, **15**, 1–23.
- 45 14 M. V. Landau, R. Vidruk and M. Herskowitz, *ChemSusChem*, 2014, **7**, 785–794.
- 15 D. A. Wood, C. Nwaoha and B. F. Towler, *J. Nat. Gas Sci. Eng.*, 2012, **9**, 196–208.
- 16 A. H. Lillebø, A. Holmen, B. C. Enger and E. A. Blekkan, *WIREs Energy Environ.*,
2013, **2**, 507–524.
- 50 17 R. Rauch, J. Hrbek and H. Hofbauer, *WIREs Energy Environ.*, 2014, **3**, 343–362.
- 18 I. Hannula, *Biomass Bioenergy*, 2015, **74**, 26–46.

- 1 19 L. Yang, X. Ge, C. Wan, F. Yu and Y. Li, *Renewable Sustainable Energy Rev.*,
2014, **40**, 1133–1152.
- 20 S. C. Kang, K.-W. Jun and Y.-J. Lee, *Energy Fuels*, 2013, **27**, 6377–6387.
- 5 21 Y. Yao, X. Liu, D. Hildebrandt and D. Glasser, *Ind. Eng. Chem. Res.*, 2011, **50**,
11002–11012.
- 22 M. V. Landau, R. Vidruk and M. Herskowitz, WO Patent 2014111919, 2014.
- 23 J. Yang, W. Ma, D. Chen, A. Holmen and B. H. Davis, *Appl. Catal., A*, 2014, **470**,
250–260.
- 10 24 M.-D. Lee, J.-F. Lee and C.-S. Chang, *Bull. Chem. Soc. Jpn.*, 1989, **62**, 2756–2758.
- 25 M. Martinelli, C. G. Visconti, L. Lietti, P. Forzatti, C. Bassano and P. Deiana,
Catal. Today, 2014, **228**, 77–88.
- 26 H. P. Bonzel, *Surf. Sci. Rep.*, 1987, **8**, 43–125.
- 27 M. E. Dry, T. Shingles, L. J. Boshoff and G. J. Oosthuizen, *J. Catal.*, 1969, **15**,
190–199.
- 15 28 E. de Smit and B. M. Weckhuysen, *Chem. Soc. Rev.*, 2008, **37**, 2758–2781.
- 29 C. Zhang, K.-W. Jun, K.-S. Ha, Y.-J. Lee and S. C. Kang, *Environ. Sci. Technol.*,
2014, **48**, 8251–8257.
- 30 T. Riedel, G. Schaub, K.-W. Jun and K.-W. Lee, *Ind. Eng. Chem. Res.*, 2001, **40**,
1355–1363.
- 20 31 M. Iglesias, C. de Vries, M. Claeys and G. Schaub, *Catal. Today*, 2015, **242**, 184–
192.
- 32 N. Park, J.-R. Kim, Y. Yoo, J. Lee and M.-J. Park, *Fuel*, 2014, **122**, 229–235.
- 33 M. E. Dry, *Catal. Today*, 1990, **6**, 183–206.
- 25 34 H. Wan, B. Wu, C. Zhang, H. Xiang and Y. Li, *J. Mol. Catal. A: Chem.*, 2008, **283**,
33–42.
- 35 B. H. Davis, *Catal. Today*, 2009, **141**, 25–33.
- 36 J. B. Butt, *Catal. Lett.*, 1990, **7**, 61–82.
- 37 K. B. Sunil, A. V. Anupama, B. Bikramjit and S. Balaram, *J. Phys. Chem. C*, 2015,
30 **119**, 6539–6555.
- 38 <http://xpssimplified.com/elements/carbon.php>.
- 39 A. Furlan, U. Jansson, J. Lu, L. Hultman, M. Magnuson and L., *J. Phys.:
Condens. Matter*, 2015, **27**, 045002.
- 35 40 X. An, B. Wu, H.-J. Wan, T.-Z. Li, Z.-C. Tao, H.-W. Xiang and Y.-W. Li, *Catal.
Commun.*, 2007, **8**, 1957–1962.
- 40
- 45
- 50

PAPER

Kinetic and economic analysis of reactive capture of dilute carbon dioxide with Grignard reagents

G. R. M. Dowson, I. Dimitriou, R. E. Owen, D. G. Reed, R. W. K. Allen and P. Styring

Received 1st May 2015, Accepted 18th June 2015

DOI: 10.1039/c5fd00049a

Carbon Dioxide Utilisation (CDU) processes face significant challenges, especially in the energetic cost of carbon capture from flue gas and the uphill energy gradient for CO₂ reduction. Both of these stumbling blocks can be addressed by using alkaline earth metal compounds, such as Grignard reagents, as sacrificial capture agents. We have investigated the performance of these reagents in their ability to both capture and activate CO₂ directly from dried flue gas (essentially avoiding the costly capture process entirely) at room temperature and ambient pressures with high yield and selectivity. Naturally, to make the process sustainable, these reagents must then be recycled and regenerated. This would potentially be carried out using existing industrial processes and renewable electricity. This offers the possibility of creating a closed loop system whereby alcohols and certain hydrocarbons may be carboxylated with CO₂ and renewable electricity to create higher-value products containing captured carbon. A preliminary Techno-Economic Analysis (TEA) of an example looped process has been carried out to identify the electrical and raw material supply demands and hence determine production costs. These have compared broadly favourably with existing market values.

Introduction

With the looming threats posed by climate change, a key plank in carbon dioxide reduction strategies is to develop new pathways to mitigate and avoid emissions by the production of low carbon, carbon neutral and even carbon negative alternatives to common and bulk chemicals.¹ One route by which this can be accomplished is to incorporate carbon dioxide, that would otherwise be emitted, into the desired product, thus delaying or avoiding its release into the atmosphere. In this way, when the product is consumed or degraded, there is a reduced change in atmospheric carbon dioxide levels associated with that product, ideally

UK Centre for Carbon Dioxide Utilization, Department of Chemical and Biological Engineering, The University of Sheffield, Sir Robert Hadfield Building, Sheffield, S1 3JD, UK

1 rendering the product itself carbon neutral. Naturally, if the product has a pro-
longed life or is recycled effectively this method represents an overall seques-
tering of the original carbon dioxide from the atmosphere to the solid state in a
5 form of long term storage which would complement geological storage
aspirations.²

This strategy of Carbon Dioxide Utilisation (CDU) is known by a variety of
names and acronyms, but in all cases involves the use of carbon sources,
including mixed and dilute ones such as flue gas and biogas, to generate prod-
ucts.³ The resulting products therefore have a reduced carbon footprint leading to
10 an overall net emissions reduction. While ambitious, if CDU processes can be
implemented with atmospheric carbon dioxide (also known as “direct air
capture”, DAC) this would represent both a key technique to form a sustainable
carbon product cycle, analogous to the natural carbon cycles, and potentially
15 allow the creation of useful products irrespective of geographical location.

This generation of products using carbon dioxide is what sets CDU apart from
Carbon Capture and Sequestration (CCS) where carbon dioxide is instead treated
as a waste to be dumped in geological storage sites, with only the environmental
benefit of net emissions reduction as a motivation. The major benefit of CDU, in
20 contrast, is the addition of value by the carbon dioxide to the product in addition
to the environmental benefit associated with shrinking, or eliminating, its carbon
footprint.

The extent of the environmental benefit will of course be product-dependent,
however recent publications have shown that even modest targets for CDU allow
25 amounts of CO₂ to be mitigated that match or even exceed current CCS targets.⁴
Indeed, while it predates this argument, global production of urea from CO₂ and
ammonia (which is essentially a CDU process) utilises *ca.* 140 million tonnes of
carbon dioxide annually.¹ Admittedly, when the production of ammonia and the
breakdown of urea as a fertilizer are taken into consideration, the net emissions
30 of the overall process are greater than unity. However, urea production acts as an
indicator of the scale that CDU processes could hope to achieve, dwarfing even
optimistic CCS targets of 102 million tonnes total stored by 2020.⁵

The fact that CDU treats carbon dioxide as a resource rather than a waste also
allows traditional economic driving forces to foster innovation. This has already
35 resulted in several examples of economically successful CDU processes.⁶ These
include the Bayer Dream process,⁷ where CO₂ is incorporated into polyurethane
plastics, Sunfire’s synthetic diesel⁸ and Carbon Recycling International, where
cheap Icelandic geothermal energy is used to turn CO₂ into methanol.⁹

40 **Importance of techno-economic analysis in CDU processes**

Since CDU primarily relies upon the addition of value through using the CO₂, it
would therefore seem essential to combine any serious attempt at the develop-
45 ment of a CDU process with at least a preliminary or generalised Techno-
Economic Analysis/Assessment (TEA) to demonstrate what value, if any, can be
added by the process in question.¹⁰

This is because the likelihood for implementation of existing and new tech-
nologies depends on the interest and motivation of private and public investors.
50 Many researchers who develop new technologies have limited knowledge of their
economic potentials and pitfalls. Therefore, understanding the investors’ needs

1 and the related economic questions enables technology developers to focus their
work on the promising options and avoid expending effort in technologies that
are fundamentally not economically viable. TEA studies of new technologies and
processes, such as CDU systems, allow us to better understand the relationship
5 between process performance (*e.g.* conversion) and costs (*e.g.* production) to help
identify the most promising process designs which can provide the highest
financial returns for the potential investors. Therefore, in the case of CDU, TEA
studies are an invaluable tool which can support policy makers and businesses in
their decision-making by establishing whether the production of chemicals and
10 fuels from waste CO₂ is economically feasible; and identifying the modifications
and conditions required to improve the economic competitiveness of CDU
technologies.

15 What has already been revealed by these analyses and assessments is that for
CDU and CCS strategies that rely on separation of carbon dioxide from dilute
sources such as flue gas, this “capture” step is a major energy sink and therefore
carries significant costs.¹¹

20 Cost of capture of CO₂

Separating carbon dioxide from other gases on a large scale is one of the biggest
challenges for CDU and also CCS. This might be surprising as thermodynamically
the cost of separation is not large (Table 1). Even the most dilute source of CO₂,
such as that which is found in the atmosphere, requires only 521.7 MJ per tonne
25 for separation (approximated from binary CO₂ : N₂ mixtures).

Despite this, calculated capture energy costs using industrial benchmark
capture agents such as monoethanolamine (MEA) and other amines frequently
exceed 3000–4000 MJ per tonne CO₂ even when starting from relatively concen-
trated CO₂ sources. This translates into both large capital and large operational
30 costs for carbon capture from power plants, with the cost of the capture plant
often exceeding the base plant costs (see Fig. 1).¹²

The cause of this discrepancy in energy cost, in the case of MEA and other
amines, is that the capture process is driven by a chemisorption reaction loop
involving the creation and then decomposition of carbamates.¹³ The high energy
35 cost of this loop is indicative of the relatively low reactivity of carbon dioxide at
standard temperatures and pressures. However, while this reactive capture
chemisorption approach has the major advantage of ensuring high carbon
dioxide selectivity over the other main component gases, nitrogen and methane

40
Table 1 Minimum thermodynamic energy cost of separating 1 tonne of CO₂ from N₂/CO₂
mixtures at STP

45 CO ₂ concentration in N ₂ (vol%)	Minimum entropic demixing cost per tonne CO ₂ (MJ)
Atmospheric (400 ppm)	521.7
1%	340.2
5%	248.0
10%	206.9
50 15%	182.0
20%	163.6

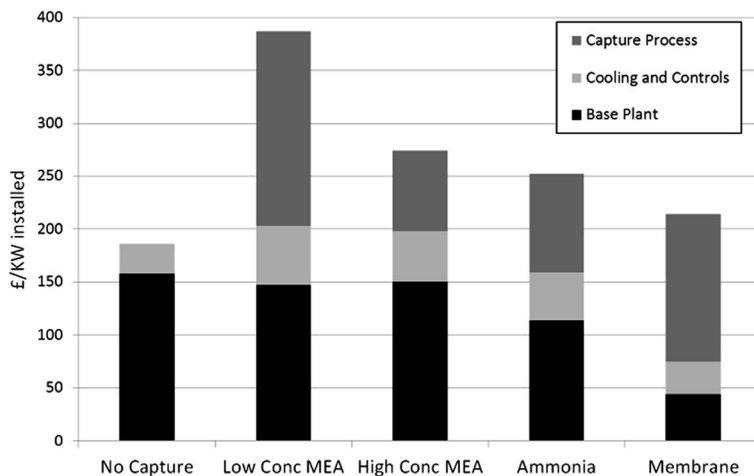


Fig. 1 Breakdown of annual operation and maintenance (O&M) costs per unit electricity by capture processes.

(in flue gas and biogas respectively), it actually represents a waste of energy from CDU perspectives as the product carbamate is itself a CDU product. As a result, the decomposition of the post-capture carbamate to create purified CO_2 only to react that CO_2 again to make another product can be seen as an energetic wild goose chase where the carbon dioxide is essentially utilised twice!

Additionally, the chemisorption approach will often allow some of the trace gases in these feed gas streams to react with the sorbent. At best, this is disadvantageous due to the displacement of CO_2 in the capture step, but at worst the trace gas poisons the sorbent permanently. This is especially problematic when dealing with gas supplies contaminated with sulfur compounds.

While for MEA the carbamate product is a mere intermediate for CO_2 purification, if an analogous process where a valuable carbon-carbon bond is formed instead were developed, it would represent a potentially attractive pathway for direct conversion of flue gas into products without a distinct gas separation step. Naturally the value of this process would be decided by the economic value of the product but it would certainly avoid much of the wasted energetic costs of the carbamate loop.

Any such process would therefore require a stoichiometric reactant of some sort with which the CO_2 must react, however this is already the case when using any capture process for the generation of CDU products. Considering the reactants that could be used, one prominent example is the Grignard reaction, involving organomagnesium halide reagents.

A fresh look at Grignard chemistry in the context of carbon dioxide reactive capture

The classic schoolroom carbon-carbon bond formation process using carbon dioxide is the reaction of a Grignard reagent with a pellet of dry ice. This standard reaction proceeds by the insertion of the carbon dioxide molecule between the

1 carbon–magnesium bond of an organomagnesium halide, formed by the reaction
of metallic magnesium with an organohalide (Scheme 1).¹⁴

5 This reaction is exothermic and readily carried out at atmospheric pressure
and ambient temperatures. Aside from requiring that all components are strin-
gently dried, due to the rapid and exothermic reaction with water, the reaction
also proceeds to typically high yields, dependent on reaction conditions and
solvents, with a wide range of possible R-groups. The resulting carboxylic acid
product is then readily isolated from the magnesium salt by-product in the
majority of cases by solvent extraction, esterification and/or distillation.¹⁵

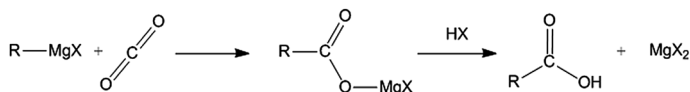
10 The strongly exothermic nature of the reaction is driven by the oxidation of the
starting elemental magnesium to the 2+ oxidation state. Coupled with the
exothermic nature of the formation of the initial organohalide (*e.g.* –42.2 kJ
mol^{–1} for methyl bromide from methanol), the overall reaction of the parent
alcohol with CO₂ becomes facile.

15 While methanol would be the parent alcohol in the example in Fig. 2, the
Grignard reaction is well-understood and offers a wide range of potential
substrates, allowing a variety of industrially interesting CDU products to poten-
tially be formed, a selection of which is shown in Fig. 3.

20 The substrates for the formation of the above products could open new
pathways of commercial or environmental interest. In particular, the use of CO₂-
derived carboxylic acids in polymers has already been targeted for large scale CDU
applications.¹⁶ For example, adipic acid, used for the synthesis of Nylon, is
currently manufactured from petrochemical phenol, cyclohexene or butadiene,
25 but could instead be created from biological 1,4-butanediol and CO₂ *via* haloge-
nation to 1,4-dihalobutane. Similarly, terephthalic acid which is a key component
of polyethyleneterephthalate (PET) plastic, the third most common plastic in use
today, is currently derived from *p*-xylene, of which there has been a long-standing
shortage and safety concerns, highlighted by the recent explosions in Zhangzhou,
30 China.¹⁷ By utilising CO₂, the terephthalic acid polymer precursor could be
derived directly from the relatively plentiful benzene (*via p*-dihalobenzene, which
is easily synthesised).

35 Collectively, the products shown in Fig. 3 are manufactured on a scale of
approximately 71 million tonnes per annum worldwide and could potentially
utilise over 40 million tonnes of CO₂, much of which would be sequestered into
various polymers and other long life products.

40 However, as previously mentioned, Grignard reactions of carbon dioxide
would typically be carried out using dry ice pellets rather than gas phase or dilute
CO₂ mixtures. A series of tests were therefore performed to determine whether
direct utilisation of gas phase CO₂ and even simulated flue gas compositions and
atmospheric concentrations were in any way suitable for Grignard chemistry. The
reaction conditions and reaction rates for different gas compositions would allow
45 a more complete techno-economic analysis of the process to be completed.



50 Scheme 1 Generalised reaction of a Grignard reagent with CO₂.

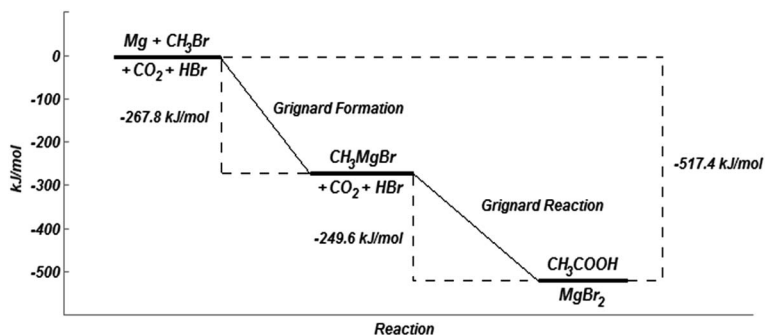


Fig. 2 Reaction enthalpy profile of each step of a Grignard reaction to form acetic acid from CO_2 and methyl bromide.¹⁶

Grignard reactions can typically be tracked by titration of the remaining active organomagnesium reagent using 1,10-phenanthroline. The phenanthroline forms a coloured, charge transfer complex in a 1 : 1 ratio with the reagent that may then be titrated by using a dry alcohol such as 2-butanol.¹⁸ However, it was found that in the case of the reaction of methylmagnesium chloride and CO_2 , no colour change was observed when injected into a solution of 1,10-phenanthroline in dry THF. A possible reason for this is that the intermediate product, a magnesium acetate bromide species, acts as a quenching agent for the charge transfer complex, thereby preventing the colour change needed for titration.

Therefore, in order to determine the rate of reaction of CO_2 with methylmagnesium chloride, a high-accuracy pressure transducer (Omega PX409USB) was used to monitor CO_2 consumption within the reaction apparatus (Fig. 4). In

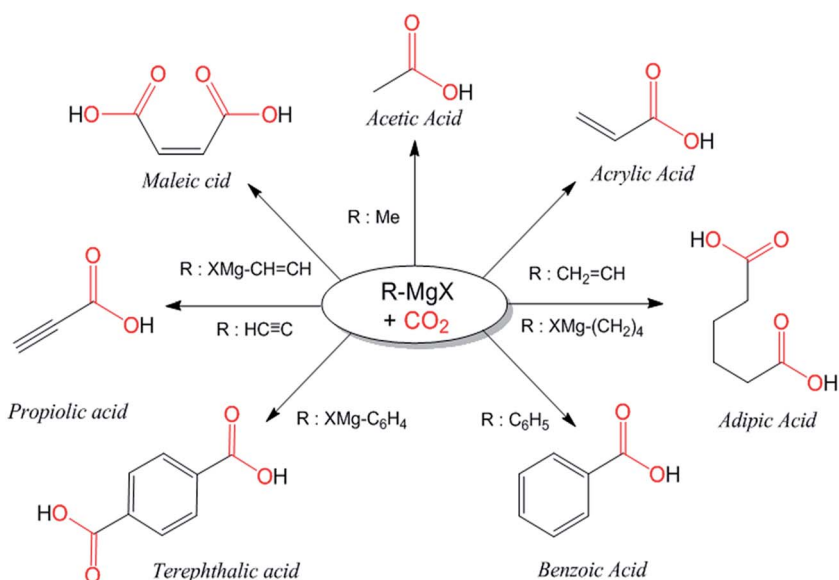


Fig. 3 A series of potential CO_2 Grignard products of potentially industrial significance.

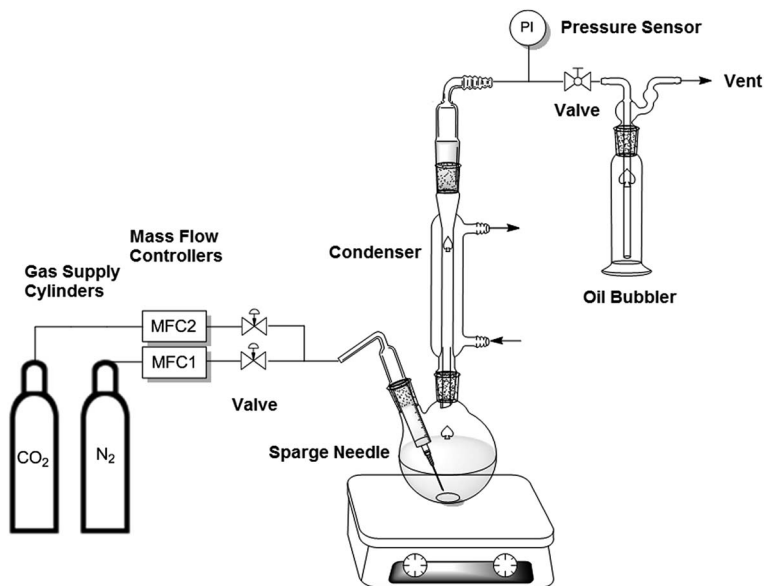


Fig. 4 Schematic of the gas sparging reaction system.

order to maintain a generally stable CO₂ partial pressure, the pressure drop was monitored intermittently between periods of CO₂ sparging.

As shown in Fig. 5, these reactions were found to proceed cleanly when using gas-phase carbon dioxide bubbled through the Grignard reagent solution. Furthermore, this intermittent sparging process demonstrated clear trends in pressure drop rate, despite the exothermic nature of the reaction causing thermal expansion and vapour generation from the ethereal solvent required for Grignard chemistry. This high degree of reactivity with CO₂ prompted tests with

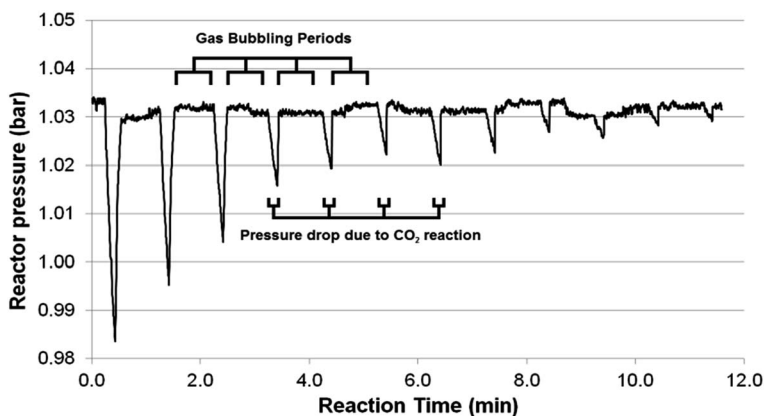


Fig. 5 Typical reaction profile showing rapid pressure drop within the sealed reactor when gas sparging of 50% CO₂/N₂ is paused for 10 seconds every 1 minute.

1 increasingly dilute CO₂ mixtures in nitrogen, comparing the rate of change of
pressure during the CO₂ interruptions.

5 The calculated rate of CO₂ consumption from the rate of pressure drop seen in
Fig. 5 is shown in Fig. 6(a). Fig. 6(b) plots individual natural log plots at varying
gas compositions. These appear initially to be pseudo-first order in the presence
of a constant supply of CO₂. However, while they are superficially similar to
pseudo-first order kinetics, where a large and essentially constant surplus of one
10 reagent is present, the change in rate constant when varying CO₂ concentration
demonstrates that the reaction system is more complex. This is because although
CO₂ concentration is static (as found in pseudo-first order reactions), it is not in

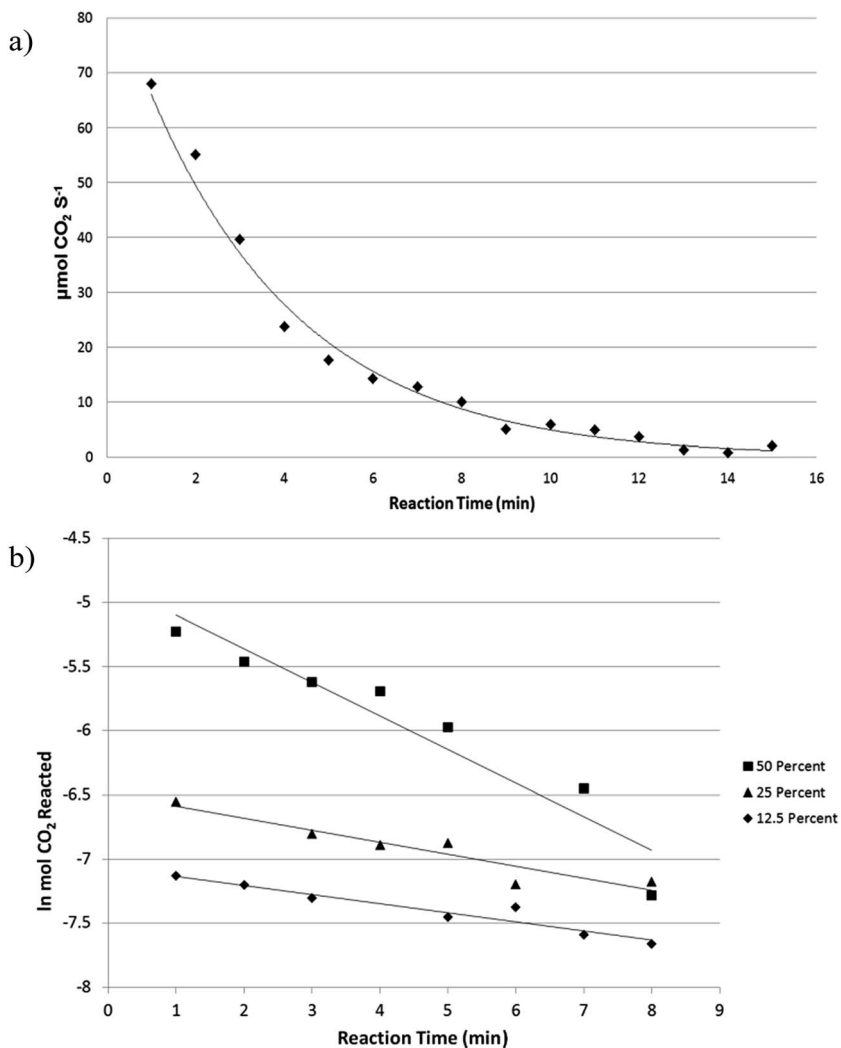


Fig. 6 (a) CO₂ consumption in the Grignard reaction of 1 M MeMgCl with 100% CO₂ by pressure drop detection. (b) Comparison of reaction rate at decreasing CO₂ compositions by dilution in N₂ with total gas flow rate of 100 mL min⁻¹.

1 excess, limiting each rate “constant” to the maximum rate that can be achieved at
the given CO₂ concentration under these conditions. As a result, there is a
decrease in reaction rate “constant” at lower concentrations. Overall combination
of these effects strongly indicates that the rate has a dependence on the
5 concentration of both reagents, appearing to be first order with respect to
Grignard.

Table 3 shows Grignard reaction yields for a selection of alkyl and aryl
substituents using different volumetric CO₂ concentrations. Grignard reactions
are often dramatically affected by the reaction solvent and conditions, so the
10 results shown in Table 3 may not be representative of those that *could* be achieved
in a dedicated process where optimisation had been carried out. However, yields
in almost all cases were high, regardless of the CO₂ concentration used and no
other product was detected in work up mixtures other than the desired carbox-
ylate salt (with the exception of the di-Grignard reagents in entries 5 and 14),
15 indicating the expected extremely high selectivity, although longer reaction times
naturally were required at lower CO₂ concentrations. Using lower concentrations
of CO₂ for the reaction tended to have somewhat reduced yields, however this is
likely due to additional exposure to potential contaminants owing to the longer
20 reaction period. Generation of terephthalic acid from the di-Grignard reagent
derived from 1,4-dibromobenzene proceeded in disappointingly modest yield
with approximately equimolar generation of the mono-substituted product, 4-
bromobenzoic acid. This can be explained by the deactivation of the *para*-position
on generation of the mono-substituted version of the starting Grignard reagent.
25 Using more forcing conditions during the synthesis of the Grignard reagent and
more reactive magnesium precursors has been found to improve yields of reactions
of this type in the past.¹⁹ Once again, optimisation of the reaction conditions
and precursor formation will be essential for high yields to be realised.

30 Potential side reactions in a capture context

With the exception of the last entry in Table 3, all reactions were carried out in the
absence of oxygen. However, in a genuine reactive capture scenario, non-
negligible quantities of oxygen would be present and would likely represent the
35 largest threat of unwanted side reactions when using a dried flue gas stream.
Commonly quoted figures for such streams usually cite O₂ concentrations of
around 3% by volume although this figure can vary dependent on combustion
process and fuel.²⁰

Oxygen is thought to react with Grignard reagents *via* the formation of
40 peroxides, which disproportionate to form the corresponding alcohols after
quenching with aqueous acid (Scheme 2).²¹

Due to their sensitivity and explosive nature, the formation of any organic
hydroperoxides, potentially by quenching the product from the first reaction
45 shown above, would be very troublesome to a potential Grignard process.
Thankfully, prior investigation of these species has shown that the second reaction
in Scheme 2 is extremely rapid in comparison with the first, keeping peroxide
concentrations negligible and preventing their isolation except when the reaction
mixture is both saturated with oxygen and very cold.²² Uncatalysed, the overall
50 reaction of Grignard with oxygen at room temperature is generally slow and has a
poor yield in comparison with that with CO₂. This is exacerbated when the

Table 3 Comparison of yields using pure CO₂ and dilute CO₂/N₂ mixtures with a selection of Grignard agents

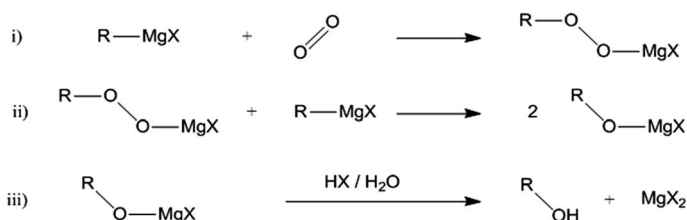
Entry	R	CO ₂ (vol%)	Yield ^a (%)	Time (min)
1	Me-	100	82.5	20
2	CH ₃ CH ₂ -	100	91.8	20
3	iPr-	100	78.1	20
4	Ph-	100	92.4	20
5	XMg-Ph-	100	41.2 ^b	20
6	H ₂ C=CH-	100	95.2	20
7	H ₂ C=C(CH ₃)-	100	89.7	20
8	Me-	50	81.2	25
9	Me-	25	79.2	45
10	Me-	12.5	80.1	60
11	CH ₃ CH ₂ -	12.5	88.9	60
12	iPr-	12.5	74.2	60
13	Ph-	12.5	88.4	60
14	XMg-Ph-	12.5	42.1 ^b	60
15	H ₂ C=CH-	12.5	95.0	60
16	H ₂ C=C(CH ₃)-	12.5	81.1	60
17	Me-	0.05 ^c	0.09	360

^a Yield of isolated sodium carboxylate salt following NaOH quenching of the product.

^b Monocarboxylated product, *p*-bromobenzoic acid isolated in equimolar yield with terephthalic acid. ^c Dry compressed air used.

Grignard reaction is carried out in a volatile ethereal solution such as diethyl ether. The ether is thought to form a protective blanket of solvent vapour at ambient or elevated temperatures.²³ However, this blanket effect may actually be an over-simplification of a more complex process than first thought since, in entry 17, the dry air was sparged through the reaction mixture in the same fashion as the other runs.

Previous literature measurements of reaction rates of simple diethyl ether-solvated alkyl Grignards at room temperature with pure oxygen atmospheres demonstrated that over the course of an hour up to 43% of the initial Grignard reagent would react.²³ These results have shown that, with excess oxygen present, this reaction has pseudo-zeroth order characteristics, reacting at a steady rate of $6.67 \times 10^{-7} \text{ mol s}^{-1}$. For comparison, the corresponding pure CO₂ atmosphere experiments demonstrate an initial reaction rate of $0.1087 \text{ mol s}^{-1}$, and an average reaction rate over the course of the reaction of approximately 5.9×10^{-3}

**Scheme 2** Generalised reaction of a Grignard reagent with oxygen.

1 mol s⁻¹ some 8850 times faster. Optimised CO₂-liquid contacting would be likely
to improve this reaction rate further.

2 The reactions carried out here, shown in Fig. 6(b) and Table 2, have demon-
3 strated that even when using 12.5% volume CO₂ gas, the addition of CO₂ is
4 comparatively rapid compared with the literature values for O₂. The discrepancy
5 in the reactivity of the two species is further demonstrated by entry 17 in Table 3,
6 where compressed air, passed through a Drierite™ column, was used as the CO₂
7 source. In dry air there is more than 500 times more oxygen than carbon dioxide
8 by volume, yet a small yield of the acetate product was isolated. While this by no
9 means demonstrates viability of atmospheric CO₂ utilisation by Grignard
10 reagents, it confirms that under the right reaction conditions, the yield reduction
11 caused by oxidation could be minimised, especially in oxygen-poor environments.

12 Other trace gases, especially the sulfur oxides, if dry, will also interfere with the
13 reaction, generating the corresponding sulfinic acids (Scheme 3).²⁴

14 While this process consumes the reagent and would diminish efficiency and
15 selectivity, unlike with some reactive capture agents such as MEA, there is no
16 irreversible loss of the capture agent by interaction with the sulfur.²⁵ In the case
17 being explored here, the magnesium chloride product is the same as that found in
18 the reaction with CO₂.

19 The other major acidic gases, nitrogen oxides, are not known to react partic-
20 ularly with Grignard reagents without the presence of a transition metal catalyst.
21 With these catalysts present, nitrous oxide, and also oxygen as previously
22 mentioned, promote homocoupling of the alkyl or aryl moieties present or form
23 other compounds such as hydrazones.²⁶

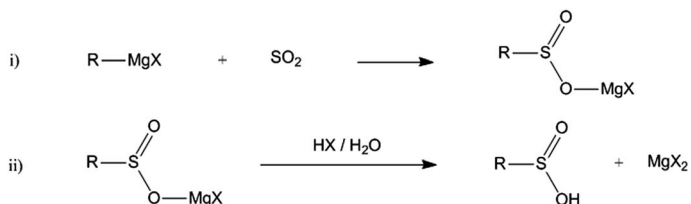
24 In general, side reactions of this type are obstacles for all flue gas capture
25 processes. However, as discussed above, the high reactivity of the Grignard
26 reagents throws this into sharp focus. The question remains: in an optimistic
27 scenario where these problems have been overcome or mitigated, what would be
28 the cost of a Grignard CDU process?

32 Calculating costs of a Grignard CDU process

33 Naturally, the fact that a stoichiometric quantity of the magnesium reagent is
34 required for the capture of the carbon dioxide could lead to the instant conclusion
35 that Grignard reagents are totally unsuitable for CDU from an environmental
36 perspective. However, further consideration of how the Grignard agent may be
37 regenerated by electrolysis, thereby forming an electrolytic magnesium cycle,
38 gives rise to a potentially sustainable, if high-energy, CDU process (Fig. 7). Note
39 that any electricity used in such a process must be derived from low-carbon

42 Table 2 Reaction rate constants of methylmagnesium chloride with CO₂/N₂ gas mixtures

Gas composition (vol% CO ₂)	Pseudo rate constants (s ⁻¹)
100	5.49 × 10 ⁻³
50	4.36 × 10 ⁻³
25	1.56 × 10 ⁻³
12.5	1.19 × 10 ⁻³



Scheme 3 Generalised reactions of a Grignard reagent with sulfur dioxide.

sources or any carbon sequestration potential for the process is immediately reversed as more carbon must be emitted from the electricity production than would be stored in the resultant products.

The net reaction of such a process would be the dehydration-carboxylation of alcohols using CO_2 and H_2 . However, it should be noted that the organohalide reagent required to make the starting Grignard reagent need not be sourced from alcohols. If instead hydrocarbons such as methane or benzene were used, no hydrogen would be required in this process as halogenation of both can be carried out directly from the elemental halide under suitable conditions.

Magnesium and halide regeneration

All steps in such a process are readily achievable and exothermic with the exception of the electrolysis step to regenerate the starting magnesium and halogen. Magnesium regeneration from magnesium dihalide, specifically magnesium dichloride, is already a fully established industrial process, and one of the two main ways that metallic magnesium is manufactured.²⁷

In this process, the magnesium dihalide (typically dichloride) is heated until molten, at $750\text{--}800\text{ }^\circ\text{C}$ and then electrolysed requiring a molar electrode potential of 3.74 V. Typically, industrial magnesium production processes are reported to require 10.5–13.2 kW h per kg, including the drying and purification of the starting magnesium dichloride, which is a significantly energy-intensive part of the overall process.²⁸ In our proposed process, this step could be avoided by using either gaseous or alcoholic HCl (which is available as a by-product of the formation of the initial alkyl chloride from the parent alcohol) to quench the Grignard product. The resulting magnesium chloride would then be much more

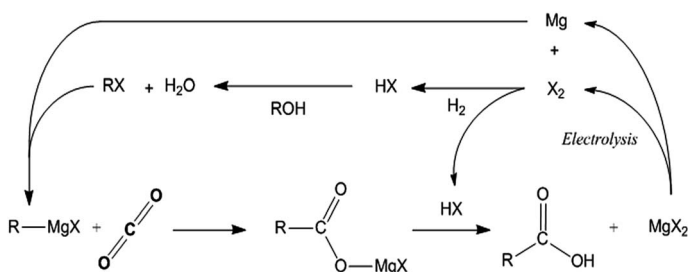


Fig. 7 Grignard reaction with regeneration.

readily dried, reducing electrical costs and opening a reaction pathway to direct formation of potentially valuable esters.

Furthermore, recent advances in the area of magnesium electrolysis particularly focused on the rapid removal of the chlorine gas by-product and have been able to demonstrate a reduction in the energy cost to just 7.0 kW h per kg.²⁹ This is very close to the theoretical minimum energy cost of this process of 6.2 kW h per kg magnesium or 542 kJ mol⁻¹, and represents an electrical efficiency of nearly 89%.

Even taking the more standard magnesium production process energy consumption figures, magnesium potentially represents an efficient energy vector for the net reduction of carbon dioxide by electricity.

The other product of magnesium electrolysis is naturally the elemental halide, which when using alcohols as reagents must be reacted with hydrogen to regenerate the acid for both the alkyl halide formation and the post reaction quenching. This reaction is also very exothermic. Typical hydrogen chlorine burners reach 2000–2500 °C, with up to half of the combustion energy being recoverable.³⁰ It is easy to imagine that this high temperature reaction would further aid the magnesium chloride electrolysis by supplying the temperatures needed to melt the starting magnesium halide salt.

Aspen Plus® modelling

The model shown in Fig. 8 was constructed and used to derive a preliminary techno economic analysis of the reaction of methanol with CO₂ and H₂ *via* methyl magnesium chloride to generate acetic acid. This example was chosen for its simplicity and to be used as a basis to show just how expensive or otherwise a Grignard-based CDU system would be.

The model assumes a magnesium regeneration energy cost of 10.5 kW h kg and a quantitative yield of HCl from the reaction of H₂ and Cl₂, comparable with industrial processes. The extremely exothermic nature of the latter reaction is modelled as supplying all the heat requirements of the plant, but no further energy recovery beyond this is included in the model.

The methanol chlorination reaction is assumed to have a 94% yield, in line with industry performance, however the 5–6% by-product of this reaction,

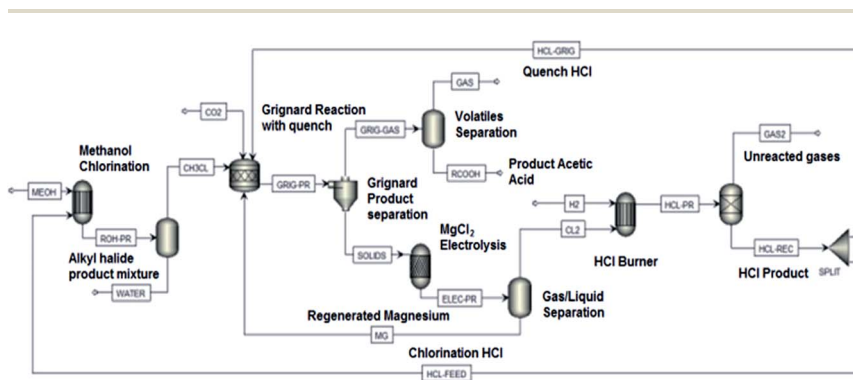


Fig. 8 Aspen Plus® model used for preliminary techno economic assessment of acetic acid production from Grignard reaction of methanol with CO₂.

1 dimethyl ether (DME), is not given a value. The 5–6% of the HCl that would
therefore be expected to remain unreacted from the methanol chlorination step,
5 primarily due to dilution by the by-product water and incomplete chlorination,
can still be potentially utilised for quenching the Grignard reaction and so HCl
utilization would be expected to be quantitative.

For simplicity, both the formation of the Grignard reagent and the subsequent
reaction with CO₂ was assumed to also be quantitative. While this may seem to be
rather optimistic, Grignard formation reactions, under appropriate conditions
10 regularly reach extremely high yields.²¹ Likewise, optimisation of the CO₂ reaction
and workup did not therefore seem to be wholly unreasonable. Furthermore, the
absence of any additional heat recovery from the essentially entirely exothermic
reaction pathway and overlooking the valuation of the DME stream will go some
15 way to offset the ignored costs of a true Grignard-based system, which will
naturally have some yield limitations, especially if an oxygen-containing gas
stream is used.

Tables 4 and 5 summarise the outputs and base conditions of the model
shown in Fig. 8. At first glance, perhaps unsurprisingly, the production cost of
acetic acid using such a process is significantly higher than that of the market
20 value of the product. However, this is primarily an effect of the small production
scale of the model, the scale of which is based on large existing Grignard plants in
the US and UK.³¹ From the point of view of acetic acid, this is an extremely small
scale plant, with commercial acetic acid production facilities reaching a scale
exceeding 500 000 tonnes per year. This point is emphasised by noting that the
25 labour costs exceed that of the electricity and raw materials costs in Table 4.

Approximating the effect of increasing plant scale on production price from
these results was then carried out using the “six-tenths rule”.³² As shown in Fig. 9,
this demonstrates that dramatic reductions in the production cost to levels
comparable with current acetic acid market value could be achieved by increasing
30 reaction scale. For example, a tripling of the reactor linear dimensions (which
would increase reactor volumes and therefore production by around a factor of
27) would drop production cost to around €865 per tonne from the base case of
over €3200. Further size increases may even allow for profitable production of
acetic acid in this way, however caution must be taken when dealing with
35 extended extrapolations of this sort.

Sensitivity analysis was also carried out to determine what effect both raw
material and electricity price would have on the production cost of the acetic acid

Table 4 Aspen Plus® model outputs

Model output	
45 Total capital costs	€4 835 230
Annual cost of capital	€567 944
Annual labour costs	€482 130
Annual electricity costs	€431 161
Annual raw materials costs	€250 444
Total operating costs	€1 367 964
50 Production cost (per tonne)	€3217
Current European acetic acid value (per tonne)	€525

Table 5 Model calculation notes

 Base case conditions, model notes and assumptions

Methanol	350 € per tonne
Hydrogen	4700 € per tonne
Carbon dioxide	12 € per tonne
Electricity supply	17 € kW ⁻¹ h ⁻¹ ; 170 € MW ⁻¹ h ⁻¹
Plant lifetime	20 years
Interest rate	10%
Production scale	602 tonne per a

(Fig. 10). Here, we can see that by far the most important cost is that of the electricity, as might be expected for an electrochemical cycle, with each change in the price per megawatt hour causing more than a four-fold change in production cost. The electricity figure used in the base case model in Table 5 is a relatively high one, representing the requisite renewable electricity, but this figure could easily be halved by more developed lower-cost low carbon sources. Dropping electricity costs in this way to €85 per MW h, within reported ranges for onshore wind and large scale photovoltaic sources, would then decrease production costs by over €360 per tonne.³³ This effect would proportionally complement any drop in production cost by increasing the reaction scale.

Other potential products

As previously mentioned, acetic acid was chosen due to its simplicity; however that same simplicity and acetic acid's market as a bulk chemical makes it an especially difficult target for this process from an economic perspective due to the relatively low value of the product. In comparison, many of the other carboxylic acids shown previously in Fig. 3 have a significantly higher value. This would

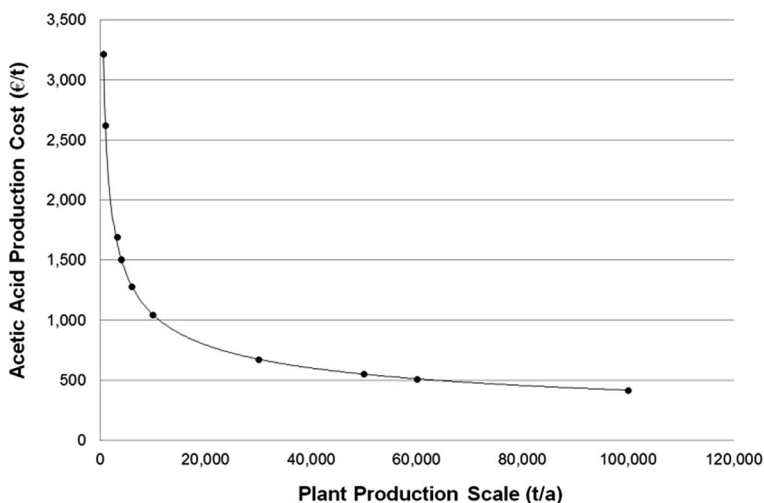


Fig. 9 Projected effect of process scale on production cost.

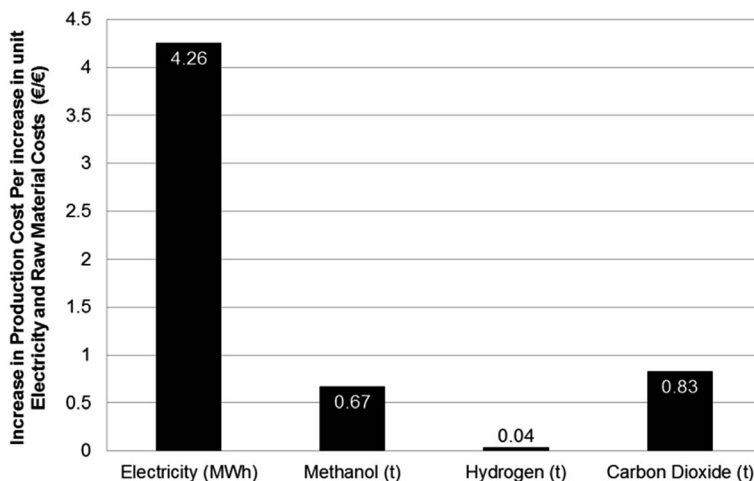


Fig. 10 Model electrical and raw material price sensitivity measured as production cost increase per increase in unit price.

mean that the value added by the addition of CO₂ *via* Grignard chemistry would be larger, making the overall process far more economically enticing, even if the process cost is high.

This effect is especially apparent in the polymer precursors; adipic, acrylic and terephthalic acids where the cost differential between the starting material and product in a putative Grignard process is significantly larger than that of acetic acid from methanol (Fig. 11).

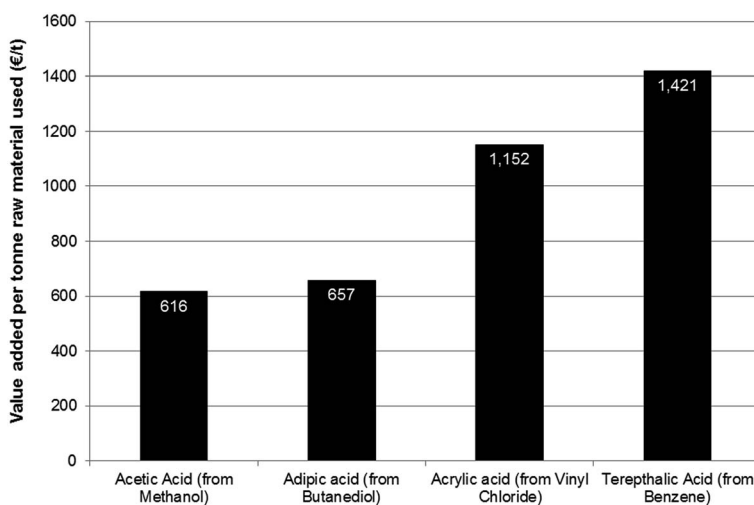


Fig. 11 Value added by addition of CO₂ to starting compound (in brackets). Average 2013 prices used.

1 However, it should be noted that no direct comparison between these putative
processes and that of the acetic acid model should be carried out due to stark
differences in reaction profile, energetics and potential yields.

5 Experimental

10 With the exception of the di-Grignard product of 1,4-dibromobenzoic acid, all
Grignard reagents were purchased in THF solution from Sigma Aldrich and used
without further purification. Reactions were performed using Schlenk techniques
under inert (N₂) atmosphere unless otherwise indicated. HPLC grade THF was
15 dried by storage over freshly-regenerated 3 Å molecular sieves *ca.* 30% by volume.
CO₂, N₂ and compressed air were supplied by BOC-Linde. CO₂ and N₂ mixture
compositions were achieved using a pair of Bronkhorst 100 mL min⁻¹ mass flow
controllers. Compressed air was dried using a Drierite™ 8 Mesh Laboratory
Drying Unit. ¹H NMR spectra were recorded using a Bruker Avance 400 MHz
20 spectrometer with D₂O (99.9% D). Pressure data were recorded using an Omega
PX409USB High Accuracy Pressure Transducer. Grignard concentrations were
verified by titration with 2-butanol (99+%) and 1,10-phenanthroline (99.5%).
Modelling was conducted using Aspen Plus® on AspenTech.

25 General procedure for kinetic investigation of Grignard reaction with dilute CO₂

An oven-dried 2-neck 100 mL round bottom flask with attached empty cold-finger
condenser was charged with THF (20 mL dried over 3 Å molecular sieve) under
nitrogen using Schlenk techniques. Using a needle adapter the flask was then
30 connected to a sparging needle and a flow of 100 mL min⁻¹ of selected CO₂ gas
mixture, venting through a silicone oil bubbler. To avoid any amount of water
condensation within the reactor during set-up, gas flow was carried out for 20
minutes before a freezing salt-ice slurry was added to the cold finger. A normal ice
bath was then placed around the reaction vessel and an additional 30 minutes
35 was given to allow the temperature to equilibrate.

A measured volume of 3 M MeMgCl sufficient to achieve 1 M overall concentration
of the Grignard solution (10 mL) was then swiftly added to the vessel under
positive nitrogen pressure, and reaction timing initiated. Every 60 seconds, the
40 CO₂-containing gas flow in and out of the reactor was paused for a set period of
time (10–20 s) before being resumed, as pressure readings were logged every 0.2
seconds. The reaction was deemed complete when no pressure drop was observed
during a prolonged gas flow pause. Aqueous HCl (3.5 M) was then slowly added to
the reaction mixture until the mixture clarified and gave an acidic reaction on
45 indicator paper. To this mixture aqueous NaOH (1 M) was then added until the
reaction mixture became basic, and a cloudy suspension of salts formed. The
basic mixture was then evaporated until dry by rotary evaporation. An accurately
weighed sample of the dry salt mixture was then dissolved in D₂O (2 mL) with the
addition of DMSO (10 µL) as an internal reference for NMR spectroscopy.

50 ¹H NMR (400 MHz D₂O) δ (ppm): 2.81 (s, 6H, DMSO), 1.94 (s, 3H, CH₃COO).
Integration of the individual peaks is then used to determine carboxylate yield.

Conclusions

In summary, a series of experiments were carried out to determine the reaction kinetics and feasibility of the reaction of Grignard reagents with dilute sources of CO₂ in N₂. From these results, it was determined that high yield reactive capture of dilute CO₂ is possible with Grignard agents. Although oxygen concentration in any gas stream will likely hamper yields, the previously-measured rate of reaction with oxygen has been found to be nearly negligible in comparison of that with CO₂.

A preliminary techno-economic analysis was also carried out, to determine the economic feasibility of such a capture process to be used for production of acetic acid from methanol, using industrially-relevant data and a simplified reaction process model. It determined that when scaling factors were taken into account, the production costs of acetic acid by this method were comparable with existing market prices.

While a more complete costing and detailed assessment could very possibly demonstrate the economic infeasibility of the described process under less favourable conditions, the assessment carried out here suggests that the use of a Grignard reaction cycle to generate acetic acid from methanol is not perhaps as absurd as would be expected.

Acknowledgements

We would like to thank EPSRC for funding from the 4CU Programme Grant (EP/K001329/1), at the University of Sheffield, which has supported this work, G. R. M. D. and I. D., and for the DTA Studentship (D. G. R.). We would also like to thank Innovate UK and BBSRC (BB/M011917/1) for funding R. E. O. We also thank EPSRC for their funding of the CO₂Chem Grand Challenge Network in CDU (EP/K007947/1 & EP/H035702/1).

Notes and references

- 1 M. Aresta, A. Dibenedetto and A. Angelini, *J. CO₂ Util.*, 2013, **3–4**, 65–73.
- 2 M. Perez-Fortez, A. Bocin-Dumitriu and E. Tzimas, *Energy Procedia*, 2014, **63**, 7968–7975.
- 3 P. Styring, D. Jansen, H. de Coninck, H. Reith and K. Armstrong, *Carbon Capture and Utilisation in the Green Economy*, CO₂Chem Media & Publishing, Sheffield, UK, 2011, ISBN: 978-0-9572588-0-8.
- 4 P. Styring and K. Armstrong, *Front. Energy Res.*, 2015, **3**, 1–9.
- 5 Global CCS Institute, *The Global Status of CCS 2014*, Victoria, Australia, 2014.
- 6 K. Armstrong, *Carbon Dioxide Utilisation: Closing the Carbon Cycle*, ed. P. Styring, E. Quadrelli and K. Armstrong, Elsevier, Cambridge, UK, 2014, pp. 237–249, ISBN: 978-0-4446274-6-9.
- 7 Bayer Dream Process: J. Langanke, A. Wolf, J. Hofmann, K. Böhm, M. A. Subhani, T. E. Müller, W. Leitner and C. Gürtler, *Green Chem.*, 2014, **16**, 1865–1870.
- 8 Sunfire, *Sunfire Now Produces Synthetic Fuel from Air, Water and Green Electrical Energy*, Dresden, Germany, 2015.
- 9 Carbon Recycling International, *Emissions to Liquid Fuels*, Reykjavik, Iceland, 2011.

- 1 10 N. von der Assen, J. Jung and A. Bardow, *Energy Environ. Sci.*, 2013, **6**, 2721–2734 and *Green Chem.*
- 11 R. M. Cuellar-Franca and A. Azapagic, *J. CO₂ Util.*, 2015, **9**, 82–102.
- 5 12 E. Catalanotti and M. Pourkashanian, *Carbon Capture: A Technology Assessment*, Leeds, UK, 2012, pp. 15–22.
- 13 P. Strying, *Carbon Dioxide Utilisation: Closing the Carbon Cycle*, ed. P. Strying, E. Quadrelli and K. Armstrong, Elsevier, Cambridge, UK, 2014, pp. 19–31, ISBN: 978-0-4446274-6-9.
- 10 14 V. Grignard, *Compt. Rendu.*, 1900, **130**, 1322–1325.
- 15 Thermodynamic data for reactions, intermediates and products was sourced from: US national Institutes of Standards and Technology (NIST), Chemistry Webbook, <http://webbook.nist.gov/chemistry/>, accessed 23/04/2015.
- 16 E. A. Quadrelli, G. Centi, J.-L. Duplan and S. Perathoner, *ChemSusChem*, 2011, **4**, 1194–1215.
- 15 17 E. Stoye, *Chemistry World News*, RSC, UK, 8 April 2015.
- 18 J. Tammiku, P. Burk and A. Tuulmets, *J. Phys. Chem. A*, 2001, **105**, 8554–8561.
- 19 R. Rieke, *Top. Curr. Chem.*, 1975, **59**, 1–13.
- 20 R. Zevenhoven and P. Kilpinen, *Control of Pollutants in Flue Gases and Flue Gases*, Helsinki, Finland, 2001, pp. 2.1-2.11.
- 21 G. S. Silverman and P. E. Rakita, *Handbook of Grignard Reagents*, Marcel Dekker, New York, USA, 1996, pp. 9–22.
- 22 C. S. Foote, J. Valentine, A. Greenberg and J. F. Liebman, *Active Oxygen In Chemistry*, Springer, Houten, Netherlands, 1995, pp. 55–58; C. Walling and S. A. Buckler, *J. Am. Chem. Soc.*, 1955, **77**, 6032–6038.
- 25 23 M. Goebel and C. Marvel, *J. Am. Chem. Soc.*, 1933, **55**, 1693–1696.
- 24 P. Allen, W. Rehl and P. Fuchs, *J. Org. Chem.*, 1955, **20**, 1237–1239.
- 25 B. R. Strazisar, R. R. Anderson and C. M. White, *Energy Fuels*, 2003, **17**, 1034–1039.
- 30 26 For homo and cross-coupling of Grignard reagents with Nitrous oxide see; G. Kiefer, L. Jeanbourquin and K. Severin, *Angew. Chem., Int. Ed.*, 2013, **52**, 6302–6305. For the same with oxygen see; G. Cahiez, C. Duplais and J. Buendia, *Angew. Chem.*, 2009, **121**, 6859–6862. For formation of hydrazones see; A. Tskhovrebov, E. Solari, R. Scopelliti and K. Severin, *Organometallics*, 2014, **33**, 2405–2408.
- 35 27 I. J. Polmear, *Magnesium and Magnesium Alloys*, ed. M. M. Avedesian and H. Baker, ASM International, OH, USA, 1999, pp. 2–6.
- 28 I. J. Polmear, *Magnesium and Magnesium Alloys*, ed. M. M. Avedesian and H. Baker, ASM International, OH, USA, 1999, pp. 2–6.
- 40 29 G. Demirci and I. Karakaya, *Magnesium Technology*, ed. S. N. Mathaudhu, W. H. Sillekens, N. R. Neelameggham and N. Hort, John Wiley & Sons, Hoboken, NJ, USA, 2012, pp. 59–62.
- 30 SGL Group, *Systems – HCl synthesis*, Meitingen, Germany, 2014.
- 45 31 D. Welter, *Grignard Manufacturing at WeylChem*, Elgin, USA, 2014.
- 32 J. Sweeting, *Project Cost Estimating: Principles and Practice*, IChemE, 1997, pp. 157–159.
- 33 C. Kost, J. N. Mayer, J. Thomsen, N. Hartmann, C. Senkpiel, S. Philipps, S. Nold, S. Lude, N. Saad and T. Schlegl, *Levelized Cost of Electricity, Renewable Energy Technologies*, Fraunhofer Institute ISE, Freiburg, Germany, 2013.
- 50